ALBERT-LUDWIGS-
UNIVERSITÄT FREIBURG

UNIVERSITÉ DE STRASBOURG

THESE en-cotutelle entre:

L'UNIVERSITE DE STRASBOURG

et

ALBERT-LUDWIGS-UNIVERSITÄT DE FREIBURG IM BREISGAU

présentée pour l'obtention du grade de

DOCTEUR DE L'UNIVERSITE DE STRASBOURG

Discipline Chimie

par

Ruth Gabriele HIELSCHER

The role of lipids and nucleotides in the catalytic mechanism of proteins from the respiratory chain: an electrochemical and infrared spectroscopic approach

Soutenue le 15 décembre 2009 devant la commission d'examen:

Prof. Dr. Petra HELLWIG	Directrice de thèse
Prof. Dr. Thorsten FRIEDRICH	Directeur de thèse en-cotutelle
Dr. Isabelle SCHALK	Examinateur
Prof. Dr. Hans-Georg KOCH	Rapporteur externe
Prof. Dr. Erik GOORMAGHTIGH	Rapporteur externe

Table of contents

List of Figures

List of Tables

List of Equations

Biochemical glossary

amino acid	molecules containing both amine and carboxyl functional groups. Amino acids are the structural units that build proteins. They join together to form short polymer chains called peptides or longer chains called either polypeptides or proteins.
amino acid sequence	sequence of amino acids in proteins, so called primary structure
ADP/ATP	adenosine diphosphate/adenosine triphosphate the main energy storage and transfer molecule in the cell
Affinity chromatography	a column chromatographic technique that employs attached functional groups that have a specific affinity for sites on particular proteins
anaerobic/aerobic	in the absence/in the presence of oxygen
Antibiotic	a natural product that inhibits bacterial growth
assembly	assembly of proteins as well as assembly of proteins into the cell
β-sheet	a hydrogen bonded secondary structure formed between two or more extended polypeptide chains, sheet-like structure
bilayer	a double layer of lipid molecules with the hydrophilic ends oriented outward, in contact with water, and the hydrophobic parts oriented inward
Chromatography	a procedure for separating chemically similar molecules
cofactor	a chemical compound that is bound (tightly or loosely) to a protein and is required for the protein biological activity or stability
cytochrome c	protein with a heme c as prothestic group. In protein complexes of the respiratory chain it can be found as cofactor or freely as electron carrier
cytoplasm	part of a cell that is enclosed within the plasma cell in bacteria
cytosol	the liquid part of the cytoplasm, including the macromolecules
denaturation	the disruption of the native folded structure of a nucleic acid or protein molecule; may be due to heat, chemical treatment, or change in pH
detergent	detergent molecule has a hydrophobic tail and hydrophilic head. Detergent can be chosen based on its hydrophilic head, either of anionic, cationic, zwitterionic, or non-ionic. Detergent micelles

	start to form when the critical micelle concentration (CMC) is reached; detergent is used to solublize hydrophobic membrane proteins and stablized them.
DNA	deoxyribonucleic acid; DNA is a nucleic acid that contains the genetic instructions used in the development and functioning of all known living organisms. The main role is the long-term storage of genetic information.
DNA base	the adenine, guanine, cytosine or thymine group attached to a nucleotide or nucleoside.
enzyme	biocatalyst, accelerates a biochemical reaction
Escherichia coli (E. coli)	a gram negative bacterium commonly found in the vertebrate intestine. It is the bacterium most frequently used in the study of biochemistry and genetics.
eukaryote	organism of animals and plants, it contains a nucleus where the gene information is found
gene	DNA part that comprise the information of the assembly of proteins.
gene's expression	gene expression is the process by which information from a gene is used in the synthesis of a functional gene product. These products are often proteins.
gene sequence	sequence of the bases of the DNA
glycolipid	a lipid containig a carbohydrate group
heme	prothestic group of cytochromes that consists of an iron atom containing heterocyclic organic ring called a porphyrin.
inhibitor	compound, that inhibits a reaction in proteins
intermembrane	space between the inner and outer mitochondria membrane
matrix	material in animal and plant cells/within mitochondrion
mutagenesis	a process by which the genetic information of an organism is changed in a stable, heritable manner, either in nature or experimentally by the use of chemicals or radiation.
oxidation/reduction	a reaction in which electrons are transferred from a donor (the reducing agent) to an acceptor molecule (the oxidizing agent).
oxidative phosphorylation	the formation of ATP as the result of the transfer of electrons to oxygen.

oxidoreductase	an enzyme that catalyzes oxidation-reduction reactions
peptide	an organic molecule in which a covalent amide bond is formed between the α-amino group of one amino acid and the α-carboxyl group of another amino acid, the elimination of a water molecule. The resulting connection is called a peptide bond.
periplasm	the region between the inner (cytoplasmic) membrane and the cell wall or outer membrane of a bacterium
phospholipid	a lipid containing hydrophilic charged phosphate group; a component of cell membranes
phosphorylation	the formation of a phosphate derivative of a biomolecule
photosynthesis	biochemical process in which light energy is absorbed by chlorophyll, and is used to fuel the building of sugar molecules.
plasmid	circular loop of DNA in prokaryotes. Eukaryotic DNA is organized into chromosomes.
porphyrin	a planar structure containing four substituted pyrroles covalently joined in a ring and frequently containing a central metal ion.
prokaryote	an unicellular organism that contains a single chromosome, no nucleus, no membrane-bound organelles.
prosthetic group	cofactor that is attached to the enzyme
quinone/quinol	oxidized/reduced form of redoxactive compound which allows the electron transfer between protein complexes, electron carrier
respiratory chain	set of a metalloproteins acting in synergy to reduce O_2 into H_2O accompanied by the creation of a proton electrochemical potential. The latter one is utilized by ATP synthese to transform ADP into ATP and produce the ubiquitous energy for the cell.
site-directed mutagenesis	the process of introducing specific base-pair mutations into a gene.
substrate	a molecule that an enzyme binds and acts upon.
subunit	functional part in proteins

The 20 common amino acids

(Ala, A) Alanine

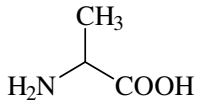

(Arg, R) Arginine

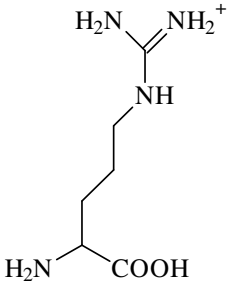

(Asn, N) Asparagine

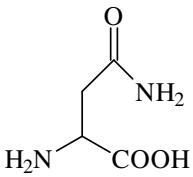

(Asp, D) Aspartic Acid

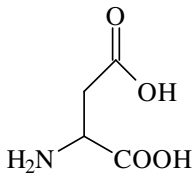

(Cys, C) Cysteine

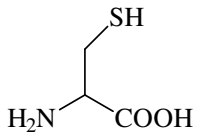

(Gln, Q) Glutamine

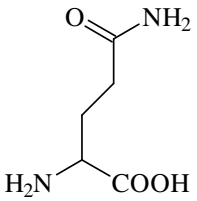

(Glu, E) Glutamic Acid

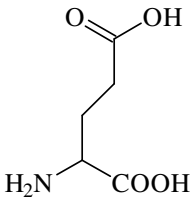

(Gly, G) Glycine

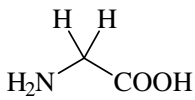

(His, H) Histidine

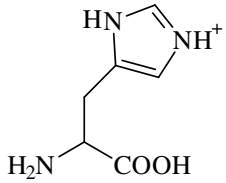

(Ile, I) Isoleucine

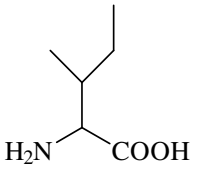

(Leu, L) Leucine

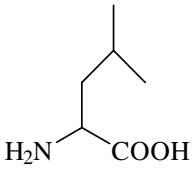

(Lys, K) Lysine

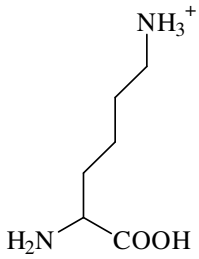

(Met, M) Methionine

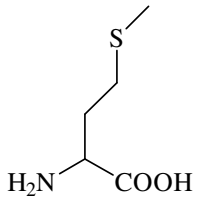

(Phe, F) Phenylalanine

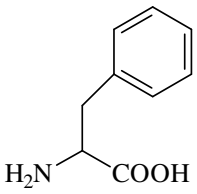

(Pro, P) Proline

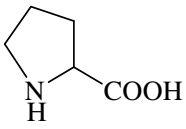

(Ser, S) Serine

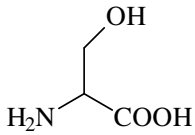

(Thr, T) Threonine

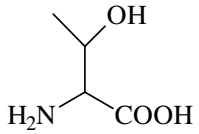

(Trp, W) Tryptophan

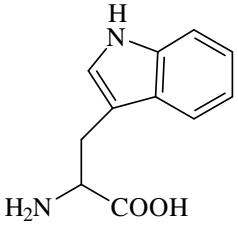

(Tyr, Y) Tyrosine

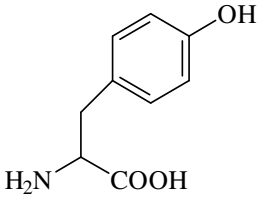

(Val, V) Valine

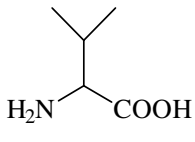

Abbreviations

Å	Angstrom
ADP	Adenosine diphosphate
AE	Auxiliary electrode
ATP	Adenosine triphosphate
ATR	Attenuated total reflection
CL	Cardiolipin
CMC	Critical micelle concentration
Da	Dalton
dGTS	Deuterated triglycine sulfate
DEAE	Diethylaminoethyl
DHPC	1,2-Dihexanoyl-*sn*-glycero-3-phosphatidylcholine
DMPC	1,2-Dimyristol-*sn*-glycero-3-phosphatidylcholine
DTT	Dithiothreitol
EDTA	Ethylenediamine tetra-acetic acid
E_m	Midpoint potential
$FADH_2$	Flavin adenine dinucleotide
FeS	Iron sulfur cluster
FMN	Flavin mononucleotide
FTIR	Fourier transform infrared
IMS	Inter membrane space
IPTG	Isopropyl β-D-thiogalactopyranoside
IR	infrared
IRE	Internal reflecting element
LB	Luria-Bertani medium
MCT	Mercury Cadmium Telluride
NAD^+	Nicotinamide adenine dinucleotide (oxidized form)
NADH	Nicotinamide adenine dinucleotide (reduced form)
NADPH	Nicotinamide adenine dinucleotide phosphate (reduced form)
nuo	NADH:ubiquinone oxidoreductase
PC	Phosphatidylcholine
PE	Phosphatidylethanolamine

PG	Phosphatidylglycerol
PI	Phosphatidylinositol
PMSF	Phenylmethylsulfonyl fluoride
QH_2	Quinol (reduced)
Q	Quinone (oxidized)
RE	Reference electrode
SHE	Standard hydrogen electrode
SHE'	Standard hydrogen electrode pH 7
U	Unit
UM	n-Undecyl β-D-maltopyranoside
UQ	Decylubiquinone
UV	Ultraviolet
v/v	Volume to volume parentage
WE	Working electrode
w/v	Weight to volume parentage
YPG	yeast extract, peptone and glycerol
YP	yeast extract, peptone

Publications

R. Hielscher, T. Wenz, S. Stolpe, C. Hunte, T. Friedrich, P: Hellwig (2006) Monitoring Redox-Dependent Contribution of Lipids in Fourier Transform Infrared Difference Spectra of Complex I from *Escherichia coli*. *Biopolymers* **82**, 291-294.

K.Yang, J. Zhang, A.S. Vakkasoglu, R. Hielscher, J.P. Osborne, J. Hemp, H. Miyoshi, P. Hellwig, and R.B. Gennis (2007) Glutamate 107 in Subunit I of Cytochrome *bd* Quinol Oxidase from *Escherichia coli* Is Protonated and near the Heme *d*/Heme *b* Binuclear Center. *Biochemistry* **46** (11), 3270-3278.

A. Prodöhl, C. Dreher, R. Hielscher, P. Hellwig, D. Schneider (2007) Heterologous expression and *in vitro* assembly of the transmembrane cytochrome b_6. *Prot. Expr. Purif.* **56**, 279-258.

C. Dreher, A. Prodöhl, R. Hielscher, P. Hellwig, and D. Schneider (2008) Multiple Step Assembly of the Transmembrane Cytochrome b_6. *J. Mol. Biol.* **382**, 1057-1065.

T. Pohl, D. Schneider, R. Hielscher, S. Stolpe, K. Dörner, M. Kohlstädt, B. Böttcher, P. Hellwig, and T. Friedrich (2008) Nucleotide-induced conformational changes in the *Escherichia coli* NADH:ubiquinone oxidoreductase (complex I). *Biochem. Soc. Trans.* **36**, 971-975.

M. Kohlstädt, K. Dörner, R. Labatzke, C. Koc, R. Hielscher, E. Schiltz, O. Einsle, P. Hellwig, and T. Friedrich (2008) Heterologous Production, Isolation, Characterization and Crystallization of a Soluble Fragment of the NADH:Ubiquinone Oxidoreductase (Complex I) from *Aquifex aeolicus*. *Biochemistry* **47** (49), 13036-13045.

R. Hielscher, T. Wenz, C. Hunte, P. Hellwig (2009) Monitoring the redox and protonation dependent contributions of cardiolipin in electrochemically induced FTIR difference spectra of the cytochrome bc_1 complex from yeast. *Biochem. Biophys. Acta* **1787** (6), 617-625.

T. Wenz, R. Hielscher, P. Hellwig, H. Schägger, S. Richers, C. Hunte (2009) Role of phospholipids in respiratory cytochrome bc_1 complex catalysis and supercomplex formation. *Biochem. Biophys. Acta* **1787** (6), 609-616.

R. Hielscher, and P. Hellwig, The temperature dependent hydrogen bonding signature of lipids monitored in the far infrared domain. *Chem. Phys. Chem*. accepted (2009)

Abstract

Membrane proteins are essential for life. The interplay with lipids, cofactors, and substrates enables basic processes like respiration, photosynthesis, protein and solute transport, signal transduction and mobility. In this thesis this interplay is studied for different membrane proteins. Particularly, reaction-induced Fourier transform infrared spectroscopy has been used to monitor protein-lipid and protein-nucleotide interaction allowing a better understanding of protein dynamics and its environment. Protein synthesis and integration into a biological membrane are coupled processes. In these regards, the following biological systems were studied:

Cytochrome b_6 is a core subunit of the cytochrome b_6f complex, which is part of the photosynthetic electron transfer chain in chloroplasts and bacteria. This protein is an excellent model not only for analyzing and understanding interactions of single transmembrane helices during folding of a *b*-type cytochrome but also for the determination of possible contributions from cofactors or soluble domains during the folding and assembly of a transmembrane protein. The redox potentials of the reconstituted cytochrome b_6 were measured in the UV/visible spectral range by a spectroelectrochemical approach. Two midpoint potentials E_m at -187 and -86 mV corresponding to the low potential and high potential heme have been found. These spectroscopic properties are similar to that of cytochrome b_6 isolated from natural sources. Mutations based on the binding side of the cofactors influence the reconstitution process. The mutants of H86 and H187, that affect heme b_L, did not assemble hemes. These mutants that affect heme b_H show clearly an alternation of the heme properties in cytochrome b_6. Therefore, the absence of heme b_H and the change in the heme b_L environment involved the midpoint potential of heme b_L. The results indicated a tight connection between heme binding and the heme midpoint potentials.

Hydrogen bonds play an important role for charge shifts or stabilization of the systems. Phospholipids allow clear temperature dependent investigations including different forms of the hydrogen bonding interaction and interaction with water. The temperature dependent infrared absorbance spectra of asolectin upon heating and the reversible process induced upon cooling were obtained in the mid infrared range. The studied spectral range includes the characteristic absorptions of the phospholipid head groups, e.g. the C=O stretching vibration at 1738 cm^{-1} and the asymmetrical PO_2^- stretching mode at 1232/1217 cm^{-1}. The intensity as well as the position of these bands are sensitive towards hydration and phase transition. A broad feature in the far infrared domain was obtained and

corresponds to the hydrogen bonding signature in phospholipids. The far infrared spectra of asolectin as a function of temperature in the spectral range from 300 to 50 cm^{-1} were recorded upon heating and cooling cycle. The different temperature behavior in the mid and far infrared spectral range gives information on structural water and the intermolecular hydrogen bonding pattern in phospholipid bilayers.

Phospholipids are essential for the function of the cytochrome bc_1 complex. Delipidation leads to reversible loss of catalytic activity. Several tightly bound phospholipids including cardiolipin were identified in the X-ray structure of the yeast cytochrome bc_1 complex. Redox-induced FTIR difference spectra were performed after addition of cardiolipin to the lipase A_2 treated enzyme, of asolectin with cardiolipin in direct comparison to the protein in the absence of lipids and wild type. The major change in the amide I range (1690-1620 cm^{-1}), that reflects an alternation of the polypeptide backbone, is only partially compensated. Certainly, not all lipid molecules are integrated in their binding sites, but are attached to the protein. Signals corresponding to lipid molecules arise at 1728 cm^{-1}. All samples studied in infrared have also been analyzed in the visible spectral range. Clearly a shift of the alpha band from 559 to 556 nm can be seen after depletion of the lipids, indicating influence of the lipids on the hemes *b* and heme *c* spectral properties.

The NADH:ubiquinone oxidoreductase, the first complex of the respiratory chain, couples the transfer of electrons from NADH to ubiquinone with the translocation of proton across the biological membrane. Binding of nucleotide NADH induces the active conformation of complex I. Its mechanism is largely unknown due to its complicated structure. It was assumed that conformational changes are caused by the substrate binding and /or the reduction of the complex. Perfusion-induced Fourier transform infrared difference spectra of the complete complex I and for the soluble fragment were performed in the presence of different nucleotides to monitor the large conformational movements upon nucleotide binding and of the reduction of the enzyme. The major alternation was monitored in the amide I range between 1700 and 1600 cm^{-1} and was based on the vibrations due to the protein polypeptide backbone. Furthermore hydrogen deuterium exchange investigations record specifically the amide proton exchange. Amide hydrogen deuterium exchange results in shifts of both amide I and amide II bands of the polypeptide backbone towards lower frequencies.

Résumé

Les protéines membranaires sont essentielles pour la vie. Les interactions entre lipides, cofacteurs, et substrats sont à l'origine de processus fondamentaux comme la respiration, la photosynthèse, le transport des protéines et des solutés, la transduction du signal, et la motilité. Dans cette thèse ces processus sont étudiés pour différentes protéines membranaires. Principalement, des réactions induites ont été suivies par spectroscopie infrarouge à transformée de Fourier dans l'objectif de comprendre les interactions protéine-lipide et protéine-nucléotide. Celles-ci permettent une meilleure compréhension de la dynamique des protéines et de leurs environnements. La synthèse des protéines et leur insertion dans une membrane biologique sont des processus couplés. Pour ces raisons, les systèmes biologiques suivant ont été étudiés :

Le cytochrome b_6 est une sous unité du complexe b_6f. Celui-ci constitue l'un des relais de la chaîne photosynthétique de transfert d'électrons dans les chloroplastes et certaines bactéries. Le cytochrome b_6 est un excellent modèle, non seulement pour l'analyse et la compréhension des interactions entre hélices transmembranaires lors du repliement mais aussi pour l'assemblage d'une protéine transmembranaire. Les potentiels redox du cytochrome b_6 reconstitué ont été déterminés par spectro-électrochimie UV/visible. Deux potentiels de demi-vague E_m sont apparents, le premier à -86 mV pour l'hème facile à réduire (b_H) et le second à -187 mV pour l'hème plus difficile à réduire (b_L). Ces résultats sont similaires à ceux du cytochrome b_6 isolé à partir de sources naturelles. Les mutations autour du site de coordination des cofacteurs ont une influence sur la reconstitution du cytochrome b_6. Les mutations des résidus H86 et H187, qui affectent le site de coordination de l'hème b_L, empêchent l'assemblage des hèmes et annulent les propriétés redox. Les mutations qui affectent l'environnement de l'hème b_H, conduisent clairement à une modification des propriétés des hèmes dans le cytochrome b_6. L'absence de l'hème b_H et la modification de l'environnement de l'hème b_L affecte le potentiel de demi-vague de l'hème b_L. Il y a donc une relation évidente entre la coordination de l'hème et les potentiels de demi-vague.

Les liaisons hydrogène jouent un rôle important dans les déplacements de charge et la stabilisation des systèmes biologiques. Selon la température, les phospholipides sont capables d'induire plusieurs types de liaisons hydrogène intramoléculaires et intermoléculaires mais aussi une interaction avec l'eau. Les spectres du moyen infrarouge de l'asolectine enregistrés en fonction de la température montrent une réversibilité. L'asolectine est un bon modèle de membrane biologique pertinent, car son contenu en phospholipides est analogue à celui que

l'on rencontre dans les systèmes naturels. Les spectres du moyen infrarouge des phospholipides sont bien décrits dans la littérature, et incluent les absorptions caractéristiques des groupements hydrophiles, de l'élongation C=O à 1738 cm^{-1} et de l'élongation antisymétrique du groupement PO_2^- à 1232/1217 cm^{-1}. L'intensité et la position de ces bandes dépendent du taux d'hydratation et de la phase lipidique. Une bande large dans le lointain infrarouge a été observée et correspond à la signature des liaisons hydrogène dans les phospholipides. L'évolution en fonction de la température, dans les domaines du moyen et du lointain infrarouge, nous informe sur la localisation de l'eau et sur le réseau de liaison hydrogène au sein des bicouches de phospholipides.

Les phospholipides sont essentielles pour le fonctionnement du complexe cytochrome bc_1. La suppression des lipides provoque une perte réversible de l'activité catalytique. Plusieurs phospholipides fortement liées, incluant la cardiolipine, ont été identifiées dans la structure du complexe cytochrome bc_1 de la levure déterminée par rayons X. Les spectres IRTF de différence induits par réduction ont été enregistrés pour l'enzyme après ajout de cardiolipine, d'asolectine, et de cardiolipine par comparaison directe avec la protéine en l'absence de lipide et par comparaison avec la forme native. La modification majeure dans la région amide I (1690-1620 cm^{-1}), qui reflète une altération de la chaîne du polypeptide, n'est que partiellement compensée. Tous les lipides ne sont certainement pas intégrés dans leurs sites de liaison mais sont attachés à la protéine. Les signaux qui croissent à 1728 cm^{-1} correspondent aux lipides. Tous les échantillons étudiés par spectroscopie IRTF ont aussi été analysés dans le domaine du visible. On observe clairement un déplacement de la bande alpha centrée à 559 nm vers 556 nm après réduction des lipides, ce qui met en évidence une influence des lipides sur les propriétés spectrales des hemes *b* et *c*.

Le NADH:ubiquinone oxydoréductase, le premier complexe dans la chaîne respiratoire, couple le transfert d'électrons du NADH vers l'ubiquinone avec la translocation de proton à travers la membrane biologique. La liaison du nucléotide NADH à la protéine induit la conformation active du complexe I. Son mécanisme est inconnu en raison de sa structure compliquée. Il est admis que ces changements sont provoqués par la liaison du substrat et/ou la réduction du complexe. Les spectres IRTF induits par perfusion ont été enregistrés en présence de différents nucléotides pour contrôler les mouvements conformationnels de grande amplitude par l'intermédiaire de la liaison des nucléotides et de la réduction de l'enzyme. L'altération majeure a été suivie dans le domaine amide I (entre 1700 et 1600 cm^{-1}) à partir des vibrations dues à la chaîne polypeptidique de la protéine. De plus, les études menées sur l'échange isotopique hydrogène deutérium permettent d'enregistrer

spécifiquement l'échange du proton de la fonction amide. Celui-ci provoque un déplacement des bandes amide I et amide II vers les basses fréquences.

Zusammenfassung

Membranproteine gehören zu den wichtigsten Bausteinen des Lebens. Die Wechselwirkung zwischen Membranproteinen und Lipiden, Kofaktoren und Substraten leitet Basisprozesse wie Zellatmung, Fotosynthese, Protein- und Stofftransport, Signal-Transduktion und Beweglichkeit. In der vorliegenden Arbeit wurden diese Prozesse für verschiedene Membranproteine untersucht. Reaktions-induzierte Fourier Transform Infrarotspektroskopie dient zur Charakterisierung von Protein-Lipid und Protein-Nukleotid Wechselwirkungen, um schließlich die Proteindynamik und seine Umgebung besser zu verstehen. Folgende biologischen Systeme wurden untersucht:

Cytochrom b_6 ist eine Schlüsseluntereinheit des Cytochrom b_6f Komplexes. Cytochrome b_6f Komplex ist ein Bestandteil der fotosynthetischen Elektronentransferkette in Chloroplasten und Bakterien. Cytochrom b_6 dient als Modell für die Charakterisierung und Wechselwirkung von einzelnen Transmembranhelixes während der Faltung von *b*-Typ Cytochrom sowie zur Bestimmung von möglichen Beiträgen von Kofaktoren oder löslichen Domänen während Faltung und Einbau des Transmembranproteins. Die Redoxpotentiale des rekonstituierten Cytochroms b_6 wurden im UV/sichtbaren Spektralbereich gemessen. Zwei Mittelpunktspotentiale E_m bei -187 und -86 mV wurden für beide Häme gefunden. Die spektralen Eigenschaften entsprechen Cytochrom b_6 aus bekannten Spektren. Mutationen, an den Bindestellen der Kofaktoren, beeinflussen den Rekonstitutionsprozess. Bei den Mutanten H86 und H187 an den Bindestellen von Häm b_L wird kein Häm eingebaut. Bei die anderen Mutanten, der b_H Bindestelle, zeigen sich Veränderungen der Hämeigenschaften von Cytochrom b_6. Die Abwesenheit von Häm b_H und die Änderungen des Häm b_L bringen eine Änderung des Mittelpunktspotentials von Häm b_L mit sich. Dieses Ergebnis verdeutlicht die Beziehung zwischen Häm Einbau und den Mittelpunktspotentialen. Es wurde gezeigt, dass das Häm b_L vor dem Häm b_H im Cytochrom b_6 eingebaut wird.

Wasserstoffbrücken spielen eine zentrale Rolle für Ladungsverteilungen oder Stabilisierung von biologischen Systemen. Phospholipide ermöglichen klare temperaturabhängige Untersuchungen einschließlich Wechselwirkungen von

Wasserstoffbrückenbindungen und der Wechselwirkung mit Wasser. Die reversiblen temperaturabhängigen IR Absorptionsspektren von Asolectin wurden im mittelinfraroten Spektralbereich aufgezeichnet. Der untersuchte Spektralbereich beinhaltet die charakteristischen Absorptionen der Phospholipid Kopfgruppe, z.B. die C=O Streckschwingung um 1738 cm^{-1} und die asymmetrische PO_2^- Streckschwingung um 1232/1217 cm^{-1}. Die Intensitäten sowie die Positionen der Signale sind empfindlich gegenüber Hydratation und der Phasenänderung. Ein breites Kontinuum wurde im Ferninfraroten beobachtet und wird der Wasserstoffbrückenbindungs-Signatur von Phospholipiden zugeordnet. Das abweichende Temperaturverhalten im mittel- und ferninfraroten Spektralbereich enthält Informationen von strukturellen Wasser und der intermolekularen Wasserstoffbrückenstruktur von der Phospholipid Doppelschicht.

Phospholipide sind essentiell für die Funktion des Cytochrom bc_1 Komplexes. Delipidation führt zu einem reversiblen Verlust der katalytischen Aktivität des Enzymes. Mehrere fest gebundene Phospholipide, insbesondere Cardiolipin, wurden in früheren Arbeiten mittels Röntgenstrukturanalyse im Cytochrom bc_1 Komplex gefunden. Redox-induzierte FTIR Differenzspektren wurden nach Zugabe von Asolectin und Cardiolipin im Vergleich zur delipidierten Form und zum Wildtyp gemessen. Die meisten Veränderungen im sogenannten Amid I Bereich (1690-1620 cm^{-1}) sind teilweise kompensiert. Typische Signale von Lipid Molekülen werden um 1728 cm^{-1} gefunden. Alle Proben die im Infraroten untersucht wurden, wurden auch im sichtbaren Spektralbereich analysiert. Eine Verschiebung der α-Bande von 559 nach 556 nm wurde nach Delipidation gefunden. Diese Beobachtung zeigt, dass Lipide die spektralen Eigenschaften der *b* Häme und des *c* Häms beeinflussen. Des Weiteren konnten Änderungen der Mittelpunktspotentiale beobachtet werden, die nach Zugabe von Lipiden teilweise kompensiert wurden.

Die NADH:Ubichinon Oxidoreduktase ist der erste Komplex der Atmungskette und koppelt den Elektronentransfer von NADH nach Ubichinon mit der Translokation von Protonen über die biologische Membran. Die Bindung des Nukleotides NADH induziert die aktive Konformation des Komplexes I. Es wird vermutet dass konformative Änderungen durch Substratbindung und/oder Redoxreaktion des gesamten Komplexes verursacht werden. Perfusions-induzierte FTIR Differenzspekren von Komplex I und dessen lösliches Fragment, die NADH Dehydrogenase, wurden durchgeführt, um die großen konformativen Bewegungen während Nukleotidbindung und Reduktion des Enzymes zu beobachten. Die meisten Änderungen wurden im Amid I Bereich zwischen 1700 und 1600 cm^{-1} aufgezeichnet und basieren auf Schwingungen des Protein Rückgrates. Des Weiteren wurden Untersuchungen

nach Wasserstoff-Deuterium Austausch durchgeführt. Der Amid Protonen Austausch induziert vorwiegend in Verschiebungen der Amid I und Amid II Bereiche des Spektrums zu kleineren Wellenzahlen.

Acknowledgements

I would like to thank Prof. Dr. Petra Hellwig for the excellent supervision and for giving me the opportunity to follow her to Strasbourg and working in her lab and in an interdisciplinary field of research. Petra is a model of patience, kindness, availability and a great source of ideas and advices. She will definitely remain an example for me to follow.

I thank Prof. Dr. Thorsten Friedrich for supervision of my work and introducing me to the small part of the big field of biochemistry.

Thanks to my colleagues in Strasbourg Youssef, Yashvin, Julian, Nesrine, Aurelien, Martine and Laurent for their moral support.

Special thanks to Mariana and Fred for reading this manuscript and discussions.

Thanks to my colleagues in Freiburg, Katerina for helping me during the protein purifications and working with the fermenter, thanks to Tom, Markus and Daniel for the discussions and thanks to Udo, Heiko and Ramona.

Thanks to my cooperation Carolin Dreher and Dirk Schneider (University of Freiburg), and Tina Wenz and Carola Hunte (University of Leed) for the samples and the discussions.

I am extremely grateful to Claude and Mamadou for their friendship and support during the time in Strasbourg.

I am very grateful to Christiane Moster, for her excellent help in the world of administration.

I especially thank my family, my mother and my twin sister Ute, my two brothers, Thomas and Simon, for supporting me in all aspects of my life and for always being their.

I would like to thank Jennifer Wytko for correction my English of this manuscript.

Finally, I would like to thank the “Volkswagen Stiftung” and the “Deutsch-Französische Hochschule” as well as the “Centre National de la Recherche Scientifique (CNRS)”, “Agence Nationale de la Recherche (ANR)” and Université de Strasbourg for their financial support.

1 Introduction

1.1 The biological cell

The living cell is the smallest structural and functional unit of all known living organisms. Cells can be divided into two types, the unicellular prokaryotic type (A), such as most bacteria, and the multicellular eukaryotic type (B), found in animal and plant cells. The cells of plants and animals are highly structured as illustrated in Figure 1.1. The major difference between prokaryotes and eukaryotes is that eukaryotic cells contain membrane-bound compartments in which specific metabolic activities take place. Prokaryotic cells are simple in structure, with no recognizable organelles. They have an outer cell wall that gives them shape. Under the rigid cell wall is the more fluid cell membrane and the cytoplasm is enclosed within the cell membrane.

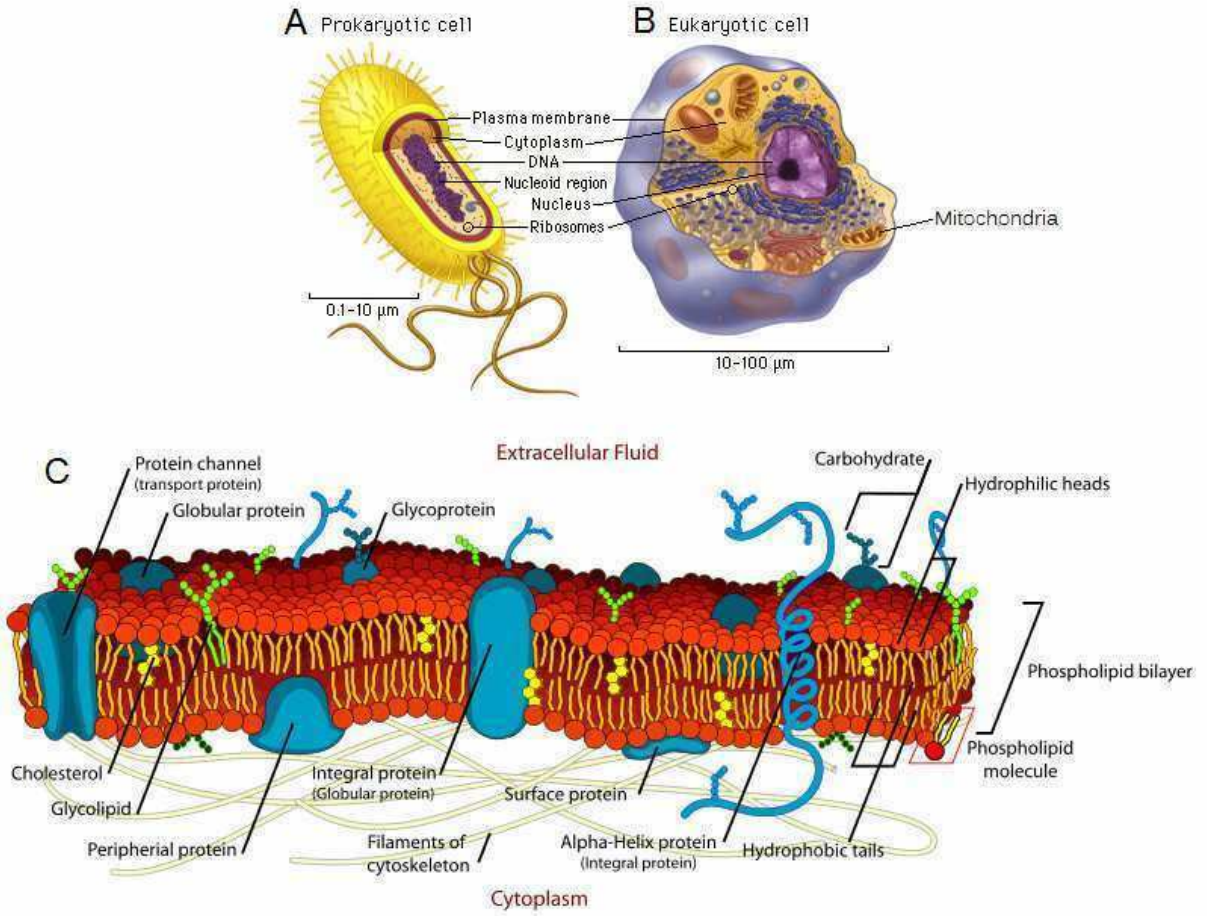

Figure 1.1: Assembly of prokaryotic (A) and eukaryotic cell (B). The model of the fluid mosaic model is illustrated in (C) according to Singer and Nicolson (1972). Integral and peripheral proteins and a number of other compounds are located in a phospholipid bilayer (for more details, see biochemical glossary).

Membranes are the natural border region of cells and subcellular compartments. Biological membranes are composed of a large number of different phospholipids and proteins. They are formed by very complex bilayer and must fulfill multiple functions in close and precise interaction, for instance oxidative phosphorylation and photosynthesis. Singer and Nicolson (1972) have published a fluid mosaic model of the structure of biological membranes. According to the fluid mosaic model in Figure 1.1 (C) the phospholipid bilayer can be considered as a two-dimensional liquid where all lipids and protein molecules diffuse more or less freely. Proteins in the cell membranes may be integral or peripheral.

The membrane bilayer is mainly composed of phospholipids, sphingomyelins, and cholesterol. In typical membrane phospholipids the phosphate group is esterified with an additional alcohol function, e. g. in phosphatidylcholine (PC), phosphatidylethanolamine (PE), phosphatidylglycerol (PG) and cardiolipin (CL) (Figure 1.2). Depending on the structure of the polar region, these phospholipid molecules are neutral at physiological pH value (zwitterionic: PC and PE) or exhibit a negative surface charge (PG, CL).

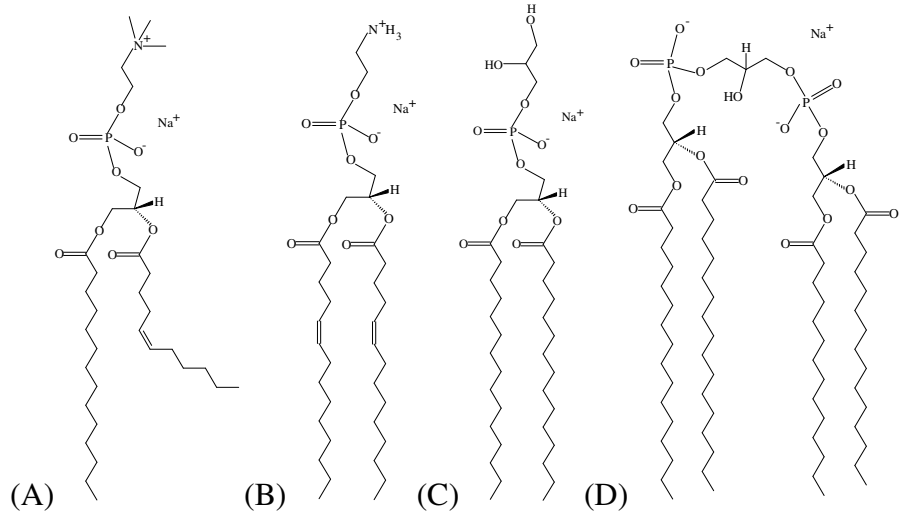

Figure 1.2: Typical membrane phospholipids like PC (A), PE (B), PG (C) and CL (D) with their unpolar hydrophobic hydrocarbon chains and polar hydrophilic head groups. The hydrocarbon chains can be saturated or unsaturated (containing one or more double bonds), e.g. seen for PC and PE.

One of the most important properties of a phospholipid bilayer is the fluidity of the lipid molecules and how this mobility changes with temperature. The phospholipid bilayer has a number of characteristic temperature dependent phase transitions (Eibl, 1984; Boggs, 1987; Lewis and McElhaney, 1996). For the heating step, the main transition is a change from an ordered to a fluid phase, alternatively from the crystalline or gel-phase to the so called

liquid or liquid-crystalline state as seen in Figure 1.3. The two phases differ in the packing density of the hydrocarbon chains. In the gel phase (A), the fatty acids are tightly packed with an all-*trans* conformation, whereas the liquid-crystalline phase (B) represents a more loosely packed matrix (*gauche* conformation).

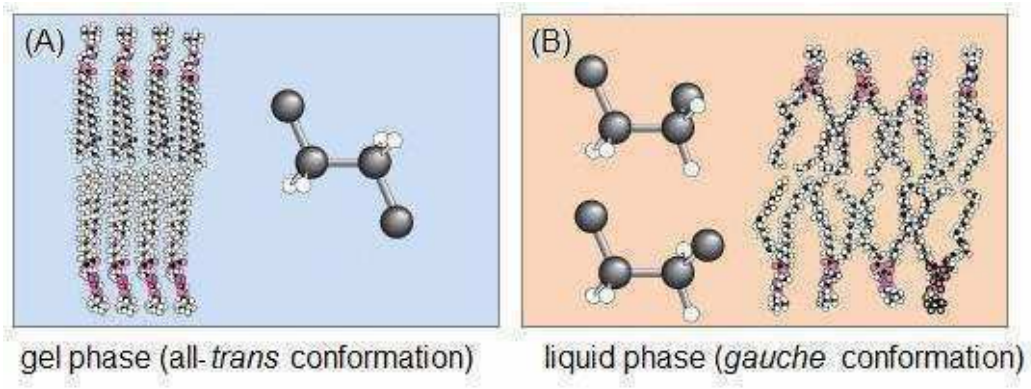

Figure 1.3: Scheme of the temperature-dependent phase transition behavior of a phospholipid bilayer. In (A) is shown the gel phase and (B) the liquid-crystalline phase.

Other properties of phospholipids can be described for the structural variations in aqueous solution. All membrane forming phospholipids contain both hydrophobic as well as hydrophilic constituents: they are amphiphilic. In an aqueous environment the phospholipids spontaneously self-assemble into structures that minimize contact between water molecules and the hydrophobic components of the lipids if their concentration exceeds a critical concentration, the so called critical micelle concentration (CMC). The type of aggregate formed depends not only on the chemical structure of the phospholipids but also on the physical behavior such as the surface charge, temperature, and the ionic environment. The most important types of organized structures (micelles, inverted micelle, lipid bilayer, and vesicles) can be convincingly explained (Figure 1.4).

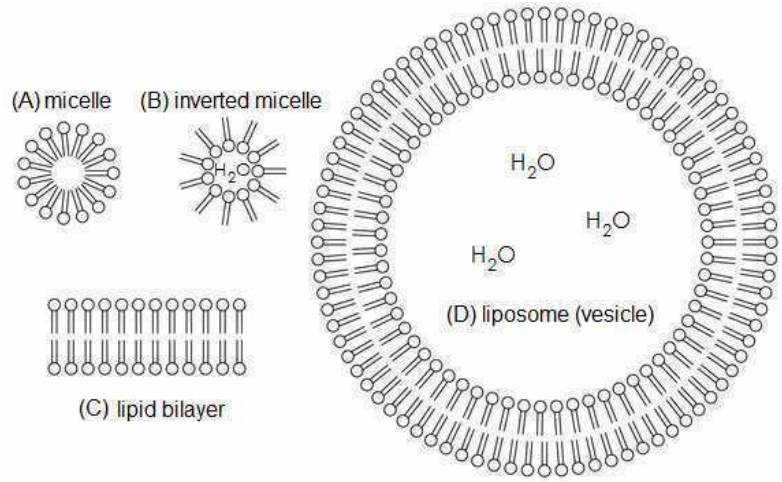

Figure 1.4: The organization of phospholipids in aqueous environment.

The decisive parameter of formation is the ratio of the relative contribution of the apolar and polar parts of the lipid. Phospholipid bilayers can form spheres enclosing water residues, so called vesicles or liposomes. In micelles, which differ, phospholipids are oriented towards the water molecules and the hydrocarbon chains congregate to form an apolar interior. No water molecules are found inside a micelle, in contrast to inverted micelles which have a large apolar region. Like vesicles, the inverted micelles enclose water molecules.

The physical properties of phospholipid membranes have been well characterized by means of infrared spectroscopic techniques. Infrared absorbance spectra of phospholipid molecules contain suitable infrared active groups which are specific for their hydrophobic, interfacial, and polar head group domains. For instance, phase transition was investigated for several model membranes using one type of phospholipids as well as mixtures of phospholipids. The mid infrared spectra of these transitions are well understood (Popova *et al.*, 2003; Blume *et al.*, 1988; Désormeaux *et al.*, 1992; Hübner *et al.*, 1991; Mantsch *et al.*, 1981; for a review see Lewis and McElhaney, 1996).

In addition to the specific role of generating a permeability barrier for cellular compartments as well as integration of integral membrane proteins in the bilayer, phospholipids and their derivatives have assigned roles in a number of physiological processes (Dowhan, 1997; Carman and Henry, 1989, Joshi et al., 2009). Cardiolipin is a characteristic phospholipid of the inner mitochondrial membrane (Daum, 1985; Schlame et al., 2000). The anionic lipid head group of cardiolipin was proposed to provide proton conducting pathways at membrane surfaces (Haines and Dencher, 2002) and it forms an internal hydrogen bonding network within its two protonable phosphate groups as monitored by means of infrared spectroscopy (Hübner et al., 1991). Furthermore evidence emerged that lipids play a role in: the catalytic activity of proteins (Lee, 2004), protein translocation (de Vrije et al., 1988), membrane protein topology (van Klompenburg et al., 1997), the transporter function (Bogdanov et al., 1996), membrane protein folding (Bogdanov and Dowhan, 1999), thermal stability (Fyfe et al., 2002), and supercomplex formation (Pfeiffer et al., 2003).

1.2 Respiratory chain and oxidative phosphorylation

The nucleotide adenosine triphosphate (ATP) is the main energy unit of the living cell. The synthesis of ATP mainly is catalyzed by ATP synthases which are energetically linked to the so called respiratory chain. This process is also called oxidative phosphorylation. In bacteria, the oxidative phosphorylation takes place in the plasma membrane. In eukaryotes, it occurs in the inner mitochondrial membrane of mitochondria. Oxidative phosphorylation comprises five multisubunit membrane protein complexes of the respiratory electron transfer chain. The role of the electron transfer chain in eukaryotic respiration couples a series of exergonic redox reactions to the translocation of protons across the inner mitochondrial membrane into the intermembrane space. The coupling of ATP synthesis by means of an electrochemical proton gradient across the membrane was described by Mitchell as the chemiosmotic hypothesis (Mitchell, 1961).

The respiratory transfer chain includes four large multisubunit membrane protein complexes which mediate the transfer of electrons from the products of glycolysis and the Krebs cycle to molecular oxygen (see Figure 1.5). Three complexes are coupled to proton translocation.

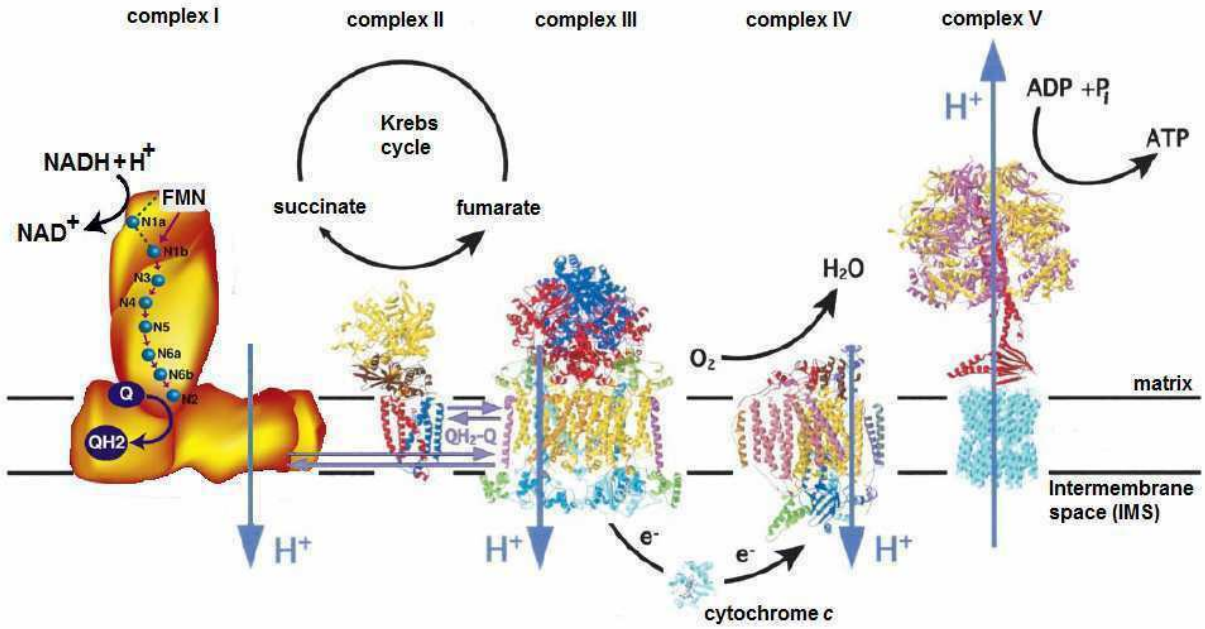

Figure 1.5: Overview of structure and function of the respiratory electron transfer chain (according to Cecchini et al., 2003). Complex I model is presented according to Lazarou et al. (2009).

In detail, enzymes within the Krebs cycle stepwise oxidize acetyl coenzyme A to CO_2, and thereby reduce three nicotinamide adenine dinucleotides (NADH) and one flavin adenine

dinucleotide ($FADH_2$) per cycle. NADH is then the substrate of the NADH:ubiquinone oxidoreductase (the so called respiratory complex I) whereas $FADH_2$ is the substrate of the intrinsic membrane bound complex II (succinate:ubiquinone oxidoreductase). Complex I and II reduce the lipophilic electron carrier ubiquinone to ubiquinol, which is the substrate of the third complex, the ubiquinol:cytochrome *c* oxidoreductase (complex III). Complex III reduces the soluble cytochrome *c* in the intermembrane space. Cytochrome *c* transfers electrons to complex IV, the cytochrome *c* oxidase. Complex IV finally reduces oxygen to H_2O. Electron transfer through complexes I, III and IV is coupled to translocation of protons across the inner mitochondrial membrane. The established gradient of protons drives ATP production by complex V, the F_1-F_0 ATP synthase.

The next sections focus on the respiratory chain complexes that were investigated in this work, namely complex I and III.

1.2.1 NADH:ubiquinone oxidoreductase (complex I)

NADH:ubiquinone oxidoreductase catalyzes the oxidation of NADH and reduction of ubiquinone coupled to the translocation of protons across the inner membrane of mitochondria or the plasma membrane in prokaryotes as described in equation 1.1 (Weiss et al., 1991; Walker, 1992; Yagi and Matsuno-Yagi, 2003; Brandt, 2006).

$$NADH + Q + 5\,H^+_n \leftrightarrow NAD^+ + QH_2 + 4\,H^+_p$$

Equation 1.1: Catalytic reaction that takes place in the complex I. Q refers to ubiquinone, and H^+_n and H^+_p to the protons translocated from the negative side to the positive side of the membrane.

The mitochondrial complex I, extracted from bovine heart consists of at least 46 different subunits including one flavin mononucleotide, and about eight iron sulfur clusters as redox active cofactors (Hirst et al., 2003; Carroll et al., 2003). This complex has a total mass of about 980 kDa. The bacterial complex I typically consists of 14 subunits and has a mass of about 550 kDa. According to the homology between the bacterial and mitochondrial NADH:ubiquinone oxidoreductase, the prokaryotic complex I is considered to be its minimal structural form (Friedrich et al., 1995; Friedrich and Scheide, 2000). The genes of the *Escherichia coli* complex I are organized in the so called *nuo*-operon (NADH:ubiquinone oxidoreductase) that has about 15,000 base pairs and contains 13 structural genes named

nuoA-N, due to the gene fusion of *nuoC* and *D* (Friedrich, 1998). The *Thermus thermophilus* complex I has an additional non-homologous subunit *nqo15*, has a fold similar to frataxin (a mitochondrial iron chaperone) and an important rolle in FeS center regeneration with a possible connection to the extreme habitat of *T. thermophilus* (Yoon and Cowan, 2003; Sazanov and Hinchliffe, 2006; Hinchliffe et al., 2006). Table 1.1 summerizes the structural genes of *E. coli* complex I in comparison to the complex I of *T. thermophilus*.

Bacteria genes			
E. coli	*T. thermophilus*	location	properties
nuoB	*nqo6*	peripheral arm	N2 [4Fe-4S]
nuoCD	*nqo4*	peripheral arm	
	nqo5	peripheral arm	
nuoE	*nqo2*	peripheral arm	N1a [2Fe-2S]
nuoF	*nqo1*	peripheral arm	NADH binding site, FMN, N3 [4Fe-4S]
nuoG	*nqo3*	peripheral arm	N1b [2Fe-2S], N4, N5, N7 [4Fe-4S]
nuoI	*nqo9*	peripheral arm	N6a, N6b [4Fe-4S]
	nqo15	peripheral arm	unique for *T. thermophilus*
nuoA	*nqo7*	membrane arm	3 transmembrane helices
nuoH	*nqo8*	membrane arm	8 transmembrane helices, ubiquinone binding
nuoJ	*nqo10*	membrane arm	
nuoK	*nqo11*	membrane arm	3 transmembrane helices
nuoL	*nqo12*	membrane arm	13 transmembrane helices
nuoM	*nqo13*	membrane arm	12 transmembrane helices
nuoN	*nqo14*	membrane arm	10 transmembrane helices

Table 1.1: Nomenclature and properties of complex I subunits from *E. coli* and *T. thermophilus* (Friedrich, 1998; Sazanov and Hinchliffe, 2006).

The subunits can be divided into a hydrophobic and hydrophilic domain. *NuoA, nuoH, J* and *nuoK-N* subunits are hydrophobic subunits predicted to fold into approximately 50 α-helices across the membrane (Weidner et al., 1993). These subunits do not contain any known cofactors; though they may provide part of the ubiquinone binding site. The hydrophobic subunits are involved in proton translocation. The *nuoB, nuoCD, nuoE-G* and *nuoI* subunits are hydrophilic and contain all known prosthetic groups, one non-covalently bound flavin mononucleotide (FMN), two binuclear FeS clusters and typically up to six tetranuclear FeS clusters.

Electron microscopic studies show the similarity between structures of complex I from *E. coli* (Guenebaut et al., 1998; Böttcher et al., 2002; Sazanov et al., 2003; Mamedova et al.,

2004), *Aquifex aeolicus* (Peng et al., 2003), *Neurospora crassa* (Guenebaut et al., 1997), *Yarrowia lipolytica* (Brandt, 2006; Djafarzadeh et al., 2000; Zickermann et al., 2003; Radermacher et al., 2006), *Arabidopsis thaliana* (Dudkina et al., 2005) and *bos Taurus*, as depicted in Figure 1.6 (for review see Grigorieff, 1999; Friedrich and Böttcher, 2004; Yagi and Matsuno-Yagi, 2003).

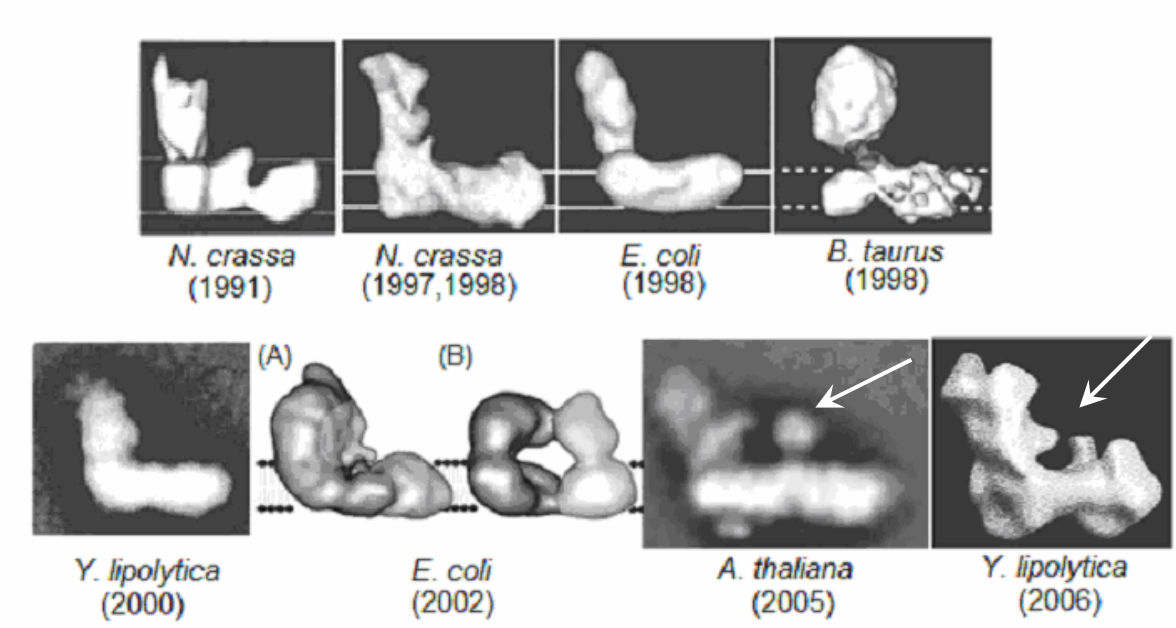

Figure 1.6: 3D models of complex I structure visualized by electron microscopy. The images are arranged in order of publication year*: N. crassa* from Hofhaus et al., 1991; *N. crassa* from Guenebaut et al., 1997; *E. coli* from Guenebaut et al., 1998; *B. Taurus* from Grigorieff, 1998; *Y. lipolytica* from Djafarzadeh et al., 2000; *E. coli* inactive (A) and active form (B) from Böttcher et al., 2002; *A. thaliana* from Dudkina et al., 2005; *Y. lipolytica* from Radermacher et al., 2006.

All structures from the different organisms reflect an L-shaped structure with a peripheral or matrix-located arm and a membrane-bound arm. Böttcher et al., 2002, proposed that the active form (B) of the *E. coli* complex I assumes a horseshoe-like structure and that the L-shaped structure is actually an inactive from. However, this proposal has yet to be clarified by other groups (Sazanov et al., 2003). The structures published in 2005 (of *A. thaliana* complex I) and 2006 (*Y. lipolytica* complex I), however, show some additional density outside of the membrane, as indicated by the arrows.

Recently, X-ray crystallography has been used to obtain a structure of the hydrophilic domain of complex I from *T. thermophilus* at a resolution of 3.3 Å (Sazanov and Hinchliffe, 2006) (Figure 1.7). The seven hydrophobic core subunits and a previously unknown subunit named *nqo15*, which is unique for *T. thermophilus*, were resolved along with the cofactors. The peripheral arm structure accounts for 280 kDa of the total mass of complex I.

2333 residues have been modeled according to the 2510 residues predicted from the sequences. These residues form a Y-shaped structure within approximately 140 Å in height, which is in agreement with previous electron microscopic studies.

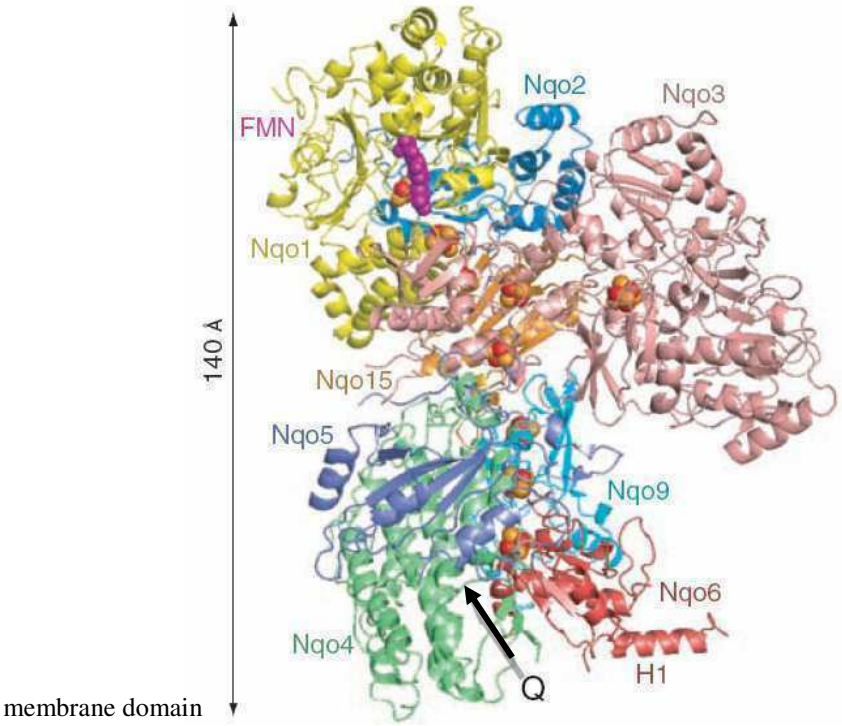

Figure 1.7: Architecture of the hydrophilic domain of *T. thermophilus* complex I at 3.3 Å resolution. Colour is by subunit which are labeled using *T. thermophilus* nomenclature *nqo1-6, nqo9, nqo15*. Atoms of FMN are shown as a purple spheric model; iron and sulfur atoms from the FeS clusters are shown in red and yellow, respectively. A possible quinone binding site (Q) is indicated by an arrow (PDB file 2FUG see Sazanov and Hinchliffe, 2006).

The crystal structure of the peripheral arm of complex I proposed by Sazanov and Hinchliffe (2005, 2006) has confirmed the organization of hydrophilic subunits and their prosthetic groups (Friedrich, 1998). Based on the locations of the prosthetic groups and their midpoint potentials the following electron transfer pathway has been proposed. The electron transfer is initialized due to the binding of NADH. Electron pairs enter complex I by hydride transfer from NADH to FMN and are then transferred to the 4Fe-4S cluster N3, and to the 2Fe-2S cluster N1a (Leif et al., 1995; Verkhovskaya et al., 2008). N3 and N1a clusters are within 14 Å of FMN, the maximum distance for physiological electron transfer (Page et al., 1999). Electron transfer proceeds linearly through clusters N1b, N4 and N5 that are located in the *nuoG* subunit and then transferred to N6a and N6b which are found in the *nuoI* subunit.

Finally, electrons pass onto the highest potential FeS cluster N2 which, in turn, is thought to be able to reduce ubiquinone to ubiquinol in two one electron steps (Sazanov and Hinchliffe, 2006). The electron transfer chain and its energetics are shown in Figure 1.8.

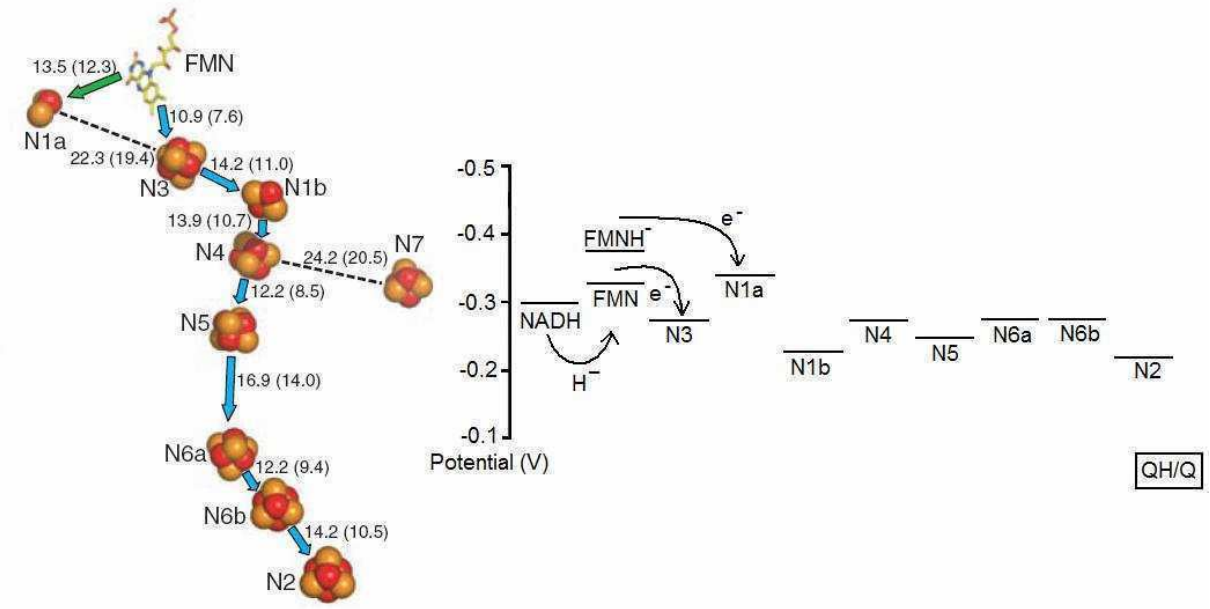

Figure 1.8: Arrangement and energetics of the complex I electron transfer chain. Left: Organization of the FeS clusters of *T. thermophilus* complex I showing the proposed pathway of the electron transfer and center-center transfer distances in Å (edge-edge distances are given in parentheses) (figure from: Sazanov and Hinchliffe, 2006). Right: Schematic view of the electron transfer chain. Standard (pH 7) midpoint potentials are shown for the substrate and redox centers of the *E. coli* complex I (Friedrich et al., 2007).

The mechanism of complex I is still unknown. The mitochondrial as well as the bacteria complex I pumps four protons across the membrane per electron pair transferred from NADH to ubiquinone (Wikström, 1984; Galkin et al., 1999). Two main hypotheses of the coupling process between electron transfer and proton translocation have been proposed: a redox-driven (direct) or a conformational-driven (indirect) coupling. Both are still under debate. The proton translocation in complex I may require two coupling sites (Friedrich, 2001). The redox reaction of the FeS cluster N2 and its interaction with the quinone could be directly linked to a proton translocation (Figure 1.9 A). The midpoint potential of cluster N2 is pH dependent. This indicates that the reduction of N2 is coupled to proton binding (Ohnishi, 1998). N2 is located in subunit NuoB/Nqo6 near the interface of subunit NuoD/Nqo4. Cluster N2 is found only 8 Å from the membrane domain interface (Sazanov and Hinchliffe, 2006). The quinone binding site could be located in a proposed cavity at the

interface between NuoB and NuoD (Savanov and Hinchliffe, 2006). This suggestion is in agreement with the EPR spectroscopic observation of a semiquinone found within 12 Å to cluster N2 (Yano et al., 2005). FTIR spectroscopic and site directed mutagenesis studies have shown that the redox reaction center N2 is coupled within the protonation state of individual amino acids (Hellwig et al., 2000; Flemming et al., 2003a, 2003b; Flemming et al., 2005, 2006). The second proposed coupling site (see Figure 1.9 A) may be described as an indirect conformational driven proton translocation (Friedrich, 2001).

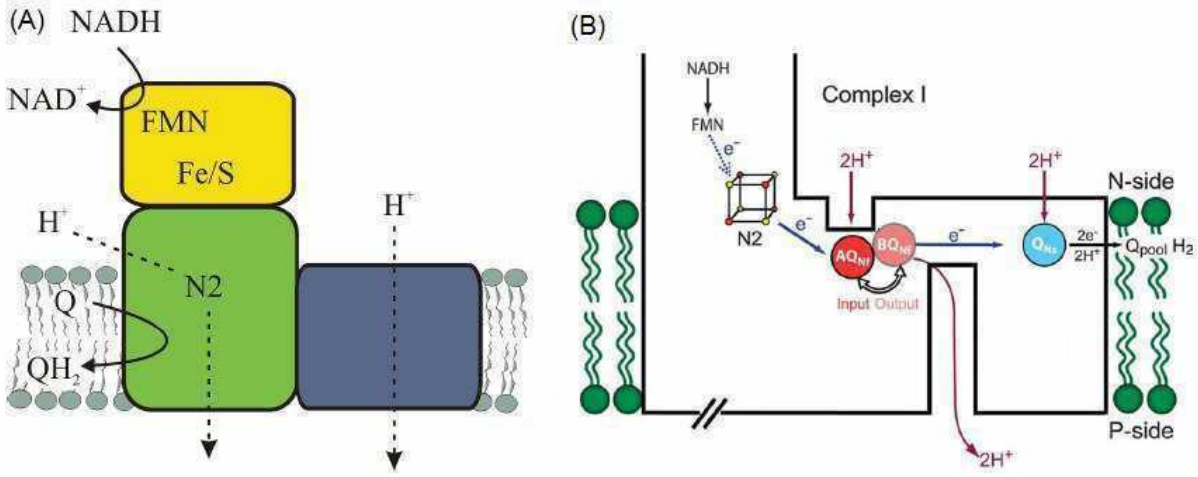

Figure 1.9: Models of coupling process between redox reaction and proton translocation in complex I. (A) proposed mechanism of complex I with two coupling sites. NADH dehydrogenase module is drawn in yellow and contains mainly the redox groups. The FeS cluster N2 is located in the hydrogenase module (green) and is involved in a proton translocation. The transporter module (blue) could participate in an indirect conformational driven proton translocation (Friedrich, 2001). (B) Hypothesis mechanism due to EPR spectroscopic studies of semiquinone. An electron from N2 and two protons from the negative side of the membrane (N-side) are transferred to a semiquinone Q_{Nf}. During a conformational change between state A and state B the environment changes for the quinone before donates an electron to the Q-pool (Ohnishi and Salerno, 2005).

It is widely accepted that the redox reaction of complex I is followed by conformational change (Mamedova et al., 2004, Brandt et al., 2003; Belogrudov and Hatefi, 1994; Sazanov, 2007). However, that the conformational change rules proton translocation is not really clear at the moment. It is assumed that the homologeous Na^+/H^+- and K^+/H^+-antiporter subunits, NuoK, NuoL and NuoM are involved in the coupling (Friedrich and Weiss, 1997; Friedrich, 2001; Mathiesen and Hägerhäll, 2002). Electron microscopic studies have shown that subunits NuoL and NuoM are located at the distal end of the membrane arm of the complex I (Holt et al., 2003; Baranova et al., 2007). If these subunits contributed to the proton translocation, then a conformational change should take place.

In an alternative hypothesis, it was proposed that coupling and proton translocation may be accomplished using a reverse Q-cycle mechanism certainly modified to that of cytochrome bc_1 complex (see chapter 1.2.2) (Dutton et al., 1998). In fact, two semiquinones, named SQ_{Nf} and SQ_{Ns}, were identified in the mitochondrial complex I (see Figure 1.9 B) (Magnitsky et al., 2002; Ohnishi et al., 2005; Yano et al., 2000; Yano et al., 2005). Other Q-cycle based mechanisms have also been proposed (Brand, 1997), but they are less related to known mechanisms of other enzymes and remain speculative (Hirst, 2005).

1.2.2 Cytochrome bc_1 complex

Ubiquinol:cytochrome *c* oxidoreductase, also known as cytochrome bc_1 complex or complex III, belongs to the family of cytochrome *bc* complexes that takes part in cellular respiration (Schulz et al., 2000; Berry et al., 2000). The cytochrome b_6f complex is found in thylakoids and cyanobacterial plasma membrane. This complex is homologeous and functions in photosynthesis (Breyton, 2000). The cytochrome bc_1 complex contains common catalytic core subunits, consisting of the so called Rieske protein (ISP), which has a [2Fe-2S] cluster, a cytochrome c_1 and cytochrome *b*, which carries two *b*-type hemes that are non-covalently bound to the polypeptide chain. The two *b* hemes are described according to their redox potential: heme b_H for the high potential and heme b_L for the low potential. The two quinone binding sites Q_i (inner membrane) and Q_o (outer membrane) are located in cytochrome *b* next to the prosthetic groups. The cytochrome bc_1 complex of *Saccharomyces cerevisiae* (yeast) contains up to seven additional subunits (deVries and Marres, 1987; Hunte et al., 2000).
In recent years, a large number of structures have been resolved by X-ray crystallography for the cytochrome bc_1 complex from bovine (Yu et al., 1999), avian (Zhang et al., 1998), yeast (Hunte et al., 2000; Lange et al., 2001) and bacterial *Rhodobacter capsulatus* (Berry et al., 2004) and with a variety of substrates or inhibitors bound (Gao et al., 2003; Lange and Hunte, 2002; Huang et al., 2005). Figure 1.10 shows the structure of bovine heart cytochrome bc_1 complex with its prosthetic groups as well as the inhibitor's binding sites.

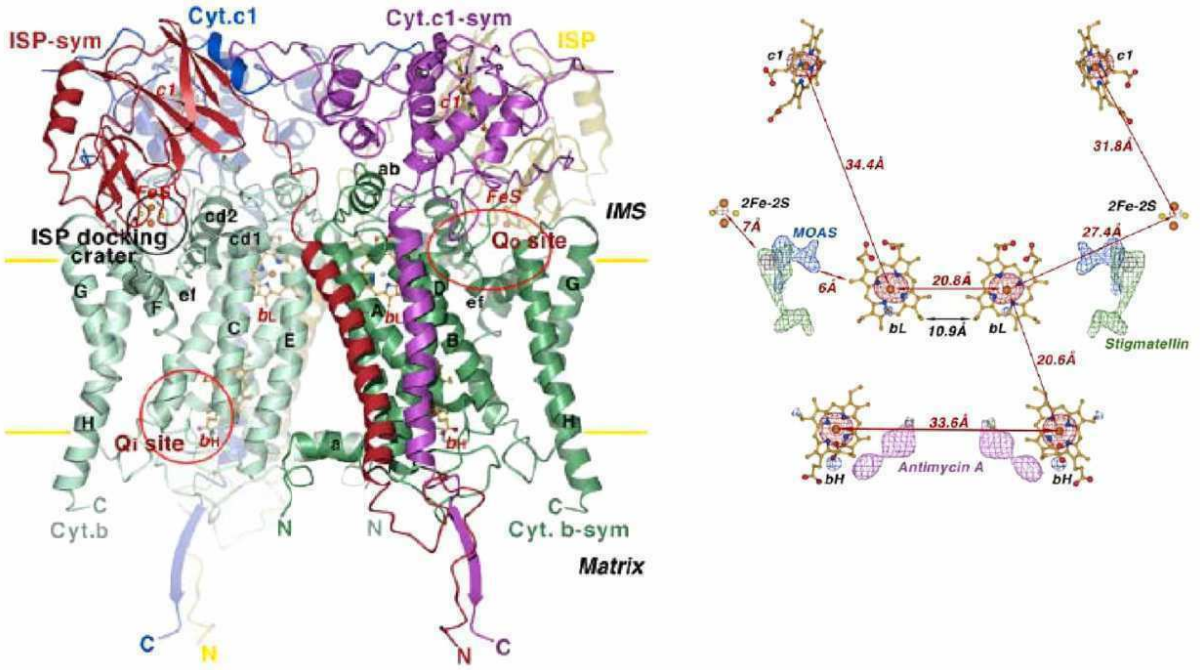

Figure 1.10: Left: Dimeric structural model of the three essential subunits of cytochrome bc_1 complex. Right: Arrangement of prosthetic groups in the dimeric bc_1 complex and the inhibitor binding sites of antimycin A (purple), stigmatellin (green) and myxothiazol (MOAS in blue) (see review Yu et al., 2008).

The mechanism of the enzyme, the so called protonmotive Q cycle, was first proposed by Mitchell (1975, 1976). Subsequently, extensive research into the enzyme mechanism has yielded a reaction scheme for this protonmotive Q mechanism (Crofts and Meinhardt, 1982; Crofts and Wang, 1989; Trumpower, 1990; Crofts, 2004) that remains under debate. The mechanism utilizes two quinone sites (Figure 1.11): the Q_o side is close to the inter membrane space side (IMS) of the membrane and Q_i is near the matrix side. The first electron from the quinol at the Q_o binding site is transferred from the iron sulfur cluster of the Rieske protein through cytochrome c_1 to cytochrome *c*. The latter then reduces the cytochrome *c* oxidase, the terminal acceptor in the mitochondrial system. The second electron is transferred via the two hemes b_L and b_H to the Q_i binding site where bound ubiquinone is reduced to a semiquinone anion radical $QH^{\bullet -}$ (deVries et al., 1980). Following the oxidation of a second ubiquinol at Q_o and reduction of the *b* hemes, semiquinol is reduced to quinol. The two successive reactions lead to an uptake of two protons at Q_i and four protons at Q_o.

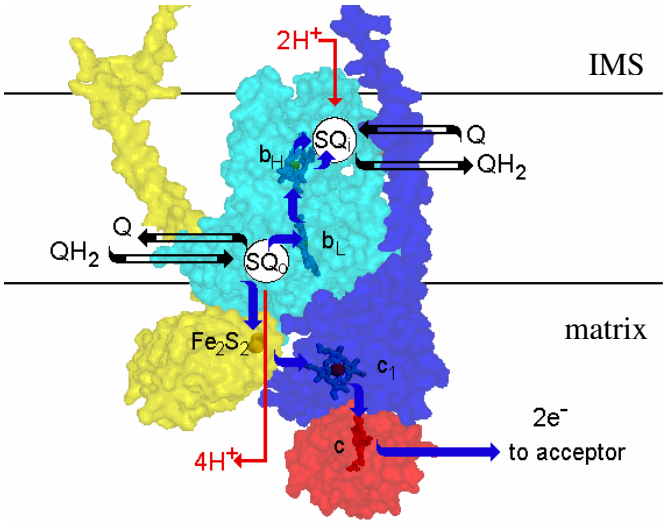

Figure 1.11: Schematic view of the modified protonmotive Q cycle (from Berry et al., 2000). The Q_i and Q_o binding site in cytochrome *b* (cyan) are indicated as SQ_i and SQ_o (due to intermediate semiquinone). The Rieske protein is shown in yellow and the cytochrome c_1 (blue) with bound cytochrome c (red).

1.2.2.1 Role of tightly bound phospholipids in the cytochrome bc_1 complex

The high resolution X-ray structure of the yeast cytochrome bc_1 complex revealed five tightly bound phospholipid molecules including a cardiolipin molecule (CL) as well as one detergent molecule per monomer (Lange et al., 2001; Palsdottir and Hunte, 2004).

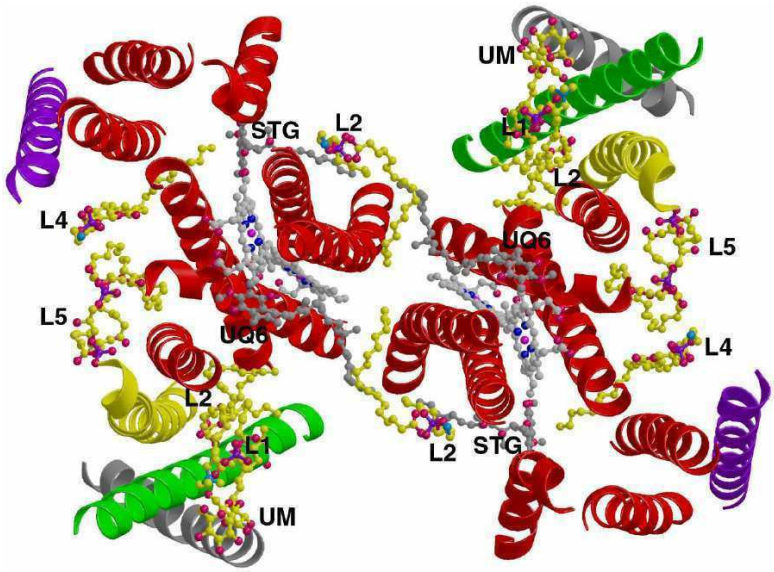

Figure 1.12: Binding of five phospholipids molecules L1 (PC), L2 (PE), L3 (PI not shown), L4 (PE), L5 (CL) and one detergent molecule (UM) in the transmembrane region of the dimeric cytochrome bc_1 complex of yeast. The relative position of the *b* heme cofactors (b_L and b_H) as well as of ubiquinone bound at the Q_i site (UQ6) and stigmatellin bound at the Q_o site (STG) are shown (Lange et al., 2001).

The tightly bound cardiolipin was suggested to have a specific role in the proton uptake pathway at the Q_i site. One of the five identified phospholipids is a phosphatidylinositol (PI) which is unusual because the head group was positioned below the estimated membrane plane (Lange et al., 2001). PI is referred to as an interhelical lipid because it is wrapped around the transmembrane helix of the Rieske protein. Other structural lipids are thought to represent definitely the surrounding annular bilayer (Figure 1.12).

1.2.2.2 The transmembrane cytochrome b_6 from cytochrome b_6f complex

Transmembrane *b* type cytochromes can be found in transmembrane protein complexes such as the succinate dehydrogenase (complex II), cytochrome bc_1 and b_6f complexes, cytochrome *bd* and bo_3 complexes, as well as in photosystem II of higher plants and cyanobacteria (Kalles, 1994). The structure of the cytochrome b_6f complex was resolved recently by X-ray crystallography and, unexpectedly, a third heme molecule (heme c_x, or heme c_i) was found to be covalently bound to cytochrome b_6 (Stroebel et al., 2003; Kurisu et al., 2003). Two heme *b* molecules are ligated by conserved histidine residues, which are located in helices B and D of the protein (Figure 1.13).

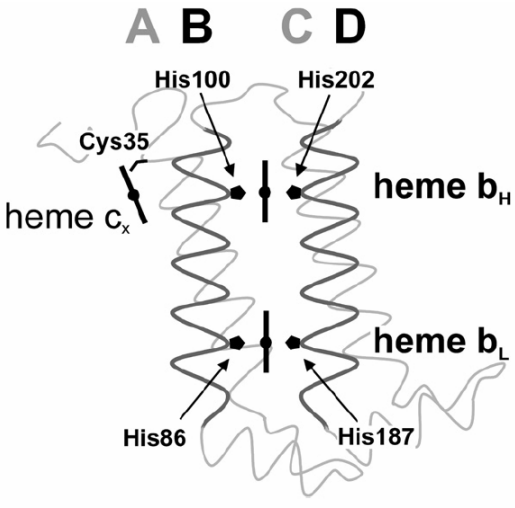

Figure 1.13: Model of the transmembrane cytochrome b_6. The protein spans the membrane with the four transmembrane helices A-D. In helix B, two conserved histidine residues, His86 and His100, serve as axial ligands for heme b_L and b_H. In helix D, His187 and His202 residues also act as axial ligands for the two *b* hemes. The covalently attached heme c_x is bound via Cys35 in helix A to the periphery (reproduced with kind permission from Carolin Dreher (Dreher et al., 2008)).

Cytochrome b_6 from spinach can be heterologously expressed in *Escherichia coli* and the protein can be reconstituted *in vitro* (Kroliczewski and Szczepaniak, 2002; Kroliczewski et al., 2005; Prodöhl et al. 2007). Therefore, cytochrome b_6 could serve as an excellent model system for *in vitro* studies to analyze the role of the protein moiety and of the heme cofactors during assembly of a transmembrane *b* type cytochrome. According to the currently accepted model, individual transmembrane helices integrate independently into a biological membrane. Individual helices associate and assemble to form higher ordered oligomeric structures. Based on this model, interactions between α-helices are important for folding of integral membrane proteins, although other factors, such as binding of cofactors and/or lipids may also be taken into account. Folding, assembly, and stability of soluble cytochromes *b*, or of synthetic soluble cytochrome *b* models have been extensively studied, however, little is known about the assembly and stability of membrane-integrated *b* type cytochromes (Koch and Schneider, 2007).

1.3 Aim of work

This thesis describes the application of reaction induced FTIR spectroscopy on cytochrome bc_1 complex from yeast and NADH:ubiquinone oxidoreductase, the so called complex I, from *Escherichia coli*. The aims of the study were:

i: *Study lipids alone:* Characterize phospholipid interactions in the far infrared domain below 600 cm^{-1}. Since the temperature dependent phase transition of lipids are well characterized in the mid infrared region, analyzing this phase transition in the far infrared is interesting.

ii: *Assembly in the lipid membrane:* Analyze the assembly of the transmembrane cytochrome b_6 from spinach and its mutants by means of UV/visible redox titrations.

iii: *Role of tightly bound lipids:* Differentiate the role of phospholipids tightly bound to the cytochrome bc_1 complex using electrochemically induced FTIR difference and UV/visible spectroscopy. The X-ray structure has shown specifically tightly bound phospholipids, in particular two cardiolipin molecules which seem to be important for the enzyme's activity and catalytic mechanism.

iv: Characterize phospholipids in complex I using electrochemically induced FTIR difference spectroscopy and isotopically labeled phospholipids. It has been

shown that the addition of lipids to complex I increases the enzyme activity, thus phospholipids may play an important role of complex I's mechanism.

v: Using an ATR perfusion cells to study substrate induced ATR difference spectroscopy of complex I and its soluble fragment. First, secondary structure determination is studied upon nucleotide binding. Then, hydrogen deuterium exchange kinetics in the absence and in the presence of nucleotides are studied to analyze the amide proton exchange of NADH dehydrogenase fragment and the entire complex I. Finally, nucleotide induced ATR difference spectra is performed to monitor the conformational movement upon NADH binding.

1.4 Technical approach

The spectroscopic technique used in this work was the ultraviolet (UV)/visible spectroscopy and Fourier transform infrared (FTIR) spectroscopy in the mid and far infrared spectral range. Figure 1.14 illustrates the classification of electromagnetic radiation from the high energetic cosmic radiation to the low energetic radio waves with associated wavelengths and frequencies. Electromagnetic radiation exists as a broad and continuous spectrum and allows different types of interactions with matter.

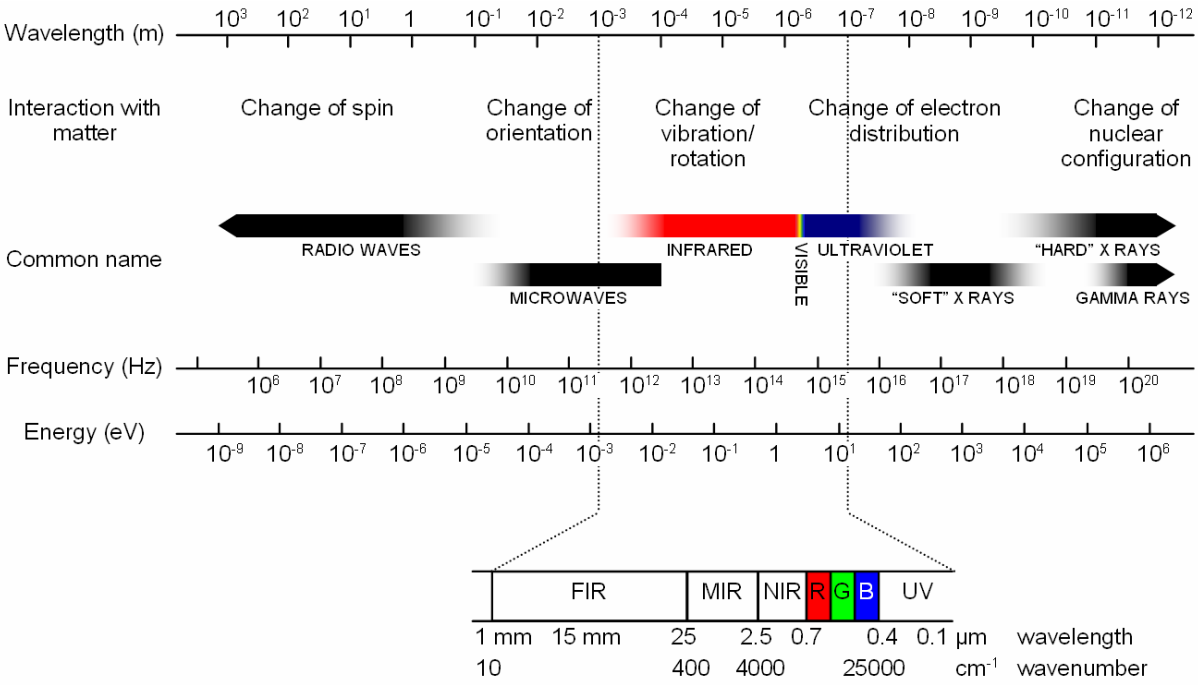

Figure 1.14: Characterization of the electromagnetic spectrum.

IR spectroscopy is the main approach of this work. The technique and its application to biomolecules will be discussed in chapter 1.4.2.

1.4.1 UV/visible spectroscopy

UV/visible spectroscopy involves the absorption of ultraviolet (UV) or visible light by an atom/molecule causing the promotion of an electron from the ground state to an excited electronic state. Electronic transitions are seen between 190 to 800 nm. The energy of the absorbed quantum light corresponds to the difference of the energy between the ground and

excited states. Different types of electronic transitions are observed. The bonding π molecular orbital is occupied by two electrons each with a different spin. The non-bonding η orbital is occupied by two electrons. The transition occurs from the empty anti-bonding π* orbital, which has a higher energy level, and is described as π-π* transition and η-π* transition.

The prosthetic groups mainly investigated in this work were hemes and iron-sulfur clusters. Heme groups of cytochromes typically show π-π* transitions. The absorbance spectra of reduced cytochromes contain the α-, β-, and γ- (Soret-) bands. The position of the α band is characteristic of the heme type and is summarized in Table 1.2.

heme type	α band position / nm
c_1	553
b_H	559-560
b_L	559-560 / 566

Table 1.2: Overview of the positions of α band of the reduced cytochromes in cytchrome bc_1 complex (Berthomieu et al., 1992; Ritter et al., 2003; 2004).

Iron-sulfur clusters show charge-transfer transitions. The absorbance band appears at about 450 nm. FMN has the major absorptions at 370 and 456 nm with a shoulder at 472 nm (Gishla, 1980). In complex I small contributions of the binuclear clusters N1b and N1c are presented at 460 and 550 nm (Dailey et al., 1993) and of the tetranuclear clusters N3 and N4 at approximately 415 nm (Malkin, 1973). Further contributions of proteins in the UV-visible range result from the peptide bond, aromatic amino acids and nucleic acids and can be used to determine protein concentration.

The absorption spectrum of matter is characterized by the molecular extinction coefficient ε at each wavelength. The Lambert-Beer law states that the absorbance is directly proportional to the path length d of the sample and the concentration c, and is described in Equation 1.2.

$$A = \log \frac{I_0}{I} = \varepsilon \cdot c \cdot d$$

Equation 1.2: Lambert-Beer law. A: absorbance; c: concentration in $mol \cdot l^{-1}$; ε: molecular extinction coefficient in $l \cdot mol^{-1} \cdot cm^{-1}$; d: path length in cm.

1.4.2 Infrared spectroscopy

Infrared (IR) radiation of the electromagnetic spectrum (Figure 1.14) is found between the visible light and the microwave region with wavelengths between 700 nm to 10^6 nm. In IR spectroscopy generally wavenumbers $\overline{\upsilon}$ are given that are directly proportional to the energy. The energies associated with molecular vibrations are lower than those required for electronic transitions. The infrared spectral region is separated into three main parts, the near (NIR: 12500 to 4000 cm^{-1}), middle or mid (MIR: 4000 to 800 cm^{-1}) and the far infrared region (FIR: 800 to 10 cm^{-1}). Molecular vibrations are mostly studied in the mid IR region, typically from 4000 to 800 cm^{-1}, which is easily accessed from a technical point of view. However, there are further interesting vibrations in the far infrared domain below 800 cm^{-1}, e.g. the broad hydrogen bonding signature or metal-ligand vibrations.

At the molecular level, infrared radiation excites vibrational or rotational modes in a molecule within a change in the electric dipole moment of the same molecule. The absorbance appears as a peak in the spectrum and is characterized by wavenumber and intensity. A normal mode is the transition of the ground state to the first excited state and its wavenumber corresponds to the chemical bond and the mass of the atom as described in Equation 1.3 for a molecule composed of two atoms.

$$\upsilon = \frac{1}{2\pi}\sqrt{k\left(\frac{1}{m_1}+\frac{1}{m_2}\right)}$$

Equation 1.3: Hooke's law of a molecule composed of two atoms with masses m_1 and m_2. *k* is the bond length.

The bond strength can be modified upon interaction with different environments. This type of modification is the basis of hydrogen-deuterium or any other labelling exchange measurement.

Normal modes can be subdivided into two classes depending on the change of the bond length or angle. A stretching vibration (υ) describes changes of the bond length and can be distinguished as symmetric and asymmetric vibrations. A bending vibration alters the bond angle and is distinguished by scissoring, rocking, wagging, twisting, and torsion motion. Figure 1.15 displays typical vibrations of ethylene chains which are found, for example, in phospholipids.

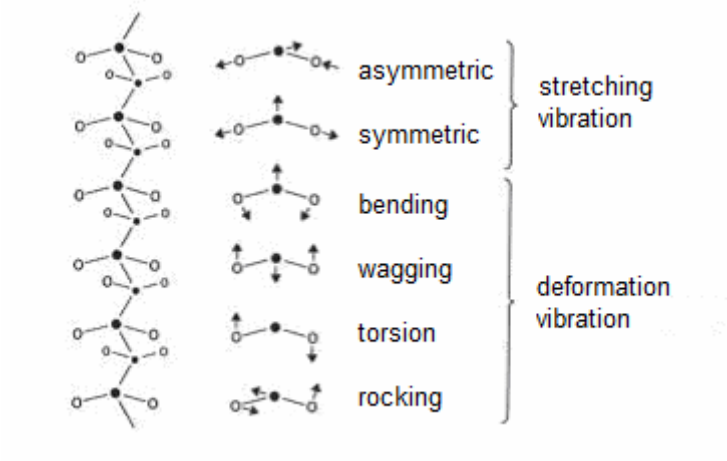

Figure 1.15: Vibrations of ethylene chains (Winter and Noll, 1998)

1.4.2.1 Fourier-transform infrared spectroscopy

Infrared spectrometers have been commercially available since the 1940s. A most significant improvement in IR spectroscopy, however, came with the introduction of so called Fourier-transform (FT) spectrometers.

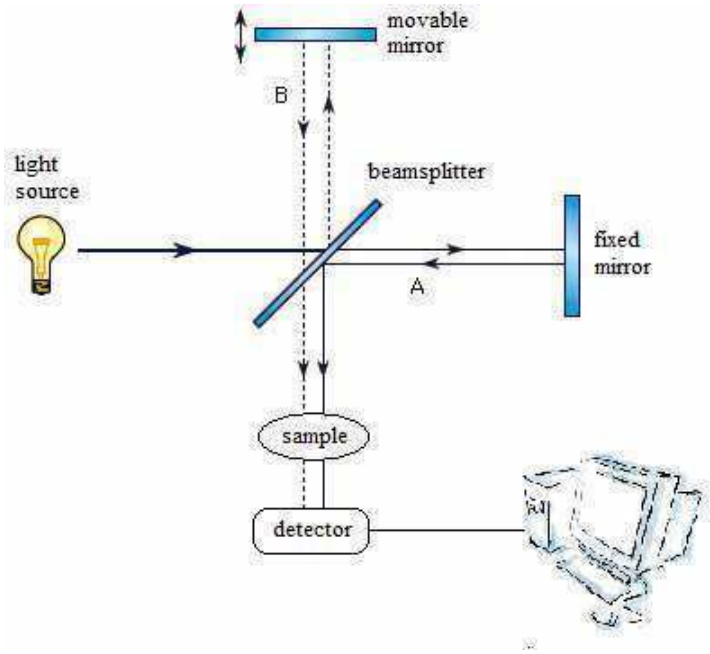

Figure 1.16: Michelson's interferometer.

The essential component of a Fourier-transform IR spectrometer is the optical hardware called an interferometer that produces the interfering light. The most common interferometer used is **Michelson's interferometer** (Figure 1.16), which consists of two mirror planes perpendicular to the optical axis. One of the mirrors can move along the optical axis. Infrared light emitted

by a Globar or Nernst source is directed to a device called a beamsplitter, which allows half of the light to pass through while reflecting the other one. The reflected part of the beam travels to the fixed mirror, where it is reflected and hits the beamsplitter. The same happens with the transmitted part of the beam.

The partial beams are spatially coherent and will interfere when they recombine. The movable mirror is the most crucial component of the interferometer. The mirror has to be accurately aligned and capable of scanning two distances so that the path difference corresponds to a known value. FTIR spectrometers use the interference pattern of a helium neon laser that acts as an internal reference for each scan. The beam leaving the interferometer is passed through the sample and focused on the detector. The light measured by the detector is the intensity $I(x)$ of the recombined IR beams as a function of the moving mirror displacement x, the so-called interferogram.

The **interferogram** is registered as an analog signal by the detector and must be digitized, prior to FT transformation, into a conventional single beam spectrum. This transformation involves integration over a finite displacement. As a consequence, the apparent line shape of a spectral line may be present as a main band which has a series of negative and positive side lobes with decreasing amplitudes. The process of **apodisation** is the removal of these side lobes by multiplying the interferogram by a suitable function, e.g. so called Blackman-Harris-3-term function, which causes the intensity of the interferogram to fall smoothly to zero at its ends. The number of data points per wavenumber in the spectrum can be increased by adding zeros to the end of the interferogram before performing Fourier transform. This increases the number of data points in the spectrum. **Zero filling** is equivalent to a very efficient data point interpolation. Every point of an interferogram contains information about all frequencies present in the spectrum. Because this frequency information depends on the distance the mirror has moved from the interferogram centerburst, or the so-called zero path difference point, sampling on either side of the centerburst provides the same frequency information. Theoretically, the interferogram should be perfectly symmetrical; however, in reality, the sample intervals are not exactly the same on each side of the maxima, corresponding to zero path difference. **Phase correction** is then required, and this correction procedure ensures that the sample intervals are the same on each side of the first interval and should thus correspond to a zero path difference.

After amplification, the analogue signal is converted to digital form by an analog-to-digital converter. The IR data acquisition yields the digitalized interferogram $I(x)$ that is being converted into a spectrum by means of a mathematical operation called Fourier-

transformation (FT). In practice, the spectrum is calculated from the interferogram by an algorithm described by Cooley and Tukey, called a fast Fourier-transform (FFT) algorithm, which reduces the number of complex calculations. The relationship between the light intensity and the concentration is given by the Lambert-Beer law (Equation 1.3).

The light entering the sample (I_0) is determined from an interferogram measured without sample in the optical path, which yields the so-called single beam background spectrum. The intensity of the light transmitted by the sample (I) collected as an interferogram with a sample in the optical path which yields the single beam sample spectrum.

In principle, the interferometer has several basic advantages over the classical dispersive instruments. These advantages are listed below.

- Multiplex advantage (Fellgett advantage) — All wavelengths are measured simultaneously in an interferometer. A complete spectrum can be collected very rapidly and several scans can be averaged.
- Throughput advantage (Jacquinot advantage) — The energy throughput in an interferometer is higher due to the use of a circular slit. This leads to a better signal-to-noise ratio and further to a higher resolution of the spectra.
- Precision advantage (Connes advantage) — An interferometer requires the use of a laser to control the velocity of the moving mirror and to time the collection of data points during the mirror movement for each scan. This leads to accuracy and precision in spectra.

1.4.2.2 Attenuated total reflection spectroscopy

FTIR spectroscopy is often performed in the so-called transmission mode in which the sample is placed between a pair of IR transmitting windows. This method is applicable to a wide range of sample types and it is relatively simple to set up a sample with, a defined path length, which allows determination of extinction coefficients. However, the transmission mode has some limitations (Harrick, 1967, Tamm and Tatulian, 1997, Fringeli et al., 1998).

Attenuated total reflection FTIR spectroscopy is an alternative method to the transmission technique. In ATR FTIR spectroscopy the IR radiation passes direct from the interferometer through an ATR accessory, principally consisting of a focusing element and an internal reflection element (IRE) and then monitored by a detector (Figure 1.17). ATR uses the

phenomenon of total reflection of infrared radiation at interfaces between materials with different refraction indices.

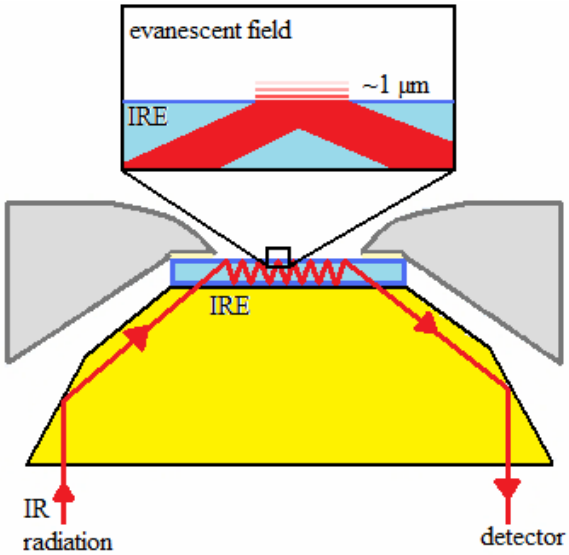

Figure 1.17: Scheme of the ATR accessory. IR radiation (red line) is emitted from a globar and after passing through an interferometer is directed into the IRE (in this study a silicium crystal) by a focusing element (e.g. ZnSe crystal drawn in yellow). Total internal reflection occurs 6 to 8 times at the sample/IRE surface. The attenuated radiation is then directed to a dGTS or MCT detector.

The physics of internal reflection is explained in detail in references (Goormaghtigh et al., 1999, Zscherp and Barth, 2001) and will be briefly discussed. A total internal reflection occurs when radiation reflects on the IRE/sample surface at an angle greater than the critical angle θ_c. The IR radiation creates an evanescent field which decays exponentially with distance from the surface. The depth to which the evanescent wave penetrates the sample is characterized by the distance d_p at which the intensity has decayed to $\frac{1}{e}$ and is described in Equation 1.4.

$$d_p = \frac{\lambda / n_1}{\sqrt{2\pi\left(\sin^2\theta - (n_2/n_1)^2\right)}}$$

Equation 1.4: Penetration depth d_p of ATR unit: λ = wavelength, n_1 = refractive index of the IRE, n_2 = refractive index of sample, and θ = angle of incidence.

Because of the exponential decay of the intensity of the electrical field, a close contact between the sample and the crystal surface is essential. The most commonly used ATR crystal units are silicium, germanium, ZnSe and diamond. By using an angle of incidence of 45°, ZnSe or diamond as the crystal (n_1) and water as the sample (n_2), a penetration depth of 1.6

µm can be calculated with equation 1.5 ($\lambda = 10^{-5}$ m). Normally between six and eight internal reflections are used, resulting in a total path length of about 10 µm.

The use of ATR FTIR spectroscopy overcomes many of the disadvantages associated with working in transmission mode, particularly with proteins. In recent studies (Nyquist et al., 2001; Iwaki et al., 2003, 2004a,b, 2005; Osyczka et al., 2006; Marshall et al., 2006) membrane protein films have been adhered directly to the IRE by drying in absence of detergent. Upon rehydration, the protein layer remains adhered to the IRE, presumably by hydrophobic interaction between the membrane protein film and the crystal surface. In control studies, this interaction was shown not to affect significantly the IR characteristics of the proteins or its functionality. This technique greatly increases the concentration of the protein within the region of the evanescent field. Most importantly, the sample is more accessible than sealed samples used in the transmission mode.

1.4.2.3 FTIR spectroscopy of proteins

The infrared spectra of proteins exhibit specific absorption bands associated with their characteristic amide group. These bands are common for all molecules of this type (Figure 1.18).

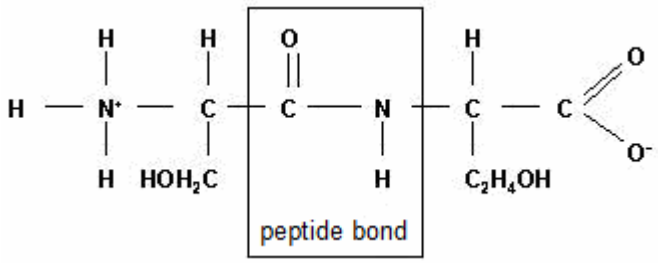

Figure 1.18: Peptide bond of the amide group in proteins.

The characteristic bands of the amide group in proteins are similar to the absorption band exhibited by secondary amides in general, and are referred to as amide bands. There are nine such bands, called amide A, amide B and amide I-VII, in order of decreasing frequency (see Table 1.3).

Designation	Wavenumber / cm^{-1}	Vibrational modes
amide A	~3300	N-H stretching in resonance with first amide II overtone
amide B	~3100	
amide I	1695-1610	80 % C=O stretching; 10 % C-N stretching; 10 % N-H bending
amide II	1575-1480	60 % N-H bending; 40 % C-N stretching
amide III	1320-1220	30 % C-N bending; 30 % N-H bending; 10 % C=O stretching, 10 % O=C-N bending; mixed with other modes
amide IV	765-625	40 % O=C-N bending; 60 % other modes
amide V	640-800	out-of-plane N-H bending
amide VI	605-535	out-of-plane C=O bending
amide VII	~200	Skeletal torsion

Table 1.3: Absorbance bands of amide vibrations (Bandekar, 1992; Arrondo et al., 1993)

The amide I band situated between 1700 and 1600 cm^{-1}, represents mostly C=O stretching vibrations of the amide group. The stretching vibrations depend on the length and the strength of the bond. The exact frequency of this vibration also depends on the nature of the hydrogen bonding involving the C=O and N-H groups. The hydrogen bonds lower the frequency of the stretching vibrations and the characteristic coupling between transition dipoles. The latter leads to characteristic distribution within the amide I band. The magnitude of this splitting depends on the orientation and distance of interacting dipoles and thus provides information about geometrical arrangements of peptide groups in a polypeptide chain. Proteins generally possess a variety of different structural elements. As a consequence, the observed amide I band is usually a complex composite consisting of a number of overlapping component bands representing helices, β-sheet structures, turns, loops and random coils. Hydrogen-deuterium (H/D) substitution also leads to small band shifts of the amide I components (I'). The degree of the shift mainly depends on the type of the secondary structure.

The amide II band essentially represents the vibrational mode of N-H bending, with some coupling to C-N stretching. Similar to the amide I band, it is possible to split the amide II band into components that depend on the secondary structure of the protein. In addition, the position of the amide II band is sensitive to H/D exchange and the mode is converted predominantly to C-N stretching coordinates, and shifted from around 1550 cm^{-1} to a frequency of 1450 cm^{-1}. The N-D bending vibration has a considerably lower frequency than

the N-H bending vibration because it no longer couples with the C-N stretching vibration. The amide II band of the deuterated proteins (II') overlaps with the H-O-D bending vibrations which makes it difficult to extract structural information from the amide II' band. However, the remainder of the amide II band at 1550 cm^{-1} may provide information on the accessibility of solvent to the peptide backbone.

Secondary amides in trans-configuration exhibit two characteristic bands at ~3300 cm^{-1} and 3100 cm^{-1}, whereas those in the *cis* configuration show two bands at ~3200 and 3100 cm^{-1}. The band between 3300-3200 cm^{-1} is the amide A band and is due to the stretching mode of the N-H bond that is engaged in hydrogen bonding. Its frequency depends on the strength of the hydrogen bond. The amide A band is usually part of a Fermi resonance coupled with the second component absorbing weakly between 3100 and 3030 cm^{-1} (amide B).

1.4.2.4 Analysis of the secondary structure of proteins using IR spectroscopy

The amide I (I') band of proteins and peptides consists of a series of overlapping component bands that occur as a result of the secondary structures present in such molecules. The individual component bands that represent different structural elements, such as α helices, β sheets, turns, loops and random coils are not resolved and are difficult to identify in the broad amide I band feature of the experimentally obtained spectra. Resolution enhancement of the amide I band allows identification of the various structures present in a protein. Fourier self-deconvolution and derivative spectroscopy are used to identify the band components and to determine their frequency position. Both methods do not increase the instrumental resolution, but are mathematical procedures that yield narrower component bands. The second derivative spectrum gives a negative peak for every band maximum or shoulder in the absorption spectrum whereas the fourth derivative spectrum gives a positive peak for every band maximum or shoulder. However, the derivatization process does not preserve the integrated areas of individual components. Additionally, these techniques greatly amplify those features in the spectra originating from random noise or uncompensated sharp water vapor band components. Thus the resolution enhancement should be performed on spectra with a high signal-to-noise ratio and after complete elimination of water vapor bands.

The use of resolution enhancement spectra for estimation of the secondary structure components in proteins is an established technique (Susi and Byler, 1983, Byler and Susi, 1986, Dong et al., 1990, Goormaghtigh et al. 1994c, Jackson and Mantsch, 1995, Fabian and

Mäntele, 2002). The resolved band components are assigned to α helix, β sheet and turns (see Table 1.4).

Conformation	Wavenumber / cm^{-1}		
	Calculated	Experimentally obtained	
		H_2O	D_2O
side chains	1621-1627	1618-1628	1610-1620
β sheet	1628-1640	1625-1640	1620-1635
Random coil	1641-1647	1652-1660	1640-1650
α helix	1651-1657	1648-1660	1650-1658
Turns and bends	1651-1657	1660-1697	1655-1685
High frequency β sheet	1658-1696	1675-1695	1680-1695

Table 1.4: Amide I (I') frequencies for the proteins secondary structures (Goormaghtigh et al. 1994c; Stuard 1997; Tamm and Tatulian, 1997; Fabian and Mäntele, 2002)

The assignment of the band components to particular secondary structure of proteins is based on theoretical calculations and on empirical spectral-structural correlations established for model polypeptides and proteins of known three-dimensional structure. However, such secondary structure assignments are by no means exact and certain proteins' band components may appear outside the calculated coordinates (Tamm and Tatulian 1997). For example, in highly solvent-exposed α-helices the amide I band can shift to 1630-1645 cm^{-1} due to additional hydrogen bonding of the solvent accessible C=O groups to water (Surewicz et al., 1993; Fabian and Mäntele, 2002).

1.4.3 Electrochemistry

1.4.3.1 General introduction

An electrochemical technique was used to investigate redox active groups in proteins. The variation of an applied potential leads to an alternation of the redox state of each prosthetic group. The electrochemical characterization of enzymes gives information about electron transfer mechanisms. The redox transition can often be monitored using UV/vis or IR spectroscopy.

The Nernst equation (Equation 1.5) describes the equilibrium redox potential which is specific for the measured redox couple.

$$E_h = E^0 + \frac{RT}{nF} \ln \frac{a_{oxidized}}{a_{reduced}}$$

Equation 1.5: Nernst equation describes the redox potential of an electrochemical half cell with E_h: redox potential vs. reference, E^0: standard potential, R: universal gas constant R = 8.31447 J K^{-1} mol^{-1}, T: temperature in K, n: number of transferred electrons, F: Faraday constant $F = 9.648533 \cdot 10^4$ C mol^{-1}, $a_{oxidized}$ and $a_{reduced}$ are the chemical activity for the relevant species.

The redox potential of a half cell is estimated relative to a second half cell. The potential of the first half cell may be constant; it is often the reference electrode. The standard hydrogen electrode (SHE) is normally defined as the so called reference electrode (E^0 = 0 V). Nevertheless, in our investigations the silver/silver chloride (Ag/AgCl) electrode we used as reference because it is easier to handle. The potential of a silver/silver chloride reference electrode as observed in relation to the standard hydrogen electrode depends on the electrolyte composition. For a Ag/AgCl 3 M KCl the potential is 208 mV versus the standard hydrogen electrode SHE' (pH 7) for biological systems.

In order to avoid that the current passes the reference electrode (RE), a three electrode electrochemical setup (Figure 1.19) is used.

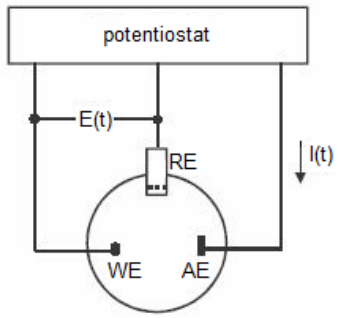

Figure 1.19: Scheme of the three electrode arrangement (Heinze, 1984). WE: working electrode, RE: reference electrode and AE: auxiliary or counter electrode.

The current I passes through the working (WE) and the auxiliary electrodes (AE), while almost no current flows through the RE. The potentiostat controls the real potential E(t) at the working electrode with respect to the RE. Amplifiers in the control circuit adjust the current passing through the WE and AE until the potential E(t) corresponds to the applied potential.

1.4.3.2 Protein electrochemistry

A large number of proteins contains redox active groups such as the NADH:ubiquinone oxidoreductase and the cytochrome bc_1 complex. Suitable experimental conditions are required to study these metalloproteins electrochemically.

Proteins often absorb irreversibly on metal electrode surfaces and subsequently denature. The irreversible adsorption is based on the electrostatic interaction between the electrode and charged groups of the protein surface. The working electrode is made of gold and has to be modified to avoid direct contact between the metal surface and the protein. This chemical compound is called a promoter or modifier. The modifier is a bifunctional organic molecule that absorbs on the metal surface on one side and interacts with the charged surface of a protein on the other side. Thiol containing compounds like mercaptopropionic acid or mercaptoethylamine covalently bind, forming self-assembled monolayers on the metal electrode (Figure 1.20).

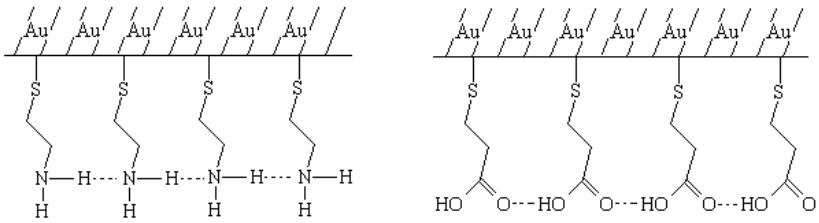

Figure 1.20: Structure of mercaptoethylamine (left) and mercaptopropionic acid (right) surface modifiers

The interaction of the charged surface of a protein is based on hydrogen bonding and/or salt bridge formation of the respective group of the modifier. For instance, a pyridyl nitrogen is capable o hydrogen bonding to lysine. Thioamide NH groups, which are weakly acidic, are suited to hydrogen bond to carboxylate groups. The interaction between protein and modifier is reversible and the electron transfer can occur between the electrode and the enzyme.

Direct electron transfer between electrodes and most proteins can be very slow due to the large size of most redox proteins. Addition of small electron carriers, so called mediators, may enhance the rate of electron exchange with the electrode (Dutton, 1978; Frew and Hill, 1988). Mediators are small redox active compounds. For example, ferrocene and viologen compounds or quinones act as effective mediators to a variety of oxidoreductases. Mediators further have the ability to diffuse into and out of the binding sites of proteins, allowing a faster electron transfer to the redox active centers.

An effective electron transfer can be ensured if the midpoint potentials of the cofactor and of the mediator are in the same potential region. The addition of a mixture of mediators allows a larger potential region to be addressed. Table 5.1 in the Appendix gives an overview of the mediator compounds which are generally used in our laboratory. Mediators should accelerate the electron transfer without any interaction within the protein. Small concentrations of mediators were used in order to avoid the contribution in IR and UV/visible.

2 Materials and methods

2.1 Sample preparation

2.1.1 Phospholipids

Asolectin from soybean was purchased from Sigma-Aldrich. It contains equal proportions of lecithin (mixture of PC), cephalin (mixture of PE) and phosphatidylinositol along with minor amounts of other phospholipids and polar lipids. The synthetic isotopically-labeled phosphatidylcholine variants 1,2-dimyristoyl[1-^{13}C]-*sn*-glycero-3-phosphocholine (14:0), 1,2-dihexanoyl(D22)-*sn*-glycero-3-phosphocholine (6:0) and 1,2-diahexanoyl(D22)-*sn*-glycero-3-phosphocholine-1,1,2,2-D4-N,N,N-trimethyl-D9 (6:0) were purchased from Avanti Polar Lipids. The unlabeled 1,2-dimyristoyl-*sn*-glycero-3-phosphocholine (14:0) and cardiolipin were purchased from Sigma-Aldrich. The lipid samples were used without further purification. The concentration of the samples is listed in Table 2.1.

lipid	concentration mg/mL	solvent
asolectin	5	H_2O, D_2O, chloroform
DMPC (14:0)	10	chloroform
DMPC C^{13} (14:0)	10	chloroform
DHPC D_{22} (6:0)	10	chloroform
DHPC D_{35} (6:0)	5	chloroform
CL	4.8	ethanol

Table 2.1: Phospholipid compounds used.

The asolectin solutions in D_2O and distilled H_2O were stirred for 30 min at 1000 rpm on a Thermomixer (Eppendorff) at 4 °C until a white suspension was obtained. The samples were stored at -20 °C. Storage at 4 °C for up to one week did not change the spectral properties.

2.1.2 Expression and purification of cytochrome b_6

The expression and purification, as well as the further preparations of the cytochrome b_6 variants from spinach, were performed by Carolin Dreher from the laboratory of J.Prof. Dr. Dirk Schneider, Institute of Biochemistry and Molecular Biology from Albert-Ludwigs-University of Freiburg, Germany. Construction of the expression plasmid pRHMb6 has been described in Prodöhl et al. (2007). Expression from this plasmid results in production of the spinach apo-cytochrome b_6 protein genetically fused at its N terminus to the *E. coli* MalE protein. The MalE protein further contains an N-terminal deca-His tail, which allows a straight forward purification of the fusion protein. For protein expression, the expression plasmids were transferred into *E. coli* HMS174(DE3). Expression of the chimeric proteins and subsequent protein purification from inclusion bodies were performed exactly as described in Prodöhl et al. (2007).

Site-directed mutagenesis was performed for the four histidine residues that serve as axial ligands for the two *b*-type hemes to alanine to study the influence of heme binding on the assembly pathway. In detail, the single mutants H86A and H187A have an effect on heme b_L whereas the double mutant H86A/H187A leads to the lacking of heme b_L. Similarly, the single mutants H100A and H202A affect the heme b_H and their double mutant H100A/H202A results in the absence of heme b_H.

In vitro reconstitution of spinach cytochrome b_6 proteins was also performed by Carolin Dreher and is described in Dreher et al. (2008). For reconstitution, the protein was mixed with heme in a 1:2 ratio since cytochrome b_6 binds two heme molecules. The heme was directly added to apo-cytochrome b_6 and the formation was followed by UV/visible spectroscopy.

2.1.3 Preparation and purification of cytochrome bc_1 complex from Sacchromyces cerevisiae

The gene expression and purification of the cytochrome bc_1 complex from yeast *S. cerevisiae* were carried out by Dr. Tina Wenz (currently at Miller School of Medicine, Department of Neurology, University of Miami, USA).

The yeast strain LLD6 (Yang and Trumpower, 1994) was grown in YPG medium containing 1% yeast extract, 2% peptone and 3% glycerol. The generation of the expression

plasmid and the transformation into the yeast strain has been described elsewhere (Lange et al., 2001). The cells were grown in YPG medium at 30 °C and harvested at stationary phase. Mitochondrial membrane preparation of wild type yeast cells and purification are essentially carried out as described in Palsdottir and Hunte (2003). All steps were done at 4 °C. The cytochrome bc_1 complex was purified using two consecutive DEAE anion exchange chromatographic steps. The enzyme is concentrated to 5-10 mg/mL, shock frozen in liquid nitrogen in the presence of 0.66 M sucrose and stored at -80 °C until further used.

The purified cytochrome bc_1 complex was diluted to 15 µM in 2 mM $CaCl_2$, 50 mM Tris/HCl pH 7.4, 250 mM NaCl, 0.05% undecyl-maltopyranoside (UM). Cytochrome bc_1 complex was delipidated by incubation with 66 U/mL phospholipase A_2 for 1 h at room temperature. Phospholipase from porcine pancreatic cleaves the ester bond at the *sn*-2 position of phospholipids into lyso-phospholipid and fatty acids. The delipidation step was stopped by addition of 10 mM EDTA and the depleted enzyme was purified again (Wenz et al., 2009).

For relipidation, 2% (w/v) lipid/water stock solution was sonified until the solution was clear (~15 min). Cardiolipin, phosphatidylglycerol, asolectin and a mixture of asolectin and cardiolipin were added to the depleted enzyme to a final concentration of 0.01% (Wenz et al., 2009). The protein/lipid mixture was used immediately or stored at 4 °C upto 3-4 days without significant change of enzyme activity or spectral properties.

2.1.4 Preparation of the NADH dehydrogenase fragment

The preparation steps of the NADH dehydrogenase fragment were performed in the laboratory of Prof. Dr. Thorsten Friedrich, Institute of Organic Chemistry and Biochemistry at Albert-Ludwigs-Universität in Freiburg i. Br., Germany.

The *Escherichia coli* strain BL21(DE3) (Studier and Moffatt (1986)) and the plasmid pET11a (AGS, Heidelberg) were used as described in Bungert *et al.* (1999). When required for maintenance of the plasmid, ampicillin was added to 100 µg/mL. All enzymes used for recombinant DNA techniques were from Pharmacia, Freiburg or Biolabs, Schwalbach.

For the overexpression of the NADH dehydrogenase fragment, a construct of pET11a was used containing *nuo*B-G with a *Strep*-tag II coding sequence C-terminal on NuoF as described in Bungert et al. (1999). Competent *E. coli* cells BL21(DE3) were transformed with pET11a/*nuo*B-G/$NuoF_C$. At first, 50 µL of the resulting transformants were grown aerobically

in 50 mL flasks in LB medium (containing 1% w/v peptone, 1% w/v NaCl and 0.5% w/v yeast extract) until an optical density OD_{600} = 2 was obtained (approximately 8 hours). All cell growth steps were performed at 37 °C. The overnight culture was grown in 400 mL LB medium, adding 3 mL of the pre-culture. Cells were grown over night, about 12 – 14 hours. The 10 L fermenter in LB medium containing 10 mg/L ferric ammonium citrate, 100 mg/L ammonium sulfate, 50 mg/L riboflavin, and 0.5 mM final concentration of L-cysteine was inoculated with the 400 mL overnight culture. Isopropyl β-D-thiogalactopyranoside (IPTG) was added (final concentration 0.4 mM) at an absorbance of approximately 0.6 at 600 nm. After about three hours (see Figure 5.1 in Appendix 5.1) , the cells were harvested after entering the stationary growth phase (OD_{600} = 2-3) by centrifugation for 10 min at 10810 g. Approximately 30 g cells (wet mass) were washed with 50mM MES/NaOH, pH 6.0. The pellet was shock frozen in liquid nitrogen and stored at -80 °C.

The soluble fragment of complex I was isolated following the protocol developed in the laboratory. All steps were carried out at 4 °C. A 30 g cell sample (wet mass) was resuspended in 100 mL of buffer containing 50 mM Mes/NaOH, 50 mM NaCl, pH 6.0, 100 µM phenylmethylsulfonyl fluoride (PMSF), 5 mM dithiothreitol (DTT). Traces of DnaseI and lysozyme were added to the suspension. The cells were broken by a single pass through a French pressure cell at 110 MPa. Cell debris and the cytoplasmic membranes were removed by ultracentrifugation at 250000 g for 60 min. The cytosol was applied to a 50 mL anion exchange chromatography column (Fractogel, EMD, Merck) equilibrated with 50 mM MES/NaOH, 50 mM NaCl, pH 6.0, 30 µM PMSF and 5mM DTT. The column was washed with the same buffer until the absorbance at 280 nm decreased. Proteins were eluted with a 300 mL linear salt gradient from 50 to 300 mM NaCl in 50 mM MES/NaOH, pH 6.0 using a flow rate of 5 mL/min. Fractions exhibiting NADH/ferricyanide reductase activity were pooled and adjusted to pH 6.6 with 0.2 M NaOH (see profil in Figure 5.2 A). The sample was applied to a 10 mL *Strep*-Tactin Sepharose column (0.4 x 1.6 cm, IBA) equilibrated with 50 mM MES/NaOH, 50 mM NaCl, pH 6.6, 30 µM PMSF and 5 mM DTT at a flow rate of 0.8 mL/min. The NADH dehydrogenase fragment was eluted with 2.5 mM D-desthiobiotine in 50 mM MES/NaOH, 50 mM NaCl, pH 6.0. The fractions with NADH/ferricyanide reductase activity were pooled (see profil in Figure 5.2 B). The samples were concentrated by ultrafiltration (100 kDa MWCO Amicon, Millipore), shock frozen in liquid nitrogen, and stored at -80 °C until use.

2.1.5 Preparation of NADH:ubiquinone oxidoreductase (complex I)

The preparation steps of the NADH:ubiquinone oxidoreductase were performed in the laboratory of Prof. Dr. Thorsten Friedrich, Freiburg.

The *E. coli* cells ANN0221 (derivative of strain AN387, Wallace and Young (1977)) were transformed with pBAD*nuo*/His-*nuoF* as described in Pohl et al. (2007). Large volumes were obtained in 200 L fermenter in YP medium (containing 0.5% w/v yeast extract, 1% w/v peptone) at Institute for Biology at Albert-Ludwigs-Universität, Freiburg, Germany. The medium was composed with 10 L of 0.3 M Na_3PO_4, 0.2 M Na_2HPO_4, 0.5 M KH_2PO_4, 1 M NH_4Cl, 0.25 M Na_2SO_4, 400 mL of 1 M $MgSO_4$, 15 mg/mL ferric ammonium citrate, 10 g riboflavin and 100 mL of 1 M L-cysteine. Cells were grown aerobically at 37 °C. The expression of the *nuo*-operon was induced with 0.2% w/v L-arabinose after 1 h. Cells were harvested until they entered the stationary growth phase by continuous flow centrifugation at 17000 g at 4 °C, shock frozen in liquid nitrogen and stored at -80 °C for general use.

Complex I was isolated using a protocol developed in the laboratory. All steps were carried out at 4 °C. A 40 g cell sample (wet mass) was resuspended in 200 mL of buffer containing 50 mM Mes/NaOH, 50 mM NaCl, pH 6.0, 100 µM phenylmethylsulfonyl fluoride (PMSF). Traces of Dnase I and lysozyme were added to the suspension. The cells were broken by a single pass through a French pressure cell at 110 MPa. Cell debris was removed by centrifugation at 36000 g for 20 min. The cytoplasmic membranes were obtained by ultracentrifugation at 250000 g for 70 min. The membranes were resuspended in 50 mM MES/NaOH, 50 mM NaCl, pH 6.0, 5 mM $MgCl_2$, 100 µM PMSF at 1 g per mL of suspension. For the detergent extract, n-dodecyl β-D- maltoside (DDM, AppliChem) from 20% stock solution in water was added to the membrane suspension to a final concentration of 3%. The solution was gently homogenized using a glass-Teflon homogenizer and incubated 15 min on ice. Unsolubilized material was removed by ultracentrifugation at 250000 g for 15 min. The supernatant was applied to a 60 mL anion exchange chromatography column (Fractogel, EMD, Merck) equilibrated in 50 mM MES/NaOH, 50 mM NaCl, 0.1% DDM, pH 6.0. The column was washed with the same buffer, respectively. Furthermore the column was washed with 35 mL of 150 mM NaCl in 50 mM MES/NaOH, 0.1% DDM, pH 6.0. Proteins were eluted with a 75 mL linear salt gradient from 150 to 350 mM NaCl in 50 mM MES/NaOH, 0.1% DDM, pH 6.0 at a flow rate of 5 mL/min. Fractions exhibiting NADH/ferricyanide oxidoreductase activity were pooled (see profile in Figure 5.3 A) and imidazole was adjusted to a final concentration of 20 mM. The sample was applied to

a 10 mL ProBond Ni^{2+}-IDA column (Invitrogen) equilibrated in 50 mM MES/NaOH, 200 mM NaCl, 20 mM imidazole, 0.1% DDM, pH 6.3 at a flow rate of 1.1 mL/min. The column was washed with the same buffer until the absorbance at 280 nm decreased to the initial value. Proteins were eluted with a step gradient from 20 to 500 mM of imidazole in 50 mM MES/NaOH, 200 mM NaCl, 0.1% DDM, pH 6.3 at a flow rate of 1.1 mL/min, respectively. Fractions exhibiting NADH/ferricyanide oxidoreductase activity were pooled (see profil in Figure 5.3 B) and washed three times with 50 mM MES/NaOH, 50 mM NaCl, 0.1% DDM, pH 6.0 and concentrated by ultrafiltration (100 kDa MWCO Amicon, Millipore). The samples were shock frozen in liquid nitrogen and stored at -80 °C until use.

2.1.6 Determination of the NADH/ferricyanide oxidoreductase activity

The enzymatic activity of the samples was measured by following the reduction of ferricyanide by NADH at 410 nm at room temperature. The essay was performed in a 1 cm thick cuvette containing 1 mL of 50 mM MES/NaOH, 50 mM NaCl, 1 mM $K_3[Fe(CN_6)]$, 0.2 mM NADH, pH 6.0. A molar absorption coefficient of $K_3[Fe(CN_6)]$ $\varepsilon_{410} = 1\ mM^{-1}\ cm^{-1}$ was used with the equation of Lambert-Beer law (equation 1.3) to determine the NADH/ferricyanide oxidoreductase activity in $\mu mol\ min^{-1}\ mL^{-1}$ (U/mL) (Friedrich et al., 1989).

2.1.7 Determination of total protein concentrations by means of biuret reaction

The total protein concentration was determined by means of biuret reaction (Gornall et al., 1949). In 50 to 100 µL of the samples were added 1 mL 6% w/v trichloroacetic acid (TCA) and centrifuged for 1 min at 15700 g at room temperature. The pellet was resuspended in 1 mL Biuret-reagent and stirred for 30 min at 1400 rpm (Eppendorff Thermomixer). The absorbance of each sample was measured at 546 nm. After addition of a small amount of potassium cyanide, the absorbance was measured at 546 nm again. The protein concentration was estimated using the difference in absorbance and the straight calibration line of 10 mg/mL bovine serum albumin stock solution.

2.1.8 SDS polyacrylamide gel electrophoresis

A sodium dodecyl sulfate (SDS)-Page was performed according to Schägger and von Jagow (1991) using a 10% T (total acrylamide-bisacrylamide monomer concentration) and 3% C (cross linker concentration) separating gel. The protein sample was dissolved in a Schägger buffer that was four times more concentrated and stirred for 30 min at 60 °C. The denatured protein sample was applied to the gel and the subunits were separated according to their molecular weight using a current of 30 mA for 2.5 h. The protein bands were colored with hot CBB solution (0.1% w/v Coomassie Brilliant Blue R-250, 25% v/v ethanol, 10% v/v acetic acid). The gel was decolorized using 30% v/v ethanol, 10% v/v acetic acid to monitor the colored protein bands.

2.1.9 'ATR ready' complex I

The concentration of DDM in the buffer solution is a problem for the hydrophobic surface of the ATR cell. A DDM exchange has to be performed for the membrane proteins. As an alternative to the protocol of the purification of the NADH:ubiquinone oxidoreductase described above, the pooled fractions of the complex I were washed three times by ultrafiltration with the buffer containing a lower DDM concentration (0.01%).

The samples containing NADH/ferricyanide oxidoreductase from the ProBond Ni^{2+}-IDA column were concentrated until a volume of 1.5 mL and applied to a 26 mL size-exclusion chromatography Superose column. The buffer was exchanged using 50 mM MES/NaOH, 50 mM NaCl, 0.01% DDM, pH 6.0 with a flow rate at 0.5 mL/min.

The protein samples were then washed 3-4 times using 50 mM MES/NaOH, 50-150 mM NaCl, pH 6.0 above the critical micelle concentration of DDM (CMC = 0.17 mM). All steps were performed at 4 °C. A washing step was carried out at 5000 g for 15 min. The diluted solution was centrifuged at 18000 g for 30 min. Variation of the salt concentration did not affect the pellet preparation. The resulting pellet was applied directly onto the crystal surface or stored at -80 °C for later use.

2.2 Spectroscopy

2.2.1 Recording infrared absorbance spectra

The infrared absorbance measurements in the different spectral ranges were performed with the equipment mentioned below. Table 2.2 gives an overview.

	MIR	FIR
spectral range	4000-800 cm^{-1}	800-50 cm^{-1} 300-0 cm^{-1} (synchrotron*)
scans	256	128
windows	CaF_2 (till 1100 cm^{-1}) BaF_2 (till 800 cm^{-1}) Si/ZnSe (ATR)	diamond (ATR) polyethylene (1 mm)
beamsplitter	KBr	Si Mylar (6 µm, synchrotron)
detector	RT-dTGS	RT-dTGS bolometer (helium-cooled, synchrotron)
mirror velocity	10 or 20 kHz	2.5 kHz

Table 2.2: Overview of the used infrared spectral range. *at ANKA, Karlsruhe.

In general, mid infrared absorbance spectra were recorded from 4000 to 800 cm^{-1} with a Bruker IFS 28 Fourier transform infrared spectrometer equipped with a KBr beamsplitter, and an external globar as conventional IR source. The data were detected with a so called room temperature, deuterated triglycine sulfate (RT-dTGS) detector. The far infrared absorbance spectra were obtained on a Bruker Vertex 70 FTIR spectrometer. The spectrometer is equipped with a removable silicon beamsplitter, an internal globar source and an adapted dTGS detector. The far IR absorbance spectra were recorded between 700 and 50 cm^{-1}. The silicon beamsplitter has a strong absorbance at about 610 cm^{-1}. Spectra were displayed from 600 to 50 cm^{-1} only. Furthermore, far infrared absorbance spectra were recorded from 300 to 0 cm^{-1} with a Bruker IFS 66 FTIR spectrometer and a Mylar (6 µm) beamsplitter and a Helium cooled bolometer as detector, using the synchrotron light at the

ANKA IR Beamline in the Forschungszentrum Karlsruhe as IR light source. The advantage of the synchrotron light is the high brilliance in the lower frequency region. All spectrometers were purged with dry air, partially they worked with vacuum conditions(ANKA). Generally, five to ten mid infrared spectra with 256 scans were averaged using a mirror velocity of 10 or 20 kHz, whereas five to ten far infrared spectra with 128 scans were averaged using a mirror velocity of 2.5 kHz. The resolution of all spectra was 4 cm^{-1} and the data were measured in the single-side, forward-backward mode. For the resulting interferograms, the Blackman-Harris-3-term function was used for apodization and Fourier transformed with a zero filling factor of two. Incomplete water vapor compensation was corrected; where necessary, smoothing with 5-13 points was performed.

An absorbance cell was used to obtain absorbance spectra in transmission mode. In detail, two 2 mm thin BaF_2 windows (Crystal GmbH) were used to investigate samples in solution as illustrated in Figure 2.1. The space between the windows is about 8 µm.

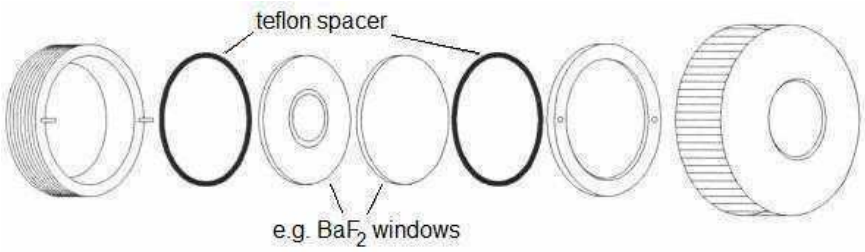

Figure 2.1: Schematic view of the absorbance cell.

In the far infrared domain, a 1 mm thin polyethylene window was used and the sample was prepared as a hydrated film on the window surface. Furthermore, hydrated films were used for absorbance spectra using in the mid infrared region an attenuated total reflexion unit with a Silicium/ZnSe bicrystal and in the far infrared region an ATR unit with a diamond crystal the ATR unit. The perfusion mode measurements are described in detail below (see section 2.2.3).

2.2.1.1 Temperature-dependent infrared absorbance spectra of phospholipids

The lipid solutions were placed on the ATR crystal or on the window surface, and the solvent evaporated under a stream of nitrogen gas at room temperature. Subsequently, the temperature was slowly decreased to the desired starting temperature at 5 °C, and after equilibration of an

hour, infrared measurements were performed as a function of increasing temperature. Then this procedure was performed in reverse by decreasing temperature. The infrared spectra were recorded between 5 and 40 °C; this range corresponds to the gel to liquid-crystalline transition temperature. The temperature inside the sample compartment was controlled with an external circulating water/ethanol mixture bath. The samples were equilibrated for at least 30 min at the respective temperature before acquisition of each data point.

2.2.1.2 Absorbance spectra of NDF and complex I adding nucleotides

NDF and complex I samples were concentrated to 200 or 250 µM. The stock solution of NADH (reduced form of nicotinamide adenine dinucleotide) and NAD^+ (oxidized form) with a concentration of 40 mM and of NADPH (reduced form of nicotinamide adenine dinucleotide phosphate) at a concentration of 10 mM were freshly prepared in the respective buffer and used immediately or stored at -80 °C. The nucleotides were added to the protein to a final concentration of 50 µM, 100 µM and 1 mM in different assays. The protein samples were incubated with the respective nucleotide on ice. UV/visible control experiments were used to monitor the reduction of the enzyme. Finally, the incubated samples were prepared as hydrated films on the ATR crystal surface. Since nucleotides have contributions in the amide I region, the same samples were also measured in the transmission mode and their absorbance spectra were interactively subtracted from the protein spectra.

2.2.2 Spectroelectrochemistry

Electrochemically induced redox spectra were measured using the spectroelectrochemical thin layer cell (Moss et al., 1990).

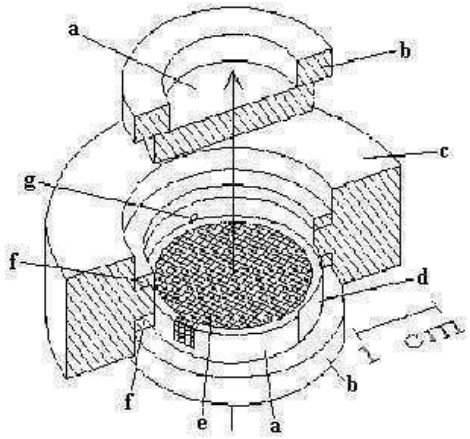

Figure 2.2: Schematic view of the spectroelectrochemical thin layer cell. (A) BaF_2 window fixed on a plexiglass ring (B); (C) plastic cell body; (D) platinum counter electrode; (E) gold grid working electrode; (F) rubber o-ring; (G) connection to reference electrode. The arrow indicates the optical axis of the IR radiation (Moss et al., 1990).

The spectroelectrochemical cell illustrated in Figure 2.2 comprises a PVC cell body (C) with four inlets. The working electrode is screwed into an inlet to have contact with the gold grid (E) whereas the counter electrode is screwed to a platinum plate (D) that has no contact to the gold grid. The third inlet (G) is the connection for the reference electrode and the last inlet is an access for the buffer solution to fill the whole cell. The cell works on the basis of the three electrode arrangement (see section 1.4.3). The working electrode (E) is a 4 µm thin gold grid with a 30 x 30 µm mesh width and an optical transparency of 55% (purchased from Goodfellow, SARL, France). The gold grid has to be chemically modified before use with a protein solution. This is carried out using a 2 mM cysteamine and 2 mM mercaptopropionic acid solution in a 1:1 ratio. After 1 h of incubation, the gold grid was washed with distilled water and placed on the BaF_2 window. Before the protein sample was placed into the cell, a mixture of mediators (see Table 5.3, Appendix) was added, to a final concentration of about 40 µM, and incubated for 30 min on ice. The sample volume was about 8 to 10 µL and was placed directly on the modified gold grid. The cell is maintained between two stainless steel plates. The two steel plates are used to obtain a thickness between 5 and 10 µm which is necessary to obtain a sufficiently intense signal on the detector. Finally, the closed cell was filled with buffer solution to obtain a connection between the electrodes.

On the top of the cell the reference electrode is placed. The reference electrode is made of a Plexiglas body that was filled with a 3 M KCl solution. A silver chloride treated silver wire is plunged into the salt solution (see Figure 2.3). The Ag/AgCl 3 M KCl reference electrode has a potential of 208 mV relative to the standard hydrogen electrode (pH 7). The reference electrode was calibrated with the cyclovoltammogram of a buffered $K_4[Fe(CN)_6]$ solution.

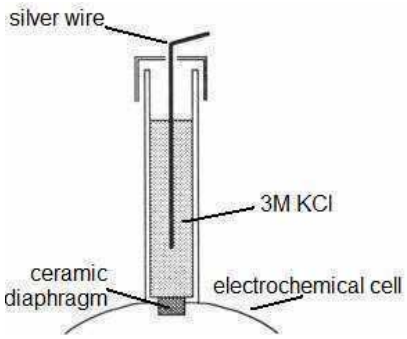

Figure 2.3: The reference electrode.

2.2.2.1 Electrochemically-induced UV/vis difference spectra of cytochrome b_6 variants

Cytochrome b_6 samples contain 50 mM Tris/HCl, pH 8.0, 100-200 mM NaCl and 5 mM *n*-dodecyl-β-D-maltoside for the electrochemical approach. Redox titrations in the UV/visible range were performed with the spectroelectrochemical thin layer cell as described above. For better equilibration, redox mediators were added (see Table 5.3 in Appendix). Data were collected from 200 to 800 nm at 15 °C on a diode array spectrometer (Agilent 8453). Three scans were averaged for each 50 mV potential step between -300 and 300/400 mV, after an equilibration time of 15 - 20 min.

2.2.2.2 Electrochemically-induced IR and UV/visible difference spectra of cytochrome bc_1 complex

The wild type cytochrome bc_1 complex was concentrated to 70 mg/mL in 50 mM Tris/HCl, pH 7.3, 250 mM NaCl and 0.05% UM. The lipid:enzyme mixtures were used as described above in the same buffer. The redox dependent signal of each heme could be differentiated in electrochemically-induced UV/visible difference spectra, on the basis of the relative contribution of the hemes b_L, b_H, and c_1 to each position in the α band (see Table 1.2 in

section 1.4.1). The redox titrations were performed by stepwise setting potentials (typically 50 mV steps) and spectra were recorded after 20 min equilibration (Ritter et al., 2003 and 2004). Similarly, the fully oxidized and fully reduced infrared spectra were performed between -0.29 and 0.71 V with an equilibration time of 5-6 min. All spectra were measured at 5 °C.

2.2.3 Perfusion-induced ATR FTIR spectroscopy

To measure perfusion-induced difference spectra a BioATR II unit from Bruker Optics (Karlsruhe, Germany) was used. The designed multi-reflection ATR cell has a performance similar to transmission systems with a path length of 6-8 microns. The ATR unit is based on a dual crystal technology. The top ATR crystal is made of silicium which has direct contact with the samples. The crystal surface is hydrophobic. The second ATR crystal, which does not come in contact with the sample, has a hemispherical design and is made of zinc selenide. The ATR body is made of stainless steel. A connection for temperature controlled measurements allows the whole cell to be cooled. A top plate can be inserted for flow-through measurements. The assembly is purged continuously with dried air to avoid interferences caused by water vapor or temperature changes in the spectrometer.

The ATR unit has a dialysis attachment. A dialysis membrane, which is stretched parallel to the ATR crystal, separates the dialysis unit into two chambers (the upper compartment and the lower compartment as shown in Figure 2.4).

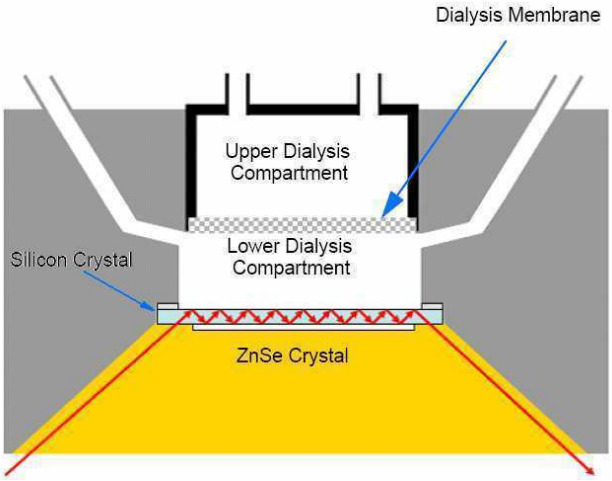

Figure 2.4: Scheme of the ATR unit with the dialysis unit.

This dialysis unit allows us to work with soluble proteins. The chemical environment in the evanescent field of the ATR crystal can be modified without causing mechanical

perturbations on the crystal surface or dilution effects in the sample compartment. Depending on the exclusion limit of the membrane, low molecular weight substrates (in this work different nucleotides) can be dialyzed into and out of the lower chamber without altering the concentrations of the protein. The protein solution in the lower chamber has direct contact with the crystal surface and can be monitored by means of FTIR spectroscopy.

2.2.3.1 Nucleotide-induced ATR FTIR difference spectra of NADH dehydrogenase fragment

First, the dialysis membrane has to be prepared. In detail, the membrane was roughly cut to the required size of approximately 2 x 2 cm. Then the membrane was swelled for about 30 min in hot distilled water. The membrane has to be kept humid during the dialysis attachment assembly. The assembly of the cell was performed as described below before starting the measurements. The tube of the upper compartment was filled with the perfusion buffer, 50 mM Mes/NaOH, 50 mM NaCl, pH 6. The swollen membrane was put directly over the round opening of the dialysis adapter and fixed with the black o-ring. Then the dialysis adapter was placed into the opening of the dialysis attachment's top plate. The upper compartment was filled with buffer solution till the solution flowed out of the outlet tube. The empty crystal surface was used as reference spectrum. The tube of the lower compartment was filled with buffer. About 20-30 µL of buffer solution was placed on the ATR crystal surface. A specially designed rubber was put on the lower plate before the cell was closed. The lower compartment was washed with the buffer solution (~100 µL) until the buffer flowed bubble-free out of the outlet tube. Now, the vial of the NDF sample (10-20 µL) was fixed on the outlet tube and the protein solution was sucked carefully and slowly into the lower compartment using the Hamilton syringe on the inlet tube (see Figure 2.5).

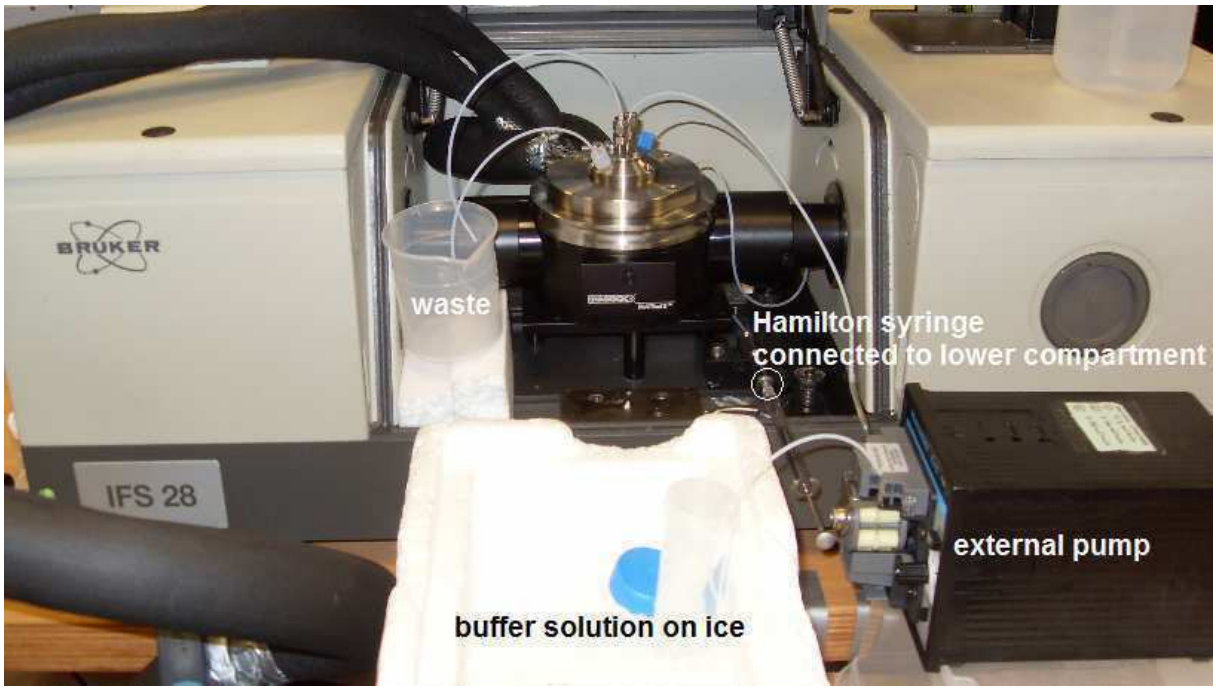

Figure 2.5: General construction for measurements of soluble proteins.

All buffer exchange was performed using the tube of the upper compartment which is connected to an external pump. All measurements were carried out at 7 °C. Before measuring the nucleotide-induced difference spectra of NDF, the upper compartment was perfused with the MES buffer at a flow rate of 0.2 mL/min for 1 h to equilibrate the system. Nucleotides (NAD^+, NADH, and NADPH) were dissolved in the perfusion buffer 50 mM Mes/NaOH, 50 mM NaCl, pH 6.0 at the respective concentration. A background spectrum of the NDF sample was first recorded during the perfusion with buffer in the absence of nucleotides. Then the buffer was changed to the same buffer containing nucleotides (variation of 50 µM, 100 µM, 1 mM final concentration). After a delay of about 20 min for equilibration, nucleotide *minus* nucleotide-free difference spectra of NDF were recorded. After 45 min, a new background was recorded and the buffer was changed back to the buffer without nucleotides. The equilibration time was again 20 min and nucleotide-free *minus* nucleotide spectra were obtained. This procedure was repeated 5 – 10 times, and the difference spectra were averaged. The flow rate was 0.2 mL/min for each perfusion step. Spectra were corrected due to protein swelling/shrinkage effect by interactive subtraction. Baseline correction and smoothing with 5-9 points were done, where necessary.

2.2.3.2 Nucleotide-induced ATR FTIR difference spectra of complex I

To monitor nucleotide induced difference spectra of complex I, the upper compartment was closed with a 2 x 2 cm plastic film. The resulting 'ATR ready' pellet (see preparation in section 2.1.10) was placed on the crystal surface. After drying under a gentle stream of nitrogen, the sample was rehydrated with the perfusion buffer (50 mM Mes/NaOH, 50 mM NaCl, pH 6). Then the ATR perfusion cell was closed. Before measuring the nucleotide interaction, the protein film was perfused with the same buffer at a flow rate of 0.2 mL/min for 1 h to remove residual detergent (DDM) which had remained bound to the protein. This procedure was monitored spectroscopically. All measurements were performed at 7 °C with a perfusion flow rate at 0.2 mL/min. As previously described for NDF, nucleotides (NADH, NAD^+, and NADPH) were dissolved in the perfusion buffer at different concentrations. A background spectrum of the hydrated complex I film was recorded during perfusion with the perfusion buffer in absence of nucleotides. After 5 min equilibration, nucleotide *minus* nucleotide free difference spectra of complex I were recorded. Data acquisition was performed for about 45 min, then a new background spectrum was recorded and the buffer was changed back to the buffer without nucleotides. In successive the next series of investigations 50 µM decylubiquinone were added to the latter buffer because no reversibility was obtained before. After an equilibration time of about 5 min, spectra in the presence of decylubiquinone *minus* nucleotide difference spectra were obtained. This procedure was repeated five times. The difference spectra were averaged. Spectra were corrected due to the swelling/shrinkage effect, where necessary.

2.2.3.3 Hydrogen deuterium exchange measurements

Hydrogen deuterium exchange investigations were performed for NDF and complex I using the perfusion cell as described. In general, a series of ten vials containing 1 mL D_2O buffer of 50 mM MES/NaOH, 50 mM NaCl, pD 6 (98% purchased from Sigma-Aldrich) were flushed with nitrogen or argon gas for 30 min before use. The pD value was measured according to $pD = pH_{reading} + 0.4$ (Glasoe and Long, 1960). The injection of the D_2O buffer was taken as the zero point of the exchange. The buffer exchange of the NDF samples was performed with the help of the upper compartment and using a dialysis membrane between the two chambers as described before (see Figure 2.4). Complex I was placed on the crystal surface and rehydrated

with 50 mM MES/NaOH, 50 mM NaCl, pH 6 as previously described. At the starting point, the inlet tube was plunged into a vial and the D_2O solution was perfused into the chamber using a flow rate of 0.2 mL/min. In the first 10 min, spectra with 32 scans were recorded every 30 s. The vial was changed after 5 min and after 10 min. Then the scan time was increased to 128 scans and after 1 h, a scan time of 256 scans was used and the vial was changed. Two hours later, spectra were recorded every 10 min and the buffer solution was cycled. The time of data acquisition in D_2O exposure was about 8-10 h. Stock solution of NADH with 20 mM concentration was freshly prepared in the respective D_2O buffer solution. The nucleotide was added to a final concentration of 100 µM in the degassed D_2O solution. Decylubiquinone 10 mM was solved in absolute ethanol. Subsequently, ubiquinone a 500 µM stock solution was prepared in the respective D_2O buffer, and added to the degassed D_2O solution to a final concentration of 100 µM.

2.3 Data analysis

2.3.1 Determination of redox midpoint potentials

The determination of the difference spectra was carried out at a significant wavelength, for instance, the α- or Soret-band for heme contributions. The absorbances at the respective wavelength were plotted in function of the applied potential. The analysis was performed with a sum of Nernst equations, depending on the number of redox active groups, as described in equation 2.1 using the program Origin 6.0 (Microcal, Northampton, MD).

$$A(p) = \sum \frac{A_{\max}}{1 + e^{(p - E_m)\frac{nF}{RT}}}$$

Equation 2.1: Determination of the midpoint potential based on the Nernst equation. Absorbance changes of redox active groups in function of applied potential. A_{max}: maximal change in absorbance, p: respective potential, E_m: midpoint potential of redox active group, n: number of transferred electron, F: Faraday constant, R: universal gas constant and T: temperature in K.

2.3.2 Secondary structure determination

The secondary structure of NDF and complex I samples was determined from the shape of amide I band between 1700 to 1600 cm^{-1}. Prior to curve fitting, a straight baseline passing through the ordinates at 1700 to 1600 cm^{-1} was subtracted. A least-squares iterative curve fitting was performed with Gaussian bands using the program Origin 6.0 (Microcal, Northampton, MD). The input parameters were chosen due to the second derivative spectra as well as typically positions that appear in protein absorbance spectra which were overlapped by highly organized structure (Byler and Susi, 1986). Curve fitting of amide I bands was performed based on the frequencies of six components of the second derivative spectra. The three central frequencies were fixed while the other bordering bands were varied. Each band of the resulting fitting was assigned to a secondary structure according to the frequency of its maximum (Goormaghtigh et al., 1994). The areas of all bands assigned to a given secondary structure element were then summed up and divided by the total area. Standard deviations were estimated to 1-2%. The assumption was made that the extinction coefficients were equal for all the secondary structures (Goormaghtigh et al., 1990).

2.3.3 Time rate constant determination of hydrogen deuterium exchange kinetics

First, buffer contributions were subtracted of all spectra. For the calculation of water and deuterium content in the sample, the protein spectrum containing 100% water and the protein spectrum containing 100% deuterium oxide were used. All spectra were integrated in the area of 3715 to 2880 cm^{-1} for the estimation of water content and in the area of 2740 to 2210 cm^{-1} for the estimation of deuterium oxide content. The subtraction coefficients were calculated at any time of the kinetic measurements according to equations 2.2 (according to Dzafic et al., 2009).

$$a \cdot [H_2O] + b \cdot [D_2O] + c \cdot [HOD] = 1$$

$$a = \frac{[S]_{2880}^{3715} - [D]_{2880}^{3715}}{[H]_{2880}^{3715} - [D]_{2880}^{3715}} \; ; \; b = \frac{[S]_{2210}^{2740} - [H]_{2210}^{2740}}{[D]_{2210}^{2740} - [H]_{2210}^{2740}}$$

Equation 2.2: Determination of subtraction coefficient. S is the area of the sample which has to be corrected, D is the area of 100% deuterium content spectrum, H is the area of 100% water content spectrum for a given frequency range.

After the subtraction procedure, the area of amide I between 1700 and 1600 cm^{-1}, and amide II between 1570 and 1510 cm^{-1}, were obtained by integration. For this purpose a straight baseline of the respective band was subtracted. For each spectrum, the area of amide II was divided by the area of amide I due the swelling effect (Goormaghtigh et al., 1994b). The swelling increases the average distance between the protein and the crystal surface (Scheirlinckx et al., 2001).

The hydrogen deuterium exchange is a first order reaction (Knox and Rosenberg, 1980; Gregory and Rosenberg, 1986). The fraction of nonexchanged amide protons can be described as a sum of exponential functions. The ratio of amide II and amide I area is described in equation 2.3 as a function of time of D_2O exposure (Vigano et al., 2004).

$$\frac{A_{\text{amide II}}}{A_{\text{amide I}}} = \sum_{i=1}^{M} a_i \exp\left(-k_i / t\right)$$

Equation 2.3: Hydrogen deuterium exchange kinetic. A_{amideII} is the area of amide II band, A_{amideI} is the area of amide I band, a_i are the fractions of slow, intermediate and fast exchange, k_i are the respective time rate constants, t is the time of deuteration.

The curve fitting procedure was realized using the program Origin 6.0 (Microcal, Northampton, MD). Standard deviations were estimated to 2-3%. It is obviously impossible to determine several parameters using an experimental multiexponential curve. Therefore, three to four exponentials were used to describe the hydrogen deuterium kinetic.

3 Results and discussions

3.1 Factors ruling properties of redoxproteins

3.1.1 Membranes and lipids

Glycerophospholipids have a key role in biological cells. Phosphatidylcholine is one of the dominating phospholipids in biological membranes and has been well characterized by means of infrared spectroscopic techniques (Popova and Hincha, 2003; Casal and McElhaney, 1990; Hübner and Mantsch, 1991; Snyder et al., 1996; Pohle et al., 1998). Asolectin containing PC, PE and PI acts as a model membrane layer since its typical phospholipid content is similar to those in biological membranes (Colbeau et al., 1971). In this section the well-known temperature dependent phase transition of these phospholipid model compounds (see Figure 3.1) is monitored in the mid infrared domain in order to detect the different phases as well as hydrogen bonding behavior in the far IR.

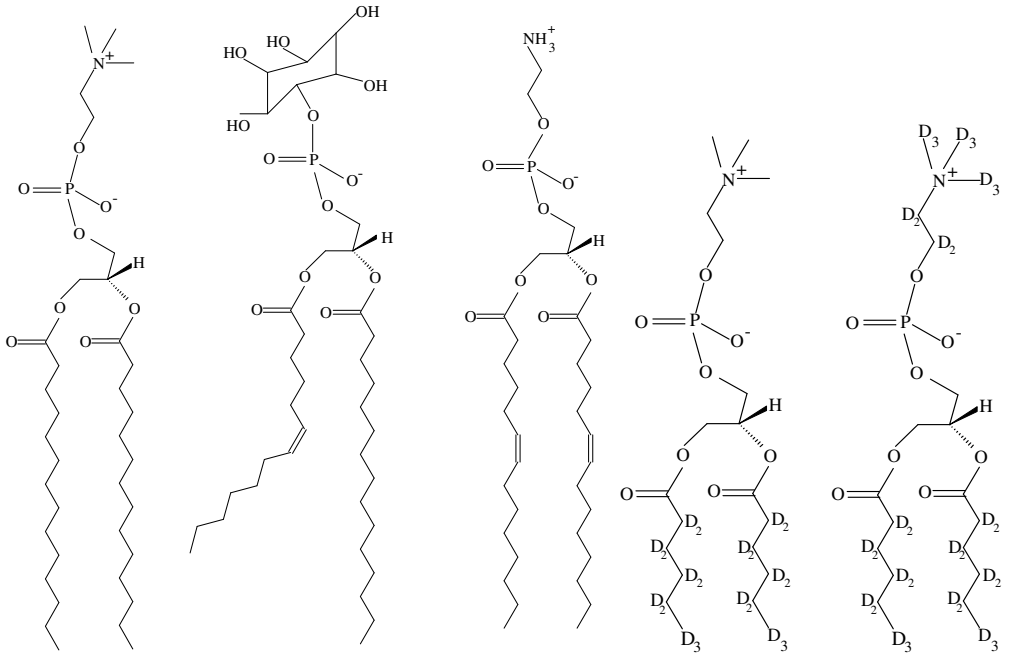

Figure 3.1: Used lipids. From left to right: phosphatidylcholine (PC), phosphatidylinositol (PI), phosphatidylethanolamine (PE), PC D_{22}, and PC D_{35}.

3.1.1.1 Temperature dependent investigations in the mid infrared domain

Figure 3.2 shows the infrared absorbance spectra of the asolectin film in D_2O obtained upon heating from 5 to 40 °C (A), the reversible process induced by cooling (B) and the pure PC (C: cooling, D: heating) in the spectral region from 1800 to 1000 cm^{-1}. The shifts were found to be perfectly reversible. No differences were found for asolectin solubilized in H_2O (see Figure 5.5 in appendix). Between 5 °C and 40 °C, the phase transition from the gel state to the liquid crystalline state can be expected, for i. e. PC at 23 °C (Gagne et al., 1985). The mid IR spectra of phospholipids are well understood. The assignments made below for asolectin, PC and their isotopically labeled derivatives PC C^{13}, PC D_{22} and PC D_{35} are summarized in table 5.4 (see appendix 5.2.1) and are based on the review from Lewis and McElhaney (1994) and quotations therein.

The studied spectral range from 1800 to 900 cm^{-1} includes the characteristic absorbance of the phospholipids head group. The C=O stretching vibration of the ester carbonyl groups from the interfacial region has a broad signal centered at 1738 cm^{-1}. The CH_2 scissoring mode of the hydrocarbon chain methylene groups can be found at 1466 cm^{-1}. Upon heating this band gets broader, indicating the increasing disorder and a higher mobility of the hydrocarbon chains. This behavior is typical for many phospholipids when changing from the gel to a liquid crystalline state (Hübner et al., 1991). The CH_3 deformation is found at 1376 cm^{-1}.

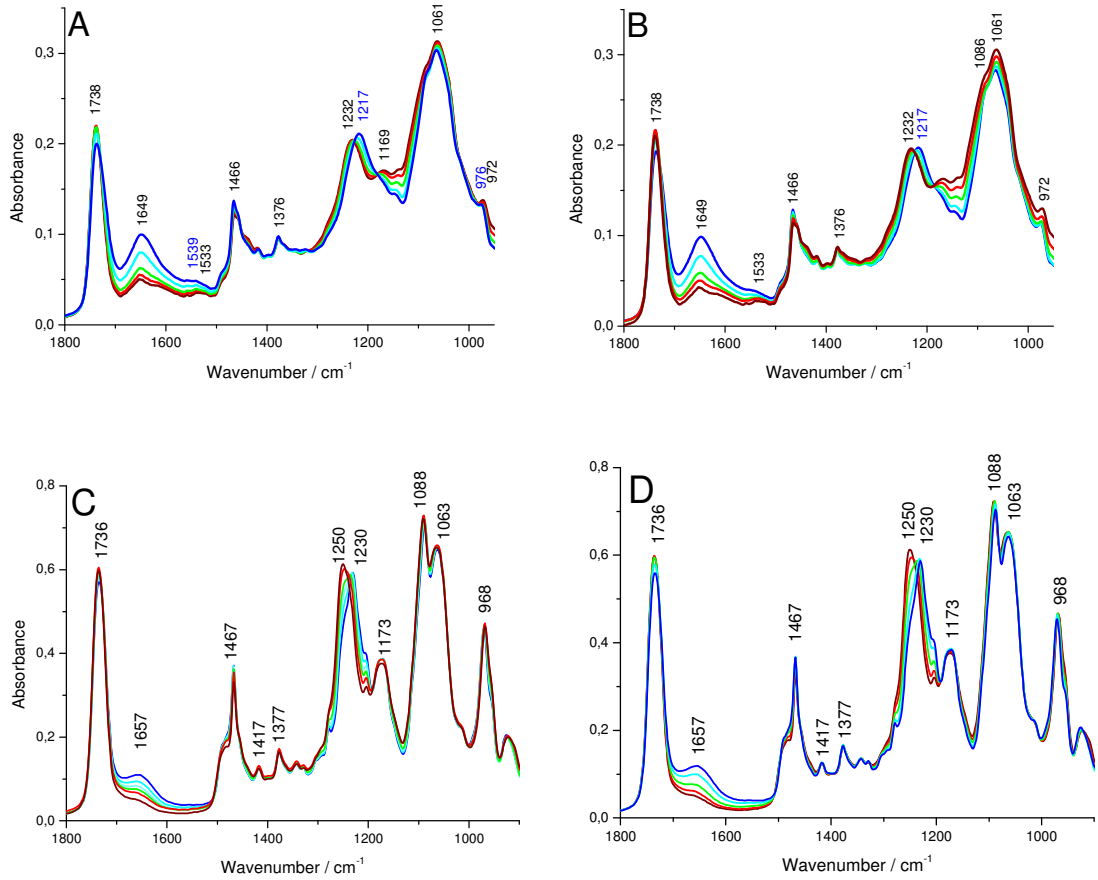

Figure 3.2: Temperature dependent ATR absorbance spectra of asolectin in D_2O, cooling (A), heating cycle (B) and phosphatidylcholine (C: cooling, D: heating). Line assignment: 5 °C blue, 10 °C cyan, 20 °C green, 30 °C red, 40 °C dark red.

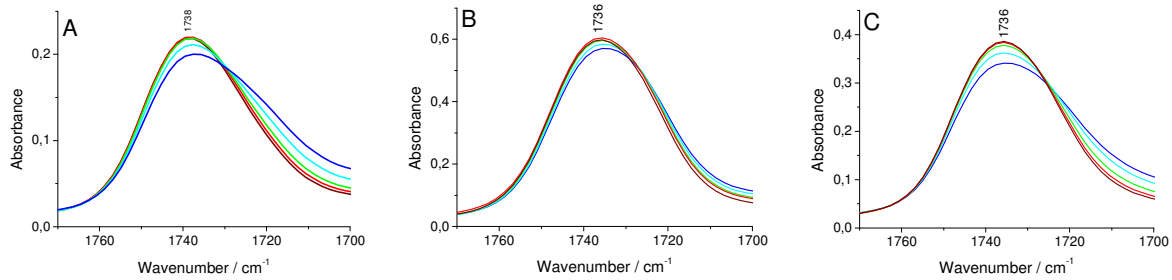

Figure 3.3: Enlarged view of the temperature dependent ν(C=O) mode of the interfacial region from asolectin (A), pure PC (B), and derivatives PC D_{35} (C). Line assignment: 5 °C blue, 10 °C cyan, 15 °C green, 30 °C red, 40 °C dark red.

In Figure 3.3 an enlarged view of the C=O stretching mode of asolectin (A), PC (B), and deuterated PC D_{35} (C) is depicted from the heating step.

The intensity of this band is sensitive towards the degree of hydration, indicating the presence of the intramolecular hydrogen bonds with large proton polarizibility (Popakostidis and Zundel, 1973). Furthermore, these ester carbonyl groups are considered of particular importance for the penetration depth of water molecules into the lipid bilayer (Simon and Mc Intosh, 1986; Scherer, 1989). The band maximum is obtained at 1738 cm^{-1} for asolectin and at 1736 cm^{-1} for PC as well as for deuterated PC D_{35}. Upon cooling a small shoulder appears at lower frequencies which corresponds to the gel phase transition (Mantsch et al., 1981).

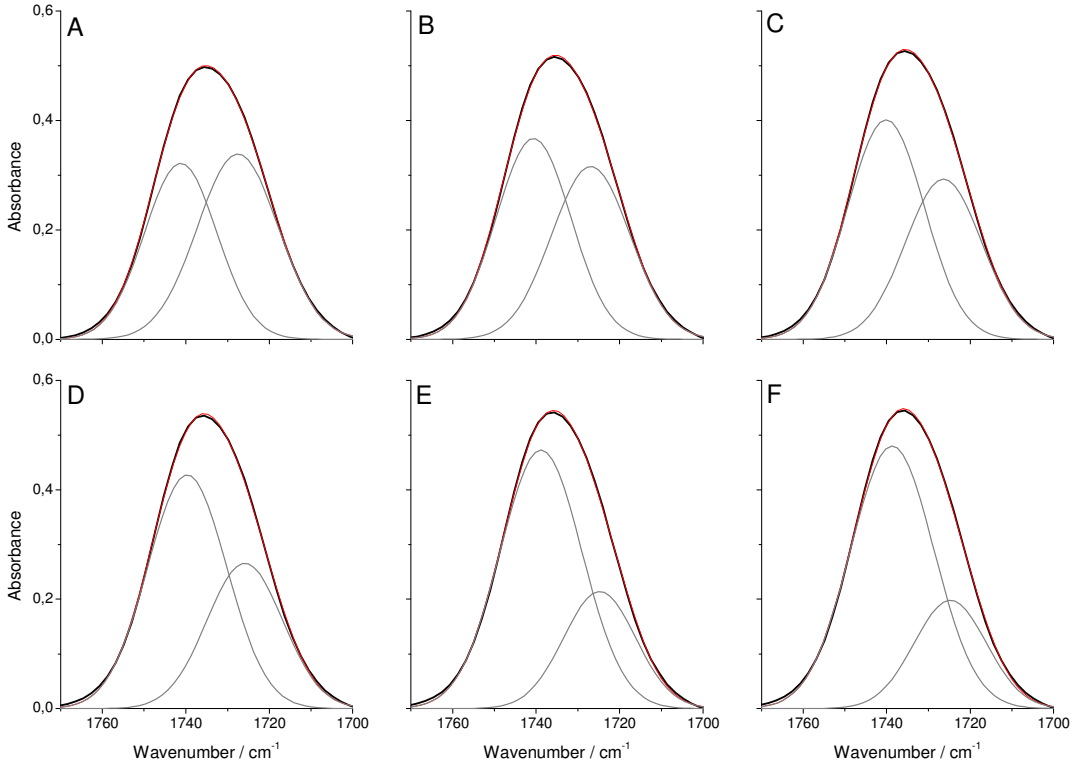

Figure 3.4: Deconvolution of the C=O stretching band of PC as a function of temperature, (A) 5 °C, (B) 10 °C, (C) 15 °C, (D) 20 °C, (E) 30 °C, (F) 40 °C.

Figure 3.4 shows the deconvolution of the C=O stretching band of PC as a function of temperature. The observation that the position of this band is only slightly temperature dependent strongly suggests that the C=O group is involved in intramolecular hydrogen bonding (Lewis et al., 1994). However, a shoulder at lower frequencies increases upon cooling (Panel A-E) suggesting that in phospholipids some of the ester C=O groups act as proton acceptors (Blume et al., 1988).

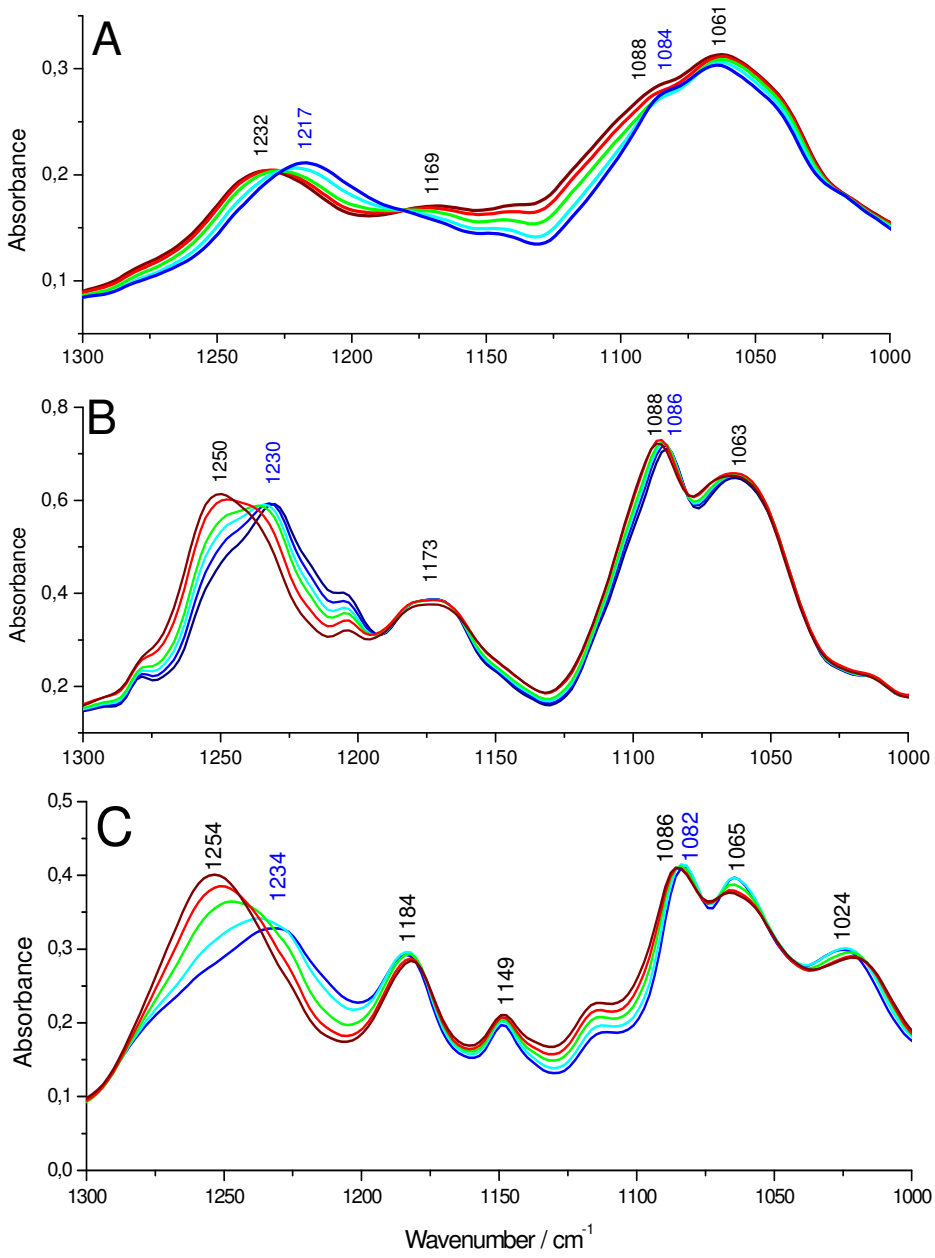

Figure 3.5: Enlarged view of the temperature dependent $\nu_{as}(PO_2^-)$ and $\nu_s(PO_2^-)$ stretching mode of asolectin (A), pure PC (B) and PC D_{35} (C). Line assignment: 5 °C blue, 10 °C cyan, 20 °C green, 30 °C red, 40 °C dark red.

The dominant absorbance bands in the region between 1300 and 1000 cm^{-1} originate from the phosphate groups of the head group and can be seen in Figure 3.5. The asymmetrical PO_2^- stretching vibration is found at 1232 cm^{-1} at 40 °C for asolectin, and for at 1250/1254 cm^{-1} (40°C) PC and PC D_{35}. The $\nu_{as}(PO_2^-)$ mode is sensitive to the temperature dependent phase transition (Lewis and McElhaney, 1998). It is a marker for the orientation between the phospholipid molecules. Formation of the gel phase induces a downshift to 1217 cm^{-1} for asolectin and to 1230/1234 cm^{-1} for PC and PC D_{35}. The symmetrical PO_2^- stretching

vibration is found in the liquid crystalline at 1088 cm^{-1} for asolectin and at 1088/1086 cm^{-1} for PC/PC D_{35} with a slight downshift to lower frequencies upon cooling. The signals of $\nu_{as}(PO_2^-)$ shift in all cases by about 20 cm^{-1} to higher wavenumbers, indicating a less strong hydrogen bonding. Furthermore, the observed shifts reveal that the hydrogen bonding between lipids and residual 'coordinated' water molecules in the lipid bilayer is reduced at higher temperature due to increased lipid spacing and stronger hydrogen bonding between the phosphate groups of the lipids.

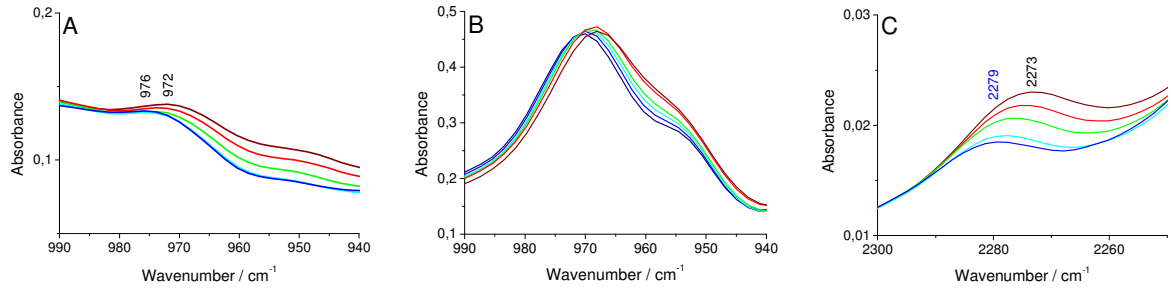

Figure 3.6: Enlarged view of the choline head group domain of asolectin (A), pure PC (B) and of the $\nu_{as}(CD_3)_3N^+$ mode from the derivative PC D_{35}. Line assignment: 5 °C blue, 10 °C cyan, 20 °C green, 30 °C red, 40 °C dark red.

The terminal part of the PC molecule is the choline group. The asymmetric $(CH_3)_3N^+$ stretching vibration is observed at 971 cm^{-1} (see Figure 3.5 Panel B). This band overlaps with the $\delta(N^+H_3)$ deformation mode of phosphatidylethanolamine which is found in asolectin. The peak position of the $\nu_{as}(CH_3)_3N^+$ mode is sensitive to dipolar interactions with molecules like water (Akutsu, 1981). The temperature dependence of the frequency of the asymmetrical C-$N^+(CH_3)_3$ stretching vibration is shown in Figure 3.6 for asolectin (A) and PC (B). The $\nu((CD_3)_3\text{-}N^+)$ stretching vibration is found at 2279 $cm^{-1}$for the PC D35 variant.

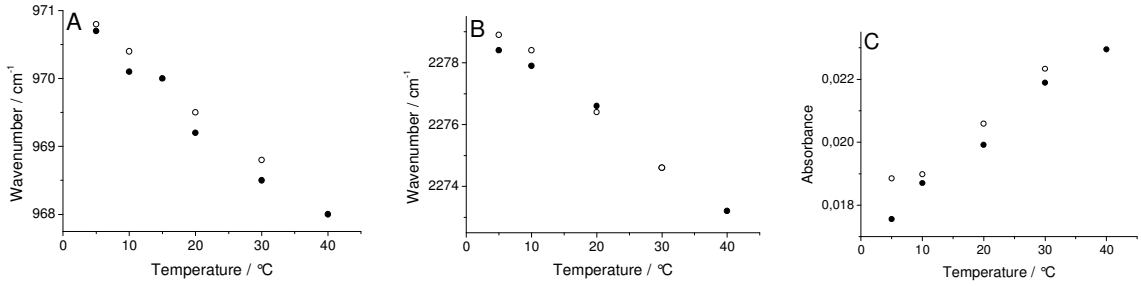

Figure 3.7: The temperature dependent profile of the $\nu_{as}(C\text{-}N^+(CH_3)_3)$ stretching mode from pure PC (A) and its derivative PC D35 (B,C). Point assignment: •: heating step, o: cooling step.

Interestingly, the absorbance bands of the choline mode downshift to lower frequencies with increasing temperature as seen in Figure 3.7. The small shift in the frequency of the $\nu_{as}((CH_3)_3N^+)$ mode upon heating is caused by the rearrangement of the choline group in response to the disrupted hydrogen bonding formed between the phosphate groups and water molecules. The latter seems to reflect the gradual weakening of structural water in the phospholipid bilayers.

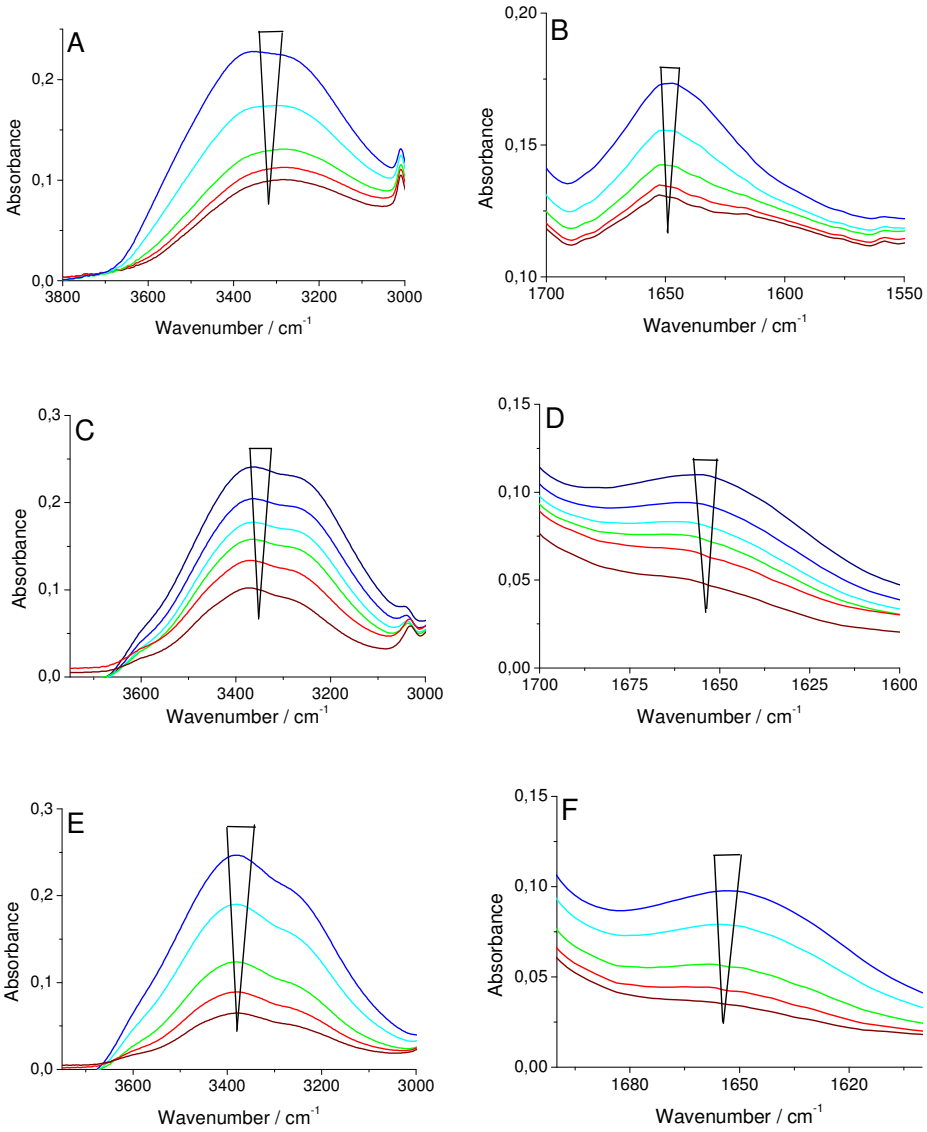

Figure 3.8: Temperature dependent behavior of the IR absorbance spectra of the ν(OH) stretching vibration from 3800 to 3000 cm^{-1} and the δ(HOH) bending vibration from 1700 to 1550 cm^{-1} of asolectin (A,B), PC (C,D) and PC D_{35} (E,F). Line assignment: 5 °C blue, 10 °C cyan, 20 °C green, 30 °C red, 40 °C dark red.

The broad feature at about 1649 cm^{-1} is assigned to the HOH bending vibration of bound water molecules (Venyaminov and Kalnin, 1990). The intensity of the δ(HOH) mode loses intensity upon heating. A dominating feature of the IR water spectrum is the band

located in the spectral range between 3600 and 3000 cm^{-1} which corresponds to the OH stretching motion. A free O-H stretching vibration is expected to absorb in the frequency range between 3500 and 3600 cm^{-1}, with a decrease in frequency if the OH group is involved in hydrogen bonding.

Figure 3.8 shows the characteristic OH stretching mode of water in asolectin (A), PC (C) as well as PC D_{35} variant (E). The band has a maximum at about 3357 cm^{-1} with a shoulder at lower frequencies. The band loses intensity upon heating and downshifts to 3288 cm^{-1} in a manner analogous to that found for the δ(HOH) mode. Importantly this process is reversible, as shown in Figure 3.9.

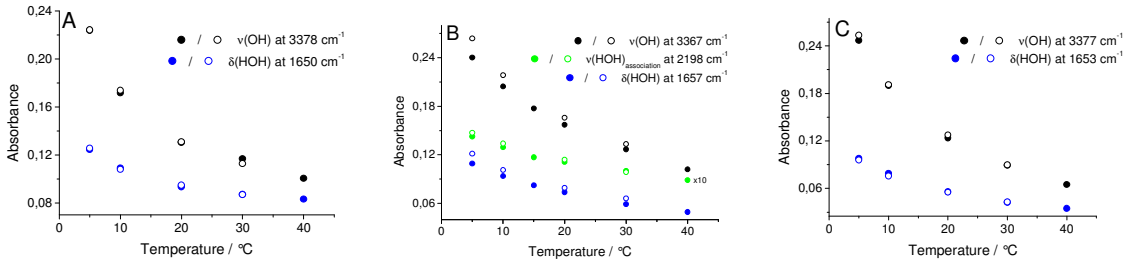

Figure 3.9: Temperature dependency of the ν(OH), $\nu(HOH)_{association}$ and δ(HOH) modes for asolectin (A), PC (B) and PC D_{35} (C). The temperature dependent absorbance spectra of the PC are shown in Figure 5.7 appendix.

It can thus be excluded that this effect is based on the drying of the sample upon heating. A likely explanation includes the change in number and arrangement of the coordinated water molecules in the different phases. The shoulder at 3288 cm^{-1} represents structured water molecules in an effective hydrogen bonded structure, the so called 'network water' (Binder, 2007). The spectral signature of protonated water molecules is a weak broad absorption extended above 2100 cm^{-1} (Garczarek et al., 2004). A very weak feature is seen there (see green symbols, Fig. 3.9 B).

	heating		cooling	
t / °C	ν(OH) /cm^{-1}	$\nu_{1/2}$(OH) /cm^{-1}	ν(OH) /cm^{-1}	$\nu_{1/2}$(OH) /cm^{-1}
5	3363	318	3363	330
10	3363	302	3363	309
15	3363	301		
20	3367	289	3367	289
30	3370	268	3369	266
40	3371	246		

Table 3.1: Temperature dependent data from the ν(OH) stretching vibration of PC.

However, the presence of protonated water is not clear. Temperature dependent variations of the broad band obtained between 3300 and 3400 cm^{-1} are summarized in Table 3.1. The relative absorbance of this band is more intense for stronger hydrogen bonds. Heating results in a shift and a marked decrease of the half width band ($\nu_{1/2}OH$) of the peak from 318 to 246 cm^{-1}.

3.1.1.2 Temperature dependent investigations in the far infrared spectral range

Figure 3.10 shows the spectroscopic properties in the far infrared domain from 600 to 50 cm^{-1} of asolectin (A), cardiolipin (B), PC (C) and its variants PC D_{22} (D), PC D_{35} (E). A significant signal is obtained in the range from 600 to 480 cm^{-1} and originates in particular from the head group domain. The peaks at 540 cm^{-1} and 503 cm^{-1} represent the O-P-O wagging and rocking vibrations from the lipid head groups (Leberle et al., 1989; Klähn et al., 2004).

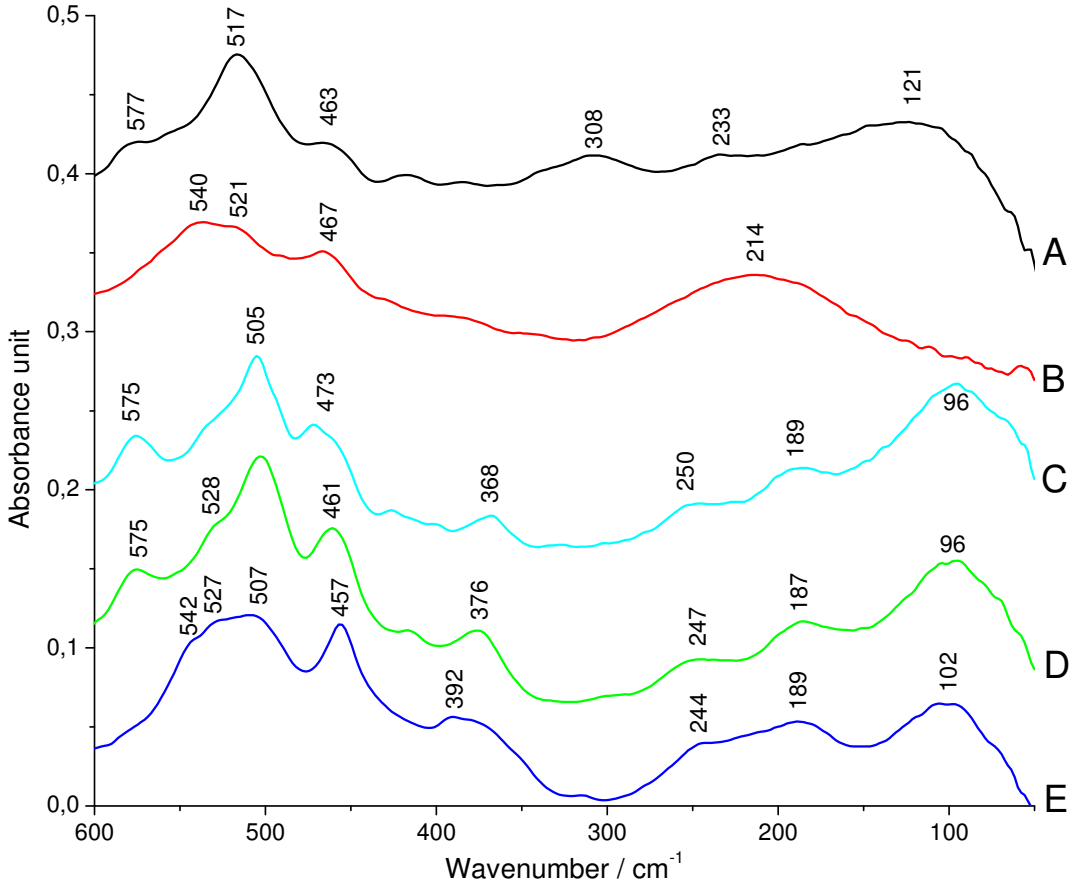

Figure 3.10: ATR far IR absorbance spectra of different phospholipids from 600 to 50 cm^{-1} at room temperature: (A) asolectin, (B) cardiolipin, (C) PC, (D) PC-D_{22} and (E) PC-D_{35}.

The peak at 575/577 cm^{-1} is assigned to the $CN^{+}(CH_3)_3$ deformation vibration which downshifts to 542 cm^{-1} for the deuterated PC D_{35} variant. Furthermore, the isotopically labeled PC C^{13} variant shows a weak shoulder at 573 cm^{-1}. The differential spectrum in Figure 3.11 shows clearly bands at 561, 503 and 473 cm^{-1}. The peak at 561 cm^{-1} can be a marker for the out of plane deformation mode of the labeled $\delta(C^{13}=O\text{-}OC)$ of the ester carbonyl groups.

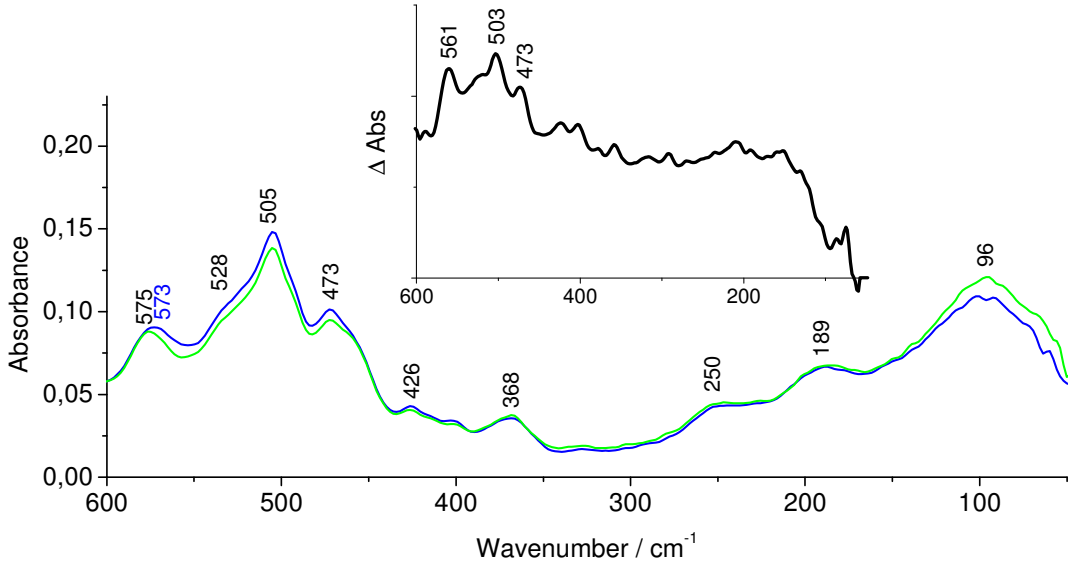

Figure 3.11: ATR far IR absorbance spectra of PC (blue line) and PC-C^{13} labeled (green line) as well as the unlabeled PC *minus* labeled PC C^{13} difference spectrum (inset). Spectra were measured at room temperature.

Table 3.2 summarizes the tentative assignments of phospholipids in the far infrared. The τ(C-CN) torsion vibration of the choline head group is found around 368 cm^{-1}. Furthermore, the prominent signals in the range of 300 to 180 cm^{-1} include coordinates of torsion motions of the hydrocarbon chains as well as deuterated carbon chains of the isotopically labeled PC variants. The most prominent signal in the lower frequency region is the broad feature below 200 cm^{-1}. This signal originates from the breathing mode of the molecule and from its intermolecular hydrogen bonding structure within the phospholipids bilayer (Knözinger, 1976). Interestingly, cardiolipin shows a broad hydrogen bonding feature at higher frequencies from 300 to 100 cm^{-1}. This observation is in agreement with hydrogen bonds with large proton polarizability, as Zundel and coworker have described (Zundel, 1996). Cardiolipin has two protonable phosphate groups. It is a unique phospholipid molecule (Haines and Dencher, 2002). Hübner and coworkers showed that cardiolipin forms an internal hydrogen bond with its phosphates (Hübner et al., 1991). The broadly defined hydrogen

bonding feature of the PC variants is slightly affected due to deuterated chains and arises from 165 to 50 cm^{-1}.

PC / cm^{-1}	PC D22 / cm^{-1}	PC D35 / cm^{-1}	CL / cm^{-1}	asolectin / cm^{-1}	Tentative assignments
575	575			577	δ ($CN^+(CH_3)_3$), [1] δ_{oop}(C-C=O) ?
561					δ_{oop}(C^{13}=O-OC) marker?
		542 (sh)			δ ($CN^+(CD_3)_3$)
528 (sh)	528 (sh)	527 (sh)	540		δ (O-P=O) [2,3]
505	503	507	521	517	δ (O-P-O) [4,5]
473	461	457	463	467	
368	376	392 (sh)			τ (CCN)
				330-260 308 (max)	
285-220 250 (max)	285-220 247 (max)	297-156 244 (max)	250 (max)		τ (C-CH_3) τ (C-CD_3) [6,7]
215-165 189 (max)	216-158 187 (max)	189 (max)			τ (CH_2 chain) τ (CD_2 chain) [8]
			300-100 214 (max)	250-200 233 (max)	τ (C-CH_3), τ (CH_2 chain), hydrogen bonds [8,9]
165-50 96 (max)	156-50 96 (max)	146-50 102 (max)		170-50 121 (max)	hydrogen or deuterium bonds [9]

Table 3.2: Tentative assignments of phospholipids vibrations in the far infrared domain. For descriptions see text. References according to: 1: Senent et al., 1998; 2: Doweidar et al., 2005; 3: Arora et al., 2001; 4: Leberle et al., 1989; 5: Klähn et al., 2004; 6: Durig et al., 2002; 7: Klug et al., 2002; 8: Maklakov and Aksakova, 1997; 9: Zundel et al., 1993.

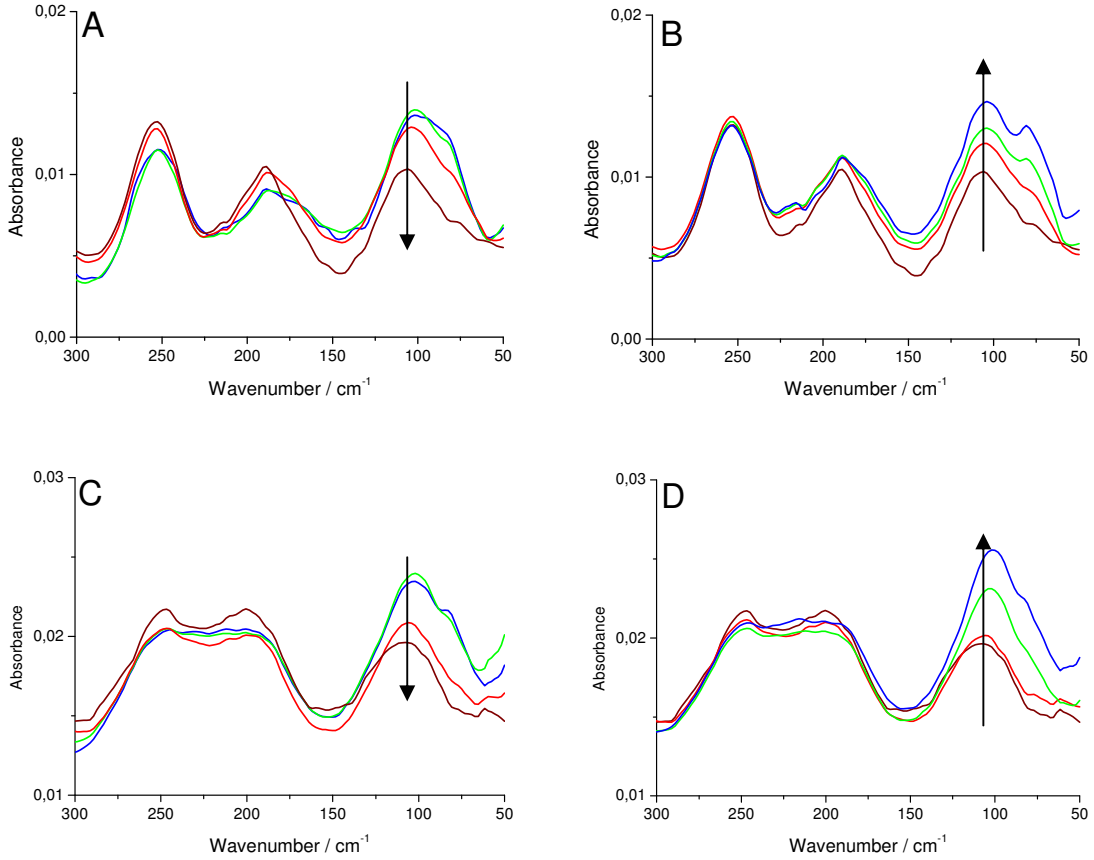

Figure 3.12: Far IR absorbance spectra of PC as a function of temperature upon heating (A) and cooling (C) cycle as well as its isotopically labeled variant PC D_{35} upon heating (C) and cooling (D). Line assignments: 5 °C blue line, 15 °C green line, 30 °C red line, 40 °C dark red line.

Figure 3.12 displays the temperature dependent behavior of pure PC in the far infrared range from 300 to 50 cm^{-1} as well as its istopically labeled variant PC D_{35} and furthermore shows the reversibility of the heating (A, C) and cooling (B, D) steps. The broad defined hydrogen bonding signature of the unlabeled PC around 102 cm^{-1} decreases upon heating and shifts to higher frequencies. The band becomes narrow at higher temperature and its half width decreases. In table 3.3 this behavior of the intermolecular stretching and bending modes of the hydrogen bonds between 50 and 141 cm^{-1} is summarized. However, this observation corroborates the development of water modes in the mid IR spectra that are based on losing bonded water molecules or weaker hydrogen bonds upon heating. The isotopically labeled variant PC D_{35} shows a behavior similar to the unlabeled PC.

	heating		cooling	
t / °C	ν(H···B)	$\nu_{1/2}$(H···B)	ν(H···B)	$\nu_{1/2}$(H···B)
5	96	41.8	98	43.6
15	98	41.2	99	41.4
30	100	40.8	100	40.4
40	106	31.6		

Table 3.3: Temperature dependent behavior of the hydrogen bonding signature of PC. B: oxygen and any other hydrogen bonding acceptors.

The far IR spectra of asolectin as a function of temperature in the spectral range from 300 to 50 cm^{-1} from 5 °C to 40 °C is shown in Figure 3.13 upon heating (A) and cooling (B). The broad feature from 280 to 100 cm^{-1} is assigned to the so called connectivity mode that includes the hydrogen bonding signature of water and any other hydrogen bond (Brubach et al., 2005).

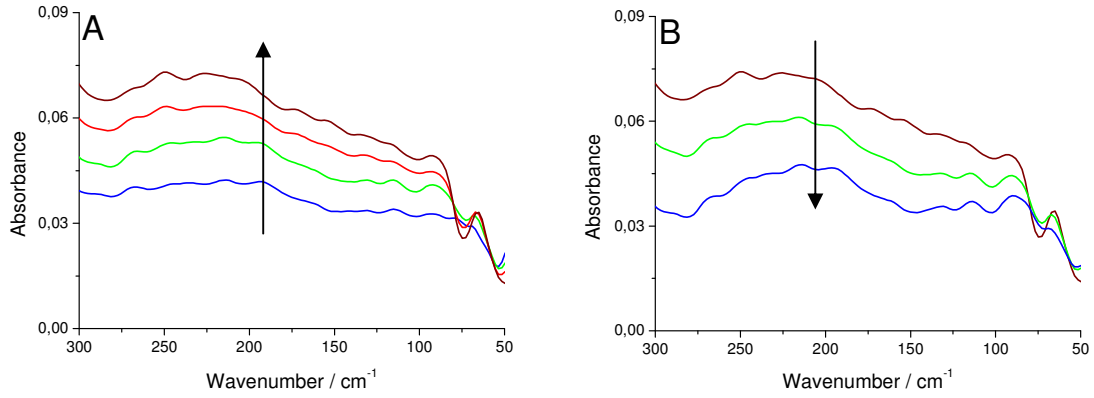

Figure 3.13: Far IR absorbance spectra of asolectin as a function of temperature upon heating (A) and cooling (B). Line assignments: 5 °C blue line, 15 °C green line, 30 °C red line, 40 °C dark red line.

However, the bands below 300 cm^{-1} cannot be determined exactly due to: the large half band width of these modes, baseline drifts based on the variation of synchrotron light, and the correction of the polyethylene window spectra (see Figure 5.9 in Appendix). In particular, the overall effects (increasing/decreasing of the intensities) were not affected at any time. The broad features of asolectin increase upon heating. This is in contrast to the decrease of the water modes in the mid IR (see Figure 3.8 before). However, the observation is in line with the increase of hydrogen bonding structure of the phosphate groups (see Figure 3.5 before). The so called connectivity mode thus follows the behavior of the hydrogen bonds

within the lipid structure. Evidently the contribution of bulk water does not dominate the spectral range in the films studied here. Water molecules compete for the phosphate group's binding site as a proton acceptor. Another important property of the mixed phospholipid bilayer is that certain lipids have the ability to interact intermolecularly with other types of lipids via hydrogen bond networks to self-associate (Boggs, 1987). Water molecules seem to be coordinated to the lipid bilayer. The far infrared shows differences in the hydrogen bonding interaction that is not evident in the mid infrared. This difference could be due to the mixture of head group types in asolectin that would allow a different interaction feature.

In conclusion, the temperature behavior of the hydrogen bonding pattern of pure PC and its isotopically labeled variant are in agreement with the observations in the mid IR range. Intermolecular hydrogen bonding between lipids with different charges at their head groups may be significantly stabilized by the fact that lipids are already intermolecular assembled as a result of the hydrophobic effect and the Van der Waals interactions between their chains.
Upon heating, the broad feature of the phospholipids mixture in asolectin increases, in contrast to the decrease of the water signature and protonated water in the mid IR spectra range for this sample and in contrast to the observation in pure PC. This indicates that the contribution of bulk water does not dominate the spectral range in the far IR.

Apparently, asolectin and pure PC, as well as its isotopically labeled variant, do not show the same temperature dependent shifts in the far infrared. In asolectin the intermolecular hydrogen bonding is stronger at higher temperature, subsequently in the liquid-crystalline phase. Pure PC seems to be less organized at higher temperature from the intermolecular point of view as confirmed by the isotopically labeled variant. An effect of the chain length can be excluded based on the comparison of the unlabeled and isotopically labeled PC, which have different chain lengths, but behave similarly. An effect based on the different degree of saturation of the chains cannot be excluded.

The main structural difference between these two samples is the variation of the head groups that induces a very different spectral signature in the far infrared. The high degree of variability of asolectin's head groups, including sugar, choline and ethanolamine, allows a more rigid structure to be built. In pure PC this cannot be expected. Interestingly, the C=O carbonyl groups of the interfacial region in lipids, monitored at 1738/1736 cm^{-1}, do not show this different behavior (see in addition Figure 5.6 in Appendix, band splitting of the C=O of asolectin). It could thus only be based on the NH_3^+ in PE and the inositol sugar group in PI, which may be monitored by a lipid titration of different types of lipids.

3.1.2 Assembly of the transmembrane cytochrome b_6 from spinach

Folding and assembly studies with α-helical membrane proteins are often hampered by the absence of high-level expression systems as well as by missing suitable *in vitro* refolding procedures. Cytochrome b_6 can serve as an excellent model system for *in vitro* studies on the dynamic interplay of an apo-protein and heme cofactors during assembly of a transmembrane *b*-type cytochrome (Prodöhl et al., 2007). We found that in *in vitro* assembled cytochrome b_6 binds two hemes with different midpoint potentials. The redox potentials of the reconstituted cytochrome b_6 were determined by a spectroelectrochemical approach (Figure 3.14).

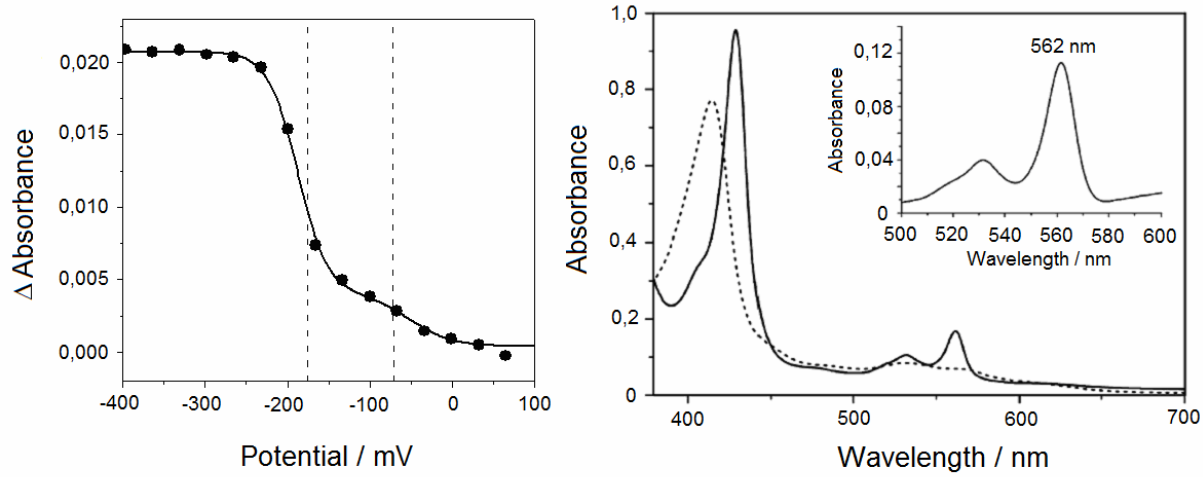

Figure 3.14: The redox dependent development of the reconstituted cytochrome b_6 as monitored in the visible spectra range is shown on the left panel. Two redox potentials were found for a best fit at 562 nm with an n-value (number of transferred electrons) of 1 for each transition. The absorbance spectra of oxidized and reduced cytochrome b_6 are shown on the right panel. Apo-cytochrome b_6 was refolded *in vitro* in 5 mM DDM and free heme was added. The inlet shows the redox difference spectrum with an α-band absorbance maximum at 562 nm.

Two potentials with a value of -187 and -68 mV (vs. SHE') were found, corresponding to the low potential and high potential heme, respectively. The electrochemical properties of the reconstituted cytochrome b_6 protein in detergent revealed no noteworthy differences compared to the same protein incorporated into the *Escherichia coli* inner membrane (Kroliczewski et al., 2005) or into the spinach thylakoid membrane (Kramer and Crofts, 1994). This similarity further confirms correct *in vitro* assembly of the protein in detergent.
In conclusion, a protein was reconstituted which displays spectroscopic characteristics similar to cytochrome b_6 isolated from natural sources.

To study the influence of heme binding on the assembly pathway of cytochrome b_6, mutations were performed on the four histidine residues that serve as axial ligands for the two *b*-type hemes (see Figure 1.13 in introduction). Histidine residues were mutated to alanine. The exact number of heme molecules bound to wild type cytochrome b_6 was deduced from heme titration experiments (for details see Dreher et al., 2008). After addition of increasing amounts of apo-cytochrome b_6 to free heme, an increase in the absorbance at 429 nm was observed until a protein/heme ratio of about 1:2 was reached. This clearly indicates that the wild type protein binds two heme molecules, as expected. Similar titrations were performed with all cytochrome b_6 variants and the results are given in Table 3.4.

cytochrome b_6	No. hemes	E_m /mV	
		b_L	b_H
Wild type	2	-187	-68
H86A	-	-	-
H187A	2	n.d.	n.d.
H86A/H187A	-	-	-
H100A	2	-187	+34
H202A	1	-14	-
H100A/H202A	1	-45	-

Table 3.4: Characteristics of wild type cytochrome b_6 and its variants. E_m potentials are referenced to the standard hydrogen electrode with a standard deviation of ±15 mV. n.d.: not determined, here the protein was unstable during the redox titration.

When both heme b_L ligands (His86 and His187) were replaced by alanine, thus preventing heme b_L binding, the resulting protein did not bind any heme molecules. In contrast, when the two heme b_H-ligating histidine residues His100 and His202 were replaced, the resulting cytochrome b_6 variant bound heme b_L with high affinity, whereas binding of heme b_H was not observed. This indicates specific differences in heme b_L and b_H binding for assembly of holo-cytochrome b_6. Binding of heme b_L seems to be required for cytochrome b_6 assembly.

To further characterize the electrochemical properties of the cytochrome b_6 variants, the midpoint potentials of the constructed variants were determined (see Figure 3.15). The midpoint potentials are summarized in Table 3.4.

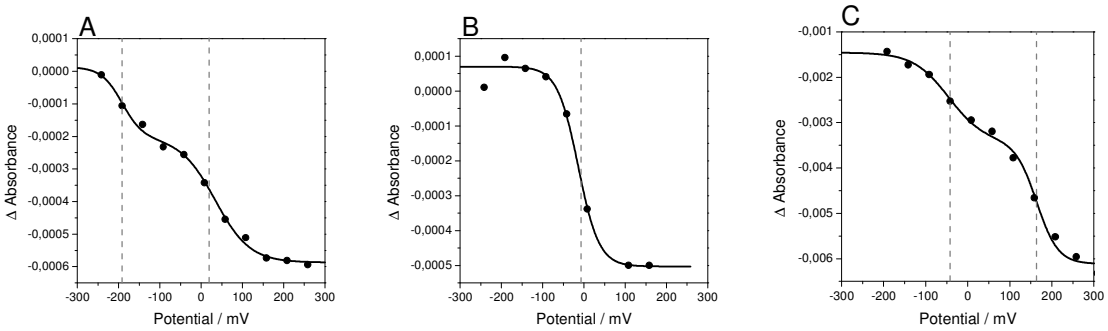

Figure 3.15: Electrochemically induced titrations of H100A (A), H202A (B) and the double mutant H100A/H202A (C).

After replacement of the two b_H-ligating residues His100 and His202, only heme b_L remained bound to the protein. Determination of the heme b_L midpoint potential showed that the potential is upshifted. The midpoint potential was -45 mV for heme b_L (Figure 3.15, panel C).

Replacement of His100 alone resulted in no change of the heme b_L (-187 mV, the same value as determined for the wild type) midpoint potential whereas the heme b_H midpoint potential was shifted to +34 mV (Figure 3.15, panel A). In contrast, when His202, the second heme b_H-ligating residue, was replaced by alanine alone or in combination with His100, only heme b_L was bound to the apo-protein and the midpoint potential of heme b_L was altered. A midpoint potential of -14 mV was determined (Figure 3.15, panel B). Therefore, the absence of heme b_H and the change in the heme b_L environment strongly affected the heme b_L midpoint potential. This observation suggests that binding of heme b_L is required for binding heme b_H (Dreher et al., 2008).

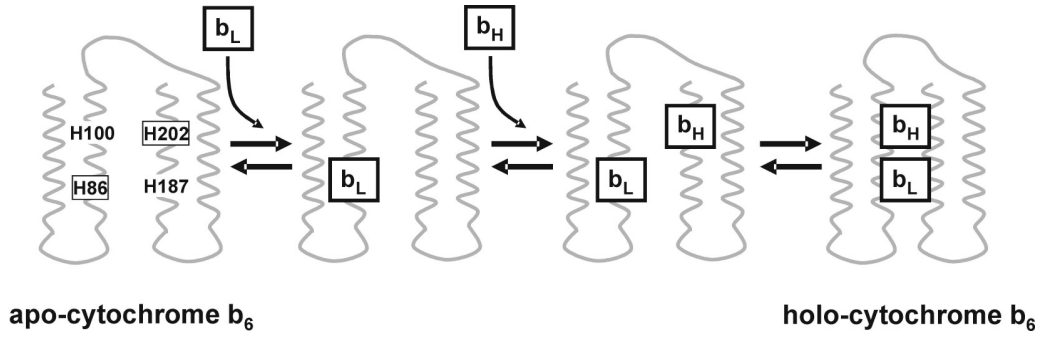

Figure 3.16: Multiple steps assembly of apo-cytochrome b_6 to holo-cytochrome b_6 (reprinted with kind permission C. Dreher et al., 2008).

The conversion of apo-cytochrome b_6 to holo-cytochrome b_6 is involved in multiple steps, as seen in Figure 3.16. After membrane integration of apo-cytochrome b_6, heme b_L binds predominately *via* His86 to the protein moiety. Subsequently, heme b_H binds primarily *via* His202 to the assembly intermediate which results in a rearrangement of the protein structure. His187 and His100 are involved in stabilization of bound heme b_L and heme b_H, respectively.

3.1.3 Protein-lipid interaction in cytochrome bc_1 complex

In this section we present the study on the role of phospholipids, bound within the protein structure and, importantly, reorganizing during the redox reaction of the protein. As described before, infrared spectroscopic studies on phospholipids, have provided insight on features of the different structures and the individual vibrational modes in model and natural membranes (Mantsch and McElhaney, 1991; Casal et al., 1979; Mendelsohn et al., 1984).

The electrochemically induced FTIR difference spectra of proteins include signals that derive from reorganizations of the protein upon the induced redox reaction and coupled protonation events as well as protonation events of the buffer. In addition, the spectra may contain contributions from the cofactors, and importantly from lipids that reorganize or protonate upon the redox reaction.

3.1.3.1 Electrochemically induced difference spectra of cytochrome bc_1 complex from Saccharomyces cerevisiae

The electrochemically induced FTIR difference spectra of the cytochrome bc_1 complex from *S. cerevisiae* for a potential step from -0.29 to 0.7 V in the spectral range from 1800 to 900 cm^{-1} are presented in Figure 3.17. In the oxidized *minus* reduced FTIR difference spectra positive bands represent signals associated with the oxidized state of the protein and negative signals with the reduced state. In general, signals from conformational changes of the protein backbone and the cofactors, protonation/deprotonation reaction, and contributions of the amino acid side chains, as well as contributions of structural lipids are expected. There are two main spectral regions: the amide I region between 1690 and 1620 cm^{-1} and the amide II region between 1560 and 1520 cm^{-1}.

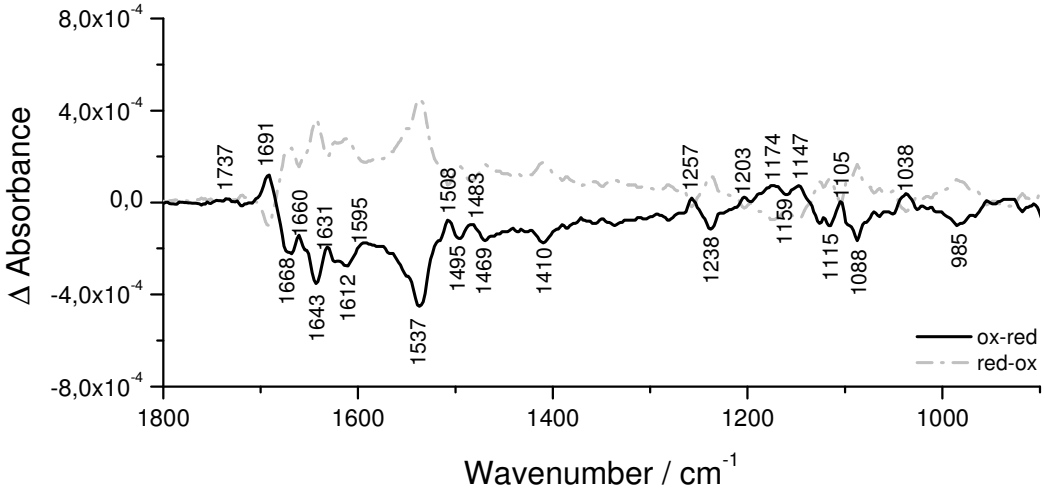

Figure 3.17: Electrochemically induced FTIR redox difference spectra of cytochrome bc_1 complex (wild type) for a full potential step from -0.29 to 0.71 V, Tris-buffer pH 7.3.

In the amide I range, modes from the ν(C=O) stretching vibrations of the polypeptide backbone can be expected and absorptions characteristic for the different secondary structure elements can be described (Goormaghtigh et al., 1994c). The band at 1691 and 1631 cm^{-1} may involve β-sheet elements, whereas the peak at 1660 cm^{-1} includes signals from the predominately α-helical structure of the enzyme. In addition, the ν(C=O) modes of the bound and free quinones are expected in the spectra. In comparison to recent FTIR studies of cytochrome bc_1 complexes from other organisms, the involvement of quinones in this spectral range is similar (Baymann et al., 1999; Ritter et al., 2003; Ritter et al., 2004; Iwaki et al., 2003; Iwaki et al., 2004; Iwaki et al., 2005; Breton et al., 1994). Further signals for the bound quinones can be expected at 1612 cm^{-1} (ν(C=C)) and 1264 cm^{-1} (δ(C-OCH_3)), while the negative signals at approximately 1495, 1469, and 1410 cm^{-1} include contributions from the reduced and protonated quinol (Hellwig et al., 1999).

In comparison to previous studies, signals from the three hemes, b_L, b_H, and c_1, including the heme propionates, vinyl side chains, and the porphyrin ring can be expected (Berthomieu et al., 1992). On the basis of heme model studies, the strong positive signal at 1691 cm^{-1} is tentatively attributed the ν(C=O) modes of protonated heme propionates (Berthomieu et al., 1992). The signal at 1574 and 1537 cm^{-1} are tentatively assigned to the antisymmetric $\nu_{as}(COO^-)$ vibrations (Behr et al., 1998), whereas the symmetric $\nu_s(COO^-)$ vibration can be found at 1410 cm^{-1}. Heme ν(C=C) modes of the porphyrin ring are typically

involved in the broad mode between 1560 and 1530 cm^{-1}. However, involvement of the coupled C-N stretching and N-H bending modes from the backbone, the so called amide II mode, are also expected in this spectral region.

Fe-S vibrations from the Rieske [2Fe-2S] cluster cannot be found in the investigated spectral range, because the Fe-S vibration is present at lower frequencies (Julian Gross and Youssef El Khoury, Institut de Chimie, personal communication).

The spectral region above 1710 cm^{-1} is characteristic for protonated aspartic or glutamic acids (Hellwig et al., 2000). A peak at 1737 cm^{-1} is present, reflecting the contribution of an aspartic or glutamic acid protonated in the oxidized form. For the deprotonated form a signal at 1537 cm^{-1} can be tentatively attributed to the $\nu_{as}(COO^-)$ mode, whereas the $\nu_s(COO^-)$ mode is involved between 1420 and 1370 cm^{-1}. Protonated tyrosine is known to contribute with the $\nu_{19}(CC)$ ring mode at approximately 1518 cm^{-1}. For deprotonated tyrosine the $\nu_{19}(CC)$ ring mode can be expected at about 1495 cm^{-1}, reflecting the sensitivity of the ring modes to the protonation state of the phenol group. The $\nu_{7'a}(C\text{-}O^-)$ vibration is found at approximately 1257 cm^{-1}, but the exact position depends on the hydrogen bond environment (Venyaminov and Kalnin, 1990; Hienerwadel et al., 1997, Wolpert 2007). However, these assignments are tentative and need to be confirmed by site directed mutagenesis. All tentative assignments made are summarized in Table 3.5.

band position in cm^{-1}	tentative assignments		remarks
1737 (+)	υ(C=O)	Asp/Glu	Lipids
1710 (+)	υ(C=O)	Asp/Glu	
1691 (+)	amide I	β-sheet	Rieske-protein
	υ(C=O)	heme propionates	cyt *b* and/or cyt c_1
1668 (-)	$\upsilon_{as}(CN_3H_5)$	Arg	
	υ(C=O)	Gln/Asn	
1660 (+)	amide I	α-helical	
	υ(C=O)	quinone	
1643 (-)	amide I		
1631 (+)	amide I	β-sheet	Rieske-protein
	υ(C=O)	quinone	
	$\upsilon_s(CN_3H_5)$	Arg	
	υ_{37}	heme	cyt c_1
1620 (+)			
1612 (-)	υ(C=C)	quinone	
1595 (+)	υ_{37}	heme	cyt *b*
1574 (+)	Amid II		
	$\upsilon_{as}(COO^-)$	heme propionates	cyt *b* and/or cyt c_1
1558 (+)	υ_{38}	heme	cyt *b* or cyt c_1
1550 (+)	υ_{38}	heme	cyt *b* or cyt c_1
1537 (-)	Amid II		
	$\upsilon_{as}(COO^-)$	Asp/Glu	
	$\upsilon_{as}(COO^-)$	heme propionates	cyt *b*, cyt c_1
1518 (+)	$\upsilon_{19}(CC)_{ring}$	Tyr-OH	
1508 (+)	Amid II		
1495 (-)		quinone ring	
	$\upsilon_{19}(CC)_{ring}$	Tyr-O^-	
1469 (-)		quinone ring	
1410 (-)		quinone ring	
	$\upsilon_s(COO^-)$	heme propionates	cyt *b*, cyt c_1
1292 (+)	υ(C-O)	methoxy group quinone	
1264 (+)	$\delta(C\text{-}OCH_3)$	methoxy group quinone	
1257 (+)	υ_{42}	heme	cyt *b*, cyt c_1
	$\upsilon_{7'a}(C\text{-}O^-)$	Tyr	
1238 (-)	δ(COH)	Tyr	
1203 (+)		quinone	
1159 (-)		quinone	(Baymann *et al.,* 1999)
1147 (+)	$(C\text{-}C)_{vinyl}$	heme	Cyt b_L (Baymann *et al*., 1999)
1105 (+)	$\delta(=CH_2)_{vinyl}$	heme	Cyt b_H (Choi *et al*., 1982; Berthomieu *et al*., 1992)
1038 (+)		Tris buffer	

Table 3.5: Tentative assignments for the electrochemically induced FTIR difference spectra of the bc_1 complex from yeast. References according to: Ritter et al., 2003, 2004; Baymann et al., 1999; Choi et al., 1982; Iwaki et al., 2003, 2004, 2005; Wolpert and Hellwig, 2005, Marboutin et al., 2006; Berthomieu et al., 1992.

3.1.3.2 Electrochemically induced difference spectra of the depleted bc_1 complex from S. cerevisiae

In order to assign contributions of lipid vibrations, the cytochrome bc_1 complex was depleted using phospholipase A_2. The sample preparation was performed by Dr. Tina Wenz (see Material and methods, section 2.1.3).

Figure 3.18 shows the electrochemically induced FTIR difference spectra of the depleted cytochrome bc_1 complex for a full potential step from -0.29 to 0.71 V in the spectral range from 1800 to 900 cm^{-1}.

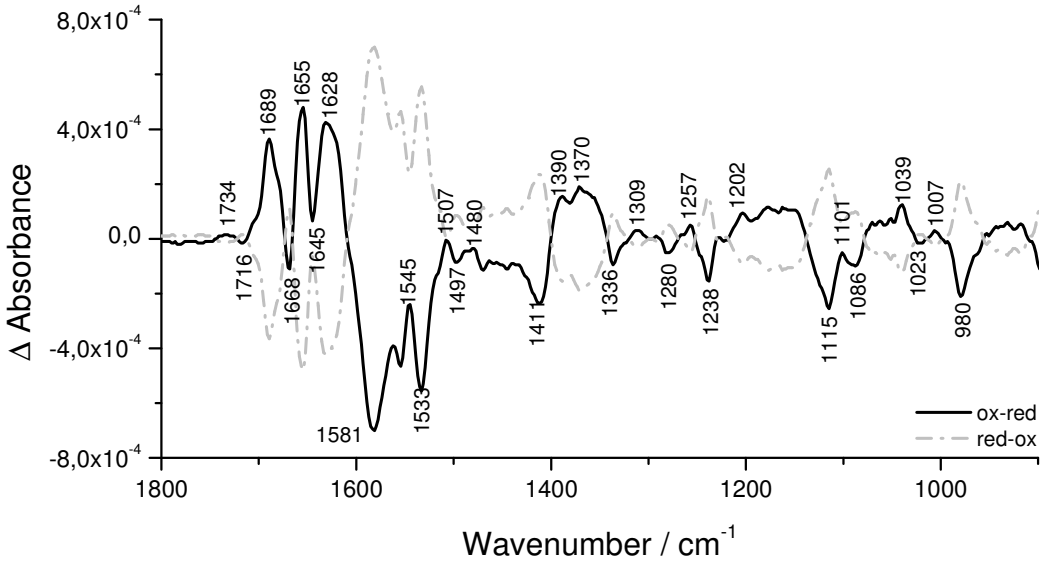

Figure 3.18: Electrochemically induced FTIR difference spectra of the depleted cytochrome bc_1 complex for a full potential step from -0.29 to 0.71 V, Tris-buffer pH 7.3.

Despite the complete inactivation of the enzyme (Gomez and Robinson, 1999; Wenz et al., 2009) electrochemically induced difference spectra of the cytochrome bc_1 complex after depletion of lipids have been found to be stable and the protein to react reversibly, as controlled by comparing the data at different points of the experiment that typically takes several hours.

The direct comparison of the oxidized *minus* reduced FTIR difference spectra of the cytochrome bc_1 complex with and without lipids reveals strong changes in the full spectral range between 1800 and 900 cm^{-1}. Figure 3.19 shows the oxidized *minus* reduced FTIR

difference spectra of the purified yeast cytochrome bc_1 complex as isolated (A) in direct comparison to the enzyme after treatment with phospholipase A_2 (B).

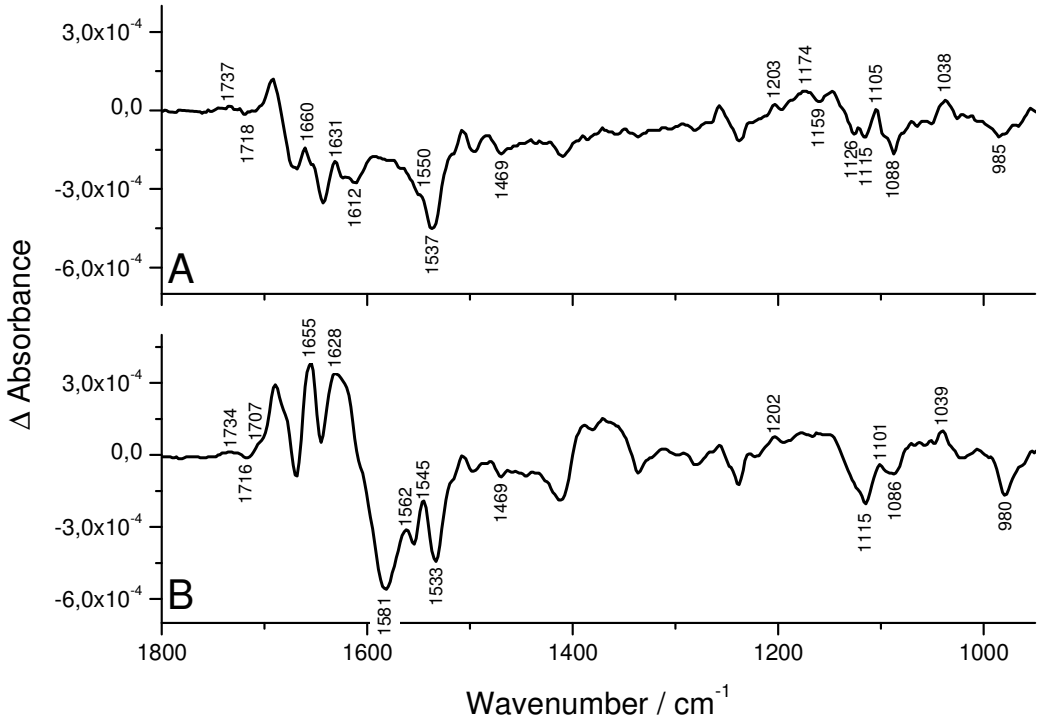

Figure 3.19: Oxidized *minus* reduced FTIR difference spectra of the wild type bc_1 complex (A) and of the depleted bc_1 complex (B), Tris-buffer pH 7.3.

These variations include changes in the amide I (1690-1620 cm^{-1}) and amide II (1560-1520 cm^{-1}) range, were contributions from the protein backbone are involved. Interestingly, a higher signal intensity can be observed, for example at 1628 and 1531 cm^{-1}. Variations of the heme modes, previously assigned for the wild type (Ritter et al., 2003; Ritter et al., 2004; Iwaki et al., 2003) around 1550 cm^{-1}, cannot be excluded. A major differential feature at approximately 1390 cm^{-1} is observable in the spectra in the absence of lipid. This spectral range is rather unspecific and a tentative assignment is not possible. The signals involving contributions from the Glu272 side chain at 1734 cm^{-1} (Wenz et al., 2006), however, are not significantly changed, indicating that this residue is not influenced by lipids and in addition that there is no significant contribution from the lipid in this spectral range as found previously for complex I and Rhodopsin (Beck et al., 1998; Isele et al., 2000; Hielscher et al., 2006).

In order to highlight the spectral range were the phosphate head groups of lipids are expected, the enlarged view of the spectral region from 1200 to 900 cm^{-1} is presented in Figure 3.20 in direct comparison to the spectra of the protonation of cardiolipin (pH 9-pH 2) together with the protonation of mixed lipids.

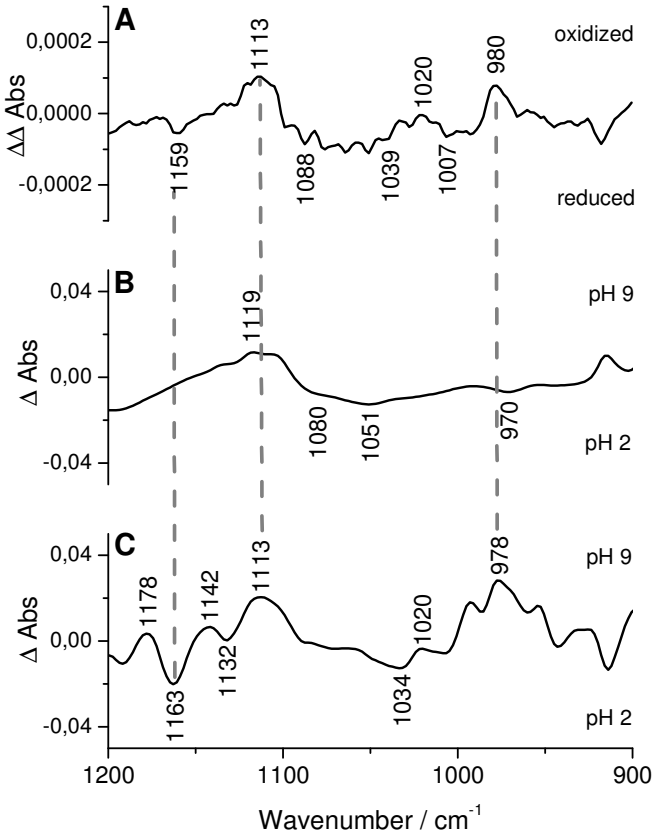

Figure 3.20: Enlarged view of the spectral region from 1200 to 900 cm^{-1}. Panel A shows the double difference spectrum obtained by subtraction the lipid-free bc_1 *minus* wild type spectra (A) in direct comparison to the difference spectra of mixed lipid (B) and cardiolipin vesicle (C) in protonated and deprotonated form, the latter obtained subtraction the absorbance spectra from pH 2 – pH 9.

The main variations seen in this spectral region concern the differential features at 1113, 1159, 1039, 1020 and 980 cm^{-1}. These modes clearly correlate with signals of the lipid head group. We note that the presence of lipids will induce positive and negative signals in the moment changes of the environment occur upon the induced electron transfer. Most of the lipids present in the enzyme will thus not be affected and not contribute in the redox induced difference spectra. We cannot exclude, that in addition to the critical cardiolipin molecule discussed, further lipids move as an indirect response to the electron transfer of the different cofactors. Furthermore contributions from amino acid side chains (Wolpert and Hellwig, 2006) or hemes are involved here (Marboutin et al., 2006; Choi et al., 1982; Berthomieu et al.,

1992). However, they are expected to be rather small. Most of the signals seen, like the broad band between 1088 and 1039 cm^{-1}, correlate with typical modes of cardiolipin molecules (Figure 3.20, panel C). The difference spectra obtained for the protonation of cardiolipin in solution (pH 2-pH9) display clear similarities with the features lost in data of the cytochrome bc_1 complex after delipidation (Figure 3.20, panel A). In contrast the comparison to the spectral features for the protonation of mixed lipids does not show the same degree of similarity. On this basis the shifts of the head group seen at 1159, 1113, 1039 and 980 cm^{-1} the protonation of cardiolipin coupled to the reduction is suggested. Since the contributions of the PO groups are sensitive to the hydrogen bonding environment, some of the spectral features may be due to the movement of the protein induced by the redox reaction.

3.1.3.3 Electrochemically induced difference spectra after addition of phospholipids

Upon addition of cardiolipin, but not other lipids, a reactivation of the yeast enzyme is observed (Wenz et al., 2009) and was also described for the bovine cytochrome bc_1 complex (Gomez and Robinson, 1999). We have performed redox induced FTIR difference spectra of the enzyme after addition of cardiolipin to the phospholipase A_2 treated enzyme (Figure 3.21).

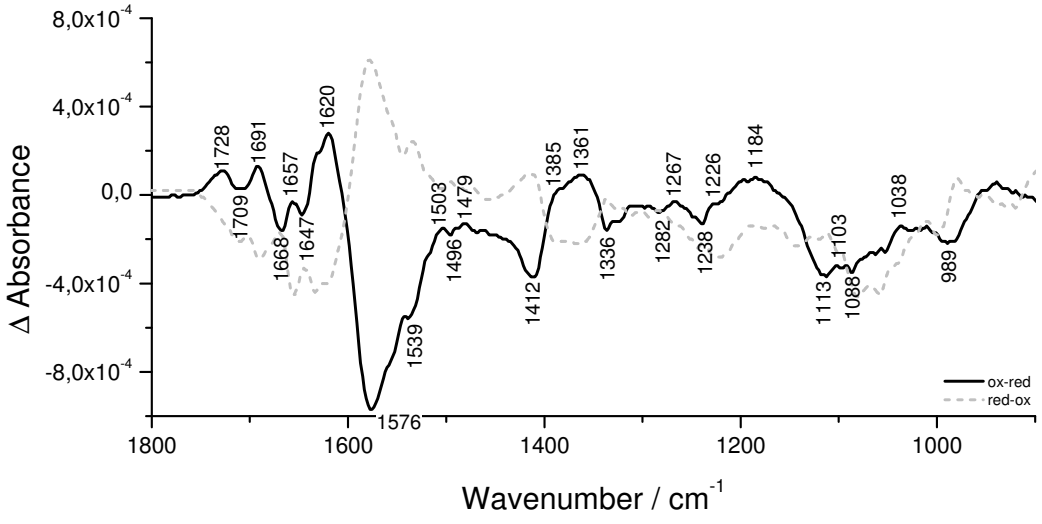

Figure 3.21: Electrochemically induced FTIR difference spectra of delipidated bc_1 complex after addition of cardiolipin for a full potential step from -0.29 to 0.71 V.

Figure 3.22 shows the redox induced FTIR difference spectra of cytochrome bc_1 complex after addition of asolectin and cardiolipin to the depleted enzyme. Overall, some of the changes induced by lipid depletion change are compensated, however, not all of them. Cardiolipin alone indicated a rather unstable sample that changed its spectral properties after several reaction cycles. The addition of asolectin was found to be essential for stabilization.

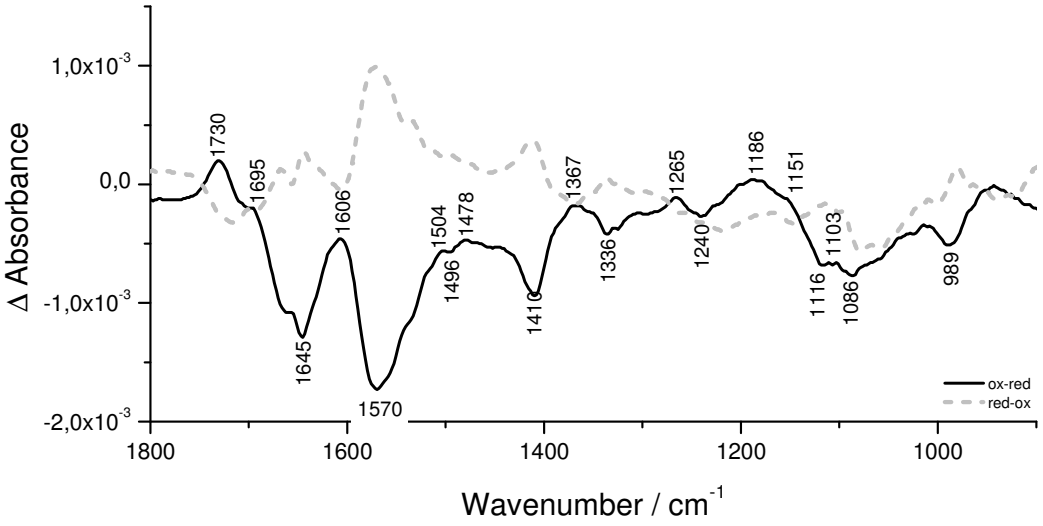

Figure 3.22: Electrochemically induced FTIR difference spectra of delipidated bc_1 complex after addition of asolectin and cardiolipin for a full potential step from -0.29 to 0.71 V.

The major change in the amide I region from 1690 to 1620 cm^{-1}, that reflects the variation of the polypeptide backbone after depletion of the lipids, is only partially compensated after addition of the lipids. Certainly, not all lipid molecules are re-integrated in their binding sites, but are attached to the protein. The binding site may also contain fragments from the original lipid or detergent molecules bound non-specifically to the site; but avoiding the new lipid molecule to accommodate at the site. This is in line with the observation that there is only partial reactivation (Wenz et al., 2009). Table 3.6 summarizes the tentative assignments of the wild type, the depleted enzyme and after addition of asolectin and cardiolipin.

wt	lipid depleted	AsoCL addition	assignments	
1737 (+)	1734 (+)		υ(C=O)	Asp/Glu
		1730 (+)	υ(C=O)	lipid contribution
1710 (+)	1707 (s)		υ(C=O)	Asp/Glu
1691 (+)	1689 (+)	1695 (+)	amide I	(Rieske/β-sheet)
			υ(C=O)	heme propionates b_L, b_H
1668 (-)	1668 (-)	1662 (-)	$\upsilon_{as}(CN_3H_5)$	Arg
			υ(C=O)	Gln/Asn
1660 (+)	1655 (+)	1658 (+)	amide I	α-helical
			υ(C=O)	quinone
1643 (-)	1645 (-)	1645 (-)	amide I	
1631 (+)	1628 (+)	1630 (s)	amide I	(Rieske/β-sheet)
			υ(C=O)	quinone
			$\upsilon_s(CN_3H_5)$	Arg
			υ_{37}	heme c_1
1620 (+)	1620 (s)	1620 (s)	υ(C=C)	quinone
1612 (-)				
1595 (+)		1606 (+)	υ_{37}	heme b_L, b_H
	1581 (-)	1570 (-)		
1574 (+)			amide II	
			$\upsilon_{as}(COO^-)$	heme propionates b_L, b_H, c_1
1558 (s)	1562 (+)	1558 (s)	υ_{38}	heme b_L, b_H
1550 (+)	1545 (+)		υ_{38}	heme c_1
1537 (-)	1533 (-)	1537 (-)	amide II	
			$\upsilon_{as}(COO^-)$	Asp/Glu
			$\upsilon_{as}(COO^-)$	heme propionates b_L, b_H, c_1
1518 (+)	1518 (s)	1518 (s)	$\upsilon_{19}(CC)_{ring}$	Tyr-OH
1508 (+)	1507 (+)	1504 (+)	amide II	
1495 (-)	1497 (-)	1496 (-)		quinone ring
			$\upsilon_{19}(CC)_{ring}$	Tyr-O^-
1469 (-)	1469 (-)			quinone ring
1410 (-)	1411 (-)	1410 (-)		quinone ring
			$\upsilon_s(COO^-)$	heme propionates b_L, b_H, c_1
1371 (+)	1370 (+)	1367 (+)		
1292 (+)	1292 (+)		υ(C-O)	methoxy group, quinone
1269 (s)	1267 (s)	1265 (+)	υ(C-O)	methoxy group, quinone
1257 (+)	1257 (+)		υ_{42}	heme b_L, b_H, c_1
			υ_{7a}(C-O^-)	Tyr
1238 (-)	1238 (-)	1240 (-)	δ(COH)	Tyr
1203 (+)	1202 (+)	1203 (+)		quinone
1174 (+)	1178 (+)	1186 (+)		lipid contribution
1159 (-)				quinone
1147 (+)	1149 (+)	1151 (+)	$(C\text{-}C)_{vinyl}$	heme b_L
1115 (-)	1115 (-)	1116 (-)		lipid contribution
1105 (+)	1101 (+)	1103 (+)	$\delta(=CH_2)_{vinyl}$	heme b_H
1088 (-)	1086 (-)	1088 (-)	$\upsilon(PO_2^-)$	lipid contribution, CL
985 (-)	980 (-)	989 (-)		lipid contribution

Table 3.6: Tentative assignments for the electrochemically induced FTIR spectra of the cytochrome bc_1 complex from yeast with and without lipids and after addition of lipids. Positions are given in cm^{-1}. References according to Table 3.5.

3.1.3.4 Electrochemically induced visible difference spectra of cytochrome bc_1 complex

All samples studied in infrared have also been analyzed in the visible spectral range. Figure 3.23 shows the reduced *minus* oxidized difference spectra in the visible spectral range for the cytochrome bc_1 complex as isolated (B) in direct comparison to the lipid depleted form (A) for the full potential step and for selected potential steps revealing the contributions of each heme.

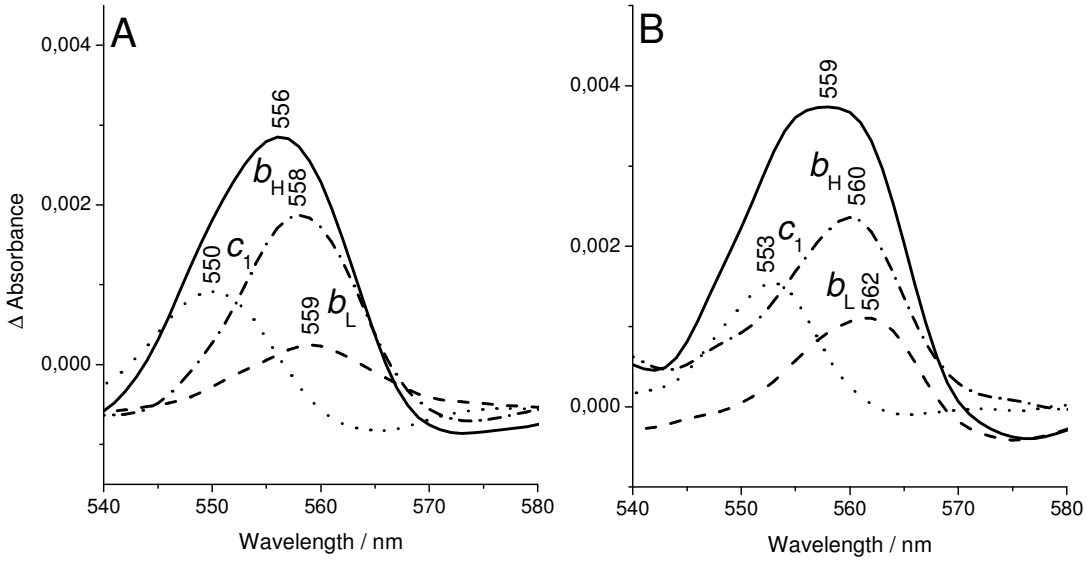

Figure 3.23: Reduced minus oxidized difference spectra in the visible range for the lipid depleted cytochrome bc_1 complex (A) from yeast at selected potential steps revealing the contributions of each heme in direct comparison to the reduced minus oxidized visible difference spectra of the wild type (B).

Clearly a shift of the alpha band from 559 to 556 nm can be seen after depletion of the lipids, indicating influence of the lipids on the hemes *b* and heme *c* spectral properties. The spectra at selected potential steps reveal that the interaction not only concern the heme b_H as found on the basis of potential titrations with the same method. The alpha band of heme c_1 is found at 553 nm for the native cytochrome bc_1 complex and downshifts to 550 nm for the depleted form. The alpha band of heme b_L is found at 562 nm. It decreases and downshifts to 559 nm for the depleted form.

For further characterization of the lipid-cofactor interplay, the midpoint redox potentials of the heme groups were determined for the as isolated cytochrome bc_1 complex, for the depleted and relipidated form. Figure 3.24 shows the redox titration curves of the native untreated complex (A) in direct comparison to the lipid-depleted complex (B) and after

supplementation of the complex with a mix of asolectin and CL (C) as well as addition of asolectin (D) and cardiolipin (E) alone.

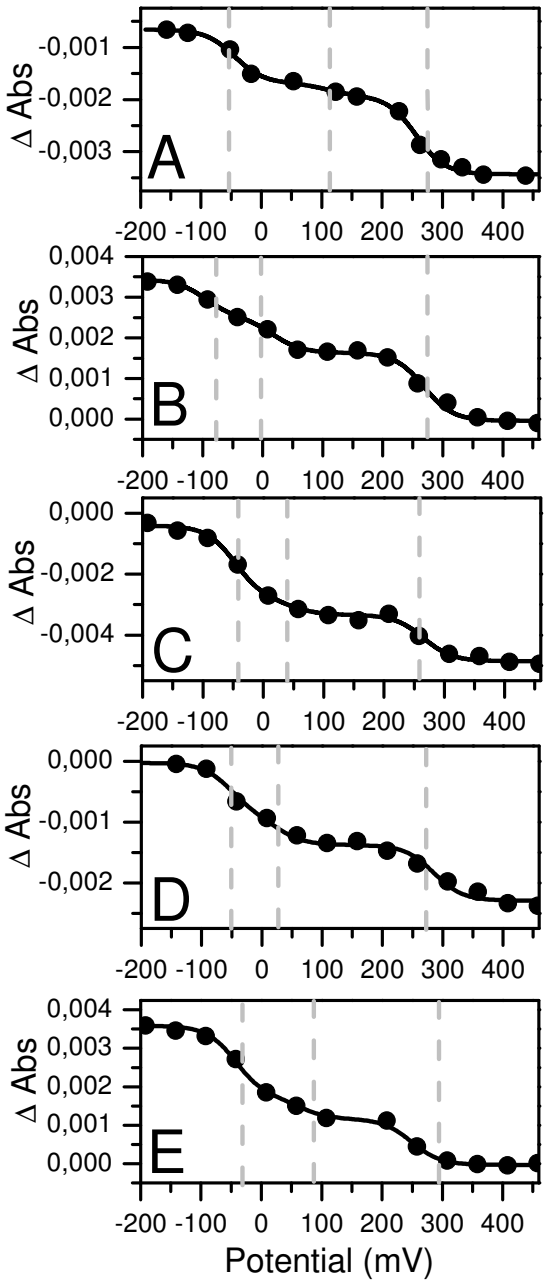

Figure 3.24: Redox titrations of cytochrome bc_1 complex samples as isolated (A), delipidated (B), relipidated with asolectin and CL (C) relipidated with asolectin (D) and with CL only (E). Oxidative and reductive titrations were fully reversible.

The midpoint potential of heme b_H of the untreated enzyme was 113 mV, and it was found to be strongly shifted (E_m=-2 mV) in the lipid depleted complex. This shift could be partially reversed (to E_m=26 mV) by addition of asolectin to the delipidated enzyme. Addition of cardiolipin further raised the midpoint potential to 64 mV. Relipidation with the mixture of

asolectin and CL raised the midpoint potential for heme b_H to 48 mV. The midpoint potentials are summarized in Table 3.7.

E_m in mV vs SHE'	heme b_L	heme b_H	heme c_1
wild type	-52	113	278
delipidated	-82	-2	278
+ asolectin	-51	26	285
+ cardiolipin	-42	64	250
+ asolectin/cardiolipin	-46	48	266

Table 3.7: Midpoint redox potentials (mV) for wild type, delipidated and relipidated yeast cytochrome bc_1 complex (vs. standard hydrogen electrode at pH 7.0).

The E_m of heme b_L was found at – 52 mV for the untreated enzyme. A slight shift to a more negative value of -82 mV was determined for the lipid depleted cytochrome bc_1 complex. In the asolectin treated enzyme, the midpoint potential was -51 mV. Addition of CL to the delipidated enzyme gave rise to a midpoint potential at -42 mV, similar to the value of the asolectin/cardiolipin mixture (-46 mV).

A midpoint potential E_m of 278 mV was determined for heme c_1 of the untreated enzyme. No major changes were observed after lipid depletion or relipidation with asolectin, CL or a mixture of asolectin and CL.

In conclusion, the midpoint redox potential of both *b* hemes, b_H and b_L, were influenced by enzyme-bound lipids. Heme b_L transfers electrons released upon ubiquinol oxidation at the Q_o site to heme b_H. The shift in the midpoint potential of heme b_L affects the electron transfer in the low potential chain. Addition of CL alone could only partially reverse this shift (-42 mV). After addition of the asolectin/CL mixture, the midpoint potential of heme b_L was comparable to the native enzyme. This finding is in accordance with the analysis of the catalytic activity and the peak position of the *b* hemes in the redox spectra upon delipidation and relipidation. Addition of asolectin or CL alone led only to a minor increase of the turnover number (see Wenz et al., 2009), whereas a ~70% recovery was detected for the relipidation with the asolectin/CL mixture. This phospholipid mixture could also completely reverse the blue shift of the *b* heme peak position in the redox spectra in contrast to addition of asolectin and CL alone (Wenz et al., 2009).

The shift of the heme b_H and heme c contribution in the reaction induced visible spectra confirms the importance of the lipids for structural and electrostatic integrity. Finally, it could be shown that reaction induced infrared difference spectroscopy is a sensitive tool for the study of the effect of lipids specially bound to membrane proteins on molecular level. This is in line with data presented for bacteriorhodopsin and complex I for lipids attached to the protein (Beck et al., 1998; Isele et al., 2000; Hielscher et al., 2006; Sinegina et al., 2005). Preparation dependent variations on lipid content may thus not only change the activity of the respective protein, significant changes in the reaction induced data and thus on the local structure of the cofactors side close to the lipid binding can be, and especially the CL, are part of the integral structure and participate in the enzyme function (see Figure 3.25).

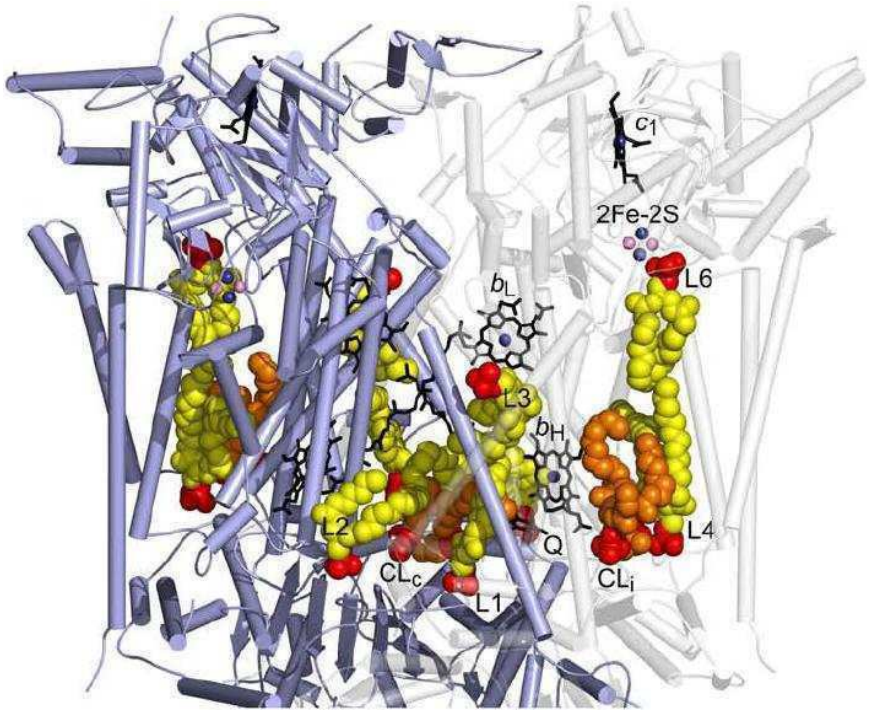

Figure 3.25: Yeast cytochrome bc_1 complex with bound lipids (reprinted with kind permission Wenz et al., 2009). Lipids are presented as sphere models in yellow and cardiolipin is highlighted in orange. All atoms of phosphate groups are shown in red.

3.1.4 Protein-lipid interaction in complex I from Escherichia coli

Finally, in this section the electrochemically induced FTIR difference spectra of NADH:ubiquinone oxidoreductase, also known as complex I, from *Escherichia coli* are discussed. The electrochemically induced FTIR difference spectra of complex I obtained from histidine tagged strain (Figure 3.26 B) is similar to the wild type spectra (Figure 3.26 A) of complex I obtained from the preparation described in Stolpe and Friedrich (2004) and presented in Hellwig et al. 2000. Small variations are based on the varying lipid content of each preparation.

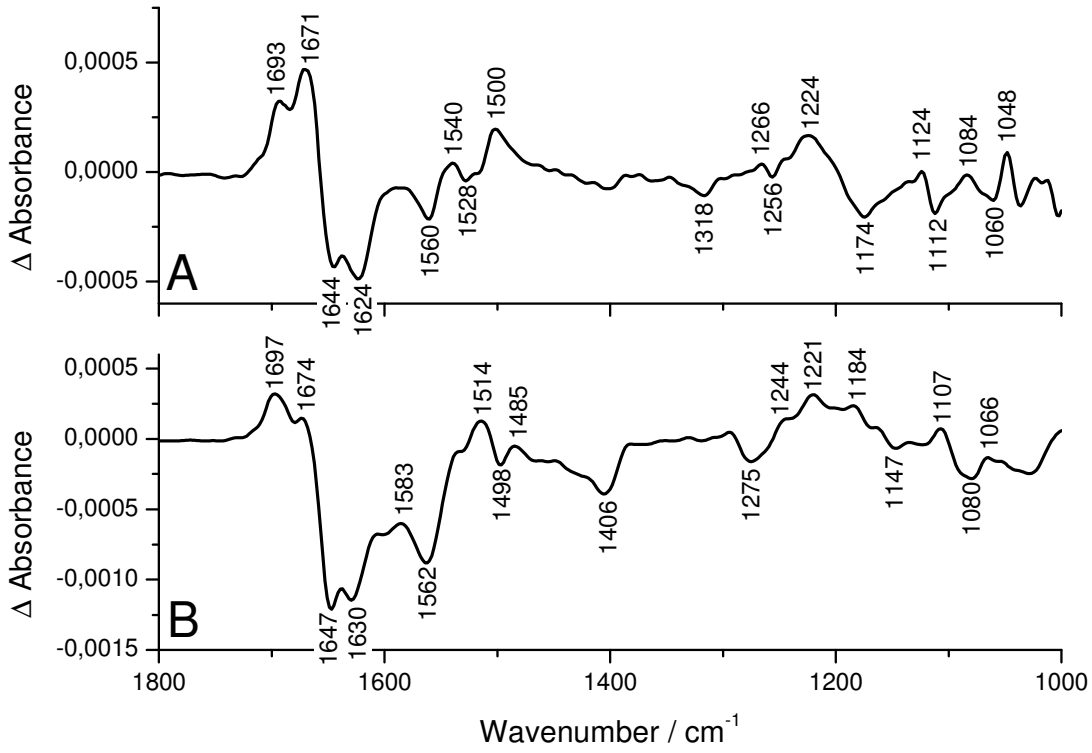

Figure 3.26: Oxidized *minus* reduced FTIR difference spectra of complex I from *E. coli* for the potential step from -0.49 to 0.21 V (A). In (B) the oxidized *minus* reduced spectra of the His tagged complex I is shown.

Peptide backbone. The oxidized *minus* reduced FTIR difference spectra of complex I (Figure 3.25) are dominated by large changes in the 1690 to 1590 cm^{-1} and 1570 to 1490 cm^{-1} regions. The amide I region from 1690 to 1590 cm^{-1} of both spectra is dominated by strong positive signals at 1693 and 1671 cm^{-1} and strong negative modes at 1644 and 1624 cm^{-1} reflecting a large reorganization of the polypeptide backbone. Modes at 1583, 1562, 1540, 1528 and 1514 cm^{-1} contribute in the amide II region (Hellwig et al., 2000).

Contributions of the flavin. The redox FTIR spectra of FMN have been described in details in both H_2O and D_2O (Hellwig et al., 2000; Wille et al., 2003). The shoulder at 1710 cm^{-1} may be attributed to the ν(C=O) vibration of the FMN. The signal at 1540 cm^{-1} is assigned to the ν(CC) mode of FMN. Further FMN modes are involved in signals at 1221, 1583, 1639, 1697 and 1674 cm^{-1}.

Contributions of ubiquinone. Iron-sulfur modes cannot be expected to appear at frequencies above 800 cm^{-1} and therefore all changes should arise from protein, FMN, ubiquinone, and possibly a yet unknown redox groups (Friedrich et al., 2000). The redox FTIR spectra of model ubiquinone have been described in details (see Burie et al., 1995; Bauscher et al., 1990; Bauscher and Mäntele, 1992; Hellwig et al., 1999; Ritter et al., 2003; Iwaki et al., 2004). Ubiquinone contributes at 1266 and 1256 cm^{-1} that involve the methoxy groups and a sharp C=C band at 1601 cm^{-1}. However, the quinone content in these samples are very small.

Amino acid side chains. The ν(C=O) modes of protonated aspartic and glutamic acid side chains appear at 1730 cm^{-1}. At 1540/1535 and 1406 cm^{-1} the $\nu_{s/as}(COO^-)$ mode of deprotonated residues contributed (Hellwig et al., 2000). Further contributions of several amino acids tend to occur at frequencies within the amide I and amide II range, and this makes their detection difficult. For example lysine, arginine, glutamine and asparagines have strong vibrations in the 1690 to 1620 cm^{-1} range (Marshall et al., 2006). The most prominent signal of tyrosine is its ν(CC) ring mode at 1514 cm^{-1} and 1498 cm^{-1} in the tyrosinate form (Flemming et al., 2003a), thus reflecting the sensitivity of the ring modes to the protonation state of the phenol group. The $\nu_{7'a}(CO)$ mode contribute at about 1266 cm^{-1} (Arrondo et al., 1993; Venyaminov and Kalnin, 1990; Hienerwadel et al., 1997; Hellwig et al., 2002). In Table 3.8 the tentative assignments are summarized.

wild type	wild type $_{His}$	tentative assignments
1742(-)	1743(-)	$\nu(C=O)_{asp,glu}$
1730(+)	1730(+)	$\nu(C=O)_{asp,glu}$
	1716(s)	$\nu(C=O)_{FMN}$
1693(+)	1697(+)	$\nu(C=O)_{FMN}$, amide I
1684(-)	1680(-)	amide I, β-loops
1671(+)	1674(+)	amide I, $\nu(C=O)_{UQ}$
1644(-)	1647(-)	amide I, α-helix, $\nu(C=O)_{asn,gln}$
1638(+)	1639(+)	
1624(-)	1630(-)	amide I, β-sheet, $\nu_{as}(CN_3H_5^+)_{arg}$
	1601(+)	$\nu(C=C)_{UQ}$
	1583(+)	$\nu(C=N)_{FMN}$, amide II
1560(-)	1562(-)	amide II
1540(+)	1535(+)	$\nu(C=C)_{FMN}$, $\nu_{as}(COO^-)_{asp,glu}$
1528(-)		amide II
1516(+)	1514(+)	ring-OH_{tyr}
1500(+)		
	1498(-)	$\nu(CC)ring_{tyr\text{-}O}$-
	1485(+)	
	1406(-)	$\nu_s(COO^-)_{asp,glu}$
1318(-)		
	1275(-)	
1266(+)		$\delta(C\text{-}OCH_3)_{UQ}$, $\nu_{7'a}(CO)_{tyr}$
1256(-)		$\delta(C\text{-}OCH_3)_{UQ}$
1224(+)	1221(+)	$\nu(S=O)_{MES}$, $ring_{FMN}$isoalloxazine
	1184(+)	$\delta(OH)_{MES}$
1174(-)		
	1147(-)	$\nu(C\text{-}O)_{MES}$
1124(+)		
1084(+)	1107(+)	
1060(-)	1080(-)	
1048(+)	1066(+)	$\nu(C\text{-}N)_{MES}$
1036(-)		$\nu(C\text{-}N)_{MES}$
1022(+)		

Table 3.8: Tentative assignments for the electrochemically induced FTIR difference spectra of complex I from *E. coli*. References see text.

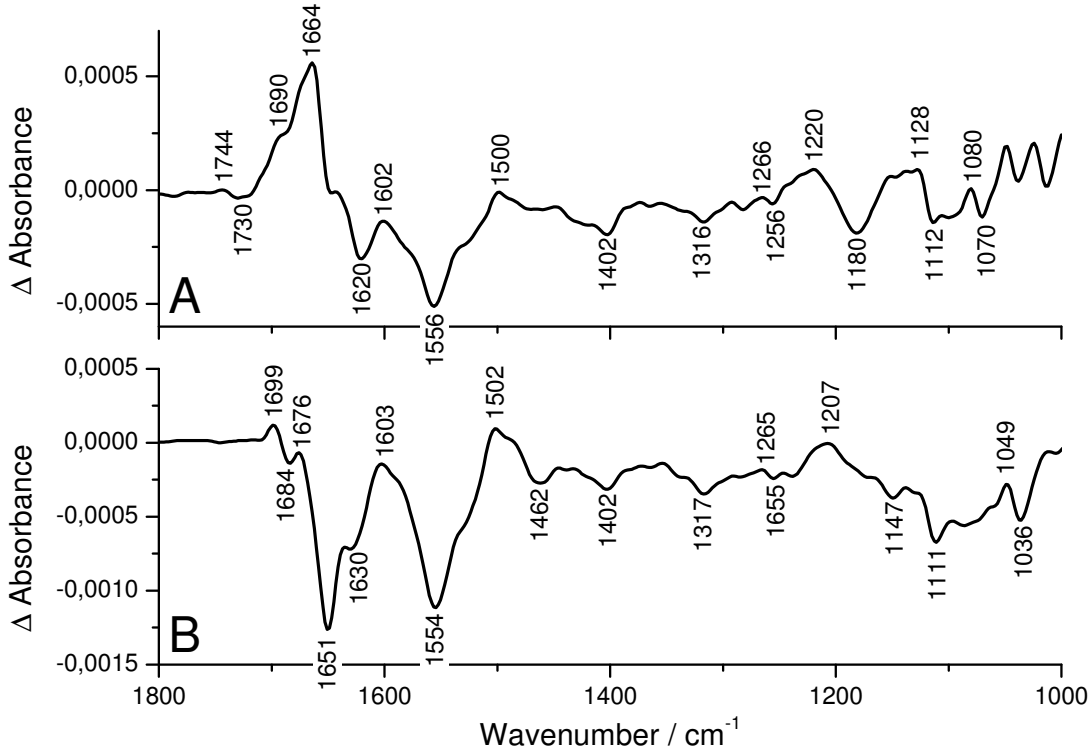

Figure 3.27: Oxidized *minus* reduced FTIR difference spectra of complex I in the presence of polar lipids (A) and of phosphatidylcholine C^{13} labeled (B) for the potential step from -0.49 to 0.21 V.

The NADH:decyl-ubiquinone oxidoreductase activity of complex I as isolated was 0.3 µmol NADH/min·mg. After incubation with *E. coli* polar lipid extract, the activity was enhanced more than 9-fold to 2.8 µmol NADH/min·mg (Hielscher et al., 2006). Thus, the presence of lipids is essential for the activity of complex I (Sharpley et al., 2006).

Figure 3.27 shows the oxidized *minus* reduced FTIR difference spectra of the complex I in the presence of polar lipids (A) and resuspended in phosphatidylcholine C^{13} labeled (B) for the potential step from -0.49 to 0.21 V. In comparison with the oxidized *minus* reduced FTIR difference spectra of the complex I in the absence of lipids strong changes in the full spectral range between 1800 and 1000 cm^{-1} can be seen. These variations include alternation in the amide I (1690 to 1590 cm^{-1}) and amide II (1570 to 1490 cm^{-1}) region, where contributions from the protein backbone are involved. Interestingly, higher signal intensity can be observed at 1664 and 1556 cm^{-1} upon addition of polar lipids and at 1699 and 1554 cm^{-1} in the presence of labeled phosphatidylcholine. The ester carbonyl group of the isotopically labeled PC may be involved at 1699 cm^{-1} (see Table 5.4 in appendix).

Figure 3.28 gives an enlarged view of the oxidized *minus* reduced FTIR difference spectra of complex I in the absence of lipids (green and gray line) and in the presence of mixed lipids (black line) and in the presence of PC C^{13} labeled (red line) in the spectral range from 1770 to 1705 cm^{-1}.

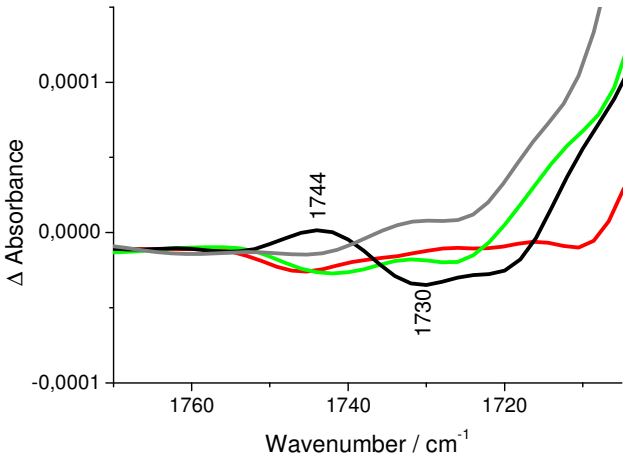

Figure 3.28: Enlarged view of the oxidized *minus* reduced FTIR difference spectra of complex I in the absence of lipids (green and gray line) and in the presence of mixed polar lipids (black line) as well as in the presence of phosphatidylcholine C^{13} labeled (red line).

In the detergent-solubilized form, only a very weak negative signal at 1742 cm^{-1} is visible (green and gray line). Upon reactivation with polar lipids, a clear signal at 1744 cm^{-1} for the oxidized form and at 1730 cm^{-1} concomitant with the reduced form arises. This spectral range is characteristic for C=O vibrations, especially from acidic residues (Siebert, et al., 1983; Engelhard et al., 1985). However, the ester group in lipids may also contribute in this spectral range, particularly if the redox reaction induces a conformational change in the protein that changes the environment of lipid ester group. Interestingly, the signals are absence in the isotopically labeled PC variant (red line), which strongly supports the assignment to the ester carbonyl group of lipids. However, the small negative signal present at 1741 cm^{-1} could arise from a partially protonated acid residue. In the data seen after addition of polar lipids, an additional differential peak at 1730 and 1744 cm^{-1} can be depicted clearly. The differential form of the peaks reflects an upshift of the carbonyl band from 1730 to 1744 cm^{-1} upon oxidation, indicating that within the protein a more hydrophobic environment is created in which the observed C=O group(s) are less hydrogen-bonded to water. Lipids in solution are not redox active, only a change in environment can be detected.

In a recent study on Rhodopsin, bands at 1744(+) and 1727(-) cm^{-1} could be assigned to a change in the lipid ester carbonyl stretching upon receptor activation, with roughly equal contributions form both lipid ester groups during Rhodospin activation on the basis of labeling experiments (Beck et al., 1998; Isele et al., 2000).

In conclusion, the data obtained indicates that there are phospholipid molecules binding very specifically to complex I. The exact type of lipid still remains to be specified.

3.2 Factors ruling conformational movements

3.2.1 Secondary structure analysis

3.2.1.1 Secondary structure determination of NADH dehydrogenase fragment

The ATR FTIR absorbance spectra of complex I and its soluble fragment, the NADH dehydrogenase fragment, from *E. coli* are illustrated in Figure 3.29. The dominant amide I band occurs in the range from 1700 to 1600 cm^{-1} and the amide II band at 1545 cm^{-1}. Both are sensitive to the hydrogen bonding environment and internal vibrational coupling. In the spectral region from 1400 to 1200 cm^{-1} the amide III mode appears (see Table 1.2 part 1.4.2.3.).

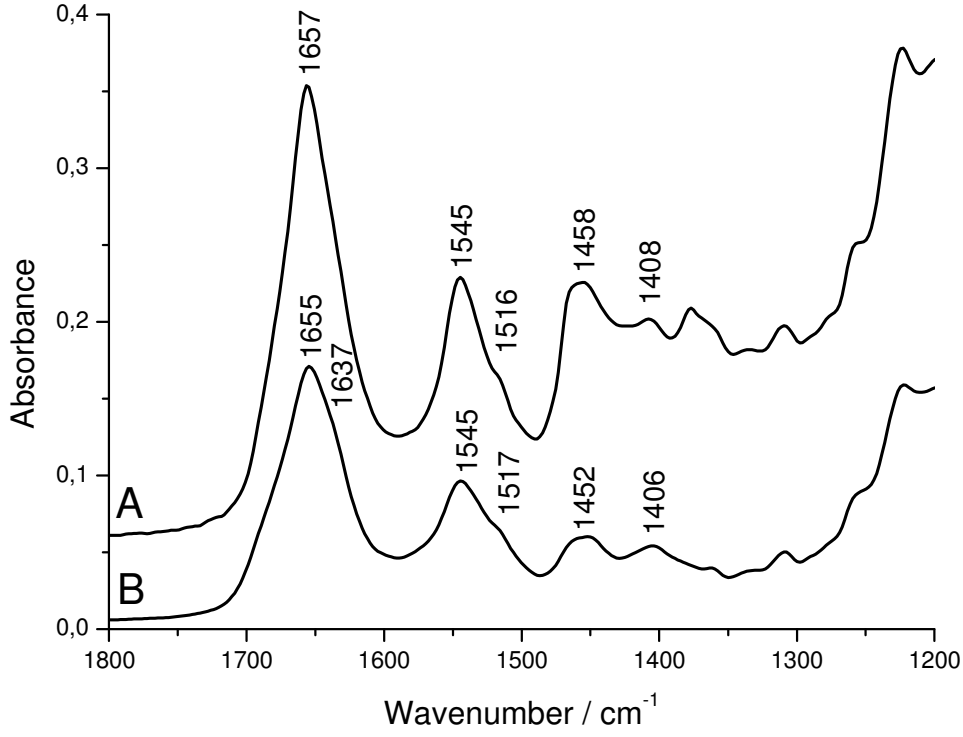

Figure 3.29: ATR FTIR absorbance spectra of complex I (trace A) and of the soluble NADH dehydrogenase fragment (trace B) from *E. coli*.

The amide I band maximum of complex I from *E. coli* (trace A) appears at 1657 cm^{-1}. This indicates a predominantely α-helical structure of complex I. The NADH dehydrogenase fragment (trace B) of the complex I from *E. coli* has an amide I band maximum at 1655 cm^{-1}

with a clear shoulder at 1637 cm^{-1}. A predominant α-helical structure and contributions of random coils and β-sheet are concluded from these observations. From the X-ray structure of the peripheral arm of the bacterial *Thermus thermophilus* complex, it is clear that the distribution of secondary structure elements of the NADH dehydrogenase fragment in the oxidized state is about 30% α-helical and 18% β-sheet (2FUG, Sazanov and Hinchliffe, 2006). According to the secondary structure analysis of the amide I band and based on its second derivative (Figure 5.7 in Appendix 5.2.2), the following overall distribution of the secondary structure elements in the soluble fragment is found: 46% α-helices, 26% β-sheet, 10% β-turns and 12% random coils (image A in Figure 3.30). This corresponds to the results obtained for the hydrophilic subunits of the complex I from *T. thermophilus*. Some differences can be expected for the protein fragment originating from a different organism.

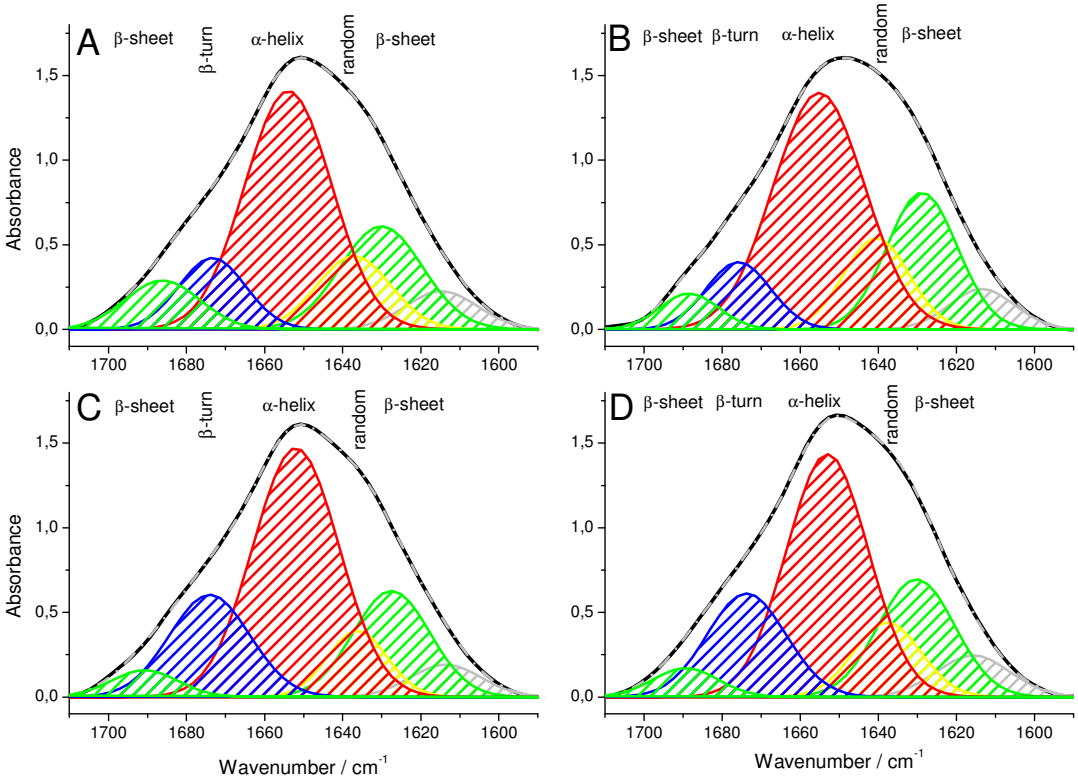

Figure 3.30: Curve fitting of the amide I bands of NDF (A), upon NAD^+ binding (B), NADH binding (C) and NADPH binding (D). The amide I region was deconvoluted into its secondary structure components: α-helix (red), β-sheet (green), β-turns (blue), random (orange) and side chains (gray). The frequency of each band was obtained from the second derivative curves (Figure 5.7 in Appendix 5.2.2). The spectrum resulting from the sum of these components is superimposed over the experimental spectrum (dotted gray line).

Figure 3.30 gives an overview of the fitting results of the amide I band of the soluble fragment before and after substrate addition. The spectra were recorded in solution as reported in section 2.2.1.2. The relative percentage obtained by the deconvolution is summarized in Table 3.9.

assignment	relative content in % (maximum in wavenumber / cm^{-1})			
	NDF	NAD^+ bound	NADH bound	NADPH bound
α-helices	46 (1654)	47 (1655)	47 (1652)	45 (1653)
β-sheet	26 (1631 + 1687)	26 (1629 + 1688)	22 (1627 + 1691)	23 (1630 + 1689)
β-turns	10 (1674)	9 (1676)	18 (1674)	17 (1673)
random	12 (1637)	13 (1640)	9 (1637)	9 (1638)
side chains	6 (1615)	6 (1613)	5 (1614)	7 (1616)

Table 3.9: Secondary structure of NADH dehydrogenase fragment upon substrate binding deduced from curve fitting of amide I infrared absorbance bands.

The overall distribution of secondary structure elements in NDF with addition of NAD^+ is: 47% α-helical, 26% β-sheets, 9% β-turns and 13% random coils. No significant variation is found in comparison to NDF in the absence of NAD^+. However, some bands are affected. The low frequency β-sheet band downshifts to 1629 cm^{-1}. The band increases and becomes narrow. The β-turn band upshifts from 1674 to 1676 cm^{-1}. The random coil band intensity increases, narrows and shifts to higher frequencies at 1640 cm^{-1}. The α-helical band broadens and increases by about 1%. However, 1-2% variation can be neglected it is within the error of the method. The amide I region from 1700 to 1600 cm^{-1} in the difference spectrum obtained by the subtraction of NDF with bound NAD^+ *minus* NDF shows the alternation in the amide I region (Panel B in Figure 5.11 in Appendix 5.2.3). The strong signals at 1631 (+) and 1699 (-) cm^{-1} reflect a reorganization of β structural elements, and the weak signals at 1662 (+) and 1653 (-) cm^{-1} reflect a reorganization of α helical or random structure.

Upon addition of NADH, the overall distribution of the secondary structure is found to include 47% α-helix, 22% β-sheets, 18% β-turns and 9% random coils. The α-helical contribution becomes narrow and shifts from 1654 to 1652 cm^{-1}. The high frequency β-sheet band shifts to 1691 cm^{-1}. The low frequency β-sheet band maximum is found at 1627 cm^{-1}.

The β-sheet contribution decreases to 22%. The β-turn contribution increases to 18% and the random coil character decreases to 9%. In the amide I region from 1700 to 1600 cm^{-1} the difference spectrum obtained by subtraction of NDF in the presence of NADH *minus* NDF is shown in Figure 5.11 panel A (in Appendix 5.2.3). It includes shifts of signals at 1695 and 1680 cm^{-1} assigned to high frequency β-sheet and β-turns, whereas the signals at 1651 and 1637 cm^{-1} reflect α-helical or random and low frequency β-sheet elements.

NADPH binding affects the overall distribution of the secondary structure elements and includes 45% α-helices, 23% β-sheets, 17% β-turns and 9% random coils. In detail, the β-sheet contributions decrease to 23%. The low frequency β-sheet band at 1630 cm^{-1} gets narrow and decreases. The high frequency β-sheet band is shifted to 1689 cm^{-1} and also decreases. The β-turn contribution increases by about 17% whereas the random character decreases to 9%. In the difference spectrum in Figure 5.11 panel C, the signal at 1631 (+) cm^{-1} of the low frequency β-sheet can be found and the signals at 1689 (+) / 1674 (-) cm^{-1} include the high frequency β-sheet proportion and β-turns, respectively.

In general, nucleotides bind to the NADH dehydrogenase fragment from *E. coli*. Contributions of the nucleotides themselves, however, are weak, based on their low concentration and can be excluded in the amide I band analysis. NAD^+ binding does not significantly affect the secondary structure. Nevertheless, NAD^+ may bind in the nucleotide binding site which is composed of a Rossmann fold-like domain (Walker, 1992; Sazanov and Hinchliffe, 2006). Importantly, NADH and NADPH binding affect the β-sheet character of the protein. The analysis shows that both NADH and NADPH are influenced in a way that β-sheet contributions decrease and β-turns contributions increase.

3.2.1.2 Secondary structure determination of complex I

The secondary structure analysis of the entire complex from *E. coli* is illustrated in Figure 3.31. Based on the second derivative (Figure 5.12 in Appendix 5.2.2), the following overall distribution of the secondary structure elements in complex I is found: 36% α-helices, 27% β-sheet, 14% β-turns and 17% random coils. The estimation in the presence of nucleotides is summarized in Table 3.10.

The relative contribution of the secondary structure elements of complex I with bound NAD^+ is unchanged. Interestingly, as described before for NDF, upon NAD^+ binding the high frequency β-sheet band decreases and shifts to higher frequencies at 1690 cm^{-1}. In addition

the low frequency β-sheet band increases and shifts to 1635 cm^{-1}. The random coil band slightly decreases and broadens. The β-turns band increases, narrows and shifts to 1675 cm^{-1}. The subtraction of the complex I spectrum from the data obtained before addition of NAD^+ is shown in Figure 5.10 (Appendix 5.2.3). The amide I region from 1700 to 1600 cm^{-1} is dominated by strong signals at 1699 (+), 1674 (-), 1653 (+) and 1635 (+) cm^{-1} reflecting the reorganization of the polypeptide backbone.

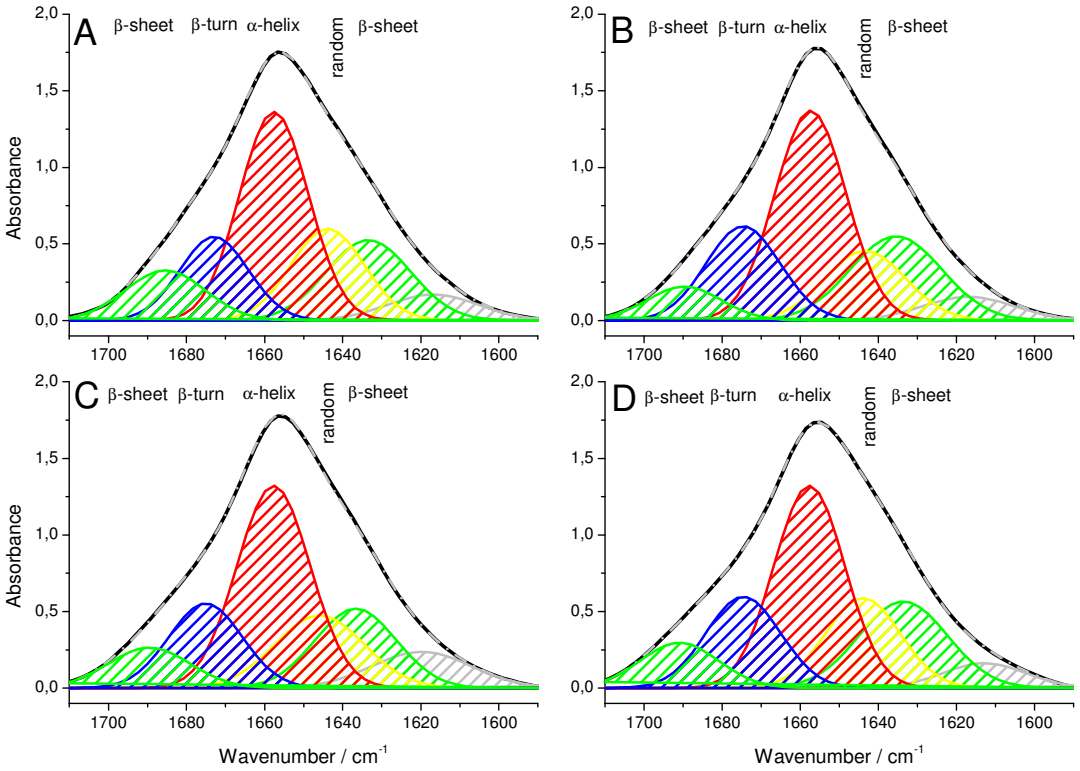

Figure 3.31: Curve fitting of the amide I bands of complex I (A), upon NAD^+ binding (B), NADH binding (C) and NADPH binding (D). The amide I region was deconvoluted in its secondary structure components: α-helix (red), β-sheet (green), β-turns (blue), random (orange) and side chains (gray). The frequency of each band was obtained from the second derivative curves (Figure 5.8 in Appendix 5.2.2.). The spectrum resulting from the sum of these components is superimposed over the experimental spectrum (dotted gray line).

After addition of NADH the overall distribution of the secondary structure elements is found to be: 36% α-helices, 24% β-sheets, 17% β-turns and 14% random coils. In detail, the low frequency β-sheet band upshifts to 1637 cm^{-1} and becomes narrow. The high frequency β-sheet band upshifts to 1690 cm^{-1} and decreases. The β-turn band increases and the maximum is found at 1675 cm^{-1}. The random coil character decreases. The band maximum

shifts to 1646 cm^{-1}. The difference spectrum shows clearly signals at 1672 (-) cm^{-1} to β-turns and 1623 (-) cm^{-1} to β-sheet.

assignment	relative content in % (maximum in wavenumber / cm^{-1})			
	complex I	NAD^+ bound	NADH bound	NADPH bound
α-helices	36 (1658)	35 (1657)	36 (1658)	37 (1658)
β-sheets	27 (1633 + 1685)	28 (1635 + 1690)	24 (1637 + 1690)	25 (1634 + 1691)
β-turns	14 (1673)	15 (1675)	17 (1675)	17 (1675)
random	17 (1644)	16 (1643)	14 (1646)	14 (1644)
side chains	6 (1617)	6 (1617)	9 (1620)	5 (1613)

Table 3.10: Secondary structure of complex I upon substrate binding deduced from curve fitting of amide I infrared absorbance bands.

NADPH binding affects the overall distribution of the secondary structure elements of complex I as follows: 37% α-helices, 25% β-sheets, 17% β-turns and 14% random coils. In detail, the percentage of β-sheet decreases. The low frequency β-sheet band is not affected. However, the high frequency β-sheet band decreases and shifts to 1691 cm^{-1}. The β-turn band increases and shifts to 1675 cm^{-1}. The random coil band is found at 1644 cm^{-1} and narrows. The relative percentage of the random character decreases about 3%.

Addition of NAD^+ did not significantly affect the secondary structure of the entire enzyme. NAD^+ binds to the nucleotide binding site of complex I as seen in the slight alternation of β-sheet elements and β-turns.

NADH and NADPH binding affects the β-sheet and β-turn character. The analysis shows that both characters are influenced; β-sheet contributions decrease and β-turns increase.

In conclusion, the nucleotide binding particularly involves β-sheet and β-turn elements of complex I. This suggests that the nucleotides bind to the Rossmann fold-like domain (Walker, 1992; Sazanov and Hinchliffe, 2006). However, binding of NAD^+ did not lead to significant structural changes as compared to the nucleotide-free protein. Addition of NADH shows similar alternation in the secondary structure elements of the NADH dehydrogenase fragment and in the entire complex I from *E. coli*. Therefore, it can be concluded that a conformational change took place upon NADH binding.

3.2.2 Hydrogen/deuterium exchange kinetics

Hydrogen-deuterium exchange was first introduced in the mid-1950s by the pioneering work of Linderstrøm-Lang and colleagues, who after discovery of protein α-helices and ß-sheets, realized that amide hydrogen exchange rates should reflect the presence and type of the hydrogen bonded structure (Hvidt and Linderstrøm-Lang, 1954; Hvidt and Linderstrøm-Lang, 1955). Futhermore the relationship between the rate of hydrogen exchange and protein dynamics and the mathematical descriptions of the current exchange models have been formulated (Hvidt and Linderstrøm-Lang, 1954; Hvidt and Linderstrøm-Lang, 1955; Hvidt and Nielsen, 1960). Hydrogen deuterium kinetics reflect solvent accessibility and the hydrogen bonding environment in protein; this implies that protein residues can be divided into a number of local structures with similar dynamic properties as used for slow, intermediate and fast exchanging fractions. In order to contribute to the understanding of the hydrogen bonding interaction and thus the dynamic structure during substrate binding to the NADH:ubiquinone oxidoreductase from *E. coli*, hydrogen/deuterium exchange kinetics were recorded as described in the materials and methods section 2.2.3.3.

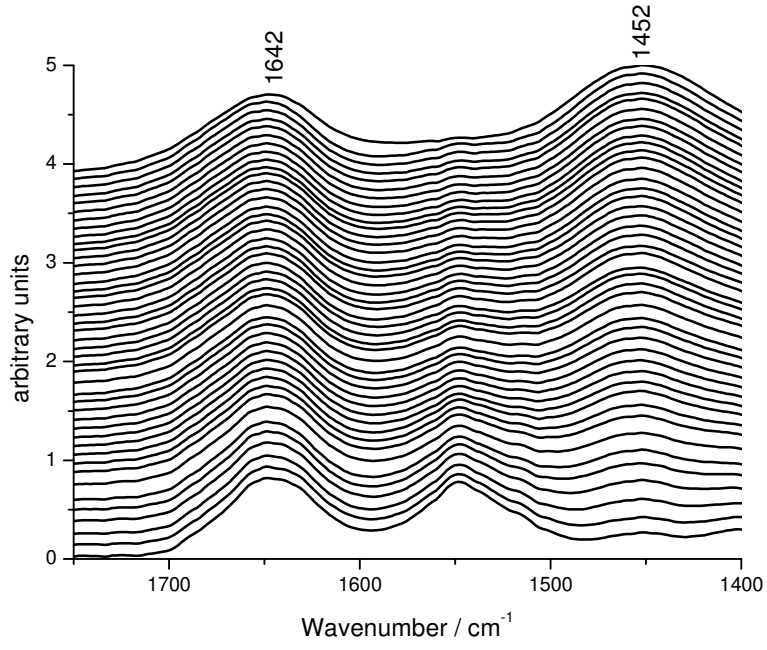

Figure 3.32: 44 infrared spectra of NADH dehydrogenase fragment recorded as a function of the deuteration time during perfusion of D_2O. The first 25 spectra are measured all 5 min between 0 and 120 min. The latter spectra are displayed between 120 and 300 min in 10 min steps. The final spectrum (on the top) was recorded on the next day (20 h after start). Spectra are shifted for better comparison.

Amide hydrogen/deuterium exchange experiments were carried out on the soluble fragment, the NADH dehydrogenase fragment, as well as on the entire complex I from *E. coli*. In the course of amide hydrogen/deuterium exchange, the amide I band with its maximum around 1653 cm^{-1} shifts to lower frequencies about 1642 cm^{-1} and is significantly reshaped, as shown in the selected spectra of the NADH dehydrogenase fragment recorded as a function of the exposure time during perfusion with D_2O (Figure 3.32). The intensity of the amide II absorbance band at approximately 1545 cm^{-1} dramatically decreases. The amide II band is located between 1570 and 1500 cm^{-1} and arises predominately from the coupled peptide backbone N-H bending and C-N stretching vibration. The rate of amide hydrogen exchange by deuterium is related to the accessibility of the solvent to the N-H amide groups and/or to the stability of the secondary structure elements. The amide II band downshifts by about 100 cm^{-1} upon H/D exchange due to the decoupling from the ν(CN) vibration. The amide II' band replaces the amide II band and includes the N-D bending vibration. It overlaps with the HOD bending mode at about 1452 cm^{-1}. Interestingly, protein denaturation is usually necessary to ensure complete H/D exchange (Vigano et al., 2003). The final spectrum of NADH dehydrogenase fragment in the top of Figure 3.32 was obtained 20 h after starting the hydrogen/deuterium exchange. The fully shifted amide II band leads to the conclusion that a nearly complete exchange took place. The correction/subtraction of H_2O and D_2O buffer contributions was realized and compared with other measurements to control reproducibility of data acquisition (see materials and methods, section 2.3.3).

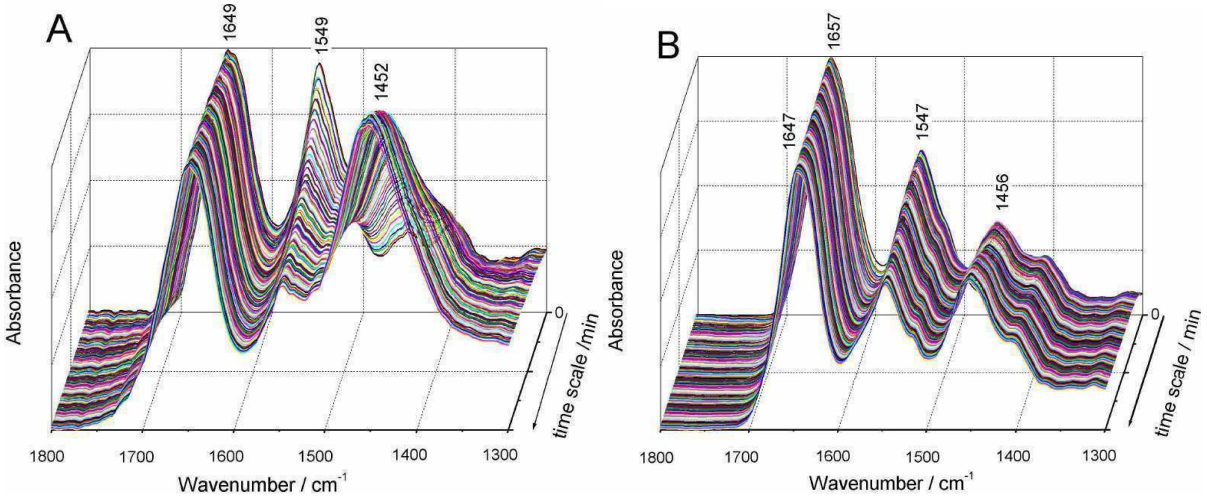

Figure 3.33: 3D-plot of hydrogen/deuterium exchange infrared spectra between 0 and 90 min induced upon exposure to D_2O. Image (A) shows the NADH dehydrogenase fragment alone and (B) shows the soluble fragment in the presence of NADH.

Figure 3.33 shows the 3-D plot of the hydrogen/deuterium exchange ATR FTIR absorbance spectra between 0 and 90 min of NADH dehydrogenase fragment from *E. coli* (A) and NDF in the presence of NADH (B) induced by D_2O buffer perfusion. During the first minutes of exposure to D_2O, the infrared spectra of NDF in the presence of NADH significantly differ from the infrared spectra of NDF without substrate. While the amide II band of NDF alone rapidly downshifts and the amide II' band appears at 1452 cm^{-1}, overlapping with the HOD bending vibration, the amide II band of NDF in the presence of NADH just slowly decreases. Nevertheless, the pure OD bending vibration at 1209 cm^{-1} arises faster in the infrared spectra in the presence of NADH during the first 90 min of the perfusion as seen in the infrared spectra of NDF alone. This result leads to the tentative conclusion that in the process of binding NADH the system allows a higher accessibility to hydrogen exchange. To compare the infrared spectra of NDF alone and in the presence of NADH, in Figure 3.34 shows the evolution of the amide II band area rescaled with respect to the amide I band area as a function of exposure to D_2O buffer.

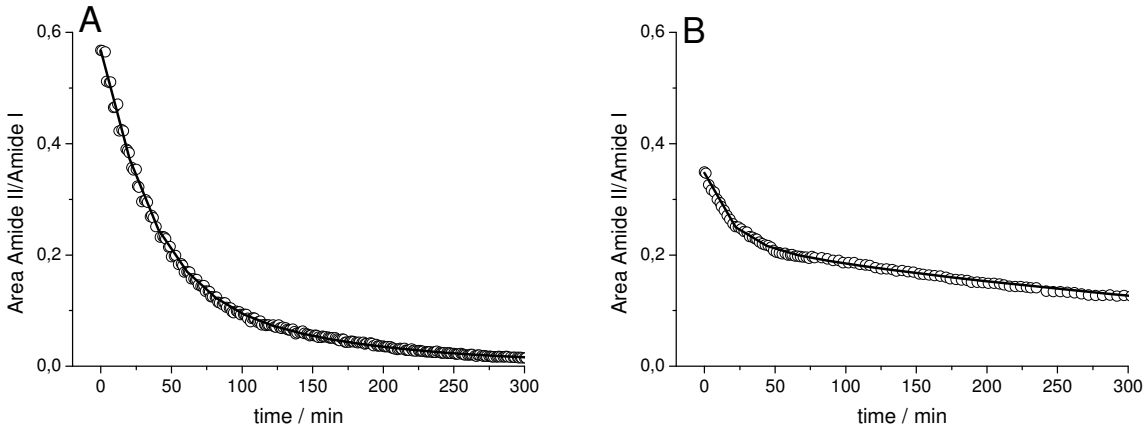

Figure 3.34: Monitoring the H/D exchange of NADH dehydrogenase fragment in the absence (A) and in the presence of NADH (B). Evolution of the amide II area rescaled with respect to the amide I area as a function of time (first 300 min). The experimental points are reported along with the result of the curve fitting by three exponentials.

The hydrogen/deuterium exchange is a first order reaction (Goormaghtigh et al. 1994; Knox and Rosenberg, 1986). The fraction of non-exchanged amide protons can be described as the sum of individual exponential functions (as reported in materials and methods, section 2.3.3). The result of the curve fitting, using equation 2.3 with three exponential decay, is summarized in Table 3.11. The kinetics of H/D exchange demonstrates the presence of three contributions which undergo fast exchange (a_1 and τ_1), intermediate exchange (a_2 and τ_2), and

slow exchange (a_3 and τ_3). The hydrogen exchange kinetics of NDF alone shows that 2.3% of all residues exchange quickly undergo fast exchange with a time rate constant of 1.1 min, 44.2% of intermediate exchange with a time rate constant of 34.5 min, and 15.9% exchange slowly with a time rate constant of 134 min. In comparison, the hydrogen exchange kinetics of NDF in the presence of NADH show that only 1.3% of all residues exchange fast with a time rate constant of 3.7 min, whereas 11.2% exchange "intermediately" with a time rate constant of 20 min. The slow exchange is found with a time rate constant of about 500 min with 22.1% of all residues.

NDF	a_1 / %	τ_1 / min	a_2 / %	τ_2 / min	a_3 / %	τ_3 / min
alone	2.3	1.1	44.2	34.5	15.9	134
100 µM NADH	1.3	3.7	11.2	20.0	22.1	542

Table 3.11: Analysis of the exchange kinetic curves of NDF alone and in the presence of NADH. Relative contribution a_i (amplitude associated with each time constant) and τ_i (time constant) (i = 1,2,3) of the different exponential components are reported for different exchange rates. Error bar is approximately 2-3%.

A further hydrogen/deuterium exchange kinetic was carried out with a sum of four exponential functions. The results are summarized in Table 3.12 and a more precise decomposition of the fast and intermediate exchange can be reported.

NDF	a_1 / %	τ_1 / min	a_2 / %	τ_2 / min	a_3 / %	τ_3 / min	a_4 / %	τ_4 / min
alone	1.3	1.0	6.5	14.8	41.4	43.2	9.5	180
100 µM NADH	1.9	3.2	9.8	8.1	20.2	14.4	22.6	478

Table 3.12: Analysis of the exchange kinetic curves of NDF alone and in the presence of NADH using a curve fitting procedure of four exponentials. Relative contribution a_i (amplitude associated with each time constant) and τ_i (time constant) (i = 1,2,3,4) of the different exponential components are reported for different exchange rate. Error bar is approximately 2-3%.

The analysis supports the previous conclusion that at the beginning of the hydrogen exchange the exchange kinetics of NDF in the presence of NADH is slower than without substrate. Instead the intermediate exchange is affected upon NADH binding and displays that 9.8% of intermediate exchange with a time rate constant of 8.1 min as well as 20.2% of all

residues exchange with a time rate constant of 14.4 min, whereas without substrate binding only 6.5% exchange with a time rate constant of 14.8 min. Here a slow exchange fraction at about 450 min is found. Saturation of the NADH concentration may take place after exposure to D_2O.

The kinetics of deuterium exchange of the entire complex I from *E. coli* with substrate binding were obtained using only one sample compartment of the ATR perfusion cell. The membrane protein was prepared as a thin film on the siliciun crystal surface as described in section 2.1.9 of materials and methods.

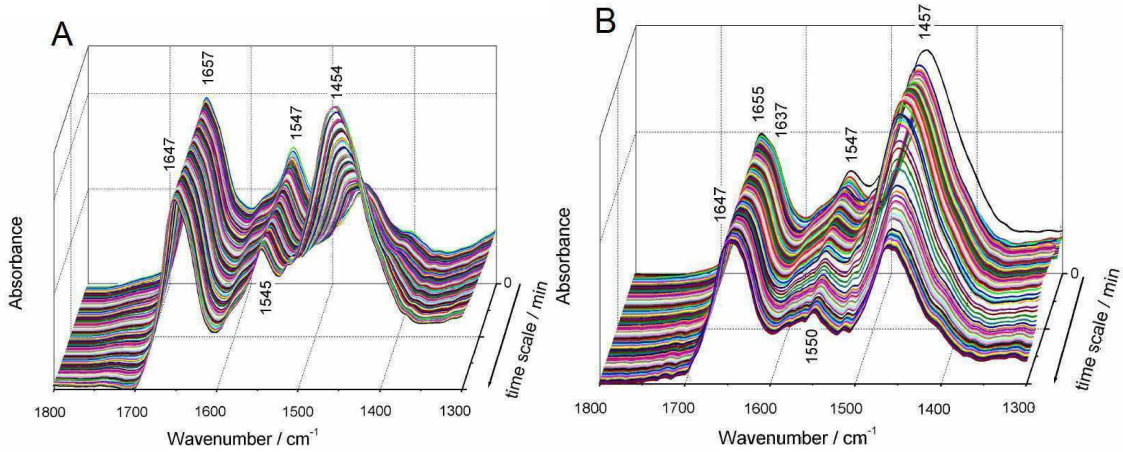

Figure 3.35: 3D-plot of hydrogen/deuterium exchange infrared spectra of complex I between 0 and 90 min induced upon exposure to D_2O buffer. Image (A) shows the complex I alone and (B) shows the complex I in the presence of NADH and decylubiquinone.

Figure 3.35 shows the 3-D plot of hydrogen/deuterium exchange ATR FTIR absorbance spectra of complex I without substrate binding (A) and complex I in the presence of NADH and decylubiquinone (B) between 0 and 90 min D_2O buffer perfusion. In the H/D exchange infrared spectra of complex I, the shift of amide I band from 1657 cm^{-1} towards lower frequencies at 1647 cm^{-1} is clearly seen. Furthermore, the amide II band at 1547 cm^{-1} decreases and the amide II' band as well as the HOD bending vibrations appear at 1454/1457 cm^{-1}. On the basis of the technical setup the delay of the diffusion is in general faster than observed for the soluble fragment where an additional membrane separated the sample compartment.

To depict the fast and slow exchanging residues, Figure 3.36 gives an overview of the hydrogen/deuterium exchange kinetics of complex I without substrate binding (A), in the presence of NADH (B), and in the presence of NADH and decylubiquinone (C).

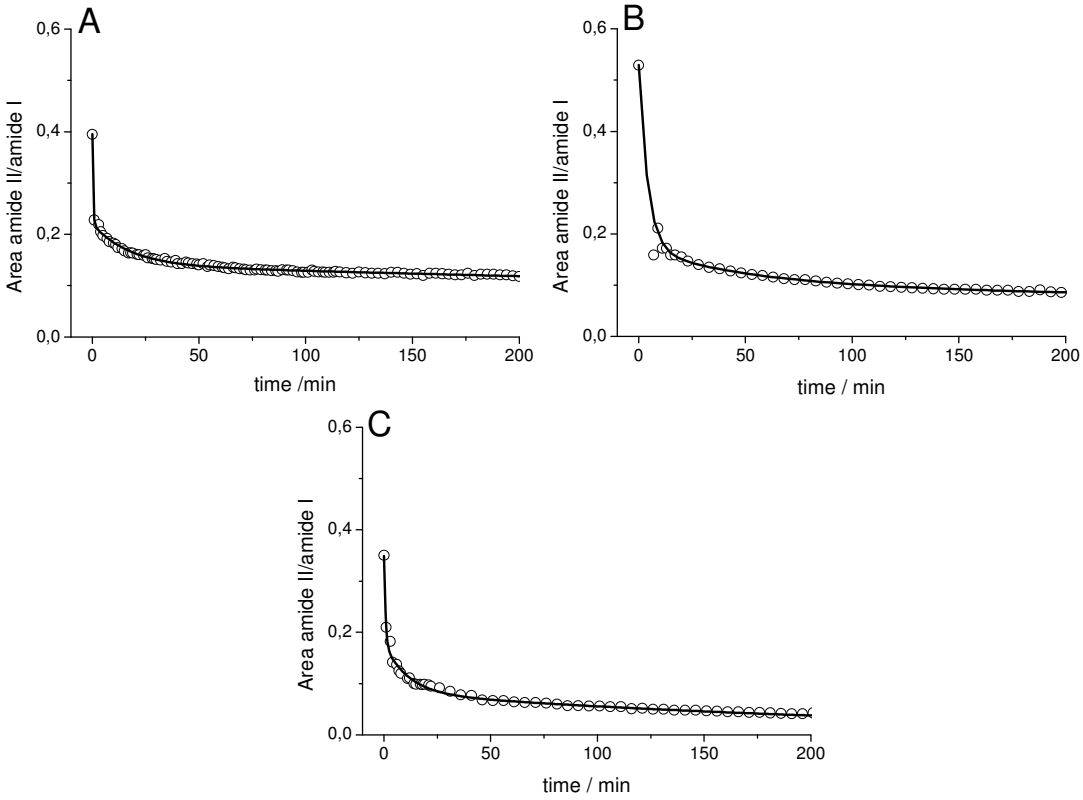

Figure 3.36: H/D exchange of complex I in the absence (A) and in the presence of NADH (B) as well as in the presence of NADH and decylubiquinone (C). Evolution of the amide II area rescaled with respect to the amide I area as a function of time (displayed the first 200 min). The experimental points are reported along with the result of the curve fitting by three exponentials.

The analysis of the hydrogen exchange curves of complex I using a curve fitting procedure with three exponentials is summarized in Table 3.13. The hydrogen exchange kinetics of complex I with no substrate bound shows that 17.4% of all residues exchange fast with a time constant of 0.4 min, 8.1% exchange moderately fast with a time rate constant of 17.4 min, and 14.0% exchange slowly with a time rate constant of about 1200 min. However, the kinetic analysis of complex I in the presence of NADH shows a fast exchange time rate constant at 4.2 min for 35.5% of all exchangeable residues. Nevertheless, the intermediate exchange rate is obtained at 47.4 min with a relative contribution of 7.1% of all residues. This result is in good agreement with the results for the soluble fragment of complex I. Finally, during the binding of NADH to the binding site in the soluble domain of the enzyme it becomes more accessible.

complex I	a_1 / %	τ_1 / min	a_2 / %	τ_2 / min	a_3 / %	τ_3 / min
alone	17.4	0.4	8.1	17.4	14.0	1208
100 µM NADH	35.5	4.2	7.1	47.4	10.3	1019
100 µM NADH + 100 µM decylQ	17.1	0.8	19.6	11.3	8.2	258

Table 3.13: Analysis of the exchange kinetic curves of complex I. Relative contribution a_i (amplitude associated with each time constant) and τ_i (time constant) (i = 1,2,3) of the different exponential components for the respective exchange rate. Error bar is approximately 2-3%.

Upon the addition of decylubiquinone to complex I in the presence of NADH, the hydrogen exchange kinetic analysis shows a fast exchange for 17.1% of all residues with a time rate constant at 0.8 min, an intermediate exchange of 19.6% with a time rate constant at 11.3 min, and the slow exchange is found at a time rate constant of 258 min for 8.2% of the fractions.

Based on the analysis of the hydrogen exchange kinetic curves of complex I using a sum of four exponential decay curves, it is demonstrated that the fast and intermediate exchange contribution can be analyzed in more detail.

complex I	a_1 / %	τ_1 / min	a_2 / %	τ_2 / min	a_3 / %	τ_3 / min	a_4 / %	τ_4 / min
alone	16.8	0.3	1.2	4.2	12.5	18.7	14	1200
100 µM NADH	2.4	0.1	33.2	4.3	7.3	51.1	9.9	1252
100 µM NADH + 100 µM decylQ	17.8	0.3	7.9	2.5	10.3	8.1	9.1	222

Table 3.14: Analysis of the exchange kinetic curves of complex I using a curve fitting procedure of four exponentials. Relative contribution a_i (amplitude associated with each time constant) and τ_i (time constant) (i = 1,2,3,4) of the different exponential components are reported for different exchange rate. Error bar is approximately 2-3%.

Table 3.14 shows that complex I alone has a higher fast exchange rate compared to complex I upon NADH binding. The intermediate exchange rate is clearly affected by the binding: 33.2% of residues are exchangeable whereas only 1.2% of the residues of complex I without bound substrate have a time rate constant of about 4 min. Interestingly, the hydrogen exchange kinetics of complex I in the presence of both, NADH and decylubiquinone, shows a

fast exchange comparable to the one obtained for complex I without substrate bound. Nevertheless, the intermediate exchange is found with a time rate constant at 2.5 min of 7.9% and a time rate constant at 8.1 min for 10.3% of all residues.

In conclusion, this observation suggests that the binding site of ubiquinone is found in the membrane domain of complex I. Complex I is accessible and flexible after addition of both substrates, NADH and decylubiquinone, which can be an indication of conformational movements of the entire enzyme upon substrate binding. Clearly the conformation of complex I alone, complex I in the presence of NADH and after addition of decylubiquinone is not the same, giving evidence for domain movements upon ubiquinone binding. Alternative normalization procedures will be performed.

3.2.3 Perfusion-induced ATR difference spectra of complex I upon nucleotide binding

In this section, the application of perfusion-induced ATR FTIR difference spectroscopy to the NADH dehydrogenase fragment and rehydrated films of the entire complex I from *E. coli* using the ATR perfusion cell is described (for details see in section 2.2.3).

3.2.3.1 Reduction of NADH dehydrogenase fragment by dithionite

Figure 3.37 shows the oxidized *minus* reduced ATR FTIR difference spectrum (black line) and the reduced *minus* oxidized ATR difference spectrum (gray line) of NADH dehydrogenase fragment after perfusion with 1 mM dithionite in 50 mM MES/NaOH, 50 mM NaCl, pH 6. After reduction, a change to a buffer solution containing 1 mM $Fe(CN)_6^{3-}$ in respective buffer is used to induce the oxidized state.

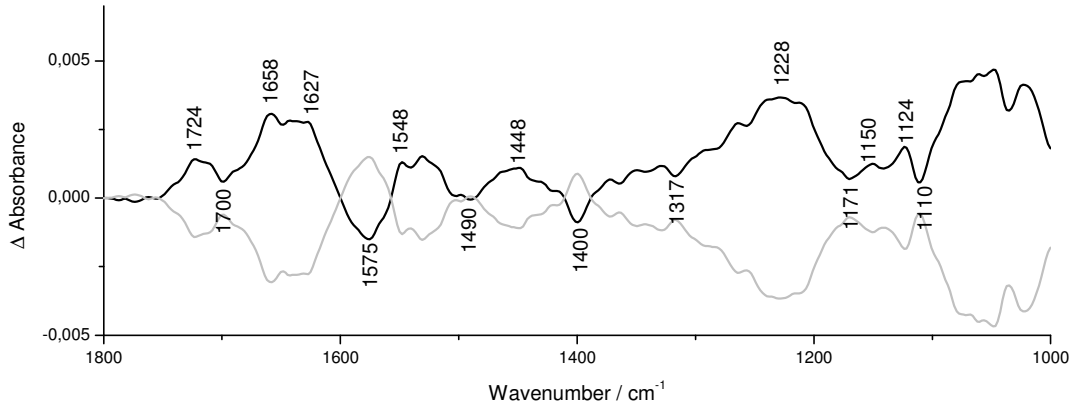

Figure 3.37: The redox induced FTIR infrared difference spectra of NADH dehydrogenase fragment in 50 mM Mes/NaOH, 50 mM NaCl, pH 6 perfused with 1 mM Dithionite (reduction of enzyme, black line: ox *minus* red) and 1mM $Fe(CN)_6^{3-}$ (oxidation of enzyme, gray line: red *minus* ox) in respective buffer. Spectra are baseline corrected.

The obtained spectra are reversible. However, a baseline drift can be observed between approximately 1300 and 1000 cm^{-1} where the main signals from the buffer component are expected. Strong positive modes are present at 1228, 1124, 1077 and 1048 cm^{-1} and negative bands at 1171, 1110, and 1035 cm^{-1}. These signals are assigned to the ν(S=O), δ(OH), ν(C-O), ν(C-N) and ring modes of the MES buffer (Hellwig et al., 2000). The tentative assignments are summarized in Table 3.15. In direct comparison to the

electrochemically induced difference spectra of the NADH dehydrogenase fragment (Hellwig et al., 2000) the spectral contributions in the full spectral range can be assigned to the reorganization from secondary structure elements, individual amino acid side chains and the flavinmononucleotide involved in electron transfer and proton translocation. In the amide I region from 1700 to 1620 cm^{-1}, strong signals at 1658 and 1627 cm^{-1} can be seen. The signal at 1627 cm^{-1} is characteristic of β-sheet contributions (Arrondo et al., 1993). In addition, contributions from the ν(C=O) vibrations of individual amino acid side chains like Asn, Gln, or Arg are possibly present in this spectral range. The ν(C=O) modes of protonated aspartic and glutamic acid side chains appear at 1720 cm^{-1}. In the electrochemically induced spectra this signal is less intense (Hellwig et al., 2000). Furthermore, in the electrochemical redox spectra, a clear shoulder can be seen at 1710 cm^{-1} which is assigned to the ν(C=O) mode of the FMN (Hellwig et al., 2000). At 1575 and 1400 cm^{-1} the $\nu_{s/as}(COO^-)$ mode of deprotonated residues contribute. Signals between 1570 and 1490 cm^{-1} contribute in the so called amide II range. FMN signals are found between 1650, 1500 cm^{-1} and at 1548 cm^{-1} (Hellwig et al., 2000). In addition, small contributions of further amino side chains can be expected from 1450 to 1300 cm^{-1}. However, it is not clear if all cofactors are reduced by dithionite during the perfusion. This would explain the differences between the data in Figure 3.37 and the electrochemically induced spectra in Figure 3.26.

3.2.3.2 Reduction of NADH dehydrogenase fragment by nucleotides

Nucleotide-induced difference spectra of NDF were recorded to investigate the reduction of the enzyme by reaction with its substrate NADH. For comparison, nucleotide induced difference spectra were also performed by perfusion of NAD^+ and NADPH. The ATR difference spectra are shown in Figure 3.38.

The ν(C=O) signal of Asp and Glu is observed at 1722 cm^{-1} upon NADH binding. NADH binds to the enzyme at the NADH binding site where the flavin is located (Sazanov and Hinchliffe, 2006). The ν(C=O) mode of the flavin is found at 1710 and 1660 cm^{-1} as described. This implies that the electron transfer from the flavin to the FeS clusters results mainly in local protein rearrangements upon NADH binding. NAD^+ interacts with the enzyme; however, no electron transfer can be induced by this nucleotide. The significant band at 1622 cm^{-1} is characteristic of the β-sheet contributions of the peptide backbone and can be

found in all spectra with addition of nucleotides. Signals in the amide I region are different than the ones in the electrochemically induced and dithionite-induced spectra.

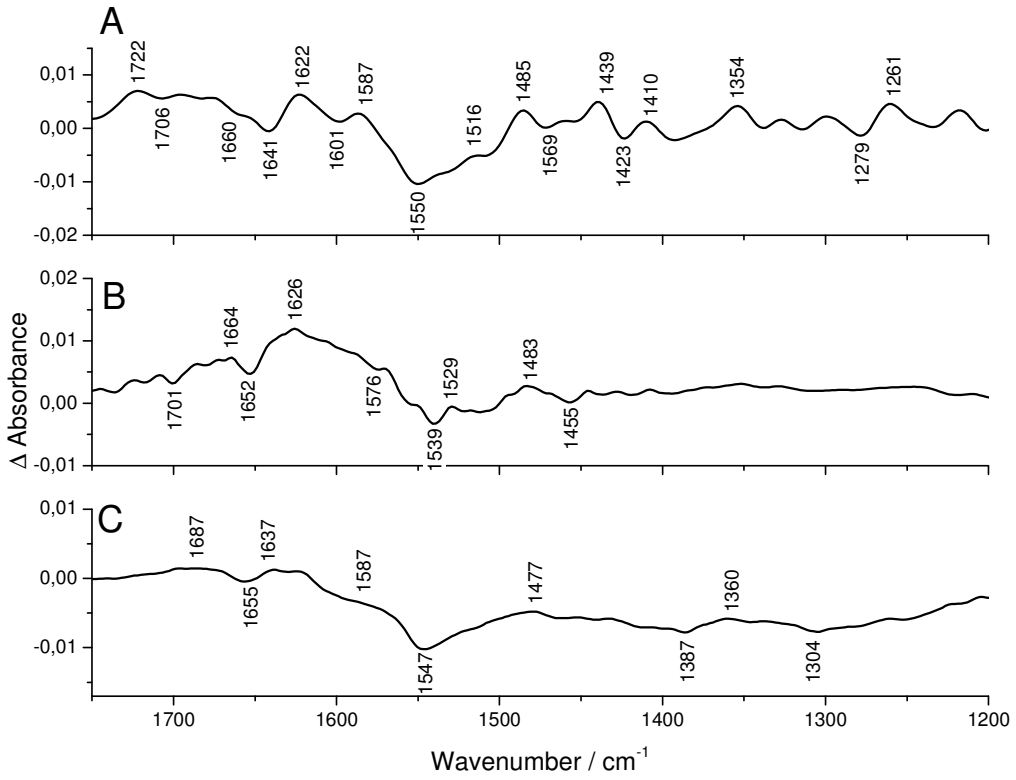

Figure 3.38: Nucleotide induced difference spectra of NADH dehydrogenase fragment upon NADH binding (A), NAD^+ binding (B) and NADPH binding (C). The spectra were corrected for the swelling/shricking effect and smoothed.

The nucleotide induced difference spectra upon NAD(P)H binding of NADH dehydrogenase fragment are dominated by large changes in the 1700 to 1590 cm^{-1} and 1570 to 1490 cm^{-1} region. They are assigned to amide I and amide II motion. Furthermore, contributions of individual amino acid side chains, like ring vibrations of tyrosine around 1516 cm^{-1} or $\nu_{as}(COO^-)$ from Asp and Glu and of Arg $\nu_s(CN_3H_5^+)$ at around 1550 cm^{-1}, are possibly involved in this spectral range where alternations in the amide II signal are also observed. It is difficult to deduce if the enzyme is fully reduced upon nucleotide binding. Signals from the FMN are obtained in all spectra. In addition, whereas upon NADH binding conformational changes are expected, NADPH binding should only lead to electron transfer (Friedrich and Hellwig, unpublished). In Table 3.15 the tentative assignments based on the ATR difference spectra of reduction with dithionite and the electrochemically obtained spectra (Hellwig, et al., 2000) are summarized.

dithionite	NADH	NAD^+	NADPH	tentative assignments
1724 (+)	1722 (+)			$\nu(C=O)_{asp,\ glu}$, $\nu(C=O)_{FMN}$
1700 (-)	1706 (-)	1701 (-)		
			1687 (+)	amide I, β-loop
1658 (+)	1660 (-)	1664 (+)	1655 (-)	amide I, $\nu(C=O)_{asn,\ gln}$
	1641 (-)	1652 (-)	1637 (+)	amide I
1627 (+)	1622 (+)	1626 (+)	1622 (+)	β-sheet, $\nu_{as}(CN_3H_5^+)_{arg}$
	1601 (-)			
1575 (-)	1587 (+)	1576 (-)	1587	amide II (ν (C=N)), $\nu_s(CN_3H_5^+)_{arg}$
1548 (+)	1550 (-)	1539 (-)	1547 (-)	$\nu(C=C)_{FMN}$, $\nu_{as}(COO^-)_{asp,\ glu}$
	1516 (+)	1529 (+)		ring-OH_{tyr}
1490 (-)				
	1485 (+)	1483 (+)	1477 (+)	
	1469 (-)	1455 (-)		
1448 (+)	1439 (+)			
	1423 (-)			
1400 (-)	1410 (+)			$\nu_s(COO^-)_{asp,\ glu}$
			1387 (-)	
	1354 (-)		1360 (+)	
1317 (-)			1304 (-)	$ring_{tyr}$
	1279 (-)			
	1261 (+)			
1228 (+)				ν(S=O) MES buffer
1171 (-)				δ(OH), ν(C-O) MES buffer
1150 (+)				ν(C-N) MES buffer
1124 (+)				
1110 (-)				Na-dithionite ν(S=O)

Table 3.15: Tentative assignments of the perfusion-induced infrared difference spectra of NDF. Positions are given in cm^{-1}. Positive signals arise either from bound nucleotides or changes in the protein, whereas negative signals can only arise from change in the protein. ν: stretching, δ: deformation, ω: wagging. References according to Venyominov and Kalnin, 1990a; Venyominov and Kalnin, 1990b; Wolpert and Hellwig, 2005; Barth, 2000; Hellwig et al., 2000; Wille et al., 2003.

3.2.3.3 Reduction of complex I

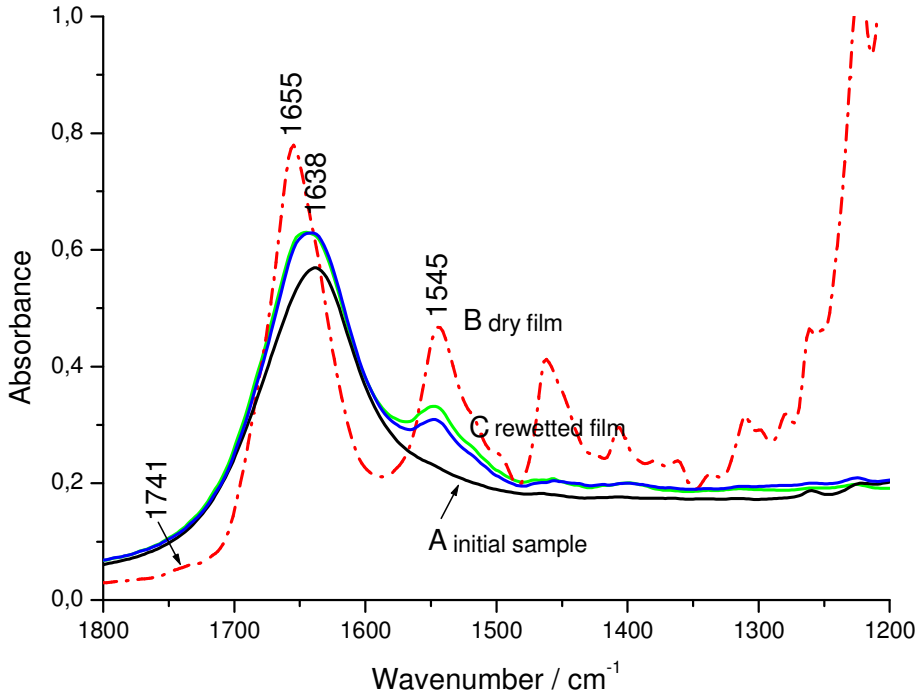

Figure 3.39: ATR FTIR absorbance spectra of complex I from *E. coli* during rehydrated film preparation. The absorption spectrum in trace A (black line) was recorded immediately after deposing the ATR ready sample on the silicon surface. The absorption spectrum was recorded again after the sample had been dried under a gentle stream of dry air or nitrogen (B red dashed dotted line). Trace C (blue line) displays the absorption spectrum after rehydration of the film on the crystal surface with 20-30 µl 50 mM MES/NaOH, 50 mM NaCl. A final spectrum was recorded for 1 h during perfusion with the same buffer (green line).

The process of the hydrated film preparation was monitored by IR spectroscopy as described in section 2.2.3.2 and is shown in Figure 3.39. The $\delta(OH)_{scissoring}$ vibration of the solvent at 1641 cm^{-1} dominates the spectrum of the initial sample after deposing on the silicium surface (see trace A). After drying, strong signals at 1655 and 1545 cm^{-1} are observed from the amide I and II region of the protein (trace B). Further contributions can be expected from the MES buffer at about 1228 cm^{-1} as well as a small shoulder at 1741 cm^{-1} which is assigned to the ν(C=O) ester carbonyl mode of lipids (Hielscher et al., 2006). Rehydration causes a decrease in the amplitude of the signals as the film swells and the water absorption is seen (trace C). However, the water absorption does not dominate the spectrum. In general, the sample became sufficiently stable for data acquisition within 1 h of buffer perfusion (green line). After rehydration a stable amide II signal of $\Delta A \geq 0.1$ was acceptable for acquisition of

difference spectra with an adequate signal/noise. The film is not always stable during the entire experiment. Swelling/shrinking may occur. This may be corrected by substracting the absorbance spectrum of the hydrated film (Marshall et al., 2006).

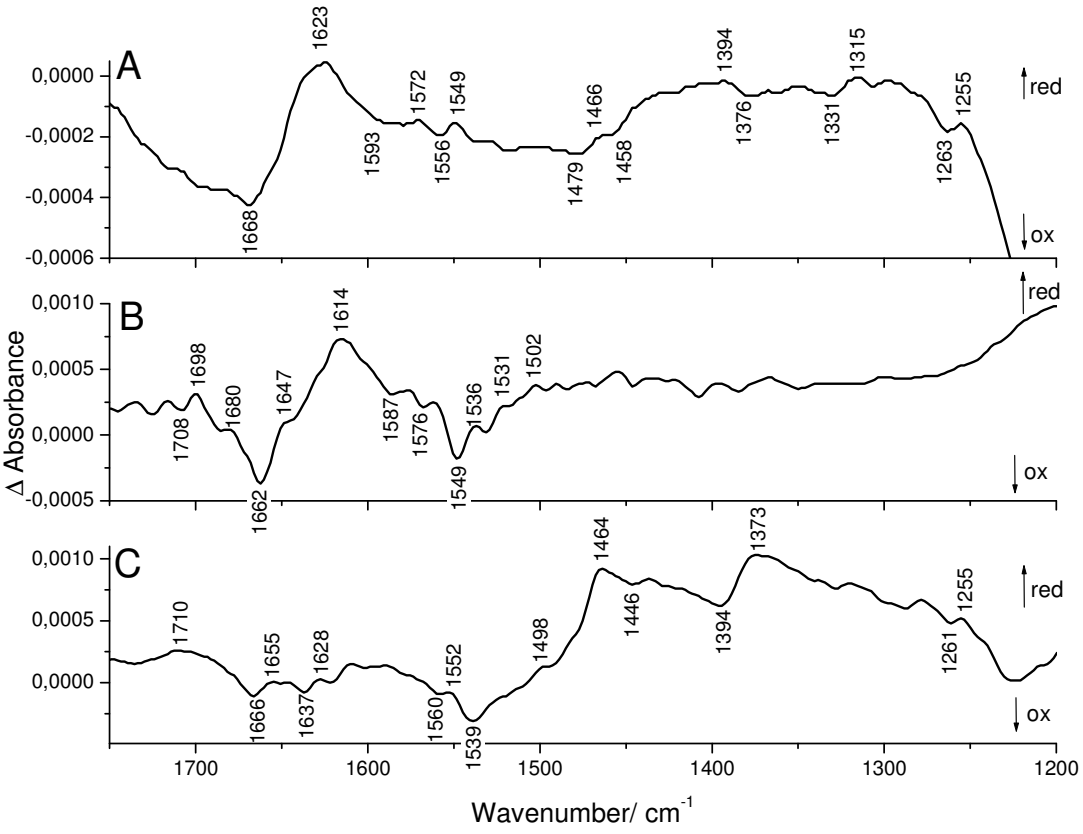

Figure 3.40: Perfusion induced ATR difference spectra of complex I from *E. coli*. In trace (A) is shown the reduced *minus* oxidized difference spectra using sodium dithionite. In comparison, trace (B) illustrates the NADH bound *minus* nucleotide free complex I spectra washed with 50 mM MES/NaOH, 50 mM NaCl, pH 6 buffer and in trace (C) the NADH bound *minus* nucleotide free complex I spectra purged with the same buffer and addition of decylubiquinone is shown. The spectra were corrected for the swelling/shricking effect and smoothed by 3-5 points.

Figure 3.40 shows the perfusion induced ATR difference spectra of complex I reduced with dithionite (A) as well as upon NADH binding (B) and in trace (C) is shown the NADH bound *minus* nucleotide free complex I spectrum after addition of decylubiquinone. Clear differences are present between complex I data and the corresponding spectra of the NADH dehydrogenase fragment (see Figure 3.38). The reduced *minus* oxidized spectrum obtained with dithionite is similar to the known, electrochemically obtained data (see Hellwig et al., 2000 or Figure 3.26). However, small alternations are found for the baseline of all spectra

measured with the perfusion cell. The signal at about 1710 cm^{-1} is not only derived from the enzyme bound FMN but also from protonated Asp/Glu residues. The most dominating feature in the spectra is a large broad difference signal within the amide I range from 1690 to 1620 cm^{-1}. Contributions of the ubiquinone at about 1261/1255 cm^{-1} and of single amino acid side chains like Arg, Asn, and Glu cannot be excluded. Subsequently, these assignments are highly tentative and need to be confirmed by site directed mutagenesis. The spectrum obtained with NADH alone was not reproducible, however it could be obtained after addition of ubiquinone. Evidently quinone is needed in this experiment.

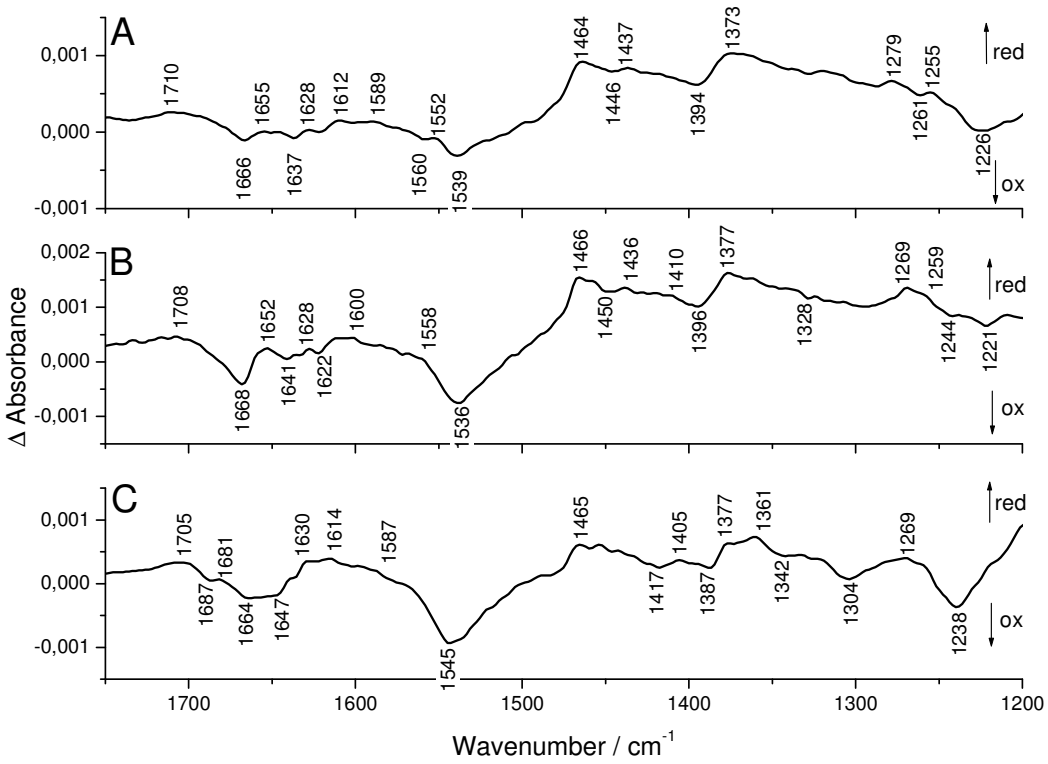

Figure 3.41: Nucleotide induced ATR difference spectra of complex I from *E. coli*. In trace (A) the NADH bound *minus* nucleotide free complex I difference spectra is illustrated, in (B) the NAD^+ bound *minus* nucleotide free complex I difference spectra and in (C) the NADPH bound *minus* nucleotide free complex I difference spectra washed with buffer and upon addition of decylubiquinone. The spectra were corrected for the swelling/shricking effect and smoothed by 3-5 points.

Figure 3.41 shows the nucleotide induced ATR difference spectra of complex I after addition of ubiquinone. It is not clear if the enzyme is fully reduced upon nucleotide binding. In all cases, the spectra are similar to the observed reduced *minus* oxidized spectrum with dithionite. Table 3.16 summarizes the tentative assignments suggested for the ATR difference

spectra. Clear marker bands for ubiquinone are the δ(C-OCH_3) contributions of the methoxy side chain of the neutral oxidized ubiquinone at 1263 cm^{-1} (dithionite, Figure 3.40 panel A) and at 1261 cm^{-1} for the data after NADH binding (Breton et al., 1994; Hellwig et al., 1999, Marshall et al., 2006) and the ν(C=C) signal at 1612/1614 cm^{-1} for NADH and NADPH binding. For NAD^+ these signals cannot confirm that NAD^+ may bind to the enzyme, however, no electron transfer takes place. Furthermore, signals are present in the amide II range from 1580 to 1500 cm^{-1}. The signal at around 1710 cm^{-1} can be further attributed to the ν(C=O) mode of either an Asp or Glu side chain which is protonated in the oxidized form or to a perturbation of a protonated group upon a change of a local environment.

Finally, contributions of nucleotides can be expected in the range of amide I between 1690 and 1590 cm^{-1} (see Figure 5.10 in appendix).

dithionite	NADH/ UQ	NAD^+/ UQ	NADPH/ UQ	tentative assignments
1710 (+)	1710 (+)	1708 (+)	1705 (+)	$\nu(C=O)_{asp, glu}$, $\nu(C=O)_{FMN}$
			1687 (-)	β-loop
			1681 (+)	amide I
1668 (-)	1666 (-)	1668 (-)	1664 (-)	amide I, $\nu(C=O)_{asn, gln}$, $\nu(C=O)_{UQ}$
	1655 (+)	1652 (+)		amide I, α-helical/random
	1637 (+)	1641 (+)	1647 (+)	amide I
	1630 (-)	1628 (-)	1630 (-)	ß-sheet, $\nu_{as}(CN_3H_5^+)_{arg}$
1623 (+)		1622		
	1612 (-)		1614 (-)	$\nu(C=C)_{UQ}$
1556 (-)	1552 (-)	1558 (-)		amide II (ν (C=N)), $\nu_s(CN_3H_5^+)_{arg}$
1549 (+)	1539 (+)	1536 (+)	1545 (+)	$\nu(C=C)_{FMN}$, $\nu_{as}(COO^-)_{asp, glu}$
	1464 (-)	1466 (-)	1465 (-)	
1458 (-)	1446 (-)	1450 (-)		
	1437 (+)	1436 (+)		
1394 (+)	1394 (+)	1396 (+)	1387 (+)	$\nu_s(COO^-)_{asp, glu}$
1376 (-)	1373 (-)	1377 (-)	1377 (-)	
1331 (-)			1361 (+)	
1315 (+)			1304 (+)	$ring_{tyr}$,
1263 (-)	1261 (-)		1269 (-)	$\delta(C\text{-}OCH_3)_{UQ}$
1255 (+)	1255 (+)			
	1226 (-)	1221 (-)	1238 (-)	ν(S=O) MES buffer

Table 3.16: Tentative assignments of perfusion-induced infrared difference spectra of complex I. Positions are given in cm^{-1}. Negative signals arise from bound nucleotides or changes in the protein (reduced state), whereas positive signals can only arise from change in the protein (oxidized state). ν: stretching, δ: deformation, ω: wagging. References according to Venyominov and Kalnin, 1990a; Venyominov and Kalnin, 1990b; Wolpert and Hellwig, 2005; Barth, 2000; Hellwig et al., 2000; Wille et al., 2003; Marshall et al., 2006.

3.2.4 Far infrared spectroscopic investigations

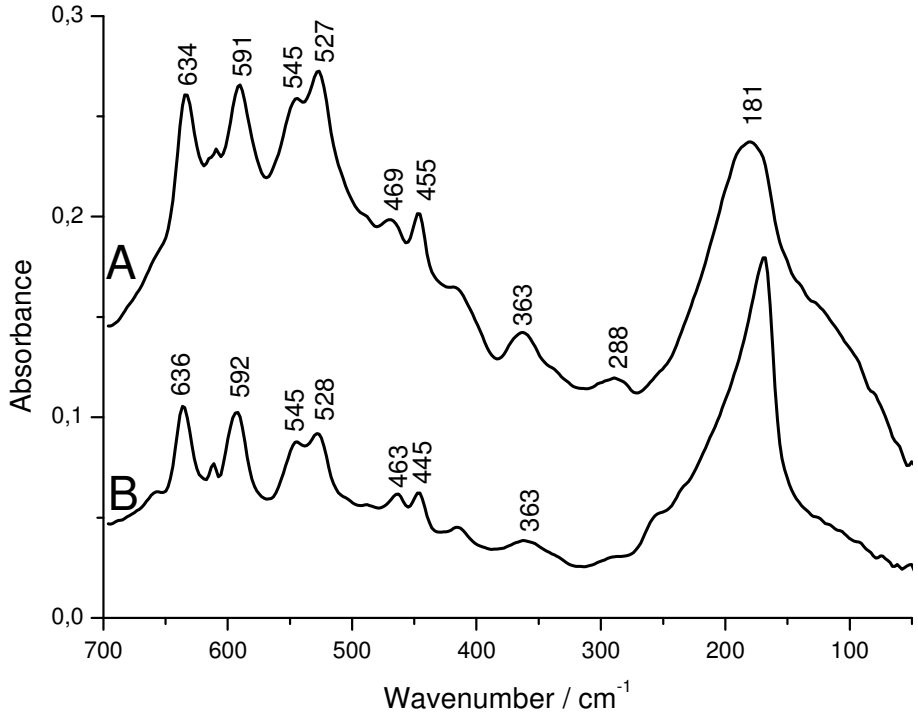

Figure 3.42: ATR absorbance spectra of films from complex I (A) and NADH dehydrogenase fragment (B) from *E. coli* in the far infrared domain from 700 to 50 cm^{-1}.

Figure 3.42 displays the far infrared spectra of complex I (A) and NDF (B) between 700 and 50 cm^{-1}. Between 700 – 500 cm^{-1} the amide IV (C=O in plane, C-C stretch), amide V (C-N torsion) and amide VI (C=O out of plane, C-N torsion) can be expected (Bandekar, 1992). The amide VII (N-H out of plane) is included at 288 cm^{-1}. In addition, metal ligand vibrations can be found at the far infrared domain (Marboutin et al., 2009; Dörr et al., 2008; El Khoury and Hellwig, 2009; Mitsuo et al., 2007). In particular, the FeS vibration of the [2Fe-2S] and [4Fe-4S] clusters can be expected at 455 and 469 cm^{-1} for complex I. The FeS modes in the NADH dehydrogenase fragment are found at 445 and 463 cm^{-1} (Youssef El Khoury, Institut de Chimie, personal communication).

The broad signal at about 181 cm^{-1} can be assigned to the hydrogen bonding collective motions (Eyster and Prohofsky, 1977). The spectroscopic characterization of the collective low frequency modes may lead to a basic understanding of the protein dynamics that give rise

to protein function, including ligand accommodation or major conformational changes within the enzyme (Zheng et al., 2006).

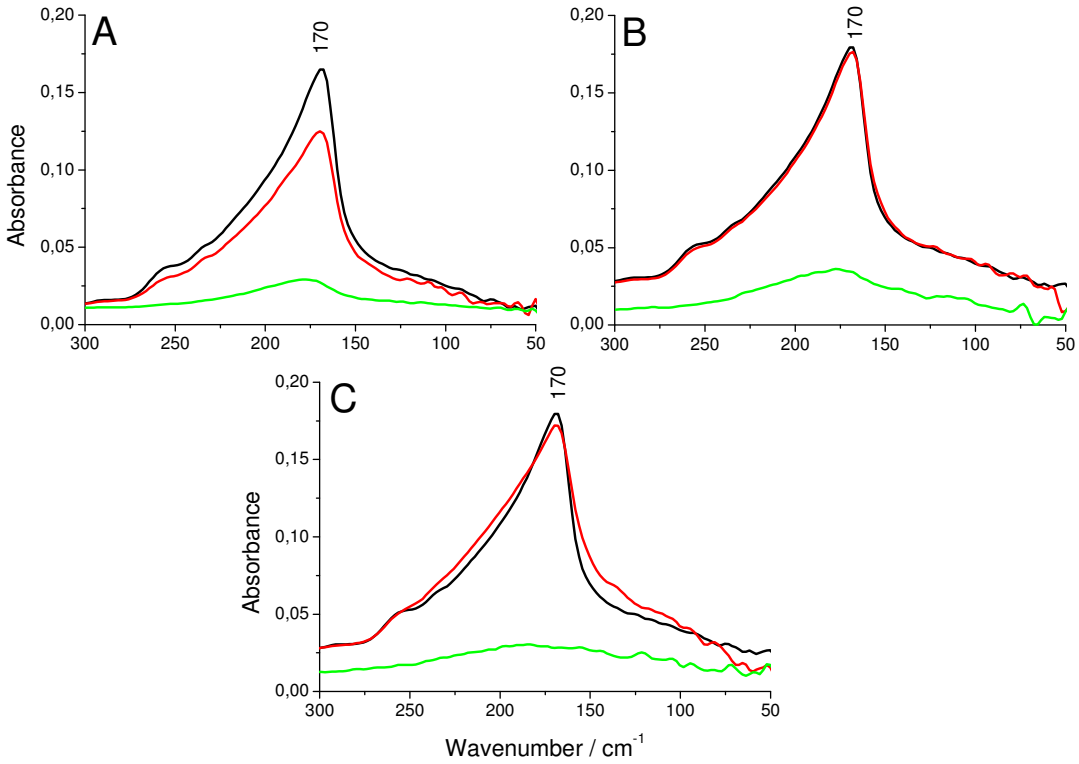

Figure 3.43: The far infrared ATR absorbance spectra of the hydrogen bonding feature of NADH dehydrogenase fragment from *E. coli* upon nucleotide binding. In (A) the NDF spectrum before (black line) and after incubation with 50 µM NADH (red line) and in (B) with 50 µM NAD^+ (red line) and in (C) with 1 mM NADPH (red line) are shown. The FIR absorbance spectra of the nucleotides in large excess (10 mM concentration) are illustrated in the respective spectra (green line).

The interesting broad signature below 300 cm^{-1} with a maximum at approximately 170 cm^{-1} (black line) includes the contribution of intra- and intermolecular hydrogen bonding ν(H…O) or in general ν(H…B) within the protein or with water molecules. It can be described as an overall breathing mode of the protein and is thus a marker of conformation of the enzyme. Figure 3.43 shows this significant broad signature of NADH dehydrogenase before (black line) and after incubation with its nucleotides (red lines). In panel A the hydrogen bonding signature upon NADH binding is shown. The signature decreases after reaction with NADH. Interestingly, the signature gets broader after incubation of NADPH (panel B) whereas after NAD^+ binding (panel C) the signature is not affected. This leads to

the conclusion that after NADH binding the broad signature changes and thus the internal hydrogen bonding.

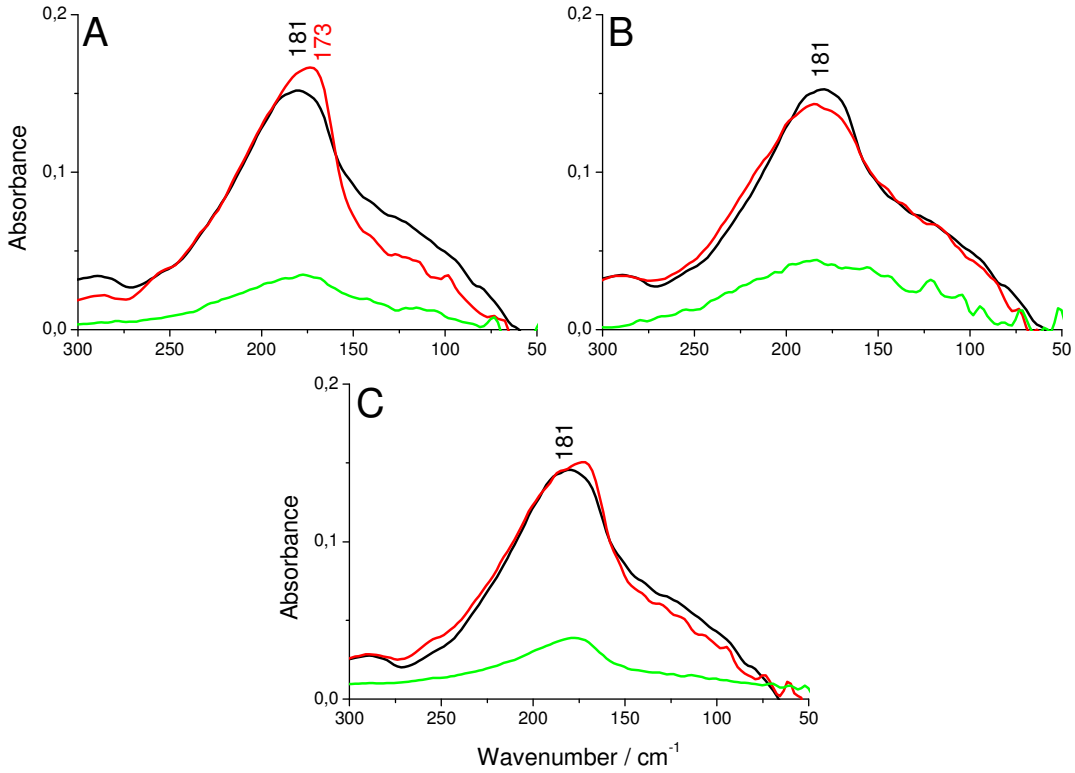

Figure 3.44: The far infrared ATR absorbance spectra of the hydrogen bonding feature of complex I from *E. coli* upon nucleotide binding. In (A) the complex I spectrum (black line) and after incubation with 50 µM NADH (red line), and in (B) with 50 µM NAD^+ (red line) and in (C) with 1 mM NADPH (red line) are shown. The FIR absorbance spectra of the nucleotides in large excess (10 mM concentration) are illustrated in the respective spectra (green line).

Figure 3.44 displays the intra- and intermolecular hydrogen bonding signature of the entire complex I with a maximum at 181 cm^{-1} (black line). In comparison to the signature of NADH dehydrogenase fragment, this signature is broader. Interestingly, upon NADH binding the signature increases at lower frequencies and the maximum shifts to 173 cm^{-1} (red line). After incubation with NAD^+ (panel B) the signature decreases weakly and after addition of NADPH the maximum of the hydrogen bonding pattern is found at lower frequencies. This observation leads to the conclusion that after binding of NADH a conformational change within the enzyme takes place and the hydrogen bonding is strengthened.

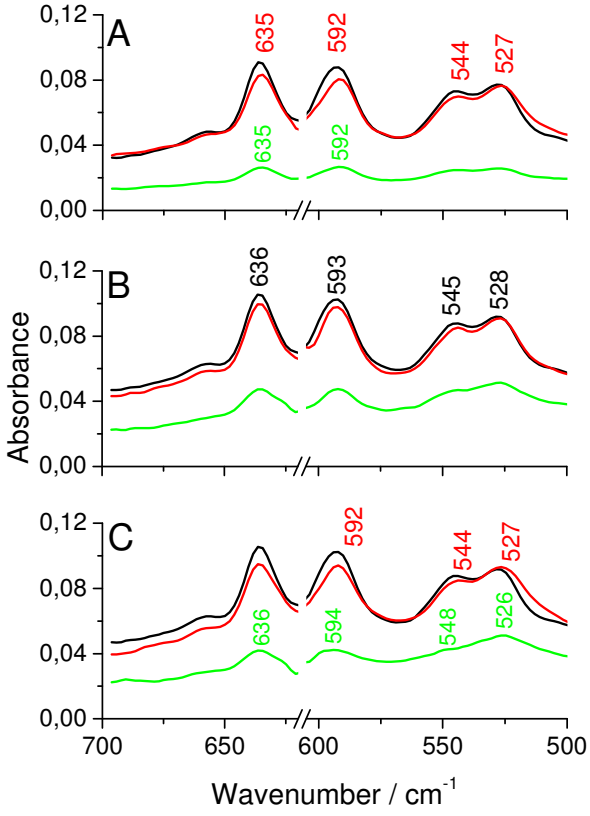

Figure 3.45: The FIR absorbance spectra of NADH dehydrogenase fragment from *E. coli* upon nucleotide binding from 700 to 500 cm^{-1}. In (A) the NDF spectrum (black line) and after incubation with 50 µM NADH (red line), and in (B) with 50 µM NAD^+ (red line) and in (C) with 1 mM NADPH (red line) are shown. The FIR absorbance spectra of the nucleotides in large excess (10 mM concentration) are illustrated in the respective spectra (green line).

In Figure 3.45 panel A the far infrared spectra of the NADH dehydrogenase fragment before (black line) and after incubation of NADH (red line) is shown. The nucleotide spectra are drawn in green. A 10-100 fold excess was used. Therefore, the contributions are small and can obviously be neglected due to the low concentration. The amide VI band is affected upon NADH binding. The secondary structure contributions are involved in the decrease of the β-sheet element at 544 cm^{-1} and a shoulder at lower frequencies appears. NAD^+ binding does not affect the NDF spectra (panel B) in the amide VI range. Upon NADPH binding (panel C), however, the peak at 544 cm^{-1} decreases. This signal is assigned to a β-sheet element and a shoulder at lower frequencies appears as described above for NADH binding. Upon NADH binding the amide VI range is affected which leads to the conclusion that a conformational change can be monitored in the far infrared domain upon NAD(P)H binding to the enzyme fragment.

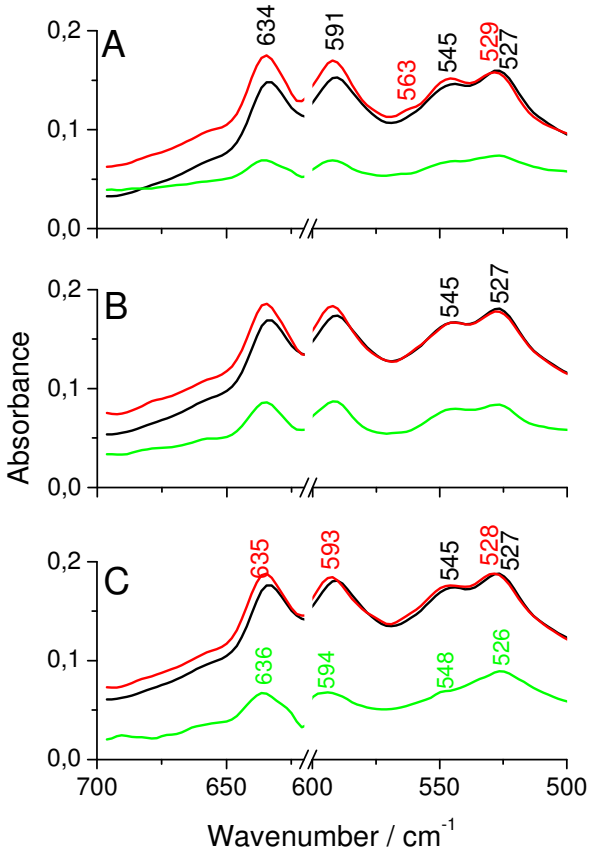

Figure 3.46: The FIR absorbance spectra of complex I from *E. coli* upon nucleotide binding from 700 to 500 cm^{-1}. In (A) the complex I spectrum before (black line) and after incubation with 50 µM NADH (red line), and in (B) with 50 µM NAD^+ (red line) and in (C) with 1 mM NADPH (red line) is shown. The FIR absorbance spectra of the nucleotides in large excess (10 mM concentration) are illustrated in the respective spectra (green line).

The same investigation was carried out for the entire complex I. In Figure 3.46 panel A the far infrared spectra of complex I (black line) and after incubation with NADH (red line) is displayed. As described above, the amide VI domain is affected upon NADH binding. The β-sheet character at 545 cm^{-1} decreases slightly whereas the α-helical contribution at 527 cm^{-1} upshifts to higher wavenumbers. Interestingly, a peak appears at 563 cm^{-1} which can be assigned to a random type structure (Youssef El Khoury, Institut de Chimie, personal communication). The incubation with NAD^+ leads to no alternation in the far infrared domain (see panel B). Upon NADPH binding (panel C) the amide VI band is only weakly affected. The α-helical contribution at 527 cm^{-1} and the β-sheet elements at 545 cm^{-1} slightly shift to higher frequencies. A small shoulder at 561 cm^{-1} is assigned to random elements. The amide VI band is sensitive towards NADH binding and indicates a large conformational change in the enzyme upon nucleotide accommodation.

4 Conclusion

In this thesis two central aspects have been treated. First, factors ruling properties on redoxproteins have been investigated. In this study is shown the characterization of the broad hydrogen bonding feature of phospholipids in the far infrared down to 300 to 50 cm^{-1}. Phospholipid bilayers allow clear temperature dependent investigations on different forms of hydrogen bonding interaction and interaction with water molecules.

The strong temperature behavior of the phospholipid layer in the mid infrared region displays an increase of hydrogen bonding structure in the phospholipid head groups. The phosphate group i.e. the asymmetrical PO_2^- stretching vibration is sensitive to the temperature dependent phase transition. Whereas the asymmetrical PO_2^- stretching mode is found at 1232 cm^{-1} for asolectin and at 1250/1254 cm^{-1} for PC and PC D_{35} at 40 °C in the liquid-crystalline phase and downshifts to lower frequencies upon cooling to the gel phase, the asymmetrical $CN^+(CH_3)_3$ at 972 cm^{-1} for asolectin and at 968 cm^{-1} for PC at 40 °C upshifts to higher frequencies. This indicates a stronger hydrogen bonding between network water and the phosphate head group. Furthermore, the C=O stretching vibration of the ester carbonyl groups from the interfacial region has a broad signal that is centered at 1738 cm^{-1}. However, a shoulder at lower frequencies increases upon cooling suggesting that in phospholipids some of the ester C=O groups act as proton acceptors.

The temperature behavior of the hydrogen bonding pattern of pure PC and its isotopically labeled variant are in agreement with the observation in the mid infrared range. Intermolecular hydrogen bonding between lipids with different charges due to their head groups may be significantly stabilized by the fact that lipids are already intermolecularly assembled as a result of the hydrophobic effect and the Van der Waals interactions between their chains. Interestingly, for the phospholipid mixture, this far infrared spectral feature increases upon heating. This is in contrast to the decrease of the water signature of the same band in the far infrared in pure PC.

In summary, the signals typical for bound water in mid infrared show analogous temperature dependence for the mixed and the pure PC whereas the hydrogen bonding feature in the far infrared shows a very different behavior for the mixed type lipid films. On this basis the contribution of water molecules and of bulk water does not exclusively dominate the spectral range in the far infrared for this type of films, or at least, it is only one of the possible contributions and any type of hydrogen bonding may contribute here. In asolectin the

intermolecular hydrogen bonding seen in the far infrared is stronger at higher temperature, subsequently in the liquid-crystalline phase. Pure PC seems to be less organized at higher temperature from the intermolecular point of view as confirmed by the isotopically labeled variant. The main structural difference between these two samples is the variation of the head groups that seems to induce a very different spectral signature in the far infrared. An effect of the chain length can be excluded due to the comparison of the unlabeled and isotopically labeled PC which present different chain lengths, they behave similarly. An effect based on the different degree of the saturation of the chains may not be excluded which maybe monitored doing a lipid titration of different types of lipids.

The high degree of variability of head groups in asolectin that includes sugar, choline and ethanolamine allows building a more rigid structure. However, in the pure PC this cannot be expected. Interestingly, the C=O groups of the interfacial region in lipids monitored at 1738 cm^{-1} do not show this difference for the two type of lipid layers. It could thus only be based on the NH_3^+ in PE and the inositol sugar group in PI.

In conclusion, the far infrared spectral range allows describing intermolecular hydrogen bonding interactions in large molecular assemblies in a very specific way and is thus a powerful tool for structural investigations.

Furthermore the assembly process of the small transmembrane model protein cytochrome b_6 protein was studied. Redox properties were characterized. Two midpoint potentials were found for the wild type at -187 mV and -68 mV. Mutations were performed for the four histidine residues. We have found that cytochrome b_6 from spinach assembles in multi step process. After membrane integration of the cytochrome b_6, heme b_L binds predominately *via* His86 to the protein moiety. Subsequently, heme b_H binds primarily *via* His202 to the assembly intermediate which results in a rearrangement of the protein structure. His187 and His100 are involved in stabilization of bound heme b_L and heme b_H.

Furthermore, in this work the possibility to study the functional role of specifically bound lipids in enzymes by means of redox induced FTIR difference spectroscopy was demonstrated. Importantly, it could be observed that the presence of lipids have a strong influence on the spectral properties.

In the case of the cytochrome bc_1 complex from yeast studied here, two cardiolipin molecules have been found in X-ray structures, one closely bound to center Q_i close to the

quinone binding site and heme b_H and a second one, which is bound in less delipidated samples at the subunit interface of cytochrome *b* and core protein 1.

The oxidized *minus* reduced FTIR difference spectra of the cytochrome bc_1 complex at pH 7.3 include marker bands found for the protonated and deprotonated form of cardiolipin and we conclude that the bound lipid are perturbed by the redox reaction. One possible explanation of the data is that cardiolipin is deprotonated in the oxidized state and uptakes a proton in the reduced state of the enzyme. Signals due to the changes in hydrogen bonding environment of the lipids and coupled structural rearrangements are also proposed and will be distinguished in future studies with means of site-directed mutagenesis and isotopically labeled lipids.

The shift of the heme b_H and heme *c* contribution in the reaction induced visible spectra confirm the importance of the lipids for structural and electrostatic integrity. In addition to the lipid-dependent position of the *b* heme absorption maximum, the midpoint redox potential of both *b* hemes, b_H and b_L, were also influenced. The E_m of heme b_L was shifted from -52 mV in the untreated complex to -82 mV in the delipidated complex. Heme b_L transfers electrons released upon ubiquinol oxidation at the Q_o site to heme b_H. The shift in the midpoint potential of heme b_L affects the electron transfer in the low potential chain. Addition of CL alone could only partly reverse this shift (-42 mV). After addition of the mixture of asolectin and CL, the midpoint potential of heme b_L was comparable to the native enzyme. This finding is in accordance with the analysis of the catalytic activity and the peak position of the *b* heme in the redox spectra upon delipidation and relipidation.

Finally, it could be shown that reaction induced infrared difference spectroscopy is a sensitive tool for the study of the effect of lipids specifically bound to cytochrome bc_1 complex on the molecular level.

Oxidized *minus* reduced FTIR difference spectra were also carried out for the complex I from *E. coli* with different lipid content. The electrochemically induced FTIR difference spectra of complex I contain contributions from redox-dependent changes in the protein structure and protonation states of cofactors and individual amino acids. However, small variations are based on varying lipid content of each preparation. Incubation with *E. coli* polar lipid extract has enhanced the specifically NADH:decyl-ubiquinone oxidoreductase activity of complex I. In comparison, the oxidized *minus* reduced FTIR difference spectra of complex I in the presence of lipids shows strong changes in the full spectral range form 1800 to 1000 cm^{-1}.

In the data seen after addition of lipids, an additional differential peak at 1730 and 1744 cm^{-1} can be observed. The differential form of the peaks reflects an upshift of the carbonyl band from 1730 cm^{-1} to 1744 cm^{-1} upon oxidation, indicating that within the protein a more hydrophobic environment is created in which the observed C=O groups are less hydrogen bonded to water. Since lipids in solution are not redox active, only a change in environment may induce such a signal. Interestingly, the signals are absence in the isotopically labeled PC variant, which underline the assignment to the ester carbonyl group of lipids.

In conclusion, the data obtained indicates that there are phospholipid molecules binding very specifically to complex I and thus be involved in conformational change. However, the exact type of lipids needs to be specified.

The second part of this thesis deals with the factors ruling the conformational movement in *E. coli* complex I. Knowledge of the mechanism of complex I is rather limited due to its enormous complexity in combination with the lack of structural data.

First, we have investigated the secondary structure of complex I and its soluble fragment upon different nucleotide binding. The NADH dehydrogenase fragment and NADH:ubiquinone oxidoreductase have a predominantly α-helical structure. Nucleotides such as NAD^+, NADH and NADPH bind in the nucleotide binding site which is composed of a Rossmann fold-like domain. Importantly, NADH and NADPH binding affect the β-sheet character of the NADH dehydrogenase fragment. The secondary structure analysis upon nucleotide binding shows that both are influenced in a way that β-sheet contributions decrease and β-turns contributions increase. However, binding of NAD^+ did not lead to significant structural changes. Addition of NADH shows similarly alternation in the secondary structure of NADH dehydrogenase fragment and in the entire complex I. Therefore, it can be concluded that a conformational change takes place upon NADH binding.

In order to contribute the understanding of the hydrogen bonding interaction and thus to the dynamic structure during substrate binding to the NADH:ubiquinone oxidoreductase from *E. coli,* hydrogen/deuterium exchange kinetics were carried out. In the course of amide hydrogen/deuterium exchange the amide I band with its maximum at about 1653 cm^{-1} shifts to lower frequencies about 1642 cm^{-1} and is reshaped. The intensity of amide II band at approximately 1545 cm^{-1} decreases. The amide II' band replaces the amide II band. It is overlapped with the δ(HOD) vibration at about 1452 cm^{-1}. The rates of amide hydrogen

exchange at which the different peptide hydrogens in protein tertiary structure exchange with protons (or in this cases deuterium), depending on hydrogen bonding and solvent accessibility. Peptide hydrogen exchange rates are thus very sensitive to protein secondary structure and conformational change. Our observation leads to the suggestion that upon addition of NADH the NADH dehydrogenase fragment gets more accessible. Therefore, the remaining possibility is that conformational movement is caused by NADH binding and occurs already in the soluble fragment of the entire complex I. Furthermore, the complex I is more accessible and flexible after addition of both substrates, NADH and decylubiquinone, and thus can be an indication for conformational change of the entire enzyme upon NADH binding. In addition, we suggest that the binding site of ubiquinone is found in the membrane domain. Clearly, the conformation of complex I alone, in the presence of NADH and after addition of decylubiquinone is not the same, giving evidence for domain movements upon ubiquinone and NADH binding.

Furthermore nucleotide induced FTIR difference spectra of NADH dehydrogenase fragment and the entire complex I were performed using a new application of an ATR perfusion cell. The soluble fragment was measured using a dialysis membrane so that only interaction with the substrate was monitored. Whereas the complex I was placed on the ATR crystal surface as a hydrated film. The perfusion-induced ATR spectra of complex I and the NADH dehydrogenase fragment are dominated by large rearrangements of the protein during substrate binding or reduction with dithionite. The signals at 1710 and 1549 cm^{-1} of the ν(C=O) and ν(C=C) modes of the isoalloxazine ring are the only detectable contributions of the enzyme-bound flavin in complex I as well as in the NADH dehydrogenase. However, it is not clear if all cofactors are reduced by dithionite during the perfusion. The perfusion-induced ATR spectra of complex I upon NADH binding allowed the conclusion, that the enzyme is reduced, because signals of the ubiquinone at 1261(-)/1255(+) cm^{-1} are observed. Whereas upon NAD^+ binding this observation cannot be obtain.

Finally, in the far infrared domain was studied for nucleotide binding. The amide VI band and the vibration of iron-sulfur clusters as well as the broad hydrogen bonding signature can be found. The interesting broad signature below 300 cm^{-1} includes the contribution of intra- and intermolecular hydrogen bonding within the protein or with water molecules. Upon NADH binding the band gets narrows and loses intensity. NAD^+ does not affect the hydrogen bonding signature of NADH dehydrogenase fragment and of the complex I. This observation leads to the suggestion that after binding of NADH a conformational change takes place within the enzyme and the internal hydrogen bonding is strengthened.

In conclusion, the results presented here, the binding of NADH induces long range global conformational changes that are possibly linked to the mechanism of the enzyme. This could not be found in control experiments upon addition of NAD^+ or NADPH. This would imply that the addition of NADH to complex I has two different effects: first, it leads to local conformational changes caused, by the reduction of the iron-sulfur clusters, and second, it leads to global conformational changes possibly linked to quinone binding. However, it is unclear whether and how both processes contribute to proton pumping mechanism, although it is widely accepted in the field that energy transduction by complex I is mainly accomplished by means of conformational movements.

5 Appendix

5.1 Appendix of material and methods

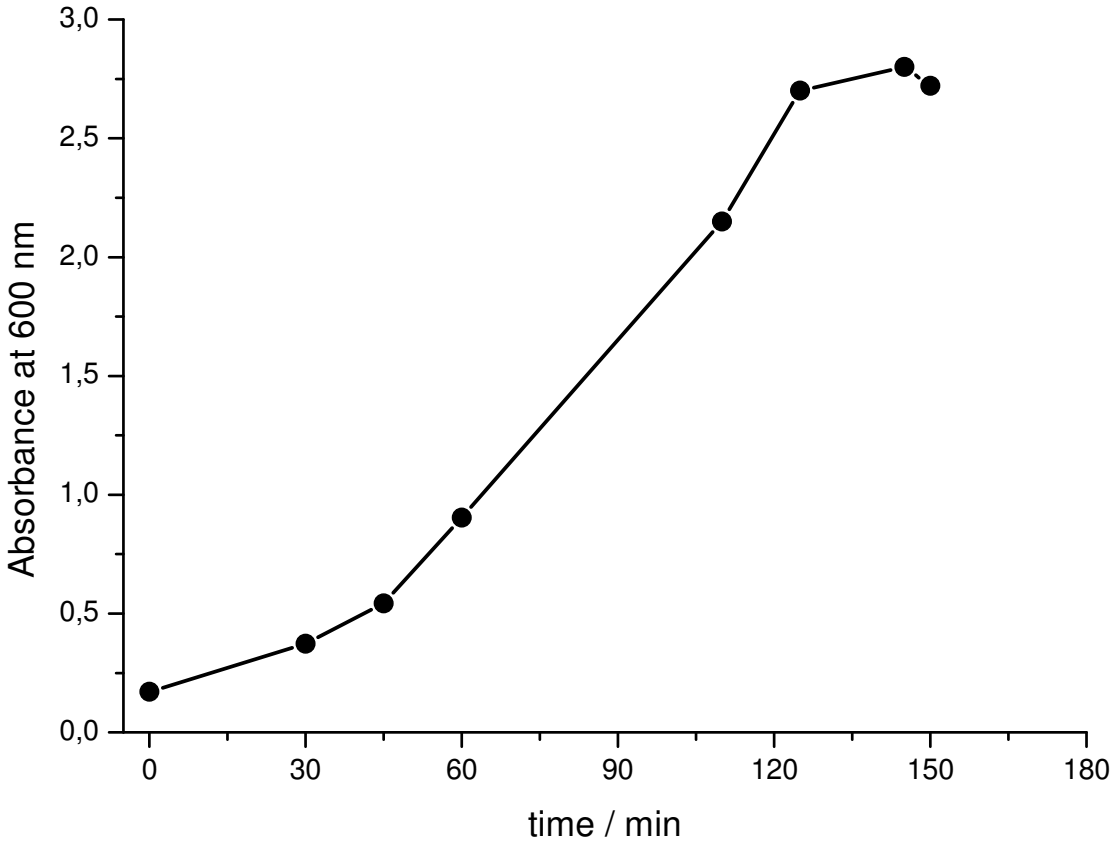

Figure 5.1: Growth curve of *E. coli* cells from cell strain BL21(DE3)pET11a/*nuo*B-G/NuoF$_C$. At about 45 min IPTG was added to the expression of the gene. The stationary growth phase is obtained at 2.8 OD, the cells were harvested at this point.

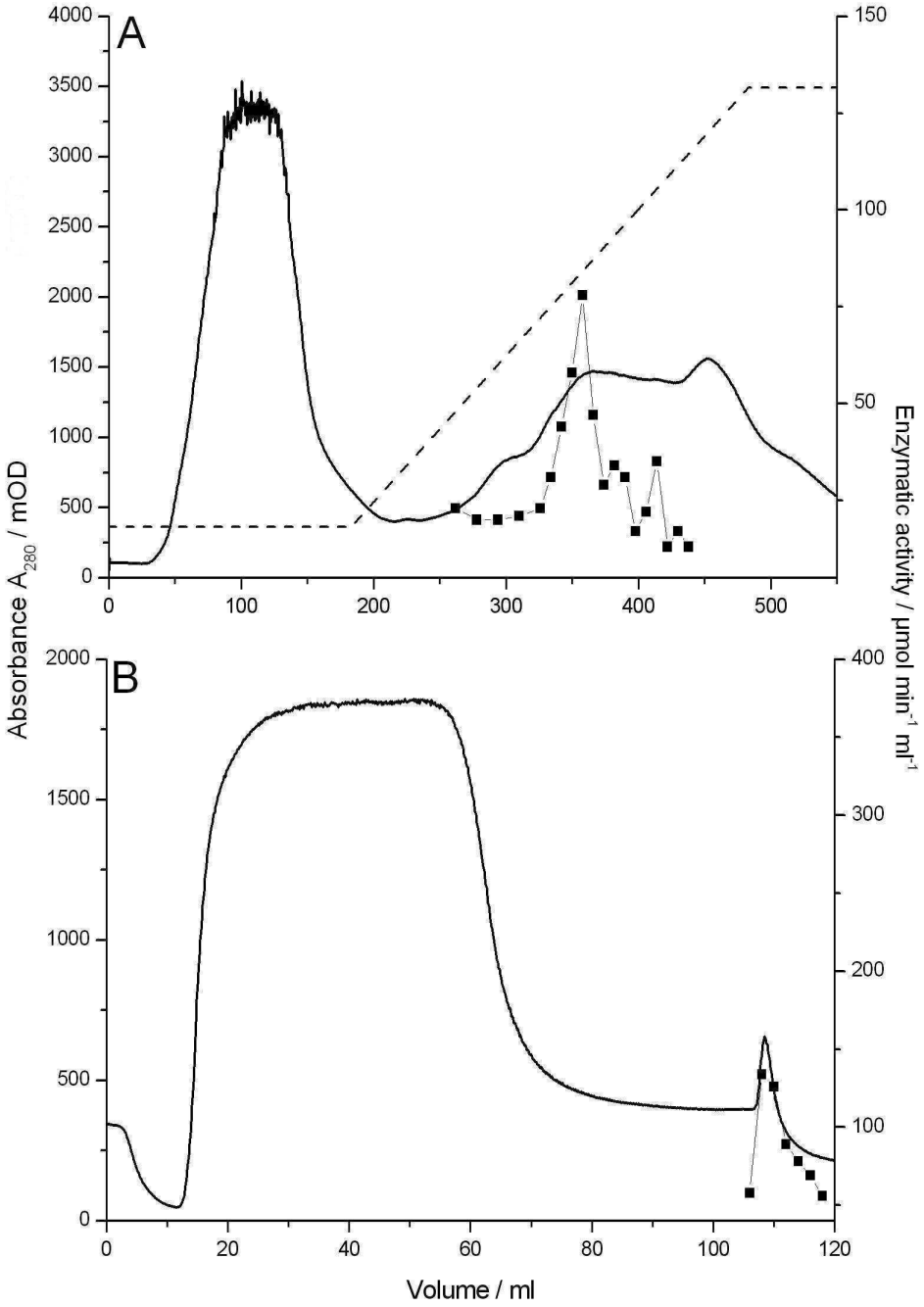

Figure 5.2: Purifcation of the *E. coli* NADH dehydrogenase fragment from complex I from the strain BL21(DE3) pET-11a/*nuoB-G*/NuoF$_C$. Chromatography on Fractogel EMD (A) and the chromatography on StrepTactin-Sepharose (B). The solid line displays the absorbance at 280 nm, the dotted line displays the NaCl gradient and the curves (-■-) show the NADH/ferricyanide oxidoreductase activity.

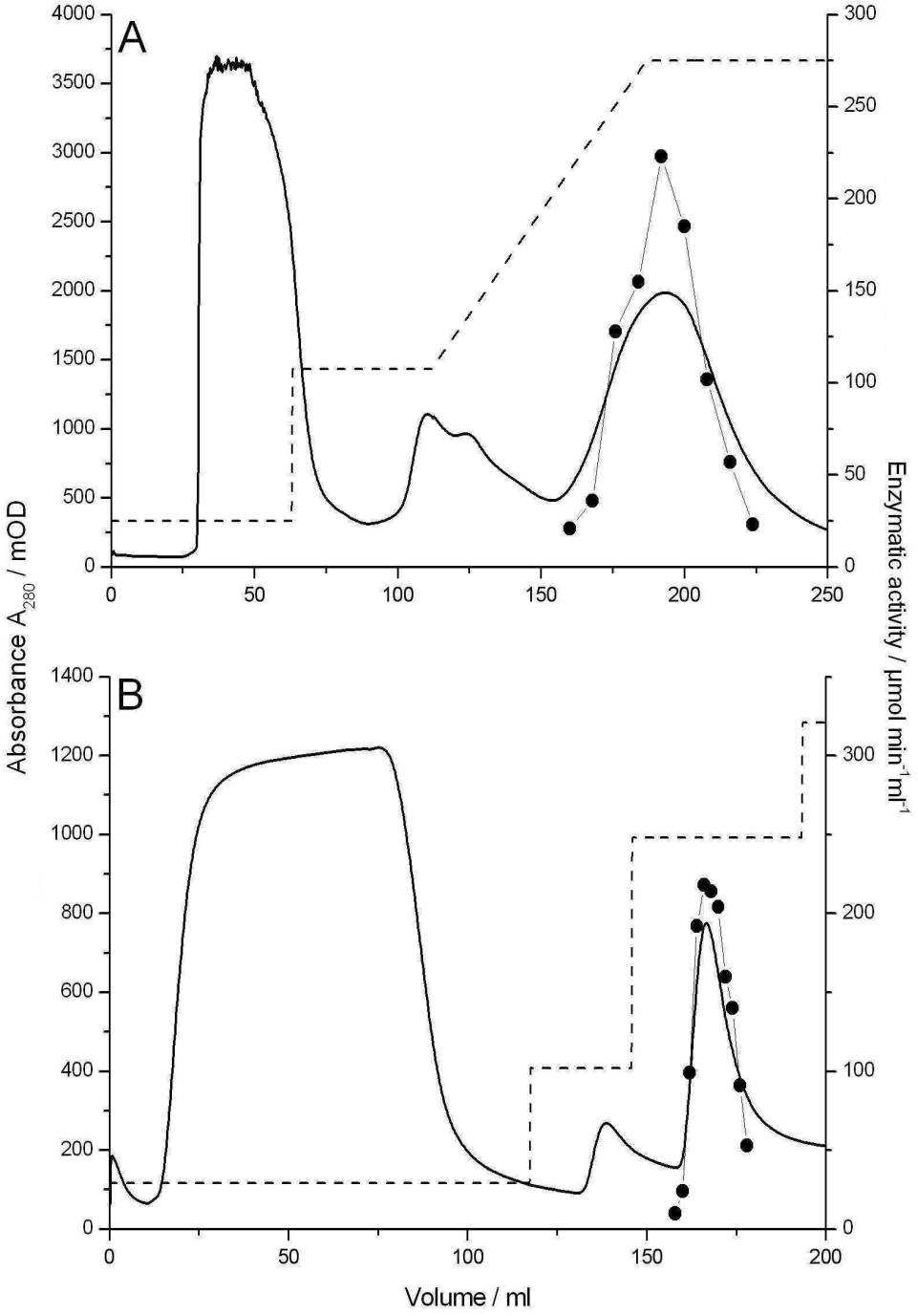

Figure 5.3: Purification of *E. coli* complex I from strain ANN0221/pBAD*nuo*/His-*nuoF*. Chromatography on Fractogel EMD (A) and the chromatography on Pro Bond Ni^{2+} -IDA (B). The solid line shows the absorbance at 280 nm, the dotted line shows the NaCl or imidazole gradient and the curves (-●-) show the NADH/ferricyanide oxidoreductase activity.

			NADH/ferricyanide oxidoreductase activity		
preparation	volume / ml	protein / mg	total / µmol min^{-1}	specific / µmol min^{-1} mg^{-1}	yield / %
cytoplasm	105	1663	7875	4.7	100
Fractogel EMD	110	611	5940	9.7	75.4
StrepTactin-Sepharose	7.8	10	796	79.6	10.1

Table 5.1: Isolation of *E. coli* NADH dehydrogenase fragment from strain BL21(DE3) pET11a/*nuoB-G*/nuoF_C from 30 g cells (wet mass).

			NADH/ferricyanide oxidoreductase activity		
preparation	volume / ml	protein / mg	total / µmol min^{-1}	specific / µmol min^{-1} mg^{-1}	yield / %
membranes	22.4	1308	9475	7.2	100
extract	59.5	1070	6962	6.5	73.5
Fractogel EMD	67	278	4556	16.4	48.1
ProBond Ni^{2+}-IDA	17.6	10	2429	242.9	25.6

Table 5.2: Isolation of *E. coli* complex I from strain ANN0221/pBAD*nuo*/His-*nuoF* from 40 g cells (wet mass).

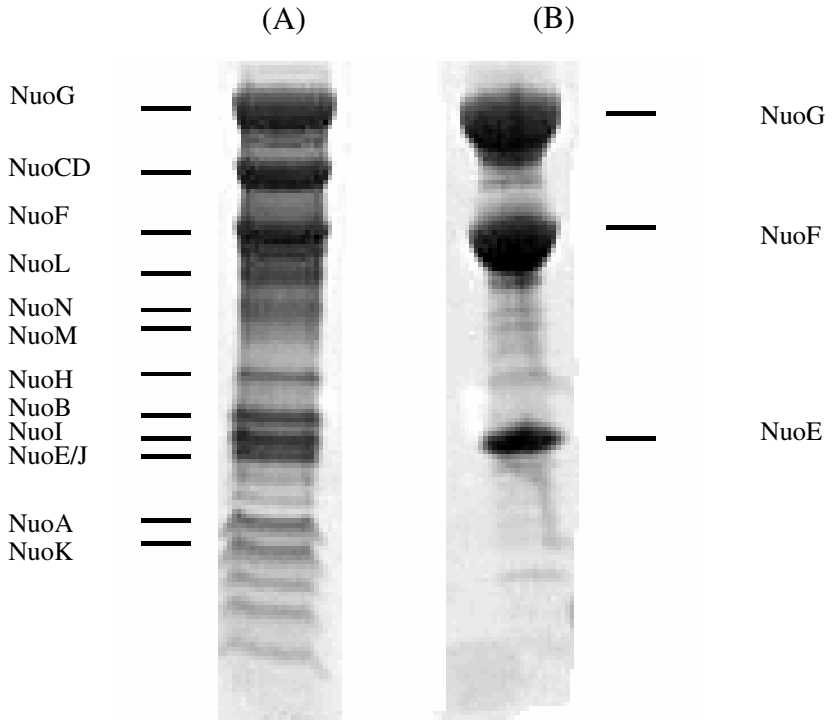

Figure 5.4: SDS-PAGE of the preparation of complex I (A) and NADH dehydrogenase fragment (B). The bands were assigned to the individual subunits due to their apparent molecular mass.

Name	purchased from	E_m vs. Ag/AgCl / mV	solvent
Ferrocenylmethyltrimethylammonium iodide	Strem Chemicals	607	ethanol
1,1‘-Ferrocenedicarboxylic acid	Fluka	436	ethanol
Potassiumhexacyanoferrate(II) trihydrate	Riedel-de Haen	212	H_2O
1,1‘-Dimethylferrocene	Aldrich	133	ethanol
Quinhydrone	Fluka	70	ethanol
Tetrachloro-1,4-benzoquinone	Aldrich	72	diethyl ether
N,N,N‘,N‘-Tetramethyl-p-phenylenediamine dihydrochloride	Fluka	62	H_2O
2,6-Dichlorophenolindophenol sodium salt hydrate	Biochemika	9	ethanol
Hexaammineruthenium(III)chloride	Aldrich	-8	H_2O
Anthraquinone-2-sulfonic acid sodium salt	Aldrich	-23	H_2O
1,4 Naphthoquinone hydrate	Aldrich	-63	ethanol
Anthraquinone	Aldrich	-108	ethanol
Duroquinone	Sigma	-198	ethanol
Menadione	Sigma	-220	acetone
2-Hydroxyl-1,4 naphthoquinone	Sigma	-333	ethanol
9,10-Antraquinone-2,6-disulfonic acid disodium salt	Sigma	-433	ethanol
Neutral Red	Sigma-Aldrich	-515	ethanol
Methyl viologen dichloride hydrate	Aldrich	-628	H_2O

Table 5.3: List of the mixture of mediators used for electrochemical approach

5. 2 Appendix of results and discussion

5.2.1 Appendix of role of phospholipids

DMPC / cm^{-1}	DMPC ^{13}C /cm^{-1}	DHPC D_{22} /cm^{-1}	DHPC D_{35} /cm^{-1}	Asolectin / cm^{-1}	CL / cm^{-1}	Assignments	Ref.
3600 sh	3587sh	3581 sh	3581 sh		3570	ν(O-H) free	
3367	3363	3377	3388	3313	3402	ν(O-H) hydrogen bonded	
3273 sh	3273sh	3259 sh	3265 sh		3280	ν(O-H)	
3035	3037	3037				$\nu(CH_3)_3N^+$	
				3008	3008	ν(C=C) olefinic	2,3
2956	2956	2960 w	2960 w	2954	2954	$\nu_{as}(CH_3)$	
2918	2918	2897 w	2897 w	2924	2924	$\nu_{as}(CH_2)_n$	
2873	2871			2868	2868	$\nu_s(CH_3)$	
2850	2850			2852	2854	$\nu_s(CH_2)_n$	
			2276			$\nu_{as}(CD_3)_3N^+$	
		2216	2216			$\nu_{as}(CD_2)_n$	9
		2190	2190			$\nu_{as}(CD_3)$	
		2102	2102			$\nu_s(CD_2)_n$	9
		2073	2073			$\nu_s(CD_3)$	
1736		1736	1736	1738	1739	ν(C=O) ester carbonyl	
	1697					$\nu(C^{13}=O)$	4
1655		1655	1655	1649	1655	δ(OH)	
1483 sh	1483 sh	1483				$\delta_{as}(N^+-CH_3)_3)$	
1468	1468			1466	1464	$\delta(CH_2)_n$ scissoring	
		1446	1452			$\delta(CD_2)_n$ scissoring	
1417	1417			1417		$\delta(\alpha-CH_2)$	
1377	1377			1377	1377	$\delta_s(CH_3)$ umbrella	
1342	1342					$\gamma_{wag}(CH_2)$ all-trans	
		1323 w	1323 w				
1275	1275			1277			
1240	1232	1246	1250	1227	1234	$\nu_{as}(PO_2^-)$	
1205							
1173		1182	1182	1178	1174	ν(C=O-OC)	5
	1163					$\nu(C^{13}=O-OC)$	5
	1153		1149		1140		
1090	1088	1086	1086	1084	1095	$\nu_s(PO_2^-)$	
1063	1065	1066	1066	1063	1068	ν(P-O-C)	6,7
	1053	1057					7
1020 w	1014 w	1014 w	1022				
					985 w	$\nu_s(PO_3^{2-})$	
968	969	969	964 w	974		$\nu_{as}(C-N^+(CH_3)_3)$	
956	955	955					
924	924	926	926			ν(PO-H)	10
			901				
876	877	874		860			
			859				
820	822	820	829	827	833	ν(P-O)	8
			810				

Table 5.4: Bands assignments of mid infrared absorbance spectra of isotopically labeled phosphatidylcholine variations, unlabeled phosphatidylcholine, asolectin and cardiolipin at room temperature. Assignments were primarily taken from the review of Lewis and McElhaney (1994). Further used references are added: 2: Mantsch et al., 1981; 3: Siminovitch et al., 1987; 4: Blume et al., 1988; 5: Hübner and Mantsch, 1991; 6: Goni and Arrondo, 1986, 7: Hübner et al., 1991; 8: Pohle et al., 1997; 9: Mendelsohn and Moore, 1998; 10: Désormeaux et al., 1992. Abbreviations: sh, shoulder; w, weak; DMPC, 1,2-dimyristoyl-*sn*-glycero-3-phosphatidylcholine (14:0); DHPC, 1,2-dihexanoyl-*sn*-glycero-3-phosphatidylcholine (6:0); CL, cardiolipin; ν: stretching; δ: deformation; γ: all-trans deformation.

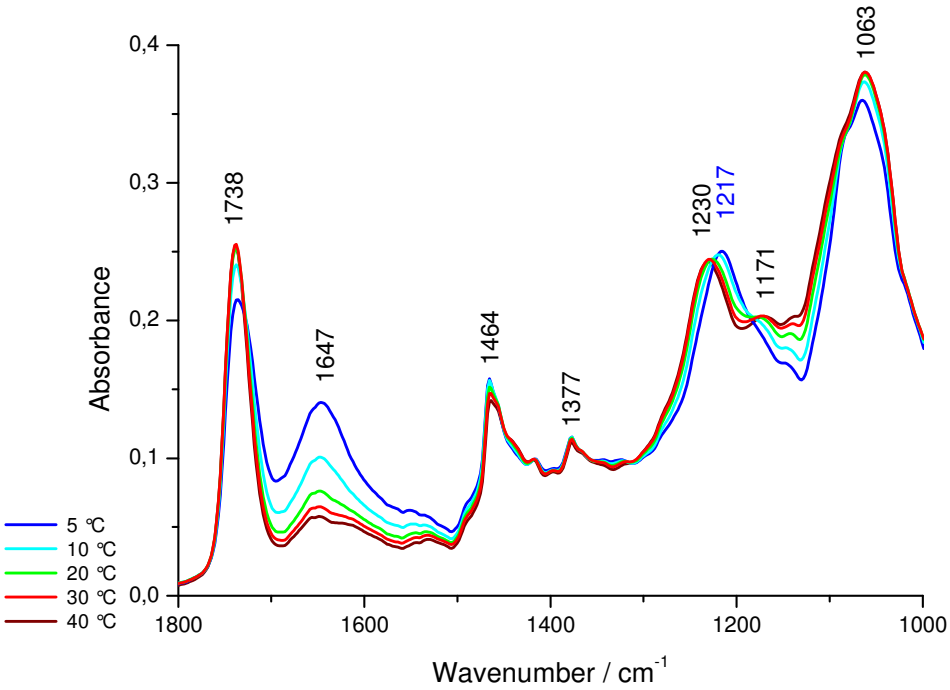

Figure 5.5: Temperature dependent ATR absorbance spectra of asolectin solved in H_2O. Line assignment: 5 °C blue, 10 °C cyan, 20 °C green, 30 °C red, 40 °C dark red.

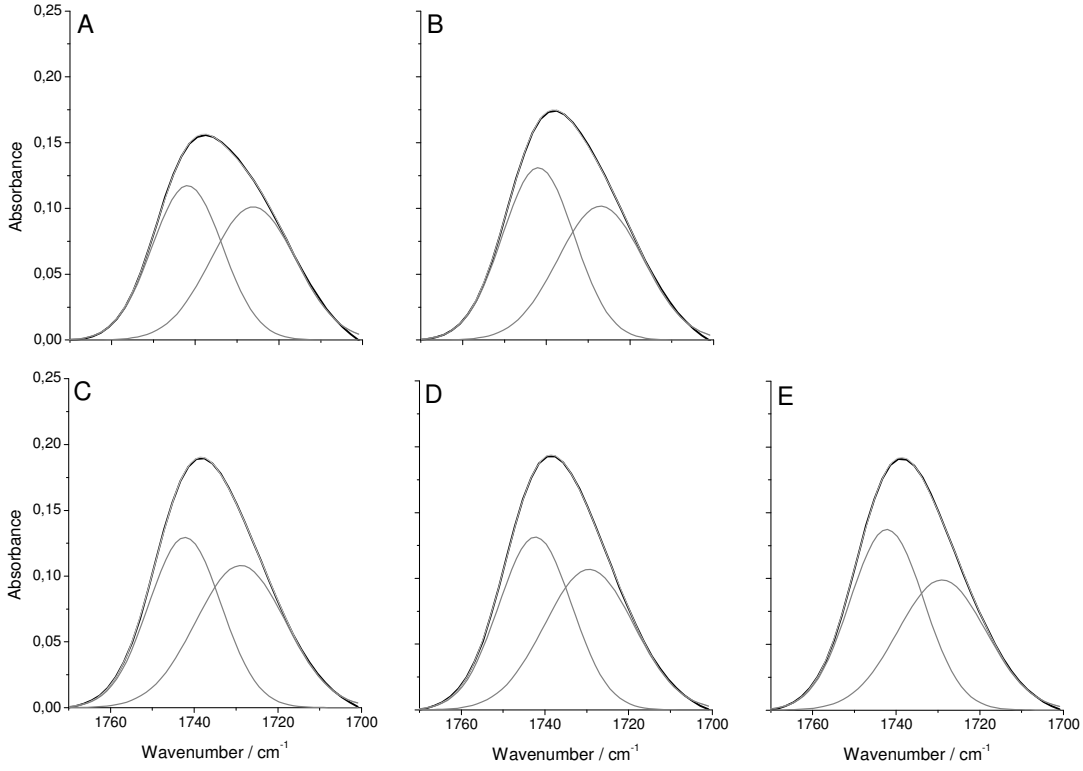

Figure 5.6: Deconvolution of the carbonyl stretching vibration of asolectin in D_2O as a function of temperature: A: 5 °C, B: 10 °C, C: 20 °C, D: 30 °C, E: 40 °C.

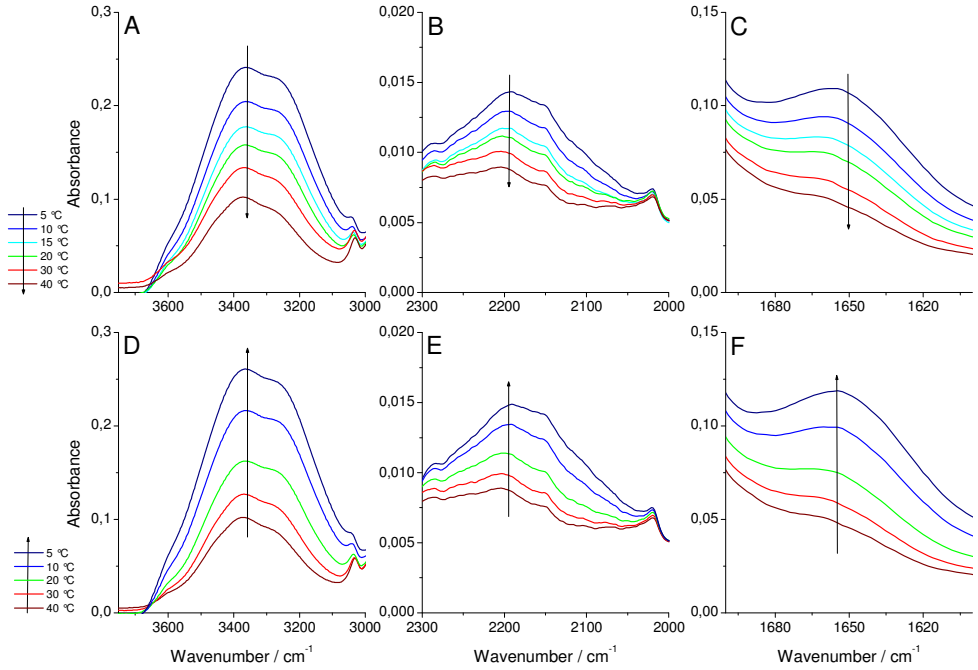

Figure 5.7: Enlarged view of the temperature dependent ATR absorbance spectra of the ν(OH) stretching vibration (A, D), the ν(HOH) assoziation mode (B,E) and δ(OH) bending vibration of phospatidylcholine.

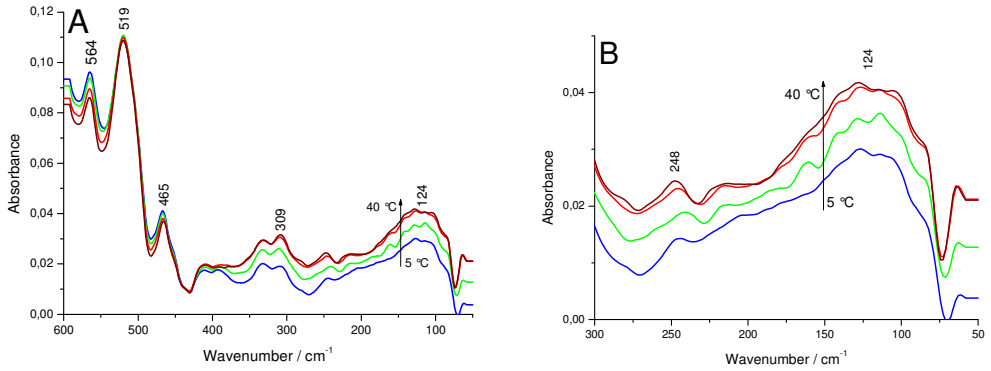

Figure 5.8: Far IR absorbance spectra of asolectin obtained on Vertex spectrometer. Line assignment: 5 °C blue, 20 °C green, 30 °C red, 40 °C dark red.

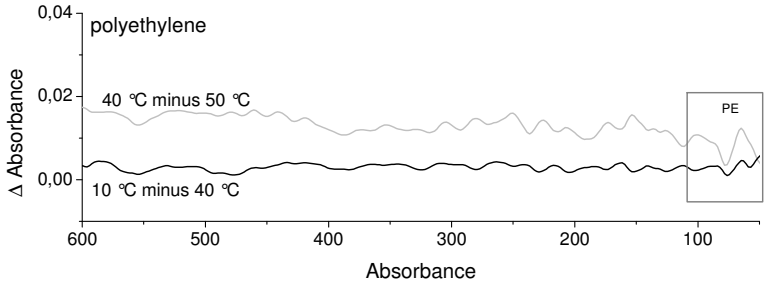

Figure 5.9: Far infrared difference spectra of polyethylene window (with kind permission from Youssef El Khoury, Institut de Chimie, Strasbourg)

5.2.2 Model compounds

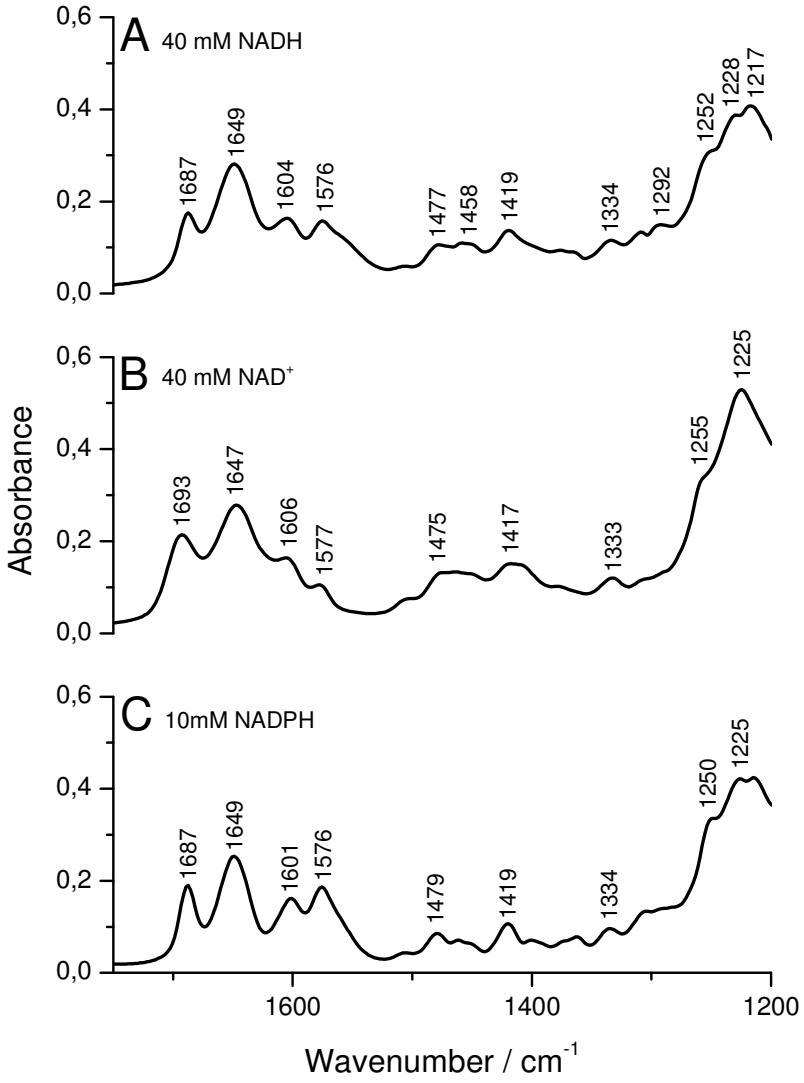

Figure 5.10: ATR FTIR absorbance spectra of nucleotides in 50 mM MES/NaoH, 50 mM NaCl, pH 6.

NADH	NADPH	NAD^+	Assignments
1687	1687	1693	ν(C=O) carbonyl carboxamide
1649	1649	1647	adenine ring
1604	1601	1606	adenine ring
1576	1576	1577	adenine ring
1545	1545		nicoinamide (C-N)
1477	1479	1475	adenine ring
1458			
1419	1419	1417	nicotinamide ν(C-N)
1334	1334	1333	adenine ring
1252	1250	1255	
1228	1225	1225	pyrophosphate ν(P=O)
1217			

Table 5.5: Tentative assignments of nucleotide vibrations.

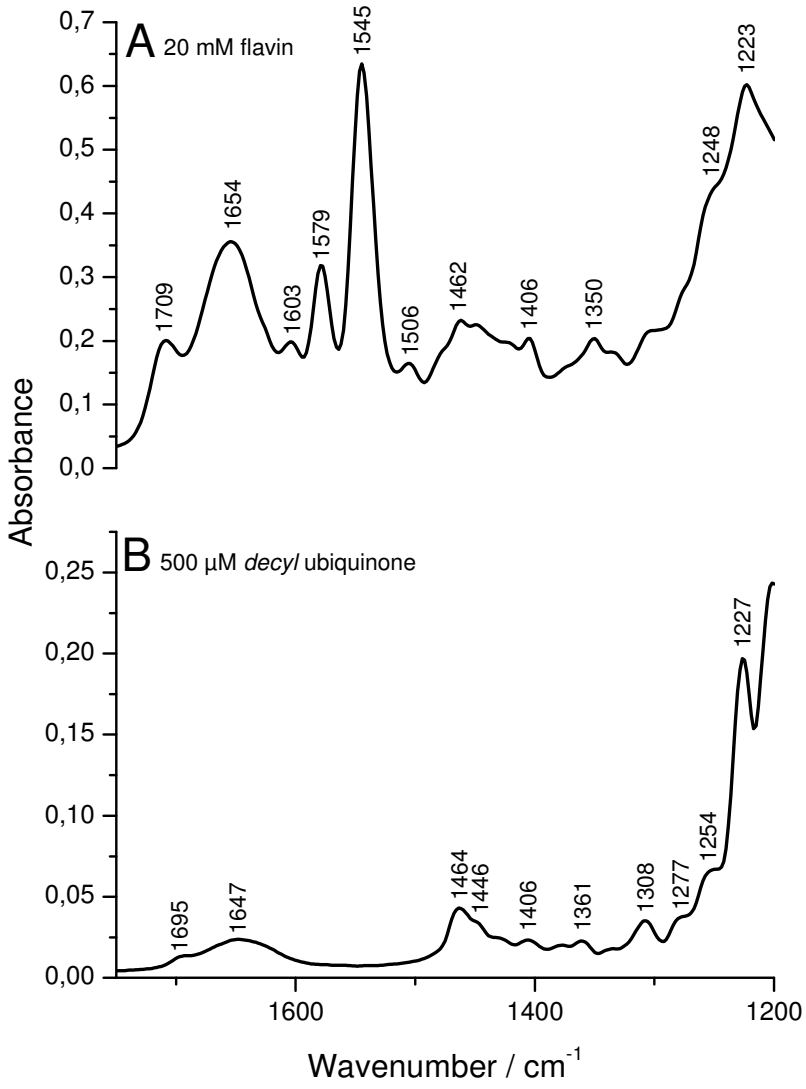

Figure 5.11: ATR FTIR absorbance spectra of (A) flavin and (B) decylubiquinone in 50 mM MES/NaOH, 50 mM NaCl, pH 6.

wavenumber / cm^{-1}	flavin (FAD)
1709	ν(C=O)
1654	
1603	ν(C-N)
1579	ν(C-N)
1545	ν(C=C)
1506	
1462	
1406	} isoalloxazine ring mode
1350	
1248	
1223	

Table 5.6: Tentative assignments of flavin.

5.2.3 Second derivative spectra of NADH dehydrogenase fragment and complex I

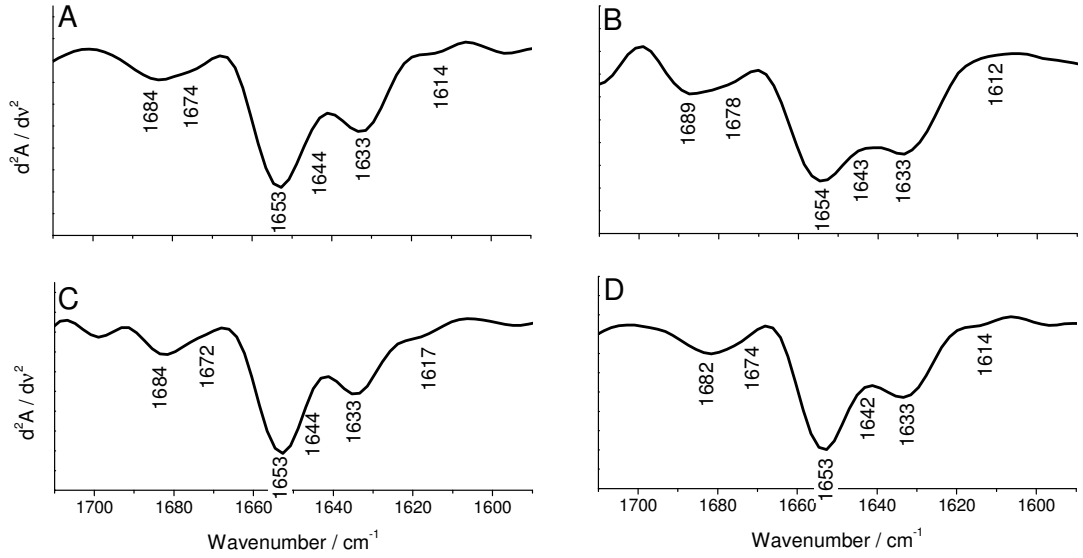

Figure 5.12: Second derivative spectra of the absorbance spectra of NADH dehydrogenase fragment (see Figure 3.2). Image (A) shows NDF alone, (B) upon NAD^+ binding, (C) upon NADH binding and (D) upon NADPH binding.

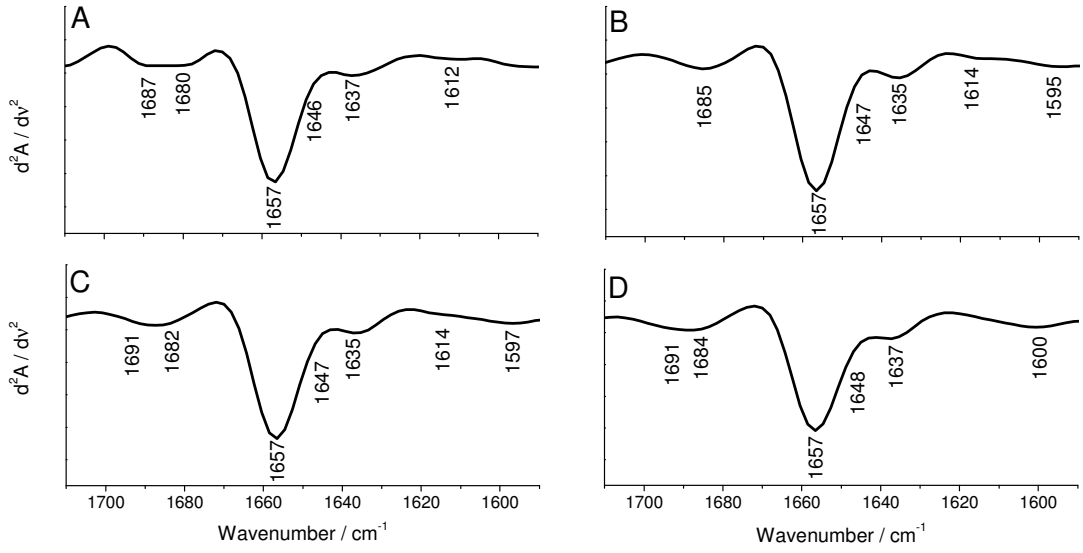

Figure 5.13: Second derivative spectra of the absorbance spectra of complex I (see Figure 3.3). Image (A) shows NDF alone, (B) upon NAD^+ binding, (C) upon NADH binding and (D) upon NADPH binding.

5.2.4 FTIR difference spectra upon nucleotide binding

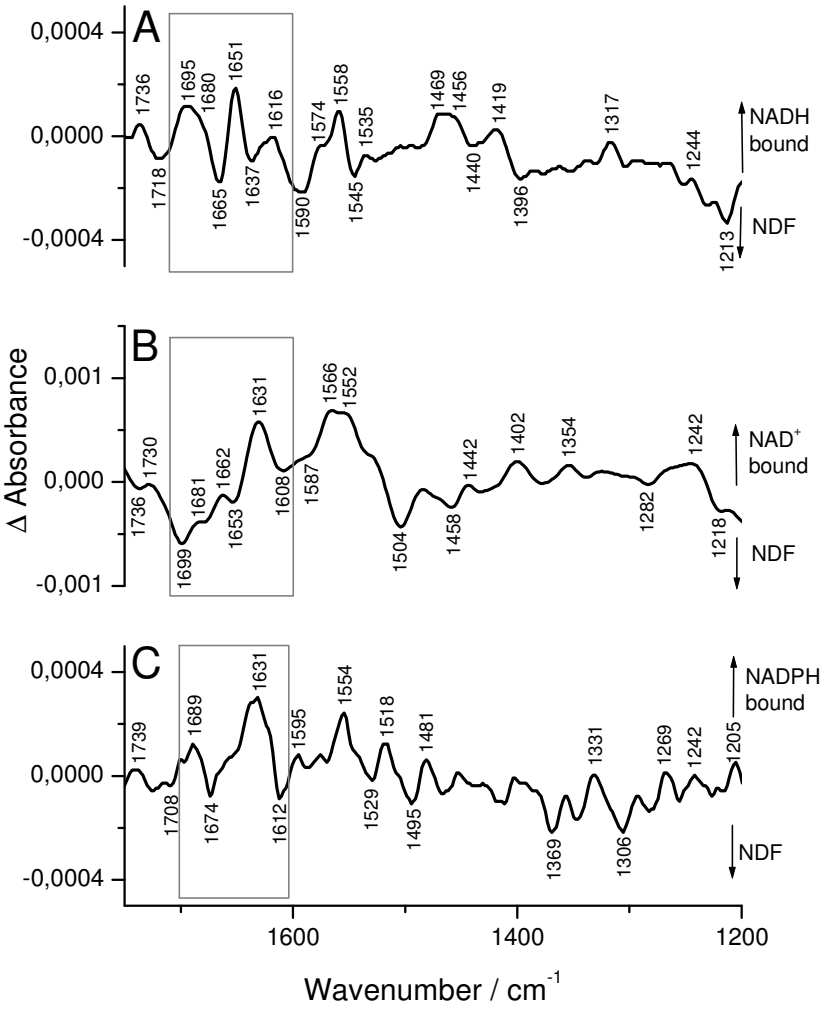

Figure 5.14: FTIR difference spectra obtained by subtracting the nucleotide bound NDF *minus* NDF. In (A) is shown the FTIR difference spectrum of NADH bound NDF, in (B) NAD^+ bound NDF and in (C) NADPH bound NDF. The amide I region 1700 to 1600 cm^{-1} is marked.

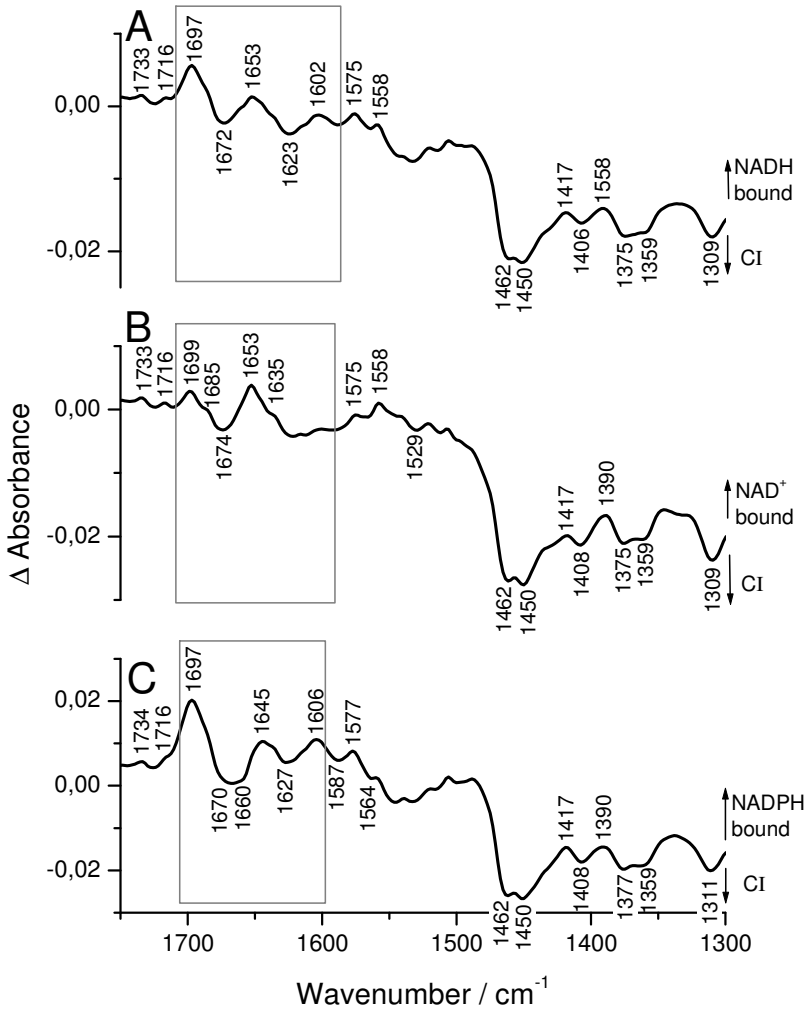

Figure 5.15: FTIR difference spectra obtained by subtracting the nucleotide bound complex I *minus* complex I. In (A) is shown the FTIR difference spectrum of NADH bound complex I, in (B) NAD^+ bound complex I and in (C) NADPH bound complex I. The amide I region from 1700 to 1600 cm^{-1} is marked.

5.2.5 Electrochemically induced FTIR difference spectra of buffer solution

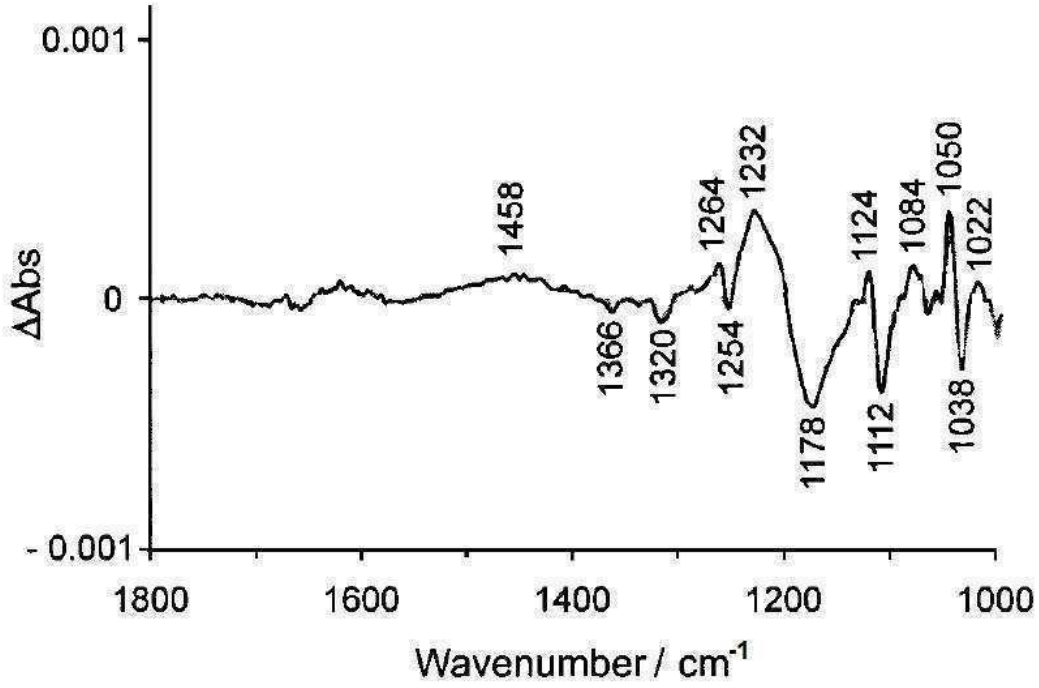

Figure 5.16: Oxidized *minus* reduced FTIR difference spectra from MES buffer (reprinted Hellwig et al., 2000)

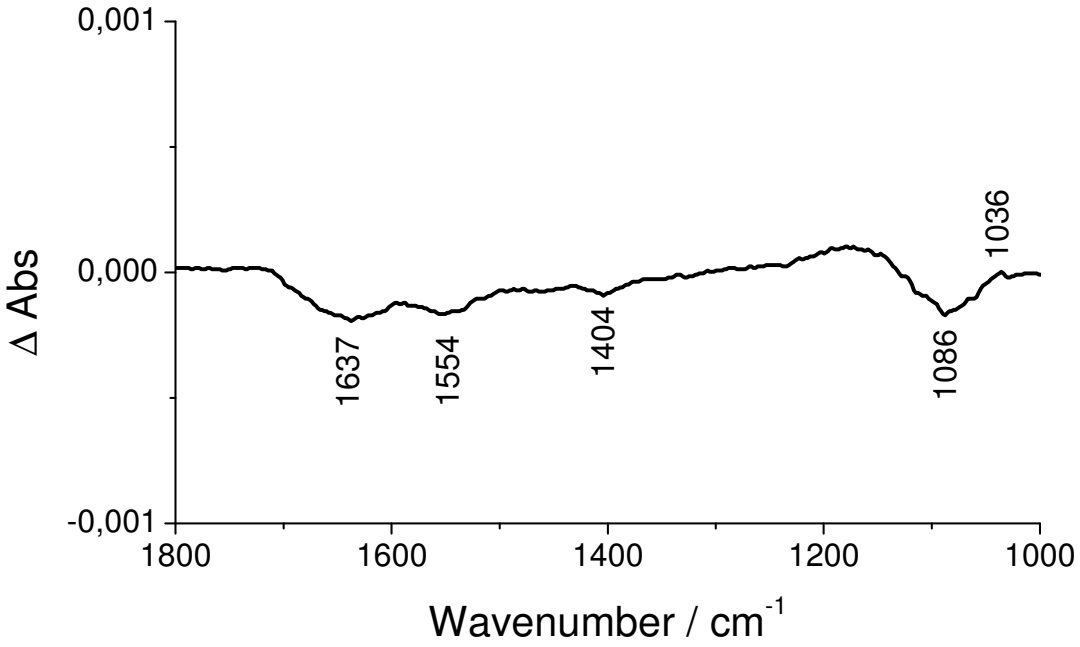

Figure 5.17: Oxidized *minus* reduced FTIR difference spectra from TRIS buffer (reprinted from Hielscher et al., 2009).

6 References

Akutsu, H. (1981) Direct determination by Raman scattering of the conformation of the choline group in phospholipids bilayer. *Biochemistry* **20**, 7359-7366.

Arora, S.K., Trivedi, T.R., Oza, A.T., Patel, V.A. (2001) IR spectroscopy of barium hydrogen phosphate. *Acta mater.* **49**, 2103-2107.

Arrondo J.L., Muga A., Castresana J., Goñi F.M. (1993) Quantitative studies of the structure of proteins in solution by Fourier-transform infrared spectroscopy. *Prog. Biophys. Mol. Biol.* **59**, 23-56.

Bandekar, J. (1992) Amide modes and protein conformation. *Biochem. Biophys. Acta* **1120**, 123-143.

Baranova, E. A., Holt, P., and Sazanov, L.A. (2007) Projection structure of the membrane domain of *Escherichia coli* respiratory complex I at 8 Å resolution. *J. Mol. Biol.* **366**, 140-154.

Bauscher, M. and Mäntele, W. (1992) Electrochemical and infrared-spectroscopic characterization of redox reactions of p-quinones. *J. Phys. Chem.* **96,** 11101-11108.

Bauscher, M., Nabedryk, E., Bagley, K., Breton, J., and Mäntele, W. (1990) Investigation of models for photosynthetic electron acceptors: Infrared spectroelectrochemistry of ubiquinone and its anions. *FEBS Lett.* **261**, 191-195.

Baymann, F., Robertson, D.E., Dutton, P.L., and Mäntele, W. (1999) Electrochemical and spectroscopic investigations of the cytochrome bc_1 complexes from *Rhodobacter capsulatus. Biochemistry* **38**, 13188-13199.

Belogrudov, G., and Hatefi, Y. (1994) Catalytic sector of complex I (NADH:ubiquinone oxidoreductase): subunit stoichiometry and substrate-induced conformation changes. *Biochemistry* **33**, 4571-4576.

Beck, M., Siebert, F., Sakmar, T.P. (1998) Evidence for the specific interaction of a lipid molecule with rhodopsin which is altered in the transition to the active state metarhodopsin II, *FEBS Lett.* **436**, 304-308.

Behr, J., Hellwig, P., Mäntele, W., and Michel, H. (1998) Redox dependent changes at the heme propionates in cytochrome *c* oxidase from *Paracoccus denitrificans*: direct evidence from FTIR difference spectroscopy in combination with heme propionate ^{13}C labeling. *Biochemistry* **37**, 7400-7406.

Berry, E.A., Guergova-Kuras, M., Huang, L., and Crofts, A.R. (2000) Structure and function of cytochrome *bc* complexes. *Annu. Rev. Biochem.* **69**, 1005-1075.

Berry, E.A., Huang, L.S., Saechao, L.K., Pon, N.G., Valkova-Valchanova, M., and Daldal, F. (2004) X-ray structure of *Rhodobacter capsulatus* cytochrome bc_1: comparison with its mitochondrial and chloroplast counterparts. *Photosynth. Res.* **81**, 251-275.

Berthomieu C., Boussac A., Mäntele W., Breton J., Nabedryk E. (1992) Molecular changes following oxidoreduction of cytochrome b559 characterized by Fourier transform infrared difference spectroscopy and electron paramagnetic resonance: photooxidation in photosystem II and electrochemistry of isolated cytochrome b559 and iron protoporphyrin IX-bisimidazole model compounds. *Biochemistry* **31**, 11460-71.

Binder, H. (2007) Water near lipid membranes as seen by infrared spectroscopy. *Eur. Biophys. J.* **36**, 265-279.

Blume, A., Hübner, W., Messner, G. (1988) Fourier Transform Spectroscopy of ^{13}C=O-Labeled Phospholipids Hydrogen Bonding to Carbonyl Groups. *Biochemistry* **27**, 8239-8249.

Bogdanov, M., and Dowhan, W. (1999) Lipid-assisted protein folding. *J. Biol. Chem.* **274**, 36827-36830.

Bogdanov, M., Sun, J., Kaback, H.R., and Dowhan, W. (1996) A Phospholipid Acts as a Chaperone in Assembly of a Membrane Transport Protein. *J. Biol. Chem.* **271**,11615-11618.

Boggs, J.M. (1987) Lipid intermolecular hydrogen bonding: influence on structural organization and membrane function. *Biochim. Biophys. Acta* **906**, 353-404.

Böttcher B., Scheide, D., Hesterberg. M. Nagel-Steger, L., and Friedrich, T. (2002) A novel, enzymatically active conformation of the NADH:ubiquinone oxidoreductase (complex I). *J. Biol. Chem.* **277**, 17970-

Brandt, U. (2006) Energy converting NADH:quinine oxidoreductase (complex I). *Annu. Rev. Biochem.* **75**, 69-92.

Brandt, U. (1997) Proton-translocation by membrane-bound NADH:ubiquinone-oxidoreductase (complex I) through redox-gated ligand conduction. *Biochim. Biophys. Acta* **1318**, 79-91.

Brandt, U., Kerscher, S., Dröse, S., Zwicker, K., and Zickermann, V. (2003) Proton pumping by NADH:ubiquinone oxidoreductase. A redox driven conformational change mechanism? *FEBS Lett.* **545**, 9-17.

Breton, J., Burie, J.R., Berthomieu, C., Berger, G., and Nabedryk, E. (1994) The binding sites of quinines in photosynthetic bacterial reaction centers investigated by light-induced FTIR difference spectroscopy: assignment of the QA vibrations in *Rhodobacter*

phaeroides using ^{18}O- or ^{13}C-labeled ubiquinone and vitamin K1, *Biochemistry* **33**, 4953-4965.

Breyton, C. (2000) The cytochrome b_6f complex: structural studies and comparison with the bc_1 complex. *Biochem. Biophys. Acta* **1459**, 467-474.

Brubach, J.-B., Mermet, A., Filabozzi, A., Gerschel, A., Roy, P. (2005) Signatures of the hydrogen bonding in the far infrared bands of water. *J. Chem. Phys.* **122**, 184509.

Bungert, S., Krafft, B., Schlesinger, R., and Friedrich, T. (1999) One-step purification of the NADH dehydrogenase fragment of the *Escherichia coli* complex I by means of *Strep*-tag affinity chromatography, *FEBS Lett.* **460**, 207-211.

Burie, J.-R:, Boussac, A., Boullais, C., Berger, G., Mattioli, T., Mioskowski, C., Nabedryk, E., and Breton, J. (1995) FTIR spectroscopy of UV-generated quinine radicals: Evidence for an intramolecular hydrogen atom transfer in ubiquinone, naphthoquinone, and plastoquinone. *J. Phys. Chem.* **99**,4059-4070.

Byler D.M. and Susi, H. (1986) Examination of the secondary structure of proteins by deconvolved FTIR spectra. *Biopolymers* **25**, 469-487.

Carman, G.M., and Henry, S.A. (1989) Phospholipid biosynthesis in yeast. *Annu. Rev. Biochem.* **58**, 635-669.

Carroll, J., Fearnley, I.M., Shannon, R.J:, Hirst, J., and Walker, J.E. (2003) Analysis of the subunit composition of complex I from bovine heart mitochondria. *Mol. Cell Proteomics* **2**, 212-224.

Casal, H.L. and McElhaney, R.N. (1990) Quantitative Determination of Hydrocarbon Chain Conformational Order in Bilayers of Saturated Phosphatidylcholines of Various Chain Lengths by Fourier Transform Infrared Spectroscopy. Biochemistry 29, 5423-5427.

Cecchini, G. (2003) Function and Strucutre of complex II of the respiratory chain. *Annu. Rev. Biochem.* **72**, 77-109.

Choi, S., Spiro, T.G., Langry, K.C., Smith, K.M., Budd, D.L., and La Mar, G.N. (1982) Structural correlations and vinyl influences in resonance Raman spectra of protoheme complexes and proteins. *J. Am. Chem. Soc.* **104**, 4345-4357.

Crofts, A.R. (2004) The cytochrome bc_1 complex: function in the context of structure. *Annu. Rev. Physiol.* 66, 689-733.

Crofts, A.R. and Meinhardt, S.W. (1982) A Q-cycle mechanism for the cyclic electron-transfer chain of *Rhodopseudomonas sphaeroides. Biochem. Soc. Trans.* **10**, 201-203.

Crofts, A.R. and Wang, Z. (1989) How rapid are the internal reactions of the UQH2:cyt c_2 oxidoreductase? *Photosynth. Res*. **22**, 69-87.

Colbeau, A., Nachbaur, J., Vignais, P.M. (1971) Enzymac characterization and lipid composition of rat liver subcellular membrane. Biochim. Biophys. Acta 249, 462.

Dailey, H. A., Finnegan, M. G. und Johnson, M. K. (1993) Human Ferrochelatase Is an Iron-Sulfur Protein. *Biochemistry* **33**, 403-407.

Daum, G. (1985) Lipids of mitochondria. *Biochim. Biophys. Acta* **822**, 1-42.

Désormeaux, A., Laroche, G., Bougis, P.E., and Pézolet, M. (1992) Characterization by Infrared Spectroscopy of the Interaction of a Cardiotoxin with Phosphatidic Acid and with Binary Mixtures of Phosphatidic Acid and Phosphatidylcholine. *Biochemistry* **31**, 12173-12182.

de Vries, S., Berden, J.A., and Slater, E.C. (1980) Properties of a semiquinone anion located in the QH_2:cytochrome *c* oxidoreductase segment of the mitochondrial respiratory chain. *FEBS Lett.* **122**, 143-148.

de Vries, D., and Marres, S.A.M. (1987) The mitochondrial respiratory chain of yeast. Structure and biosynthesis and the role of cellular metabolism. *Biochim. Biophys. Acta* **895**, 205-239.

de Vrije, T., de Swart, R.L.., Dowhan, W., Tommassen, J., and de Kruiff, B. (1988) Phosphatidylglycerol is involved in protein translocation across *Escherichia coli* inner membranes. *Nature* **334**, 173-175.

Djafarzadeh, R., Kerscher, S., Zwicker, K., Radermacher, M., Lindahl, M., Schägger, H., and Brandt, U. (2000) Biophysical and structural characterization of proton-translocating NADH-dehydrogenase (complex I) from the strictly aerobic yeast *Yarrowia lipolytica. Biochim. Biophys. Acta* **1459**, 230-238.

Dong A., Huang P., Caughey W.S. (1990) Protein secondary structures in water from second-derivative amide I infrared spectra. *Biochemistry* **29**, 3303-3308.

Dörr, S., Schade, U., and Hellwig, P. (2008) Far infrared spectroscopy on hemoproteins: A model compound study from 1800-1000 cm^{-1}. *Vib. Spectrosc.* **47**, 59-65.

Doweidar, H., Moustafa, Y.M., El-Egili, K., Abbas, I. (2005) Infrared spectra of Fe_2O_3-PbO-P_2O_5 glasses. *Vibrational Spectroscopy* **37**, 91-96.

Dowhan, W. (1997) Molecular basis for membrane phospholipid diversity: why are there so many lipids? *Annu. Rev. Biochem.* **66**, 199-232.

Dreher, C., Prodöhl, A., Hielscher, R., Hellwig, P., and Schneider, D. (2008) Multiple Step Assembly Of The Transmembrane Cytochrome b_6, *J. Mol. Biol.* **382**, 1057-1085.

Dröse, S., Zwicker, K., Brandt, U. (2002) Full recovery of the NADH:ubiquinone qctivity of complex I (NADH:ubiquinone oxidoreductase) from *Yarrowia lipolytica*. *Biochim. Biophys. Acta* **1556**, 65-72.

Dudkina, N.V., Holger, E., Wilko, K., Boekema, E. J., and Braun, H.-P., (2005) Structure of a mitochondrial supercomplex formed by respiratory-chain complexes I and III. *Proc. Natl. Acad. Sci. USA* **102**, 3225-3229.

Durig, J.R., Jin, Y., Phan, H.V., Liu, J., Durig, D.T. (2002) Far-infrared Spectra, Conformational Stability, Barriers to Internal Rotation, *Ab initio* Calculations, r_0 Structural Parameters, and Vibrational Assignments of Ethyl Methyl Ether. *Structural Chemistry* **12** (1), 1-26.

Dutton, P.L. (1978) Redox potentiometry: Determination of midpoint potentials of oxidation-reduction components of biological electron transfer systems. *Meth. Enzym.* LIV, Academic Press, 411-435.

Dutton, P. L., Moser, C.C., Sled, V.D., Daldal, F., and Ohnishi, T. (1998) A reductant-induced oxidation mechanism for complex I. *Biochim. Biophys. Acta* **1364**, 245-257.

Dzafić E., Klein O., Screpanti E., Hunte C., Mäntele W. (2009) Flexibility and dynamics of NhaA Na+/H+-antiporter of Escherichia coli studied by Fourier transform infrared spectroscopy. *Spectrochim. Acta A Mol. Biomol. Spectrosc.* **72**, 102-109.

Ebbinghaus, S., Kim, S.J., Heyden, M., Yu, X., Heugen, U., Gruebele, M., Leitner, D.M., and Havenith, M. (2007) An extended dynamical hydration shell around proteins. *PNAS* **104** (52), 20749-20752.

Eibl, H. (1984) Phospholipids as Functional Constituents of Biomembranes. *Angew. Chemie Int. Ed.* **23**, 257-328.

El Khoury, Y., and Hellwig, P. (2009) Infrared spectroscopic characterization of copper-polyhistidine from 1800 to 50 cm^{-1}: model systems for copper coordination. *J. Biol. Inorg. Chem.* **14**, 23-34.

Engelhard, M., Gerwert, K., Hess, B., Kreutz, W., Siebert, F. (1985) Light-driven protonation changes of internal aspartic acids of bacteriorhodopsin: an investigation by static and time-resolved infrared difference spectroscopy using [4-^{13}C]aspartic acid labeled purple membrane. *Biochemistry* **24**, 400-407.

Eyster, J.M., and Prohofsky, E.W. (1977) Soft modes and the structure of the DNA double helix. *Phys. Rev. Lett.* **38**, 371-373.

Fabian, H., and Mäntele, W. (2002) Infrared Spectroscopy of Proteins. Handbook of Vibrational Spectroscopy. J.M.C.a.P.R. Griffiths. Chichester, John Wiley & Sons Ltd. 5, 3399-3425.

Flemming, D., Hellwig, P. and Friedrich, T. (2003a) Involvement of tyrosines 114 and 139 of subunit NuoB in the proton pathway around cluster N2 in *Escherichia coli* NADH:ubiquinone oxidoreductase. *J. Biol. Chem.* **278**, 3055-3062.

Flemming, D., Schlitt, A., Spehr, V., Bischof, T., and Friedrich, T. (2003b) Iron-sulfur cluster N2 of the *Escherichia coli* NADH:ubiquinone oxidoreductase (complex I) is located on subunit NuoB. *J. Biol. Chem.* **278**, 47602-47609.

Flemming, D., Stolpe, S., Schneider, D., Hellwig, P., and Friedrich, T. (2005) A possible role for iron-sulfur cluster N2 in proton translocation by the NADH:ubiquinone oxidoreductase (complex I). *J. Mol. Microbiol. Biotechnol.* **10**, 208-222.

Flemming, D., Hellwig, P., Lepper, S., Kloer, D.P., and Friedrich, T. (2006) Catalytic importance of acidic amino acids on subunit NuoB of the *Escherichia coli* NADH:ubiquinone oxidoreductase (complex I). *J. Mol. Chem.* **281**, 24781-24789.

Frew, J.E., and Hill, H.A.O. (1988) Direct and indirect electron transfer between electrodes and redox proteins. *Eur. J. Biochem.* **172**, 261-269.

Friedrich, T. (1998) The NADH:ubiquinone oxidoreductase (complex I) from *Escherichia coli*. *Biochim. Biophys. Acta* **1364**, 134-146.

Friedrich, T. (2001) Complex I: a chimaera of a redox and conformation-driven proton pump? *J. Bioenerg. Biomembr.* **33**, 169-177.

Friedrich, T., and Böttcher, B. (2004) The gross structure of the respiratory complex I: a Lego system. *Biochim. Biophysa. Acta* **1608**, 1-9.

Friedrich, T., Brors, B., Hellwig, P., Kintscher, L., Rasmussen, T., Scheide, D., Schulte, U., Mäntele, W., Weiss, H. (2000) Characterization of two novel redox groups in the respiratory NADH:ubiquinone oxidoreductase (complex I). *Biochim. Biophys. Acta* **1459**, 305-309.

Friedrich, T., Hofhaus, G., Ise, W., Nehls, U., Schmitz, B., and Weiss, H. (1989) A small isoform of NADH:ubiquinone oxidoreductase (complex I) without mitochondrially encoded subunits is made in chloramphenicol-treated *Neurospora crassa*, *Eur. J. Biochem.* **180**, 173-180.

Friedrich, T., Pohl, T., and Hellwig, P. (2007) The bacterial NADH:ubiquinone oxidoreductase: Molecular biology, structure, FT-IR spectroscopy and mechanism.

Transworld Research Network 37/661 in Complex I and Alternative Dehydrogenase (Ed. M.I. Gonzalez Siso), 1-31

Friedrich, T., and Scheide, D. (2000) The respiatory complex I of bacteria, archaea and eukarya and ist module common with membrane-bound multisubunit hydrogenases. *FEBS Lett.* **479**, 1-5.

Friedrich, T., Steinmüller, K., and Weiss, H. (1995) The proton-pumping respiratory complex I of bacteria and mitochondria and ist homologue in chloroplasts. *FEBS Lett.* **367**, 107-111.

Friedrich, T., and Weiss, H. (1997) Modular evolution of the respiratory NADH:ubiquinone oxidoreductase and the origin of its modules. *J. Theor. Biol.* **187**, 529-540.

Fringeli, U.P., Goette, J., Reiter, G., Siam, M., Baurecht, D. (1998) Structural investigations of oriented membrane assemblies by FTIR-ATR spectroscopy. *Fourier Transform Spectroscopy* **430**, 729-747.

Fyfe, P.K., Isaacs, N.W., Cigdell, R.J., and Jones, M.R. (2002) Disruption of a specific molecular interaction with a bound lipid affects the thermal stability of the purple bacterial reaction centre. *Biochim. Biophys. Acta* **1608**, 11-22.

Gagné J., Stamatatos L., Diacovo T., Hui S.W., Yeagle P.L., Silvius J.R. (1985) Physical properties and surface interactions of bilayer membranes containing N-methylated phosphatidylethanolamines. *Biochemistry* **24**, 4400-4408.

Galkin, A.S., Grivennikova, V.G., and Vinogradov, A.D. (1999) $H^+/2e^-$ stoichiometry in NADH-quinone reductase reactions catalyzed by bovine heart submitochondrial particles. *FEBS Lett.* **451**, 157-161.

Gao, X., Wen, X., Esser, L., Quinn, B., Yu, L., Yu, C.-A., and Xia, D. (2003) Structural basis for the quinone reduction in the bc_1 complex: A comparative analysis of crystal structures of mitochondrial cytochrome bc_1 with bound substrate and inhibitors at the Q_i site. *Biochemistry* **42**, 9067-9080.

Garczarek, F. and Gewert, K. (2006) Functional water in intraprotein proton transfer monitored by FTIR difference spectroscopy. *Nature* **439**, 109-112.

Garczarek, F., Wang, J., El-Sayed, M.A., and Gerwert, K. (2004) The Assignment of the Different Infrared Continuum Absorbance Changes Observed in the 3000-1800 cm^{-1} Region during the Bacteriorhodopsin Photocycle. *Biophys. J.* **87**, 2676-2682.

Gishla, S. (1980) Fluorescence and Optical Characteristics of Reduced Flavin and Flavoproteins. *Methods Enzymol.* **66**, 360-373.

Gomez, B., and Robinson, N.C. (1999) Phospholipase digestion of bound cardiolipin reversibly inactivates bovine cytochrome bc_1. *Biochemistry* **38**, 9031-9038.

Goñi, F.M., Arrondo, J.L.R. (1986) A Study of Phospholipid Phosphate Groups in Model Membranes by Fourier Transform Infrared Spectroscopy. *Faraday Discuss. Chem. Soc.* **81**, 117-126.

Goormaghtigh E., Cabiaux V., Ruysschaert J.M. (1994a) Determination of soluble and membrane protein structure by Fourier transform infrared spectroscopy. I. Assignments and model compounds. *Subcell. Biochem.* **23**, 329-62.

Goormaghtigh E., Cabiaux V., Ruysschaert J.M. (1994b) Determination of soluble and membrane protein structure by Fourier transform infrared spectroscopy. II. Experimental aspects, side chain structure, and H/D exchange. *Subcell. Biochem.* **23**, 363-403.

Goormaghtigh E., Cabiaux V., Ruysschaert J.M. (1994c) Determination of soluble and membrane protein structure by Fourier transform infrared spectroscopy. III. Secondary structures. *Subcell. Biochem.* **23**, 405-450.

Goormaghtigh, E., Raussens, V., and Ruysschaert, J.-M. (1999) Attenuated total reflection infrared spectroscopy of proteins and lipids in biological membranes. *Biochim. Biophys. Acta* **1422**, 105-185.

Gornall, A.G., Bardawill, C.J., and David, M.M., (1949) Determination of serum proteins by means of the biuret reaction, *J. Biol. Chem.* **177**, 751-766.

Gregory R.B., Rosenberg A. (1986) Protein conformational dynamics measured by hydrogen isotope exchange techniques. *Methods Enzymol.* **131**, 448-508.

Grigorieff, N. (1999) Structure of the respiratory NADH:ubiquinone oxidoreductase. *Curr. Opin. Struct. Biol.* **9**, 476-483.

Guenebaut, V., Schlitt, A., Weiss, H., Leonard, K., and Friedrich, T. (1998) Consistent structure between bacterial and mitochondrial NADH:ubiquinone oxidoreductase (complex I). *J. Mol. Biol.* **276**, 105-112.

Guenebaut, V., Vincentelli, R., Mills, D., Weiss, H., and Leonard, K. (1997) Three-dimensional structure of NADH-dehydrogenase from *Neurospora crassa* by electron microscopy and conical tilt reconstruction. *J. Mol. Biol.* **265**, 409-418.

Haines, T.H., and Dencher, N.A. (2002) Cardiolipin: a proton trap for oxidative phosphorylation. *FEBS Lett.* **528**, 35-39.

Harrick, N.J. (1967) Internal Reflection Spectroscopy. John Wiley & Sons, New York.

Hellwig, P., Mogi, T., Tomson, F.L., Gennis, R.B., Iwata, J., Miyoshi, H., and Mäntele, W. (1999) Vibrational modes of ubiquinone in cytochrome bo_3 from *Escherichia coli* identified by Fourier transform infrared difference spectroscopy and specific ^{13}C labeling. *Biochemistry* **38**, 14683-14689.

Hellwig, P., Pfitzner, U., Behr, J., Rost, B., Pesavento, R.P., Donk, W.V., Gennis, R.B., Michel, H., Ludwig, B., Mäntele, W. (2002) Vibrational modes of tyrosine in cytochrome *c* oxidase from *Paracoccus dentrificians*: FTIR and electrochemical studies of Tyr-D4-labeled and on Tyr280His and Tyr35Phe mutant enzymes. *Biochemistry* **41**, 9116-9125.

Hellwig, P., Scheide, D., Bungert. S., Mäntele, W., and Friedrich, T. (2000) FT-IR spectroscopic characterization of NADH:ubiquinone oxidoreductase (complex I) from *Escherichia coli*: oxidation of FeS cluster N2 os coupled with the protonation of an aspartate and glutamate side chain, *Biochemistry* **39**, 10884-10891.

Hellwig, P., Stolpe. S., and Friedrich, T. (2004) Fourier Transform Infrared Spectroscopic Study on the Conformational Reorganization in *Escherichia coli* Complex I Due to Redox-Driven Proton Translocation, *Biopolymer* **74**, 69-72.

Heugen, U., Schwaab, G., Bründermann, E., Heyden, M., Yu, X., Leitner, D.M., Havenith, M. (2006) Solute-induced retardation of water dynamics probed directly by terahertz spectroscopy. *PNAS* **103** (33), 12301-12306.

Hielscher, R., Wenz, T., Stolpe, S., Hunte, C., Friedrich, T., Hellwig, P. (2006) Monitoring redox-dependent contribution of lipids in Fourier transform infrared difference spectra of complex I from *Escherichia coli*. *Biopolymers* **82**, 291-294.

Hienerwadel, R., Boussac, A., Breton, J., Diner, B.A., and Berthomieu, C. (1997) Fourier transform infrared difference spectroscopy of photosystem II tyrosine D using site-directed mutagenesis and specific isotope labeling. *Biochemistry* **36**, 14712-14723.

Hinchliffe, P., Carroll, J., and Sazanov, L.A. (2006) Identification of a novel subunit of respiratory complex I from *Thermus thermophilus*. *Biochemistry* **45**, 4413-4420.

Hinchliffe, P., and Sazanov, L.A. (2005) Organization of iron-sulfur clusters in respiratory complex I. *Science* **309**, 771-774.

Hirschmann, H. (1960) *J. Biol. Chem.* **235**, 2762.

Hirst, J. (2005) Energy transduction by respiratory complex I- an evaluation of current knowledge. *Biochem. Soc. Trans.* **33**, 525-529.

Hirst, J., Carroll, J., Fearnley, I.M., Shannon, R.J., and Walker, J.E. (2003) The nuclear encoded subunits of complex I from bovine heart mitochondria. *Biochim. Biophys. Acta* **1604**, 135-150.

Hofhaus, G., Weiss, H., and Leonhard, K. (1991) Electron microscopic analysis of the peripheral and membrane parts of mitochondrial NADH dehydrogenase (complex I). *J. Mol. Biol.* **221**, 1027-1043.

Holt, P.J., Morgan, D.J., and Sazanov, L.A. (2003) The location of NuoL and NuoM subunits in the membrane domain of the *Escherichia coli* complex I: implications for the mechanism of proton pumping. *J. Biol. Chem.* **278**, 43114-43120.

Hübner, W. and Mantsch, H.H. (1991) Orientation of specifically $^{13}C{=}O$ labeled phosphatidylcholine multilayers from polarized attenuated total reflection FT-IR spectroscopy. *Biophys. J.* **59**, 1261-1272.

Hübner, W., Mantsch, H.H., and Kates, M. (1991) Intramolecular hydrogen bonding in cardiolipin. *Biochim. Biophys. Acta* **1066**, 166-174.

Hunte, C., Koepke, J., Lange, C., Roßmanith, T., and Michel, H. (2000) Structure at 2.3 Å resolution of the cytochrome bc_1 complex from yeast *Saccharomyces cerevisiae* co-crystallized with an antibody F_v fragment. *Structure* **8**, 669-684.

Huang, L.-S., Cobessi, D., Tung, E.Y., and Berry, E.A. (2005) Binding of the respiratory chain inhibitor antimycin to the mitochondrial bc1 complex: A new crystal structure reveals an altered intramolecular hydrogen-bonding pattern. *J. Mol. Biol.* **351**, 573-597.

Hunte, C., and Richers, S. (2008) Lipids and membrane protein structures. *Curr. Opi. Struc. Biol.* **18**, 406-411.

Isele, J., Sakmar, T.P., Siebert, F. (2000) Rhodopsin activation affects the environment of specific neighboring phospholipids: an FTIR spectroscopic study. *Biophys. J.* **79**, 3063-3071.

Iwaki, M., Giotta, L., Akinsiku, A.O., Schägger, H., Fisher, N., Breton, J., Rich, P.R. (2003) Redox-induced transitions in bovine cytochrome bc(1) complex studied by perfusion-induced ATR-FTIR spectroscopy. *Biochemistry* **42**, 11109-11119.

Iwaki, M., Osyczka, A., Moser, C.C., Dutton, P.L., and Rich, P.R. (2004a) ATR-FTIR spectroscopy studies of ion-sulfur protein and cytochrome c_1 in the *Rhodobacter capsulatus* cytochrome bc_1 complex, *Biochemistry* **43**, 9477-9486.

Iwaki, M., Punstinen, A., Wikström, M., Rich, P.R. (2004b) ATR-FTIR spectroscopy and isotope labelling of the P-M intermediate of Paracoccus dentrificans cytochrome c oxidase. *Biochemistry* **43**, 14370-14378.

Iwaki, M. Yakovlev, G., Hirst, J., Osyczka, A., Dutton, P.L., Marshall, D., Rich, P.R. (2005) Direct observation of redox-linked histidine protonation changes in the iron-sulfur protein of the cytochrome bc(1) complex by ATR-FTIR spectroscopy. *Biochemistry* **44**, 4230-4237.

Jackson, M., and Mantsch, H.H. (1995) The use and misuse of FTIR spectroscopy in the determination of protein-structure. *Crit. Rev. Biochem. Mol. Biol.* **30**, 95-120.

Joshi, A.S., Zhou, J., Gohil, V.M., Chen, S., Greenberg, M.L. (2009) Cellular functions of cardiolipin in yeast. *Biochim Biophys Acta.* **1793**, 212-218.

Kalles, T. (1994) The Cytochrome b_6f Complex, in: Bryant, D.A. (Ed.), The Molecular Biology of Cyanobacteria, Kluwer Academic Publishers, pp. 259-317.

Klähn, M., Mathias, G., Kötting, C., Nonella, M., Schlitter, J., Gewert, K., and Tavan, P. (2004) IR Spectra of Phosphate Ions in Aqueous Solution: Predictions of a DFT/MM Approach Compared with Observations. *J. Phys. Chem. A* **108**, 6186-6194.

Klug, D.D., Zgierski, M.Z., Tse, J.S., Liu, Z., Kincaid, J.R., Czarnecki, K., Hemley, R.J. (2002) Doming modes and dynamics of model heme compounds. *PNAS* **99** (20), 12526-12530.

Knözinger, E. (1976) Far-Infrared Fourier Spectroscopy as a Method for Structure Determination in Chemistry. Angew. Chem. Int. Ed. 15, 25-39.

Knox, D.G., and Rosenberg, A. (1980) Fluctuations of protein-structure as expressed in the distribution of hydrogen-exchange rate constants. *Biopolymers* **19**, 1049-1068.

Koch, H.G.and Schneider, D. (2007) Assembly and stability of transmembrane cytochromes. *Curr. Chem. Biol.* **1**, 59-74.

Köhlstädt, M., Dörner, K., Labatzke, R., Koç, C., Hielscher, R., Schiltz, E., Einsle, O., Hellwig, P., and Friedrich, T. (2008) Heterologous Production, Isolation, Characterization and Crystallization of a Soluble Fragment of the NADH:Ubiquinone Oxidoreductase (Complex I) from *Aquifex aeolicus*, *Biochemistry* **47**, 13036-13045.

Kramer, D.M., and Crofts, A.R. (1994) Re-examination of the properties and function of the b cytochromes of the thylakoid cytochrome bf complex. *Biochim. Biophys. Acta* **1184**, 193-201.

Kroliczewski, J., Hombek-Urban, K., Szczepaniak, A. (2005) Integration of the thylakoid membrane protein cytochrome b_6 in the cytoplasmic membrane of *Escherichia coli*, *Biochemistry* **44**, 7570-7576.

Kroliczewski, J., Szczepaniak, A. (2002) In vitro reconstitution of the spinach chloroplast cytochrome b_6 protein from a fusion protein expressed in *Escherichia coli*. *Biochim. Biophys. Acta* **1598**, 177-184.

Kurisu, G., Zhang, H., Smith, J.L., Cramer, W.A. (2003) Structure of the cytochrome b_6f complex of oxygenic photosynthesis: tuning the cavity. *Science* **302**, 1009-1014.

Lange, C., and Hunte, C. (2002) Crystal structure of the yeast cytochrome bc_1 complex with its bound substrate cytochrome *c*. *Proc. Natl. Acad. Sci. USA* **99**, 2800-2805.

Lange, C., Nett, J.H., Trumpower, B.L., and Hunte, C. (2001) Specific roles of protein-phospholipid interactions in the yeast cytochrome bc_1 complex structure. *EMBO J.* **20**, 6591-6600.

Lazarou, M., Thorburn, D.R., Ryan, M.T., McKenzie, M. (2009) Assembly of mitochondrial complex I and defects in disease. *Biochim. Biophys. Acta* **1793**, 78-88.

Leberle, K., Kempf, I., and Zundel, G. (1989) An intramolecular hydrogen bond with large proton polarizability within the head group of phosphatidylserine. An infrared investigation. *Biophys. J.* **55**, 637-648.

Lee, A.G. (2004) How lipids affect the activities of integral membrane proteins. *Biochim. Biophys. Acta* **1666**, 62-87.

Leifm H., Sled, V.D., Ohnishi, T., Weiss, H., Friedrich, T. (1995) Isolation and characterization of the proton-translocating NADH:ubiquinone oxidoreductase from *Escherichia coli*. *Eur. J. Biochem.* **230**, 538-548.

Lewis, R.N. and McElhaney, R.N. (1996) Fourier Transform Infrared Spectroscopy in the Study of hydrated lipid bilayer membranes – in Infrared Spectroscopy of Biomolecules, edited by Mantsch, H.H and Chapman, D., Wiley-Liss, New York.

Lewis, R.N.A.H., McElhaney, R.N. (1998) The structure and organization of phospholipids bilayers as revealed by infrared spectroscopy. Chem. Phys. Lipids 96, 9-21.

Lewis, R.N.A.H., McElhaney, R.N. (2000) Calorimetric and Spectroscopic Studies of the Thermotropic Phase Behavior of Lipid Bilayer Model Membranes Composed of a Homologous Series of Linear Saturated Phosphatidylserines. *Biophys. J.* **79**, 2043-2055.

Lewis, R.N.A.H., McElhaney, R.N., Monck, M.A., Cullis, P.R. (1994) Studies og highly asymmetric mixed-chain diacyl phosphatidylcholines that form mixed-interdigitated

gel phases- Fourier-transform infrared and H-2 NMR spectroscopic studies of hydrocarbon chain conformation and orientational order in the liquid-crystalline state. *Biophys. J.* **67,** 197-207.

Magnitsky, S., Toulokhonova, L., Yano, T., Sled, V.D., Hägerhäll, C., Grivennikova, V.G., Burbaev, D.S., Vinogradov, A. D. and Ohnishi, T. (2002) EPR characterization of ubisemiquinones and iron-sulfur cluster N2, central components of the energy coupling in the NADH-ubiquinone oxidoreductase (complex I) in situ. *J. Bioenerg. Biomembr.* **34**, 193-208.

Maklakov, L.I., Aksakova, S.V. (1997) Low-frequency vibrational spectroscopy of amides and urethanes. *Russian Chemical Reviews* **66** (5), 375-388.

Malkin, R. (1973) The Chemical Properties of Ferredoxins. *in* Iron Sulfur Proteins (Lovenberg, W., Ed.), Vol. 2, 235-244, Academic Press, Orlando, Florida.

Mamedova, A.A., Holt, P.J., Carroll, J., Sazanov, L.A. (2004) Substrate-induced conformational change in bacterial complex I. *J. Biol. Chem.* **279**, 23830-23836.

Mantsch, H.H., Martin, A., Cameron, D.G. (1981) Characterization by Infrared Spectroscopy of the Bilayer to Nonbilayer Phase Transition of Phosphatidylethanolamines. *Biochemistry* **20**, 3138-3145.

Marboutin, L., Boussac, A., Berthomieu, C. (2006) Redox infrared markers of the heme and axial ligands in microperoxidase: bases for the analysis of *c*-type cytochromes. *J. Biol. Inorg. Chem.* **11**, 811-823.

Marboutin, L., Desbois, A., and Berthomieu, C. (2009) Low-frequency heme, iron-ligand, and ligand modes of imidazole and imidazolate complexes of iron protoporphyrin and microperoxidase in aqueous solution. An analysis by far-infrared difference spectroscopy. *J. Phys. Chem. B* **113**, 4492-4499.

Marshall, D., Fisher, N., grigic, L., Zickermann, V., Brandt, U., Shannon, R. J., Hirst, J., Lawewnce, R., and Rich, P.R. (2006) ATR-FTIR redox difference spectroscopy of *Yarrowia lipolytica* and bovine complex I. *Biochemistry* **45**, 5458-5467.

Mathiesen, C., and Hägerhäll, C. (2002) Transmembrane topology of the NuoL, M and N subunits of NADH:quinone oxidoreductase and their homologues among membrane-bound hydrogenases and bona fide antiporters. *Biochim. Biophys. Acta* **1556**, 121-132.

Mendelsohn, R., and Moore, D.J. (1998) Vibrational spectroscopic studies of lipid domains in biomembranes and model systems. *Chem. Phys. Lipids* **96**, 141-157.

Mitchell, P. (1961) Coupling of phosphorylation to electron and hydrogen transfer by a chemiosmotic type of mechanism. *Nature* **191**, 144-148.

Mitchell, P. (1975) The protonmotive Q cycle: a general formulation. *FEBS Lett.* **59**, 137-139.

Mitchell, P. (1976) Possible molecular mechanisms of the protonmotive function of cytochrome systems. *J. Theor. Biol*. **62**, 327-367.

Mitsuo, S., Kenichi, K., Yasutaka, K., Shusuke Y., Mitsutaka, O:, and Kizashi, Y. (2007) Theory of chemical bonds in metalloenzymes IV: Hybrid-DFT study of Rieske-type [2Fe-2S] clusters. *Int. J. Quantum Chem.* **107,** 609-627.

Moss, D., Nabedryk, E., Breton, J., and Mäntele, W. (1990) Redox-linked conformational changes in proteins detected by a combination of infrared spectroscopy and protein electrochemistry. *Eur., J., Biochem.* **187**,565-572.

Nyquist, R.M., Heitbrink, D., Bolwien, C., Wells, T. A., Gennis, R.B., Heberle, J. (2001) Perfusion-induced redox differences in cytochrome c oxidase: ATR/FT-IR spectroscopy. *FEBS Lett.* **505**,63-67.

Ohnishi, T. (1998) Iron-sulfur clusters/semiquinones in complex I. *Biochim. Biophys. Acta* **1364**, 186-206.

Ohnishi, T., Johnson, J.E. Jr., Yano, T., Lobrutto, R., and Widger, W.R. (2005) Thermodynamic and EPR studies of slowly relaxing ubisemiquinone species in the isolated bovine heart complex I. *FEBS Lett.* **579**, 500-506.

Ohnishi, T., Salerno, J.C. (2005) Conformation-driven and semiquinone-gated proton-pump mechanism in the NADH-ubiquinone oxidoreductase (complex I). *FEBS Lett.* **579,** 4555-4561.

Osyczka, A., Zhang, H.B, Mathe, C., Rich, P.R., Moser, C.C., Dutton, P.L. (2006) Role of the PEWY glutamate in hydroquinone-quinone oxidation-reduction catalysis in the Q(o) site of cytochrome bc(1). *Biochemistry* **45**, 10492-10503.

Palsdottir, H., and Hunte, C. (2003) Purification of the cytochrome bc_1 complex from yeast. In: Membrane protein purification and crystallization (Hunte, C., von Jagow, G., and Schägger, H., Eds.) Academic Press, USA, pp. 191-203.

Palsdottir, H., and Hunte, C. (2004) Lipids in membrane protein structures. *Biochim. Biophys. Acta* **1666**, 2-18.

Page, C.C., Moser, C.C., Chen, X., and Dutton, P.L. (1999) Natural engineering principles of electron tunneling in biological oxidation-reduction. *Nature* **402**, 47-52.

Papakostidis, G., and Zundel, G. (1973) Polarizable hydrogen bond formation and ionic interactions in model phospholipid polar head molecules. *Z. Naturforsch.* **28b**, 323-330.

Peng, G., Fritzsch, G., Zickermann, V., Schägger, H., Mentele, R., Lottspeich, F., Bostina, M., Radermacher, M., Huber, R., Stetter, K.O., and Michel, H. (2003) Isolation, characterization and electron microscopic single particle analysis of the NADH:ubiquinone oxidoreductase (complex I) from the hyperthermophilic eubacterium *Aquifex aeolicus*. *Biochemistry* **42**, 3032-3039.

Pfeiffer, K., Gohil, V., Stuart, R.M., Hunte, C., Brandt, U., Greenberg, M.L. and Schägger, H. (2003) Cardiolipin stabilizes respiratory chain complex. *J. Biol. Chem.* **278**, 52873-52880.

Pohl, T., Uhlmann, M., Kaufenstein, M., and Friedrich, T. (2007) Lambda Red-Mediated Mutagenesis and Efficient Large Scale Affinity Purification of the *Escherichia coli* NADH:Ubiquinone Oxidoreductase (Complex I), *Biochemistry* **46**, 10694-10702.

Pohle, W., Selle, C., Fritzsche, H., Binder, H. (1998) Fourier Transform Infrared Spectroscopy as a Probe fort he Study of the Hydration of Lipid Self-Assemblies. I. Methodolgy and General Phenomena. Biospectroscopy 4, 267-280.

Pohle, W., Selle, C., Fritzsche, H., Bohl, M. (1997) Comparative FTIR spectroscopic study upon the hydration of lecithins and cephalins. *J. Mol. Struct.* **408/409**, 273-277.

Popova, A.V., Hincha, D.K. (2003) Intermolecular Interactions in Dry and Rehydrated Pure and Mixed Bilayers of Phosphatidylcholine and Digalactossyldiacylglyerol: A Fourier Transform Infrared Spectroscopy Study. *Biophys. J.* **85**, 1682-1690.

Prodöhl, A., Dreher, C., Hielscher, R., Hellwig, P., Schneider, D. (2007) Heterologous expression and *in vitro* assembly of the transmembrane cytochrome b_6, *Prot. Ex. Purif.* **56**, 279-285.

Radermacher, M., Ruiz, T., Clason, T., Benjamin, S., Brandt, U:, and Zickermann, V: (2006) The three-dimensional structure of complex I from *Yarrowia lipolytica*: a highly dynamic enzyme. *J. Struct. Biol.* **154**, 269-279.

Ritter, M., Anderka, O., Ludwig, B., Mäntele, W., and Hellwig, P. (2003) Electrochemical and FTIR spectroscopic characterization of the cytochrome bc_1 complex from *Paracoccus denitrificans*: Evidence for protonation reactions coupled to quinone binding, *Biochemistry* **42**, 12391-12399.

Ritter, M., Palsdottir, H., Abe, M., Mäntele, W., Hunte, C., Miyoshi, H., and Hellwig, P. (2004) Direct evidence for the interaction of stigmatellin with a protonated acidic group in the bc_1 complex from *Saccharomyces cerevisiae* as monitored by FTIR difference spectroscopy and ^{13}C specific labeling. *Biochemistry* **43**, 8439-8446.

Sazanov, L.A. (2007) Respiratory complex I: mechanistic and structural insights provided by the crystal structure of the hydrophilic domain. *Biochemistry* **46**, 2275-2288.

Sazanov, L.A., Carroll, J., Holt, P., Toime, L. and Fearnley, I.M. (2003) A role for native lipids in the stabilization and two-dimensional crystallization of the *Escherichia coli* NADH-ubiquinone oxidoreductase (complex I). *J. Biol. Chem.* **278**, 19483-19491.

Sazanov, L.A., and Hinchliffe, P. (2006) Structure of the hydrophilic domain of respiratory complex I from *Thermus thermophilus. Science* **311**, 1430-1436.

Schägger, H., Hagen, T., Roth, B., Brandt, U., Link, T.A. and von Jagow, G. (1990) Phospholipid specificity of bovine heart bc_1 complex . *Eur. J. Biochem.* **190**, 123-130.

Schägger, H. and von Jagow, G. (1991) Blue native electrophoresis for isolation of membrane protein complexes in enzymatically active form, *Anal. Biochem.* **199**, 223-231.

Scheirlinckx F., Raussens V., Ruysschaert J.M., Goormaghtigh E. (2004) Conformational changes in gastric H+/K+-ATPase monitored by difference Fourier-transform infrared spectroscopy and hydrogen/deuterium exchange. *Biochem J.* **382**, 121-9.

Scherer, J.R. (1989) On the position of the hydrophobic/hydrophilic boundary in lipid bilayers. *Biophys. J.* **55**, 957-964.

Schlame, M., Rua, D., and Greenberg, M.L. (2000) The biosynthesis and function role of cardiolipin. *Prog. Lipid res.* **39**, 257-288.

Schulz, M., Brugna, M., Lebrun, E., Baymann, F., Huber, R., Stetter, K.-O., Günter, H., Toci, R., Lemesle-Neunier, D., Tron, P., Schmidt, C., and Nitschke, W. (2000) Early evolution of cytochrome *bc* complexes. *J. Mol. Biol.* **300**, 663-675.

Senent, M.L, Smeyers, Y.G., Moule, D.C. (1998) An *ab initio* three-dimensional torsion-torsion-wagging analysis of the far infrared spectra of dimethylamine. *Molecular Physics* **94** (6), 949-961.

Siebert, F., Mäntele, W., Gerwert, K. (1983) Fourier-transform infrared spectroscopy applid to rhodopsin. The problem of the protonation state of the retinylidene Schiff base re-investigated. *Eur. J. Biochem.* **136**, 119-127.

Siminovitch, D.J., Wong, P.T.T., and Mantsch, H.H. (1987) Effects of Cis and Trans Unsaturation on the Structure of Phospholipid Bilayers: A High-Pressure Infrared Spectroscopic Study. *Biochemistry* **26**, 3277-3287.

Simon, S.A. and McIntosh, T.J. (1986) Depth of water penetration into lipid bilayers, in *Methods in Enzymology*, Academic Press, Inc., London, pp. 511-521.

Sinegina, L., Wikström, M., Verkhovsky, M.I., and Verkhovskaya, M.L. (2005) Activation of isolated NADH:ubiquinone reductqse I (complex I) from *Escherichia coli* by detergent

and phospholipids. Recovery of ubiquinone reductase activity and changes in EPR signals of iron-sulfur clusters. *Biochemistry* **44**, 8500-8506.

Singer, S.J., and Nicolson, G.L. (1972). The fluid mosaic model of the structure of cell membranes. *Science* **175**,720-731.

Sharpley, M.S., Shannon, R.J., Draghi, F., and Hirst, J. (2006) Interactions between phospholipids and NADH:ubiquinone oxidoreductase (complex I) from bovine mitochondria. *Biochemistry* **45**, 241-248.

Snyder, R.G., Liang, G.L., Strauss, H.L., Mendelsohn, R. (1996) IR Spectroscopic Study of the Structure and Phase Behavior of Long-Chain Diacylphosphatidylcholines in the Gel State. Biophys. J. 71, 3186-3198.

Stolpe, S., and Friedrich, T. (2004) The *Escherichia coli* NADH:ubiquinone oxidoreductase (complex I) is a primary proton pump but may be capable of secondary sodium antiport. *J. Biol. Chem.* **279**, 18377-18383.

Stroebel, D., Choquet, Y., Popot, J.L., Picot, D. (2003) An atypical haem in the cytochrome b(6)f complex, *Nature* **426**, 413-418.

Stuard, B. (1997) Biological Applications of Infrared Spectroscopy. John Wiley & Sons, Ltd., Chichester.

Studier, F. and Moffatt, B. (1986) Use of bacteriophage T7 RNA polymerase to direct selective high-level expression of cloned genes, *J. Mol. Biol.* **189**, 113-130.

Surewicz, W.K., Mantsch, H.H., And Chapman, D. (1993) Determination of protein secondary structure by Fourier transform infrared spectroscopy: a critical assessment. *Biochemistry* **32**, 389-394.

Susi, H., and Byler, D.M. (1983) Protein Structure by Fourier Transform Infrared Spectroscopy: second derivative spectra. *Biochem. Biophys. Res. Commun.* **115**, 391-397.

Tamm, L.K., and Tatulian, S.A. (1997) Infrared spectroscopy of proteins and peptides in lipid bilayers. *Q. Rev. Biophys.* **30**, 365-429.

Trumpower, B.L. (1990) The protonmotive Q cycle. Energy transduction by coupling of proton translocation to electron transfer by the cytochrome bc_1 complex. *J. Biol. Chem.* **265**, 11409-11412.

van Klompenburg, W., Nilsson, I., von Heijne, G., and de Kruijff, B. (1997) Anionic phospholipids are determinants of membrane protein topology. *EMBO J.* **16**, 4261-4266.

Venyaminov, S.Y. and Kalnin, N.N. (1990) Quantitative IR Spectrophotometry of Peptide Compounds in Water (H2O) Solutions. I. Spectral Parameters of Amino Acid Residue Absorption Bands. Biopolymers 30, 1243-1257.

Verkhovskaya, M.L., Belevich, N., Euro, L., Wikström, M., and Verkhovsky, M.I. (2008) Real-time electron transfer in respiratory complex I. *Proc. Natl. Acad. Sci. USA* **105**, 3763-3767.

Vigano, C., Smeyers, M. Raussens, V., Scheirlinckx, F., Ruysschaert, J.M., Goormaghtigh, E. (2004) Hydrogen-deuterium exchange in membrane proteins monitored by IR spectroscopy: A new tool to resolve protein structure and dynamics. *Biopolymers* **74**, 19-26.

Walker, J.E. (1992) The NADH:ubiquinone oxidoreductase (complex I) of respiratory chains. *Q. Rev. Biophys.* **25**, 253-324.

Wallace, B.J., and Young, I.G. (1977) Role of quinines in electron transport to oxygen and nitrate in Escherichia coli. Studies with a ubiA- menA- double quinine mutant, *Biochim. Biophys. Acta* **461**, 84-100.

Weidner, U., Geier, S., Ptock, A., Friedrich, T., Leif, H., and Weiss, H. (1993) The gene locus of the proton-translocating NADH:ubiquinone oxidoreductase in *Escherichia coli*. Organization of the 14 genes and relationship between the derived proteins and subunits of mitochondrial complex I. *J. Mol. Biol.* **233**, 109-122.

Weiss, H., Friedrich, T., Hofhaus, G., and Preis, D. (1991) The respiratory-chain NADH dehydrogenase (complex I) of mitochondria. *Eur. J. Biochem.* **197**, 563-576.

Wenz, T., Hellwig, P., MacMillan, F., Meunier, B., Hunte, C. (2006) Probing the role of E272 in quinol oxidation of mitochondrial complex III. *Biochemistry* **45**, 9042-9052.

Wenz, T., Hielscher, R., Hellwig, P., Schägger, H., Richers, S., Hunte, C. (2009) Role of phospholipids in respiratory cytochrome bc(1) complex catalysis and supercomplex formation. *Biochim. Biophys. Acta* **1787**, 609-616.

Wikström, M. (1984) Two protons are pumped from the mitochondrial matrix per electron transferred between NADH and ubiquinone. *FEBS Lett.* **169**, 300-304.

Wille, G., Ritter, M., Friedemann, R., Mäntele, W., and Hübner, G. (2003) Redox-triggered FTIR difference spectra of FAD in aqueous solution and bound to flavoproteins. *Biochemistry* **42**, 14814-14821.

Wong, P.T.T. and Mantsch, H.H. (1988) High-pressure infrared spectroscopic evidence of water binding sites in 1,2-diacyl phospholipids. *Chem. Phys. Lipids* **46**, 213-224.

Wong, P.T.T., and Huang, C. (1989) Structural Aspects of Pressure Effects on Infrared Spectra of Mixed-Chain Phosphatidylcholine Assemblies in D_2O. *Biochemistry* **28**, 1259-1263.

Wolpert, Martina (2007) Ein kombinierter infrarotspektroskopischer und DFT-Ansatz zur Charakterisierung von Chinonen im Atmungskettenkomplex III. Dissertation, Frankfurt, Germany.

Yagi, T., and Matsuno-Yagi, A. (2003) The proton-translocating NADH-quinone oxidoreductase in the respiratory chain: the secret unlocked. *Biochemistry* **42**, 2266-2274.

Yang, M.J., Trumpower, B.L. (1994) Deletion of QCR6, the gene encoding subunit 6 of the mitochondrial cytochrome bc1 complex, blocks maturation of cytochrome-c1, and causes temperature-sensitive peptide growth in Sacchromyces-cerevisae. *J. Biol. Chem.* **269**, 1270-1275.

Yano, T. Dunham, W.R. and Ohnishi, T. (2005) Characterization of the $\Delta\mu_H^+$-sensitive ubisemiquinone species SQ_{Nf} and the interaction with cluster N2: new insight into the energy-coupled electron transfer in complex I. *Biochemistry* **44**, 1744-1754.

Yano, T., Magnitsky, S., and Ohnishi, T. (2000) Characterization of the complex I-associated ubisemiquinone species: toward the understanding of their functional roles in the electron/proton transfer reaction. *Biochim. Biophys. Acta* **1459**, 299-304.

Yoon, T., and Cowan, J.A. (2003) Iron-sulfur cluster biosynthesis. Characterization of frataxin as an iron donor for assembly of [2Fe-2S] clusters in ISU-type proteins. *J. Am. Chem. Soc.* **125**, 6078-6084.

Yu, C.A., Cen, X., Ma, H.W., Yin, Y., Yu, L., Esser, L., Xia, D. (2008) Domain conformational switch of the iron-sulfur protein in cytochrome bc1 complex is induced by the electron transfer from cytochrome bL to bH. Biochim. Biophys. Acta **1777**, 1038-1043.

Yu, C.A., Tian, H., Zhang, L., Deng, K.P., Shenoy, S. K., Yu, L., Xia, D., Kim, H., Deisenhofer, J. (1999) Structural basis of multifunctional bovine mitochondrial cytochrome bc(1) complex. *J. Bioenerg. Biomembr.* **31**,191-199.

Yu, C.A. and Yu, L. (1980) Structural role of phospholipids in ubiquinol-cytochrome *c* reductase. *Biochemistry* **19**, 5715-5720.

Zhang, Z., Huang, L., Shulmeister, V.M., Chi, Y.I., Kim, K.K., Hung, L.-W., Crofts, A.R., Berry, E.A., and Kim, S.-H. (1998) Electron transfer by domain movement in cytochrome bc_1. *Nature* **392**, 677-684.

Zheng, W., Brooks, B.R., and Thirumalai, D. (2006) Low-frequency normal modes that describe allosteric transitions in biological nanomachines are robust to sequence variations. *Proc. Natl. Acad. Sci. U.S.A.* **103**, 7664-7669.

Zickermann, V., Bostina, M., Hunter, C., Ruiz, T., Radermacher, M., and Brandt, U. (2003) Functional implications from an unexpected position of the 49-kDa subunit of NADH:ubiquinone oxidoreductase. J. Biol. Chem. 278, 29072-29078.

Zinser, E., Sperka, G., Fasch, E.V., Kohlwein, S.D., Paltauf, F., and Daum, G. (1991) Phospholipid synthesis and lipid composition of subcellular membranes in the unicellular eukaryote *Saccharomyces cerevisiae*. *J. Bacteriol.* **173**, 2026-2034.

Zscherp, C., and Barth, A. (2001) Reaction-induced infrared difference spectroscopy for the study of protein reaction mechanisms. *Biochemistry* **40,** 1875-1883.

Zundel, G. (1996) The far infrared vibration of hydrogen bonds with large proton polarizability. *J. Mol. Struct.* **381**, 23-37.

Zundel, G. (2000) Hydrogen bonds with large proton polarizability and proton transfer processes in electrochemistry and biology. *Adv. Chem. Phys.* **111**, 1-218.

Zundel, G., Brzezinski, B., and Olejinik, J. (1993) On hydrogen and deuterium bonds as well as on Li^+, Na^+ and Be^{2+} bonds: IR continua and cation polarizabilities. *J. Mol. Struct.* **300**, 573-592.